ULPGC
Universidad de Las Palmas de Gran Canaria
Instituto Universitario de Oceanografía y Cambio Global
IOCAG

Doctorado en Oceanografía y Cambio Global
Universidad de Las Palmas de Gran Canaria

Tesis Doctoral

Thirty years of GO-SHIP and WOCE data: Atlantic overturning of mass, heat, freshwater, and anthropogenic Carbon transport

Verónica Caínzos Díaz

Las Palmas de Gran Canaria, Junio de 2023

ULPGC
Universidad de Las Palmas de Gran Canaria | Escuela de Doctorado

Dª MAGDALENA SANTANA CASIANO, COORDINADORA DEL PROGRAMA DE DOCTORADO EN OCEANOGRAFÍA Y CAMBIO GLOBAL DE LA UNIVERSIDAD DE LAS PALMAS DE GRAN CANARIA

INFORMA,

De que la Comisión Académica del Programa de Doctorado, en su sesión de fecha XX de XXXX de 2023 tomó el acuerdo de dar el consentimiento para su tramitación, a la tesis doctoral titulada ”*Thirty years of GO-SHIP and WOCE data: Atlantic overturning of mass, heat, freshwater, and anthropogenic Carbon transport*” presentada por la doctoranda Dª Verónica Caínzos Díaz y dirigida por el Doctor Alonso Hernández Guerra y la Doctora María Dolores Pérez Hernández.

Y para que así conste, y a efectos de lo previsto en el Artículo 11 del Reglamento de Estudios de Doctorado (BOULPGC 04/03/2019) de la Universidad de Las Palmas de Gran Canaria, firmo la presente en Las Palmas de Gran Canaria, a XX de XXXXX de dos mil veintitrés.

ULPGC
Universidad de
Las Palmas de
Gran Canaria | Escuela de
Doctorado

UNIVERSIDAD DE LAS PALMAS DE GRAN CANARIA
ESCUELA DE DOCTORADO

Programa de doctorado en Oceanografía y Cambio Global.

Título de la Tesis: Thirty years of GO-SHIP and WOCE data: Atlantic overturning of mass, heat, freshwater, and anthropogenic Carbon transport

Tesis Doctoral presentada por Dª Verónica Caínzos Díaz.

Dirigida por el Dr. D Alonso Hernández Guerra.
Codirigda por la Dra. Dª María Dolores Pérez Hernández.

Las Palmas de Gran Canaria, a XX de XXXXX de 2023.

El Director, La Codirectora, La Doctoranda,

Á miña familia

Agradecimientos
Acknowledgments

Ahora que he llegado al momento de escribir esta parte, me asombro de la cantidad de personas que han contribuido a que haya conseguido salir victoriosa. No puedo decir que haya sido un camino fácil, sobre todo teniendo en cuenta las dificultades que surgieron para realizar estancias y participar en congresos. Sin embargo, esta trayectoria ha sido mejor tras haberla compartido con toda esta gente.

En primer lugar, me gustaría dar las gracias a mis directores, Alonso Hernández Guerra y Lola Pérez Hernández. Sin ellos llegar hasta aquí no habría sido posible. Les debo su motivación y visión de futuro que ha hecho posible que pueda seguir con mi carrera investigadora. Además, he tenido la suerte de trabajar con Pedro Vélez del IEO, que, aunque finalmente no haya sido mi director, ha hecho muchas veces esas funciones.

Esta tesis no sería lo mismo sin la ayuda que me han ofrecido durante mis estancias de investigación. En primer lugar, Elaine McDonagh, que me recibió en Bergen y me ayudó a entender los entresijos del modelo inverso y a darle forma en mi cabeza. Durante las varias estancias cortas que realicé en el Instituto de Investigacións Mariñas de Vigo y las numerosas videollamadas en medio, tanto Fiz Fernández Pérez como Antón Velo me han ayudado enormemente y se han interesado en sacar adelante esa parte de la tesis. Gracias por abrirme las puertas y por tener paciencia conmigo. Y, por último, he tenido el privilegio de trabajar con Renellys Perez y Shenfu Dong en el Atlantic Oceanographic and Meteorological Laboratory de la NOAA en Miami. Desde el primer momento me acogieron e hicieron todo lo posible para que pudiera cumplir los objetivos que nos habíamos marcado.

Me gustaría agradecer a mi familia el apoyo incondicional que siempre he recibido de su parte. A los que están y a los que ya no están. Siento que el destino me haya llevado lejos del Farragoto. A mis padres Antonio e Isabel, por su comprensión y por recordarme de vez en cuando lo orgullosos que están de mí. A mi hermano Emilio (y casi hermana Desi) por conseguir hacerme sacar siempre mi lado más infantil y a mis abuelos por su cariño. A Lola, Beti y Elena por empujarme siempre a nuevas aventuras.

Estos cuatro años en la Universidad de Las Palmas de Gran Canaria los he podido compartir con Cris, Dani, Tania, Marta, Melania, Neus, Miguel, David Curbelo, Patri y David Sosa. Gracias por hacer más amenas las horas muertas en Tafira y por recordarme lo que era tener 25 años. Y a Maria, porque ella fue mi guía cuando llegué aquí y nunca dudó en ofrecerme su ayuda. Echamos de menos la forma en la que contagiaba su alegría y energía a todo el mundo.

A toda la gente de Galicia a la que quiero. A Inés por estar siempre ahí para aguantarme. A Ainho, Sara y Rita por alegrarse siempre de mis buenas noticias y de sacarme una risa con las malas. Y por acogerme cada vez que me presentaba en Vigo para disfrutar del buen tiempo que hacía allí.

Y por el grupo de exiliadas en Las Palmas: Lulu, Sara, Amparo y Alicia. Echaré de menos nuestras charlitas y tener que apurar para ponernos al día cada vez que nos vemos. Gracias por hacerme un hueco en vuestra casa.

Y, por último, no me quiero olvidar de toda la gente que conocí en Mallorca y que me ayudó a crecer como persona e investigadora durante mis dos años en el Centro Oceanográfico de Baleares y que me animaron a dar este paso. En especial a Safo por toda su ayuda e información y a las topitas que nunca se sorprenderán de una desgracia ajena. Gracias Safo, Lara, Laura, Cati, Javi, Merlu, Vero, Ro, Victoria, Quique, Vicenç, Alex, Albert, Andrea y Sergio.

Abstract

The Atlantic Meridional Overturning Circulation (AMOC) plays a vital role in global climate, redistributing heat and freshwater by upper warm waters flowing northward and cold deep waters flowing southward. Accurately assessing AMOC strength with in situ observations has inspired a number of dedicated observing systems in the Atlantic since the 2000s. The AMOC is predicted to decline due to anthropogenic climate change, with major implications for global climate. However, no consensus has been reached on whether the slowdown of the AMOC and its associated heat and freshwater transports is occurring. These dedicated systems are too recent to detect long-term trends. On the other hand, high-resolution hydrographic data provide the opportunity to characterize the AMOC and its associated heat and freshwater transports for the whole water column over the last thirty years.

We have analysed hydrographic data from the available zonal sections across the Atlantic for thirty years that predate and overlap the era of AMOC observing systems. For each decade, 1990-99, 2000-09 and 2010-19, we have used the thermal wind equation together with an inverse model to depict the circulation for the whole Atlantic basin, attending to horizontal and vertical transports between sections.

The circulation pattern describes two counter-rotating cells in the upper and abyssal ocean, which follow the path of the main water masses of the Atlantic – the northward upper layers of thermocline and intermediate waters, the southward deep layers of North Atlantic Deep Water and the abyssal layers of Antarctic Bottom Water flowing northward. Our results show no changes in the AMOC intensity for all sections analyzed of the whole Atlantic Ocean for the last thirty years. We also find an increased export of freshwater from the South Atlantic associated with an increase in the salinity of upper layers.

Moreover, the circulation in the Atlantic Ocean is marked by the complex system of pathways of the AMOC. These currents change meridionally due to the interaction with nearby water masses and geographic features. Inverse methods enable the quantification of absolute meridional transports across these sections, determining the strength of each current at a certain latitude in terms of mass, heat and freshwater, as well as their transport-weighted temperature and salinity.

Generally, no changes can be found among decades for each of the currents in terms of mass, heat or freshwater transports or the properties. In the South Atlantic, nearly 61 Sv enter from the Southern and Indian Oceans at 45°S. The South Atlantic subtropical gyre exports northward 17.0 ± 1.2 Sv and around 1 PW via the North Brazil Current and -55 Sv southward at 45°S into the Antarctic Circumpolar Current. In the north Atlantic, most of the transport is advected northward via the western boundary currents, which reduce in strength as they take part in convection processes in the subpolar North Atlantic, reflected also in the northward progress of mass and heat transport. Deep layers carry waters southward along the western boundary, maintaining similar values of mass and heat transport until the separation into an eastern branch that crosses the mid-Atlantic ridge in the south Atlantic. Abyssal waters originating in the Southern Ocean distribute along the South Atlantic mainly through its western basin, flowing northward up to 24.5°N, subjected to an increasing trend in their temperature with time.

The change in anthropogenic CO_2 (C_{anth}) in the Atlantic Ocean is linked to the AMOC, that redistributes C_{anth} meridionally and in depth. With the results from the inverse model not only we can study physical parameters associated with the AMOC, but also how biogeochemistry is affected. We have employed direct biogeochemical measurements and hydrographic data from the last thirty years and adjusted the mass and biogeochemical property transports using inverse models for each decade. In addition, we have computed the meridional transports and the vertical transports between two sections by advection and diffusion at the interphases between layers. We have focused on the repeated sections at three latitudes – 30°S, 24.5°N and 55°N, breaking up the Atlantic into two boxes. The net transport estimated presents an upper and abyssal northward transport of C_{anth} and a southward component in deep layers.

The change in time in the net transports of C_{anth} appears to be mainly due to modifications in the transport of upper layers. The lower layer of the AMOC, a combination of deep and abyssal waters, maintain more consistent transports in time. Vertical advection plays an important role in the North Atlantic, exporting C_{anth} from upper to deep layers. In the South Atlantic, the newly formed Antarctic Bottom Water exports C_{anth} from abyssal to deep layers. The strong gradient in C_{anth} concentration at the interphase of upper and deep layers results in a strong vertical diffusion.

Resumen

La Circulación Latitudinal de Retorno del Atlántico (AMOC, por sus siglas en inglés *Atlantic Meridional Overturning Circulation*) desempeña un papel vital en el clima terrestre, redistribuyendo calor y agua dulce mediante flujos hacia el norte de aguas cálidas superficiales y flujos hacia el sur de aguas frías profundas. Se prevé que la intensidad de la AMOC disminuya debido al cambio climático antropogénico, con importantes consecuencias para el clima mundial. La evaluación con precisión de la magnitud de la AMOC mediante observaciones *in-situ* ha inspirado la aparición de una serie de sistemas de observación específicos en el Atlántico desde la década de los 2000. Sin embargo, aún no se ha podido establecer un consenso sobre si se está produciendo o no una ralentización de la AMOC y de sus transportes asociados de calor y agua dulce. Estos sistemas de monitorización son demasiado recientes para detectar tendencias a largo plazo. Sin embargo, los datos hidrográficos de alta resolución ofrecen la oportunidad de caracterizar la AMOC y sus transportes asociados de calor y agua dulce para toda la columna de agua en los últimos treinta años.

Hemos analizado los datos hidrográficos de todas las secciones zonales disponibles del Atlántico durante treinta años que preceden y se solapan con la era de los sistemas de observación de la AMOC. Para cada década, definidas en el periodo 1990-99, 2000-09 y 2010-19, hemos construido un modelo inverso que permite estimar los transportes horizontales y verticales entre secciones y que nos da una representación de la circulación para toda la cuenca atlántica. El modelo de circulación describe dos celdas que rotan en sentido contrario en el océano superior y abisal, siguiendo la trayectoria de las principales masas de agua del Atlántico: las capas superiores hacia el norte que transportan aguas de la termoclina e intermedias, las capas profundas que llevan hacia el sur el Agua Profunda del Atlántico Norte (NADW, por sus singlas en inglés *North Atlantic Deep Water*) y las capas abisales que fluyen hacia el norte con el Agua de Fondo Antártica (AABW, por sus siglas en inglés *Antarctic Bottom Water*). Nuestros resultados no muestran cambios en la AMOC para todas las secciones analizadas en todo el Océano Atlántico durante los últimos treinta años. Sin embargo, encontramos un aumento de la exportación de agua dulce desde el Atlántico Sur asociado a un aumento de la salinidad en capas superficiales.

Por otra parte, la circulación en el Océano Atlántico está marcada por el complejo sistema de

trayectorias de la AMOC. Estas corrientes cambian meridionalmente debido a la interacción con las masas de agua cercanas y con la geomorfología de la cuenca. Los métodos inversos permiten cuantificar los transportes meridionales absolutos a través de estas secciones, determinando la intensidad de cada corriente en una determinada latitud en términos de masa, calor y agua dulce, así como su temperatura y salinidad ponderadas por el transporte.

En general, no se encuentran cambios entre décadas para cada una de las corrientes en términos de transporte de masa o de sus propiedades. En el Atlántico Sur, a una latitud de 45°S, fluyen hacia el norte 61 Sv procedentes de los océanos Austral e índico. El giro subtropical del Atlántico Sur exporta hacia el norte 17,0 ± 1,2 Sv y alrededor de 1 PW a través de la Corriente del Norte de Brasil (*North Brazil Current* en inglés) y -55 Sv hacia el sur a la Corriente Circumpolar Antártica (*Antarctic Circumpolar Current* en inglés) en 45°S. En el Atlántico norte, la mayor parte del transporte se desplaza hacia el norte a través de las corrientes de contorno occidentales, cuya intensidad disminuye a medida que participan en los procesos de convección en el Atlántico norte subpolar, lo que se refleja también en el avance hacia el norte del transporte de masa y calor. Las capas profundas transportan las aguas hacia el sur a lo largo del borde occidental, manteniendo valores similares de transporte de masa y calor hasta la separación en una rama oriental que cruza la dorsal mesoatlántica en el Atlántico sur.

El cambio de CO_2 antropogénico (C_{anth}) en el Océano Atlántico está vinculado a la AMOC, que redistribuye el C_{anth} meridionalmente y en profundidad. A partir del ajuste del transporte con modelo inverso, no sólo podemos estudiar los parámetros físicos asociados a la AMOC, sino también cómo se ve afectada la biogeoquímica. Hemos empleado mediciones biogeoquímicas directas y datos hidrográficos de los últimos treinta años, ajustando el transporte de masa y de otras propiedades biogeoquímicas mediante modelos inversos para cada década con condiciones tanto físicas como biogeoquímicas. A continuación, hemos calculado los transportes meridionales y los transportes verticales por advección y difusión en las interfases entre pares de secciones. Nos hemos centrado en las tres secciones repetidas – 30°S, 24,5°N y 55°N, dividiendo el Océano Atlántico en dos cajas, con transportes netos para capas superiores, profundas y abisales. En capas superiores y abisales aparece un transporte hacia el norte de C_{anth}, con un componente hacia el sur en capas profundas.

El cambio en el tiempo de los transportes netos de C_{anth} parece deberse principalmente a modificaciones en el transporte de las capas superiores. La capa inferior de la AMOC, una combinación de aguas profundas y abisales, mantiene transportes más consistentes en el tiempo. La advección vertical desempeña un papel importante en el Atlántico Norte, exportando C_{anth} de las capas superiores a las profundas. En el Atlántico Sur, la AABW, de formación reciente, exporta C_{anth} de las capas abisales a las profundas. El fuerte gradiente de concentración de C_{anth} en la interfase entre capas superiores y profundas da lugar a una fuerte difusión vertical.

Contents

List of Figures

List of Tables

List of Abbreviations

AABW	Antarctic Bottom Water
AC	Antilles Current
ACC	Antarctic Circumpolar Current
AMOC	Atlantic Meridional Overturning Circulation
AMV	Atlantic Multidecadal Variability
AOU	Apparent Oxygen Utilization
A_T	Total Alkalinity
BeC	Benguela Current System
BODC	British Oceanographic Data Centre
BrC	Brazil Current
C_{anth}	Anthropogenic CO_2
CANYON-B	CArbonate system and Nutrients concentration from hYdrological properties and Oxygen using a Neural-network
CC	Canary Current
CCHDO	CLIVAR and Carbon Hydrographic Data Office
CLIVAR	Climate and Ocean: Variability, Predictability and Change
C_T	Total inorganic Carbon concentration
DEBC	Deep Eastern Boundary Current
DSOW	Denmark Strait Overflow Waters
DWBC	Deep Western Boundary Current
dWGC	Deep West Greenland Current

EGC	East Greenland Current
ERRC	East Reykjanes Ridge Current
FC	Florida Current
FS	Florida Strait
GLODAPv2	Global Ocean Data Analysis Project version 2
GO-SHIP	Global Ocean Ship-Based Hydrographic Investigations Program
GS	Gulf Stream
IC	Irminger Current
IES	Inverted EchoSounder
ISOW	Iceland-Scotland Overflow Waters
ITCZ	Intertropical Convergence Zone
LC	Labrador Current
MAR	Mid Atlantic Ridge
MC	Malvinas Current
MOVE	Meridional Overturning Variability Experiment
NAC	North Atlantic Current
NADW	North Atlantic Deep Water
NAO	North Atlantic Oscillation
NBrC	North Brazil Current
NCAR	National Center for Atmospheric Research
NCEP	National Centers for Environmental Prediction
NIIC	North Icelandic Irminger Current
OSNAP	Overturning in the Subpolar North Atlantic Program
OVIDE	Observatoire de la Variabilité Interannuelle à DEcennale
RAPID	Rapid Climate Change-Meridional Overturning Circulation and Heatflux Array
SAMBA	South Atlantic MOC Basin-wide Array
SEC	South Equatorial Current
SPNA	Subpolar North Atlantic

TrOCA	Tracer combining Oxygen, inorganic Carbon and total Alkalinity
TSAA	Tropical South Atlantic Array
TSS	Transient steady state
TTD	Transient time distributions
TW	Transport-weighted
UMO	Upper mid-ocean
uWGC	Upper West Greenland Current
WOCE	World Ocean Circulation Experiment
XBT	Expendable bathythermograph
$\varkappa_z$	Diffusion coefficient
ω	Advection velocity

Chapter 1

Introduction

1.1 The Atlantic Meridional Overturning Circulation

The Atlantic Ocean is characterized by its net northward transport of heat across the whole basin, achieved mainly by the Atlantic Meridional Overturning Circulation (AMOC). This is one of the primary mechanisms redistributing heat in the ocean, along with mass, salt, carbon, nutrients and other biogeochemical properties (Chidichimo et al., 2023; Kersalé et al., 2020; McCarthy et al., 2020; Steinfeldt et al., 2009). The AMOC is composed of a system of complex and irregular three-dimensional pathways that carry water masses in surface, intermediate, deep and abyssal layers, transforming these water masses on their way (Cessi, 2019).

The overturning circulation appears as two counter-rotating cells (Figure 1.1). In the upper cell, a net northward transport carries warm thermocline and intermediate waters occupying the first kilometer of the water column. On their way northward, these waters lose buoyancy due to

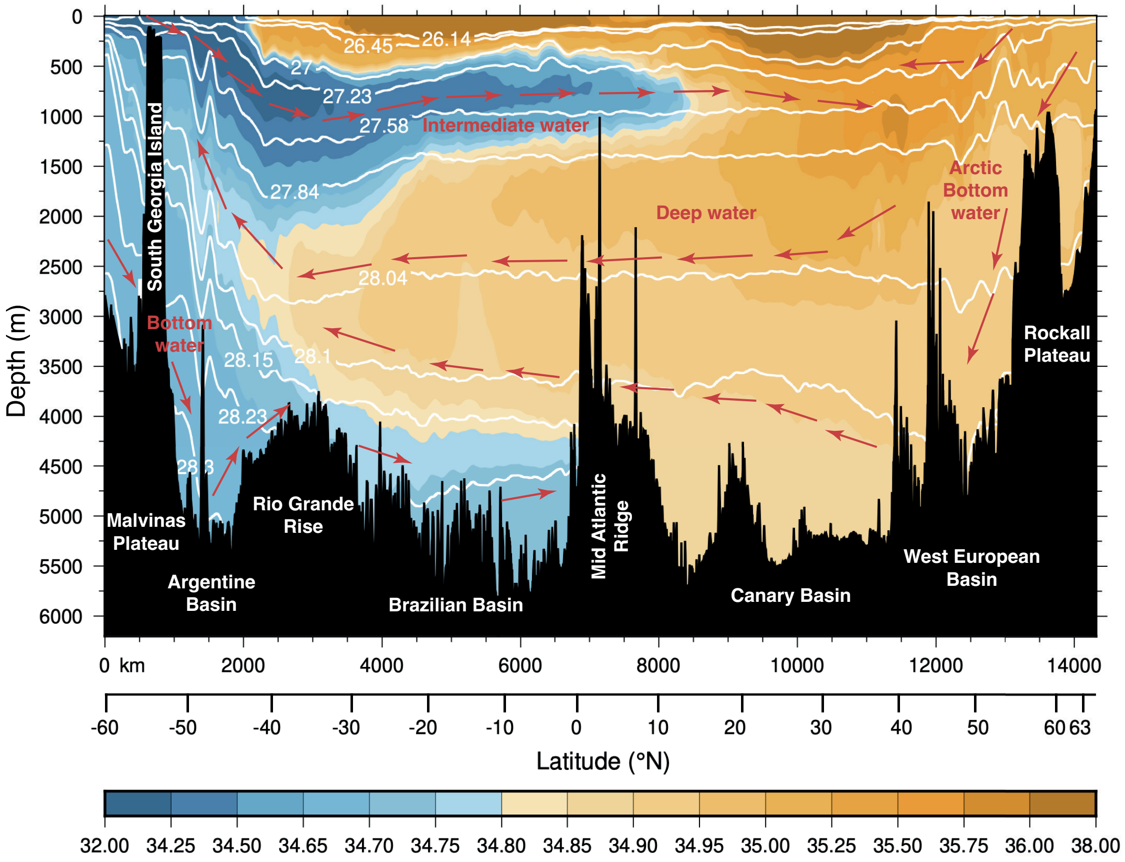

Figure 1.1. Vertical section of salinity along meridional section A16 at 25°W tracing the flow pathways and manifesting the presence of two counter-rotating overturning cells. Figure adapted from Lozier (2012).

strong cooling in the subpolar North Atlantic (SPNA), originating the North Atlantic Deep Water (NADW) that flows southward throughout the basin via deep layers. The presence of monitoring arrays at this northern border of the Atlantic Ocean enables the quantification of this water mass transformation. Results from the OVIDE (Observatoire de la Variabilité Interannuelle à DEcennale) section have manifested the complex eastern subpolar gyre that is responsible for most of the water mass formation in the SPNA (Lherminier et al., 2010; Mercier et al., 2015). Recent studies profiting from the Overturning in the Subpolar North Atlantic Program (OSNAP) monitoring array have shown that the deep limb of the AMOC includes, mainly, waters from Irminger and Iceland basins and the Nordic Seas, while the Labrador basin contributes minimally to the total overturning (Lozier et al., 2019a).

This upper cell is mainly closed by the buoyancy gain in the Southern Ocean due to the strong westerly winds that drive an Ekman transport favouring the upwelling (Figure 1.1). Wind-driven diapycnal mixing in the ocean interior can also help in the transformation of water from lower to upper layers (Johnson et al., 2019b).

In the lower cell, the southward transport flowing along deep layers is balanced by the northward flow of the densest deep-water mass, the Antarctic Bottom Water (AABW, Figure 1.1). The AABW is formed by the sinking of colder waters formed in the Southern Ocean, particularly in the Weddell Sea (McCarthy et al., 2020; Talley, 2013). However, the northward extension of the AABW is restricted by the topography, mainly confined to the western basin due to the presence of the Walvis Ridge in the eastern basin that blocks its northward advance.

1.1.1 Interbasin exchange: “cold” vs ”warm” water routes

In the southern hemisphere, the south Atlantic suffers from contributions from the Southern Ocean as well as from the Pacific and Indian basins through the Drake Passage, and the Agulhas Leakage, respectively (Figure 1.2). These two last contributions have been traditionally referred to as the “cold” and fresher (Rintoul, 1991; Speich et al., 2001) and “warm” and saltier (Gordon & Greengrove, 1986) water routes, respectively, due to the different properties of the water masses involved in each pathway. However, the contributions of both these pathways to the AMOC remain largely unresolved.

The warm and salty waters originated in the Indian Ocean and transported by the Agulhas Current enter the South Atlantic via the Agulhas leakage in the form of a continuous jet, mesoscale eddies and filaments. Cold and fresh waters from the Pacific Ocean enter the South Atlantic through the Malvinas Current after crossing the Drake Passage. The balance between the contributions of these pathways with remarkably different thermohaline properties affects the variability and stability of the AMOC due to its influence on the characteristics of the water masses in the South Atlantic. Lagrangian analysis using models with different resolutions have found a prevalence of the warm water route (Rousselet et al., 2023). The Agulhas Current

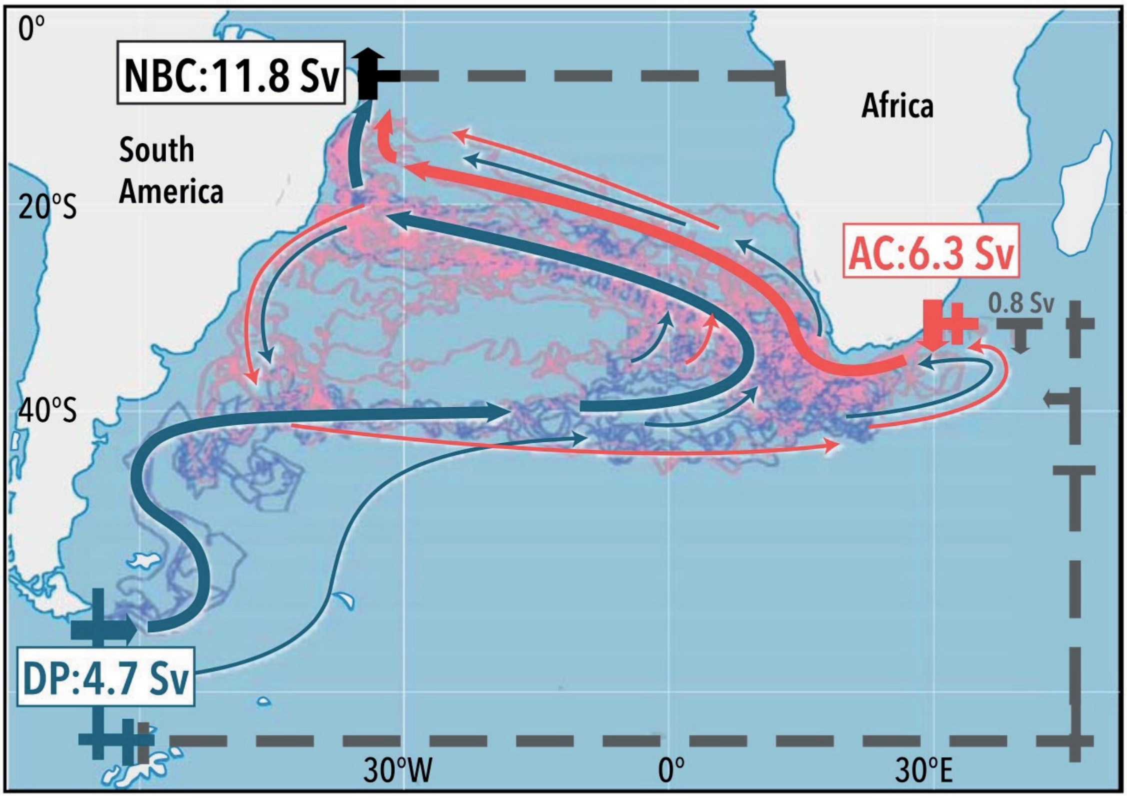

Figure 1.2. The upper limb of the AMOC in the South Atlantic with the direct "cold" (in blue) and "warm" (in red) water routes from simulated Lagrangian particle trajectories. The arrows represent the modelled trajectories as curly thin lines, with major and minor pathways with thick and thin arrows, respectively. Time-mean transports appear in the narrow arrows with the volume transport values in the boxes. Figure from Bower et al. (2019), adapted from Rühs et al. (2019).

(along with other minor Indian Ocean contributions) yields a total northward transport of 85%-99% (Donners & Drijfhout, 2004; Rousselet et al., 2020, 2023; Speich et al., 2001, 2007; Xu et al., 2022), while other authors lower this value to 60% (Rühs et al., 2019). Moreover, the distinction of these water masses should rely on their salinity rather than temperature, which cannot be clearly distinguished.

1.1.2 Influence on climate

The excess solar radiation absorbed by the tropics results in an imbalance in the heat budget between the tropics and the poles. The AMOC is crucial in redistributing this energy imbalance, carrying up to 25% of the net global ocean and atmospheric heat transport (Buckley & Marshall, 2016; Johns et al., 2011; Kersalé et al., 2020; Trenberth & Caron, 2001).

Moreover, by altering exchanges with the atmosphere and cryosphere, the upper cell of the AMOC influences regional weather and climate (Jackson et al., 2015; Liu et al., 2017). In the North Atlantic, the north-eastward transport in upper and intermediate layers by the North Atlantic Current (NAC) carries warm waters to the eastern boundary of the Atlantic. The release of heat to the atmosphere in the SPNA provides a relatively mild climate in northwest Europe (Palter, 2015). In addition, the interannual or longer timescales of AMOC variability can affect the variability of climate in Europe and North America, the amount of rain in Africa, the intensity of hurricanes in the Atlantic and the extent of sea ice coverage in the Arctic (Lozier et al., 2017).

Furthermore, the intensity of the AMOC is related to convection processes that regulate the deep ocean ventilation. Thus, the timescales in which the AMOC varies are connected to the uptake and storage of heat and carbon in the ocean interior (Kersalé et al., 2020; Pérez et al., 2013).

1.1.3 AMOC variability

An enormous amount of effort has gone into comprehending the variability of the AMOC on various timescales. The variability of the AMOC appears mostly on timescales from seasonal, intra-annual, interannual to decadal. The mechanisms underlying interannual to decadal AMOC variations are highly dependent on the region of study. In the subtropics, wind forcing dominates AMOC variability at higher frequencies, with contributions from buoyancy forcing at lower frequencies. The SPNA, in contrast, is dominated by low-frequency variability forced by buoyancy and wind. Both modes of variation of the AMOC are linked to the North Atlantic Oscillation (NAO), which is the main source of atmospheric variability in the North Atlantic (Jackson et al., 2022; Johnson et al., 2019b).

Coupled climate models indicate that decadal variability can occur naturally as a result of climate system internal interactions (Jackson et al., 2022). However, the AMOC is predicted to respond to external forcing, including anthropogenic aerosols, volcanic eruptions and solar changes, as well as anthropogenic greenhouse gas emissions. Strong observational and modelling data support the idea that multidecadal AMOC variability is a key factor in the observed Atlantic Multidecadal Variability, leading by 2.5 years in terms of sea surface temperature (Fraser & Cunningham, 2021; Zhang et al., 2019).

1.1.4 AMOC reconstruction and projectionss

Recently, Caesar et al. (2021) compared several diverse reconstructions of the AMOC using proxy records covering a wide range of time periods. They have found relatively stable values for the AMOC from AD 400 to 1800, followed by an initial decline in the nineteenth century and then a more rapid decline in the 1950s that results in the current weakened AMOC. Similarly, Thornalley et al. (2018) have found a weak AMOC over the last 150 years, with a persistent weak state in the twentieth century.

Several climate models show an AMOC fluctuating on decadal and multidecadal timescales (Muir & Fedorov, 2015, 2017). Most models also forecast a steady weakening of the AMOC in response to anthropogenic forcing over the next century (Cheng et al., 2013; Weaver et al., 2012). Moreover, Rahmstorf et al. (2015), and Caesar et al. (2018) contend that such a gradual slowing has already begun and is visible in proxy records of the AMOC dating back to the mid-twentieth century.

The stability of the AMOC is mainly maintained by the salt-advection feedback, by which the AMOC transports high-salinity water from the subtropics to the SPNA. Hence, high salinity can be found in regions of convection. However, a weakened AMOC would transport less salt into the SPNA, leading to a reduction of deep-water formation and, therefore, a decrease in AMOC intensity (Chidichimo et al., 2023; Weijer et al., 2019). The collapse of the AMOC would be a tipping point in the climate system with global impacts. The Sixth Assessment Report of the Intergovernmental Panel on Climate Change has assessed this risk with a low probability of occurrence but with a potentially high impact.

The AMOC can modify the consequences of anthropogenic climate change, as it regulates the extra heat and CO_2 introduced from the atmosphere to the surface ocean and then, in turn, into the deep ocean. However, all the predictions using scenarios of greenhouse gas emissions predict a reduction in the strength of the upper limb of the AMOC in the 21st century due to anthropogenic climate forcing. Thus, this reduction can affect the uptake and storage of heat and carbon in the ocean. Moreover, it can also affect other components of the climate system such as sea level, water cycle, the patterns of atmospheric circulation, extreme events and marine ecosystems (Chidichimo et al., 2023).

Climate and ocean models offer the opportunity to understand better the AMOC, as well as provide projections of its future evolution (Jackson et al., 2022). Using ensembles of coupled models from CMIP5 and CMIP6, Weijer et al. (2020) have found a consistent decline in the strength of the AMOC over the 21st century in response to anthropogenic climate change. However, this AMOC simulation can be affected by model biases due to a misrepresentation of certain processes, such as mixing by mesoscale eddies, transports in narrow boundary currents, mixing in overflows, deep convection and atmosphere–ocean feedbacks.

1.2 Motivation

As stated above, estimating the evolution of the AMOC is exceptionally important. Model reconstructions and direct observational data have found contrasting results regarding its stability. Assessing how the AMOC has changed over the last thirty years can help comprehend the role of the AMOC in the North Atlantic climate and define forecasts of future AMOC.

The use of in-situ data, like monitoring programs, enabled the observation of interannual changes in AMOC. The subtropical RAPID array at 26.5°N suggests a weakening AMOC between 2004 and 2012 by 0.5 Sv/year (Roberts et al., 2014; Smeed et al., 2014). However, a recovery until 2018 leaves no significant declining trend of the AMOC (Moat et al., 2020). Moreover, recent studies using empirical analysis of hydrographic RAPID data dating back to the 1980s show no overall decline (Worthington et al., 2021). In the subpolar North Atlantic, the OSNAP record is still too short to determine long-term changes. Similarly, in the South Atlantic, the South Atlantic MOC Basin-wide Array (SAMBA) array estimates the strength of the AMOC at 34.5°S. However, their record is still limited, and the main variability appears in the range of days to weeks (Kersalé et al., 2020). These monitoring arrays have revolutionized the way we study the AMOC. However, with the first data dating back to the 2000s, we still have to rely on other types of in-situ datasets to observe the AMOC in the previous decade.

This thesis attempts to answer the underlying question of whether there exist differences in the strength of the AMOC at certain latitudes carried out between 1990-99, 2000-09 and 2010-19. Hydrographic data provide high resolution, full water column, and low uncertainty direct observations with temporal resolutions of 5-10 years. Thus, repeated hydrographic sections enable the determination of circulation over a considerably longer time range than array observations. This research has taken advantage of these datasets to investigate the meridional distribution of the AMOC over the last thirty years in terms of mass, heat and freshwater. We have also tried to understand the relative importance of the increase in the partial pressure of CO_2 in the air-sea interphase and the changes in mass transport in the net transport of anthropogenic Carbon (C_{anth}).

1.3 Thesis outline

This thesis describes the results of three inverse models of the Atlantic Ocean for three decades: 1990-99, 2000-09, and 2010-19. We propose new perspectives on some of the questions that have arisen since the last study for the 1990-99 decade by Ganachaud & Wunsch (2000). This has been extensively discussed in our area of study, comparing the results of hydrographic data and model outputs. The text is divided in three main chapters, addressing different aspects of the AMOC. Within each chapter, there is a specific introduction, a description of the data and methodology employed, and a discussion of the results obtained.

Chapter 2 examines the intensity of the AMOC over the last thirty years using hydrographic data in an inverse method, published in *Geophysical Research Letters* (Caínzos et al., 2022a). We have estimated the strength of the AMOC over these three decades, providing a tool to assess the variability of the meridional overturning circulation of the Atlantic Ocean using hydrographic data. We have diagnosed the transport of mass, heat and freshwater, and present a basin-wide summary of the great effort to sample the ocean since the 1990s.

Furthermore, profiting from these estimations, we have analysed the regional circulation in the Atlantic basin in Chapter 3, quantifying the contribution of each main current flowing along the sections in terms of mass, heat and freshwater transports. This helps paint a picture of the circulation in the Atlantic basin for the whole water column, consistent with Lagrangian depictions of these complex system of currents. This chapter is now under consideration for publication in *Ocean Science* (Caínzos et al. 2023, submitted).

Biogeochemical measurements are used in Chapter 4 to estimate the budget of C_{anth} in the Atlantic Ocean and how it has changed in the last thirty years. We have provided new results assessing the variability of the C_{anth} associated to the meridional overturning circulation of the Atlantic Ocean using hydrographic data. Combining physical results with biogeochemical variables, we have been able to assess the importance of horizontal and vertical fluxes along the whole Atlantic basin. These results have been published in *Global Biogeochemical Cycles* (Caínzos et al., 2022b).

Finally, Chapter 5 offers a general summary with the main conclusive remarks, and perspectives for future work.

Chapter 2

Overturning of mass, heat, and freshwater transport

This chapter has been published as:

Caínzos, V., Hernández-Guerra, A., McCarthy, G. D., McDonagh, E. L., Cubas Armas, M., and Pérez-Hernádez, M. D. (2022). Thirty Years of GOSHIP and WOCE Data: Atlantic Overturning of Mass, Heat, and Freshwater Transport. Geophysical Research Letters, 49(4). https://doi.org/10.1029/2022GB007475.

2.1 Introduction

The AMOC transports relatively warm surface, thermocline, and intermediate waters northwards. This warm upper limb of the overturning circulation releases heat to the atmosphere on its way northward, loses buoyancy, and eventually sinks in the subpolar North Atlantic (SPNA) and Nordic Seas, returning south as North Atlantic Deep Water (NADW; Srokosz et al. 2012). Recent publications have addressed the long-term millennial evolution of the AMOC and suggest that it has been in a relative weak state in recent decades (Caesar et al., 2021). AMOC also varies on timescales from seasonal to decadal (Desbruyères et al., 2019; Moat et al., 2020; Sévellec & Sinha, 2018).

A great effort to sample the global ocean has been carried out since the 1990s under the WOCE and, later, the GO-SHIP (Talley et al., 2016) programs. As a result, a global network of zonal and meridional transoceanic hydrographic sections is available, with repetitions every 5-10 years. The WOCE hydrographic cruises enabled the computation of a global ocean linear inverse box model for the 1990s focused on estimating the transports of mass, heat, and freshwater in every ocean (Ganachaud & Wunsch, 2000; Ganachaud, 2003b), thus creating a consistent picture of the global ocean circulation.

The need for further information about the evolution of the AMOC led to the deployment of several mooring arrays in key latitudes to continuously measure the AMOC. The OSNAP (Lozier et al., 2017), RAPID/MOCHA/WBTS array (hereafter the RAPID array; Cunningham et al. 2007; Johns et al. 2011), MOVE (Kanzow et al., 2006), TSAA (Hummels et al., 2015) and SAMBA (Meinen et al., 2013) projects in the Atlantic Ocean have measured the overturning transport variability on timescales of days, months or seasons (Frajka-Williams, 2019; McCarthy et al., 2020). However, with the earliest results dating the 2000s, these mooring arrays cannot address the longer-term decadal changes in the Atlantic Ocean. Hydrographic data, therefore, offer the only opportunity to understand longer-term subsurface variability. Thus, different studies have compared hydrographic sections conducted at different times, to determine changes of these transports at selected latitudes (Baringer & Molinari, 1999; Bryden et al., 2005b; Fu et al., 2018; Hernández-Guerra et al., 2014, 2019; Hernández-Guerra & Talley, 2016; Koltermann et al., 1999; McDonagh et al., 2015).

2.2 Materials and Methods

We have constructed three inverse models in a neutral density (Jackett & McDougall, 1997) framework, one for each of the last three decades, using hydrographic data for the entire Atlantic Ocean. The latitudinal configuration in each decade varies depending on the available transoceanic sections.

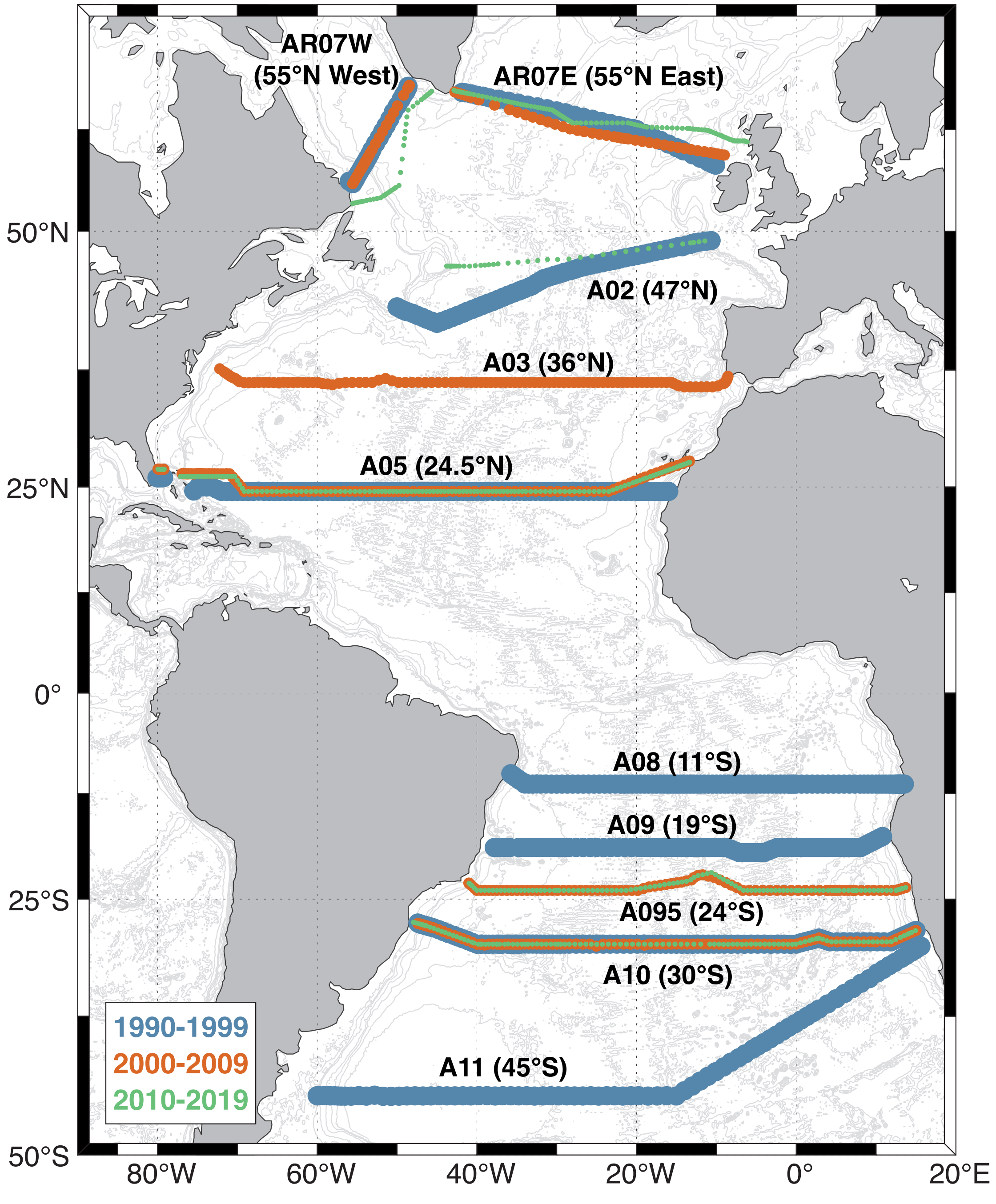

Figure 2.1. Map of the zonal sections included in each decade for the inverse model. Each section is accompanied by its WOCE name and its nominal latitude (between parenthesis) and the colours represent each decade, blue for 1990-99, orange for 2000-2009 and green for 2010-2019. Three sections have been repeated in every decade (A10 – 30°S, A05 – 24.5°N, AR07W and AR07E – 55°N).

Table 2.1. Zonal sections used for each decade, including the reference layer where no-motion is assumed. The Ekman transport is computed for the time of the cruise using NCEP-NCAR products of wind stress.

Section	Year	Latitude	Country	PI	Reference	No. stns	ref. layer	T_{Ek} (Sv)
A11	1992	30-45°S	UK	P. Saunders	Saunders & King (1995)	91	28.15	3.1 ± 0.4
A10	1992	30°S	DE	T. Müller	Siedler et al. (1996)	110	28.15	-0.3 ± 0.2
A09	1991	19°S	DE	G. Siedler	Siedler et al. (1996)	89	28.15	-4.7 ± 0.3
A08	1994	11°S	DE	T. Müller	Siedler et al. (1996)	110	27.58-28.10	-8.3 ± 0.7
A05	1992	24.5°N	SP	G. Parrilla	Parrilla et al. (1994)	11+99	28.15	5.8 ± 0.2
A02	1993	40-50°N	DE	A. Sy	Koltermann et al. (1999)	74	28.15	-0.56 ± 0.15
AR07W	1990	55-60°N	CA	J. Lazier	Lazier et al. (2002)	22	27.84	-0.02 ± 0.04
AR07E	1991	55-60°N	UK	J. Gould	Våge et al. (2011)	38	27.84	-0.76 ± 0.11
A10	2003	30°S	JA	Y. Yoshikawa	Katsumata & Fukasawa (2011)	111	28.15	-0.5 ± 0.2
A095	2009	24°S	UK	B. King	Johns et al. (2011)	94	28.15	-3.3 ± 0.1
A05	2004	24.5°N	UK	S. Cunningham	Bryden et al. (2005b)	9+115	28.15	3.9 ± 0.4
A03	2005	36°N	UK	E. McDonagh	McDonagh et al. (2010)	112	28.04	-0.2 ± 0.2
AR07W	2005	55-60°N	CA	G. Harrison	Bersch et al. (2007); Våge et al. (2011)	24	27.84	-0.01 ± 0.02
AR07E	2007	55-60°N	NE	G.-J. Brummer	Yashayaev & Loder (2016, 2017)	42	27.84	-1.51 ± 0.15
A10	2011	30°S	US	M. Baringer & A. Macdonald	Hernández-Guerra et al. (2019)	120	28.15	-3.5 ± 0.4
A095	2018	19°S	UK	B. King	King et al. (2019)	117	28.15	-1.8 ± 0.3
A05	2011	24.5°N	SP	A. Hernández-Guerra	Hernández-Guerra et al. (2014)	14+152	28.04	3.9 ± 0.5
A02	2013	40-50°N	DE	D. Kieke	Rhein et al. (2019)	39	27.84	-0.48 ± 0.13
AR07W	2014	55-60°N	UK	B. King & P. Holliday	Lozier et al. (2019a)	40	27.84	0.04 ± 0.05
AR07E	2014	55-60°N	UK	B. King & P. Holliday	Lozier et al. (2019a)	103	27.84	-0.30 ± 0.07

2.2.1 Hydrographic data

Basinwide, zonal sections, collected since the 1990s, are part of a collective effort to characterize the ocean in the frame of the international GO-SHIP Program (Talley et al., 2016). We have prioritized the repeated zonal sections for each decade in our study, which are: 55°N (AR07W+AR07E), 24.5°N (A05), and 30°S (A10) (Figure 2.1). Table 2.1 summarizes the chosen sections and their characteristics.

Atlantic water masses are identified with potential temperature, salinity, and neutral density (γ^n) vertical sections (Figures A.1, A.2,A.3, A.4, A.5, A.6, A.7,A.8 and A.9), which allow defining the reference layer for each section to be used in the thermal wind equation to estimate the geostrophic velocities and transports. The level of no motion is set at the interphase of water masses with different directions, such as the southward NADW and the northward AABW. To compute the mass transports, the water column is divided into several γ^n layers (Hernández-Guerra et al., 2019; Talley, 2008). Additionally, the surface Ekman transport at the time of the cruise is estimated using the NCEP–NCAR surface winds.

2.2.2 Inverse box model

The estimated mass transport is not balanced with its adjacent hydrographic sections, as the assumed level of no motion has indeed a velocity different from zero. Thus, inverse box models were introduced in oceanography to estimate the unknown geostrophic reference velocities for hydrographic station pairs, subject to chosen constraints and uncertainties, the most basic

Table 2.2. Regional constraints applied to each section for the 1990-99 inverse model. The sixth column represents the imposed value in the model; the seventh column is the transport before the model, and the eighth column is the value after the inverse model. The uncertainties for the transport adjusted with the inverse model (eighth column) are part of the results of the inverse model using the Gauss-Markov estimator. Salt constraints are expressed in 10^{-3} Sv psu and the mass constraints in Sv.

	Long	Depth	Stations	Layers	Constraint value	Initial transport	Adjusted transport	References
Salt constraints								
A11 (1992)								
Bering Strait	All	All	1:90	1:11	-26 ± 21	360	-26 ± 8	McDonagh et al. (2015)
A10 (1992)								
Bering Strait	All	All	1:110	1:11	-26 ± 21	864	-28 ± 6	McDonagh et al. (2015)
A09 (1991)								
Bering Strait	All	All	1:93	1:11	-26 ± 21	1548	-20 ± 7	McDonagh et al. (2015)
A08 (1994)								
Bering Strait	All	All	1:109	1:11	-26 ± 22	486	-19 ± 6	McDonagh et al. (2015)
A05 + Florida (1992)								
Bering Strait	All	All	1:108	1:11	-26 ± 22	484	-26 ± 7	McDonagh et al. (2015)
A02 (1993)								
Bering Strait	All	All	1:73	1:11	-26 ± 22	225	-24 ± 8	McDonagh et al. (2015)
A07 = AR07W + AR07E								
Bering Strait (total)	All	All	1:58	1:11	-26 ± 21	238	-28 ± 9	McDonagh et al. (2015)
Mass constraints								
A11 (1992)								
WBC (Malvinas current)	60-57.8°W	All	1:4	1:11	37.1 ± 6.6	37.1	38.0 ± 2.0	Artana et al. (2018)
Cape Basin AABW	8.2°W-10.9°E	Bottom	58:80	9:11	0 ± 0.5	1.0	0.0 ± 0.9	McDonagh & King (2005)
Argentine Basin AABW	57-15°W	Bottom	9:51	9:11	6 ± 1	-1.5	5.9 ± 1.6	McDonagh & King (2005)
A10 (1992)								
Brazil basin	45-15.3°W	Bottom	12:63	9:11	6.9 ± 1.8	3.0	4.5 ± 1.7	Hogg & Owens (1999)
Vema channel	39.7-37.7°W	AABW	21:25	9:11	4.0 ± 0.4	1.5	3.8 ± 0.4	Hogg et al. (1982)
Walvis R. North	7.3°W-1.7°E	Bottom	75:87	9:11	0 ± 1	-0.2	-0.5 ± 0.9	Warren & Speer (1991)
Walvis R. South	2.2-13.4°E	Bottom	88:106	9:11	0 ± 1	0.7	-0.8 ± 1.3	Warren & Speer (1991)
Brazil current	Coast-44.8°W	Surf - interm	1:12	1:7	-38.9 ± 2.1	-16.3	-38.2 ± 1.3	Hernández-Guerra et al. (2019)
Benguela current	11.8°E-Coast	Surf - interm	101:110	1:7	26.3 ± 2.4	19.7	25.8 ± 1.4	Hernández-Guerra et al. (2019)
A05 + Florida (1992)								
Florida Current	All	All	1:10	1:5	31.8 ± 3.5	31.8	31.8 ± 0.3	Florida Current Project
AR07W (1990)								
Bering Strait (Davis Strait)	All	All	1:21	1:11	-1.6 ± 0.2	1.0	-1.6 ± 1.2	Curry et al. (2014)
AR07E (1993)								
Bering Strait (East)	All	All	22:58	1:11	0.80 ± 0.63	5.7	0.7 ± 3.5	Lozier et al. (2019a)

of which is mass conservation (Wunsch, 1978, 1996), described in Appendix B. Conservation of mass is imposed for each box for the whole water column and each layer. For every single section, mass is conserved for regional constraints, related to independent in situ measurements and topographic features. The salinity content of each section is also constrained (Tables 2.2, 2.3 and 2.4) to make sure that mass is conserved while allowing changes in freshwater. The Gauss-Markov estimator is applied to solve these matrices (Wunsch, 1996). The same model configuration is used for each decade, so that differences in the model solution are attributable to changes in circulation.

Conservation equations

The inverse model for each decade links boxes between contiguous sections, from South to North. For each single box, the matrix form of the inverse model equation has the following form:

Table 2.3. Same as Table 2.2 for the 2000-09 decade.

	Long	Depth	Stations	Layers	Constraint value (10^{-3} Sv psu)	Initial transport (10^{-3} Sv psu)	Adjusted transport (10^{-3} Sv psu)	References
Salt constraints								
A10 (2003)								
Bering Strait	All	All	1:110	1:11	-26 ± 21	625	-28 ± 7	McDonagh et al. (2015)
A095 (2009)								
Bering Strait	All	All	1:93	1:11	-26 ± 21	1376	-16 ± 8	McDonagh et al. (2015)
A05 + Florida (2004)								
Bering Strait	All	All	1:122	1:11	-26 ± 21	676	-30 ± 8	McDonagh et al. (2015)
A03 (2005)								
Bering Strait	All	All	1:122	1:11	-26 ± 21	1110	-19 ± 9	McDonagh et al. (2015)
A07 = AR07W + AR07E								
Bering Strait (total)	All	All	1:66	1:11	-26 ± 20	-218	-29 ± 8	McDonagh et al. (2015)
Mass constraints								
A10 (2003)								
Brazil basin	45-15.3°W	Bottom	12:63	9:11	6.9 ± 1.8	2.4	4.2 ± 1.8	Hogg & Owens (1999)
Vema channel	39.7-37.7°W	AABW	21:25	9:11	4.0 ± 0.4	1.3	3.8 ± 0.4	Hogg et al. (1982)
Walvis R. North	7.3°W-1.7°E	Bottom	75:87	9:11	0 ± 1	0.3	-0.4 ± 0.9	Warren & Speer (1991)
Walvis R. South	2.2-13.4°E	Bottom	88:106	9:11	0 ± 1	1.2	-0.8 ± 1.3	Warren & Speer (1991)
Brazil current	Coast-44.8°W	Surf - interm	1:12	1:7	-38.9 ± 2.1	-21.7	-38.2 ± 1.3	Hernández-Guerra et al. (2019)
Benguela current	11.8°E-Coast	Surf - interm	101:110	1:7	26.3 ± 2.4	27.8	26.3 ± 1.5	Hernández-Guerra et al. (2019)
A095 (2009)								
Brazil current	Coast-38.8°W	¡ 300 dbar	1:4	1:4	-4.9 ± 1.2	-3.1	-3.5 ± 0.2	Bryden et al. (2011)
A05 + Florida (2004)								
Florida Current	All	All	1:8	1:6	31.9 ± 3.3	31.9	32.2 ± 0.3	Florida Current Project
A03 (2005)								
DWBC	Coast-70°W	γ^n 27.8-28.125	1:9	7:9	-25.1 ± 2.7	2.8	-23.4 ± 0.1	Toole et al. (2011)
AR07W (2005)								
Bering Strait (Davis Strait)	All	All	1:25	1:11	-1.6 ± 0.2	-6.4	-1.6 ± 1.3	Curry et al. (2014)
AR07E (2007)								
Bering Strait (East)	All	All	26:66	1:11	0.80 ± 0.63	0.1	0.7 ± 2.9	Lozier et al. (2019a)

Table 2.4. Same as Table 2.2 for the 2010-19 decade.

	Long	Depth	Stations	Layers	Constraint value (10^{-3} Sv psu)	Initial transport (10^{-3} Sv psu)	Adjusted transport (10^{-3} Sv psu)	References
Salt constraints								
A10 (2011)								
Bering Strait	All	All	1:119	1:11	-26 ± 21	888	-26 ± 8	McDonagh et al. (2015)
A095 (2018)								
Bering Strait	All	All	1:116	1:11	-26 ± 21	1061	-23 ± 8	McDonagh et al. (2015)
A05 + Florida (2011)								
Bering Strait	All	All	1:151	1:11	-26 ± 21	911	-24 ± 7	McDonagh et al. (2015)
A02 (2013)								
Bering Strait	All	All	1:138	1:11	-26 ± 23	110	-25 ± 7	McDonagh et al. (2015)
A07 = AR07W + AR07E								
Bering Strait (total)	All	All	1:80	1:11	-26 ± 23	89	-26 ± 6	McDonagh et al. (2015)
Mass constraints								
A10 (2011)								
Brazil basin	45-15.3°W	Bottom	10:65	9:11	6.9 ± 1.8	4.7	4.8 ± 1.9	Hogg & Owens (1999)
Vema channel	39.7-37.7°W	AABW	22:28	9:11	4.0 ± 0.4	2.5	3.9 ± 0.4	Hogg et al. (1982)
Walvis R. North	7.3°W-1.7°E	Bottom	76:92	9:11	0 ± 1	0.6	-0.4 ± 0.9	Warren & Speer (1991)
Walvis R. South	2.2-13.4°E	Bottom	93:116	9:11	0 ± 1	1.1	-0.8 ± 1.2	Warren & Speer (1991)
Brazil current	Coast-44.8°W	Surf - interm	1:25	1:7	-38.9 ± 2.1	-16.9	-38.4 ± 1.5	Hernández-Guerra et al. (2019)
Benguela current	11.8°E-Coast	Surf - interm	105:119	1:7	26.3 ± 2.4	39.0	26.8 ± 1.6	Hernández-Guerra et al. (2019)
A095 (2018)								
Brazil current	Coast-38.8°W	¡ 300 dbar	1:4	1:10	-4.9 ± 1.2	-4.0	-5.2 ± 0.6	Bryden et al. (2011)
A05 + Florida (2011)								
Florida Current	All	All	1:13	1:6	31.3 ± 3.4	30.1	30.1 ± 0.2	Florida Current Project
AR07W (2014)								
Bering Strait (Davis Strait)	All	All	1:39	1:11	-1.6 ± 0.2	1.0	-1.6 ± 1.5	Curry et al. (2014)
AR07E (2014)								
Bering Strait (East)	All	All	40:141	1:11	0.80 ± 0.63	1.3	0.7 ± 2.4	Lozier et al. (2019a)

$$\begin{pmatrix}
\mathrm{e}_{\mathrm{A}_{\mathrm{t},1}} & \cdots & \mathrm{e}_{\mathrm{A}_{\mathrm{t},\mathrm{n}}} & \mathrm{e}_{\mathrm{B}_{\mathrm{t},1}} & \cdots & \mathrm{e}_{\mathrm{B}_{\mathrm{t},\mathrm{m}}} & 1 & 1 & & \\
\mathrm{e}_{\mathrm{A}_{\mathrm{reg}}} & \cdots & \mathrm{e}_{\mathrm{A}_{\mathrm{reg}}} & 0 & \cdots & 0 & 0 & 0 & & \\
0 & \cdots & 0 & \mathrm{e}_{\mathrm{B}_{\mathrm{reg}}} & \cdots & \mathrm{e}_{\mathrm{B}_{\mathrm{reg}}} & 0 & 0 & & \\
\mathrm{e}_{\mathrm{A}_{1,1}} & \cdots & \mathrm{e}_{\mathrm{A}_{1,\mathrm{n}}} & \mathrm{e}_{\mathrm{B}_{1,1}} & \cdots & \mathrm{e}_{\mathrm{B}_{1,\mathrm{m}}} & 1 & 1 & & \\
\mathrm{e}_{\mathrm{A}_{2,1}} & \cdots & \mathrm{e}_{\mathrm{A}_{2,\mathrm{n}}} & \mathrm{e}_{\mathrm{B}_{2,1}} & \cdots & \mathrm{e}_{\mathrm{B}_{2,\mathrm{m}}} & 0 & 0 & & \\
\vdots & \ddots & \vdots & \vdots & \ddots & \vdots & \vdots & \vdots & & \\
\vdots & \ddots & \vdots & \vdots & \ddots & \vdots & \vdots & \vdots & & \\
\mathrm{e}_{\mathrm{A}_{\mathrm{q}-1,1}} & \cdots & \mathrm{e}_{\mathrm{A}_{\mathrm{q}-1,\mathrm{n}}} & \mathrm{e}_{\mathrm{B}_{\mathrm{q}-1,1}} & \cdots & \mathrm{e}_{\mathrm{B}_{\mathrm{q}-1,\mathrm{m}}} & 0 & 0 & & \\
\mathrm{e}_{\mathrm{A}_{\mathrm{q},1}} & \cdots & \mathrm{e}_{\mathrm{A}_{\mathrm{q},\mathrm{n}}} & \mathrm{e}_{\mathrm{B}_{\mathrm{q},1}} & \cdots & \mathrm{e}_{\mathrm{B}_{\mathrm{q},\mathrm{m}}} & 0 & 0 & 0 & 0 \\
\mathrm{s}_{\mathrm{A}_{\mathrm{t},1}} & \cdots & \mathrm{s}_{\mathrm{A}_{\mathrm{t},\mathrm{n}}} & 0 & \cdots & 0 & \overline{\left(\frac{\mathrm{s}_{\mathrm{A}_1}}{\mathrm{e}_{\mathrm{A}_1}}\right)} & 0 & & \\
0 & \cdots & 0 & \mathrm{s}_{\mathrm{B}_{\mathrm{t},1}} & \cdots & \mathrm{s}_{\mathrm{B}_{\mathrm{t},\mathrm{m}}} & 0 & \overline{\left(\frac{\mathrm{s}_{\mathrm{B}_1}}{\mathrm{e}_{\mathrm{B}_1}}\right)} & &
\end{pmatrix}
\begin{pmatrix}
\mathrm{b}_{\mathrm{A}_1} \\ \vdots \\ \mathrm{b}_{\mathrm{B}_\mathrm{n}} \\ \mathrm{b}_{\mathrm{B}_1} \\ \vdots \\ \mathrm{b}_{\mathrm{B}_\mathrm{m}} \\ \Delta \mathrm{T}_{\mathrm{A}_{\mathrm{Ek}}} \\ \Delta \mathrm{T}_{\mathrm{B}_{\mathrm{Ek}}}
\end{pmatrix}
=
\begin{pmatrix}
\mathrm{y}_{\mathrm{A}_\mathrm{t}} + \mathrm{y}_{\mathrm{B}_\mathrm{t}} + \mathrm{T}_{\mathrm{A}_{\mathrm{Ek}}} + \mathrm{T}_{\mathrm{B}_{\mathrm{Ek}}} \\
\mathrm{y}_{\mathrm{A}_{\mathrm{reg}}} \\
\mathrm{y}_{\mathrm{B}_{\mathrm{reg}}} \\
\mathrm{y}_{\mathrm{A}_1} + \mathrm{y}_{\mathrm{B}_1} + \mathrm{T}_{\mathrm{A}_{\mathrm{Ek}}} + \mathrm{T}_{\mathrm{B}_{\mathrm{Ek}}} \\
\mathrm{y}_{\mathrm{A}_2} + \mathrm{y}_{\mathrm{B}_2} \\
\vdots \\
\vdots \\
\mathrm{y}_{\mathrm{A}_{\mathrm{q}-1}} + \mathrm{y}_{\mathrm{B}_{\mathrm{q}-1}} \\
\mathrm{y}_{\mathrm{A}_\mathrm{q}} + \mathrm{y}_{\mathrm{B}_\mathrm{q}} \\
\mathrm{z}_{\mathrm{A}_\mathrm{t}} + \mathrm{T}_{\mathrm{A}_{\mathrm{Ek}}} \overline{\left(\frac{\mathrm{S}_{\mathrm{A}_1}}{\mathrm{e}_{\mathrm{A}_1}}\right)} \\
\mathrm{z}_{\mathrm{B}_\mathrm{t}} + \mathrm{T}_{\mathrm{B}_{\mathrm{Ek}}} \overline{\left(\frac{\mathrm{S}_{\mathrm{B}_1}}{\mathrm{e}_{\mathrm{B}_1}}\right)}
\end{pmatrix}$$

where n is the number of station pairs for section A, m is the number of station pairs for section B, q is the number of layers, b are the reference velocities for each station pair, $\Delta\mathrm{T}_{\mathrm{Ek}}$ is the Ekman transport correction, e is mass, s is salt, y is mass transport and z is the salt transport.

The first equation included in each box is the total conservation for the whole box (denoted with a t for total). This equation applies to all station pairs of A and B and consider both Ekman corrections, as the first layers must be corrected. The following equations are the regional constraints applied to section A, with different station pairs and neutral density layers affected. Similarly, regional equations for section B are found in subsequent files. The following 11 (q layers) equations correspond to the conservation of each layer between both sections with Ekman correction in the outcropping layers.

In addition to mass conservation, we have also constrained the salinity content of each single section A and B (last two equations). Using salinity instead of mass allows for changes in freshwater across the section while still conserving mass. The salinity transport constrained is 26.0 Sv resulting from a Bering Strait mass transport of 0.8 Sv with an average salinity of 32.5. For mass conservation, the Ekman parameter used was 1. For salinity conservation, this parameter is expressed as the average ratio between salt and mass at the outcropping layer.

No other properties are conserved in these models. Heat and salt are largely dependent on mass and do not increase the rank of the matrix, therefore failing to add information to the system. The use of property anomalies increases the noise in the system solutions and does not provide a better solution to the inverse model. Top-to-bottom silica conservation has been applied in inverse models when the solution presented large imbalances on the silica budget as in the Indian Ocean (Robbins & Toole, 1997). In the Atlantic Ocean, and specifically in these inverse models, the models already provide solution that satisfy the conservation of silica within each box. Therefore, we do not include these extra equations in the matrix as it would not increase the rank of the matrix or reduce the size of the uncertainties.

The 1990-99 inverse model has 643 unknowns in 105 equations, the 2000-09 model has 545 unknowns in 78 equations, and the 2010-19 inverse model has 589 unknowns and 77 equations. Therefore, the solutions come from a highly undetermined system of equations. The system unknowns include the velocities at the reference level and the adjustment to the Ekman transport in the first layer. The Gauss-Markov estimator is applied to solve these matrices (Wunsch, 1996).

Reference level and velocities

The choice of reference level is summarized in Table 2.1. In the South Atlantic, the general choice for reference level is the interphase between the southward flowing North Atlantic Deep Waters (NADW) and the northward flowing Antarctic Bottom Waters (AABW), which lies in the neutral density surface of 28.15 kg m^{-3} (Hernández-Guerra et al., 2019; McDonagh & King, 2005). Section A08 (11°S) in the decade of 1990-99 has basin-specific reference levels between 27.58 and 28.10 kg m^{-3} (Speer et al., 1996). In the North Atlantic subtropical gyre, the reference level of section A05 (24.5°N) is situated in the interphase between NADW and AABW, at 28.15 kg m^{-3} for the 1990-99 and 2000-09 decades and at 28.04 kg m^{-3} for the last decade (Fu et al., 2018; Hernández-Guerra et al., 2014). Section A02 (47°N) for the 1990-99 decade presents a reference level at 28.15 kg m^{-3} at the interphase between NADW and AABW, whereas for the decade of 2010-19 it is at the interphase between the MOC upper and lower limb at 27.84 kg m^{-3} (Ganachaud, 1999). At A03 (36°N), the reference level at the interphase between NADW and AABW is at a neutral density of 28.04 kg m^{-3} (McDonagh et al., 2010). The northernmost sections at 55°N (AR07W+AR07E) show better results when choosing the reference level at the interphase between the MOC upper and lower limb, which lies at 27.84 kg m^{-3} (Holliday et al., 2018; Lozier et al., 2019a).

A priori estimates and uncertainties

The Gauss-Markov method solves this system of equations with a minimum error variance solution from the initial estimates of the unknowns (the velocities at the reference level, b, and the corrections to the Ekman transport, $\Delta \mathrm{T}_{\mathrm{Ek}}$) (Wunsch, 1996). To solve it, we first need a priori estimates and uncertainties that give an initial approximation to the actual value. The preliminary variance of the adjusted velocity at the reference level is 8 cm^2 s^{-2} for the station pairs closer to coast, where shear is stronger and 4 cm^2 s^{-2} in the deepest stations. The initial estimates for the mass transport are 9 Sv^2 for the net mass transport between two sections, therefore allowing for compensation within each box. For layer conservation, the variance is between 13 and 1 Sv^2, decreasing towards deeper layers. The salinity uncertainties are computed as the square of the uncertainty of the Bering Strait transport (0.6 Sv) times the square of the ration between the total salt transport and the mass transport of each section.

Despite obtaining similar results, this study provides smaller uncertainties than other global inverse solutions (Ganachaud, 2003a) and decadal studies (Fu et al., 2020). This was achieved by

Table 2.5. Sensitivity tests for the constraints applied to the South Atlantic in sections A10 (30°S) and A11 (45°S) for regional mass transports. The original inverse model includes these constraints and the inverse model T1 is not constrained by regional and topographic features at 30°S and 45°S. The uncertainties associated with the mass and property transports are part of the results of the inverse model using the Gauss-Markov estimator.

		1990-99 Mass Transport (Sv)	2000-09 Mass Transport (Sv)	2010-19 Mass Transport (Sv)
Argentine Basin (45° S)	Original	5.9 ± 1.6		
	T1	2.3 ± 2.8		
Brazil Basin (30° S)	Original	4.4 ± 1.7	4.2 ± 1.8	4.8 ± 1.9
	T1	-0.4 ± 2.1	-1.2 ± 2.3	-0.7 ± 2.5
Vema Channel (30° S)	Original	3.8 ± 0.4	3.8 ± 0.4	3.9 ± 0.4
	T1	1.5 ± 0.9	1.2 ± 0.9	2.0 ± 0.8

		1990-99		2000-09		2010-19	
		Heat (PW)	Freshwater (Sv)	Heat (PW)	Freshwater (Sv)	Heat (PW)	Freshwater (Sv)
Total	Original	0.37 ± 0.06	0.28 ± 0.08	0.42 ± 0.06	0.19 ± 0.07	0.49 ± 0.07	0.09 ± 0.06
	T1	0.43 ± 0.06	0.28 ± 0.08	0.49 ± 0.06	0.19 ± 0.07	0.58 ± 0.07	0.09 ± 0.06
Throughflow	Original	0.01 ± 0.05	0.04 ± 0.05	0.01 ± 0.05	0.04 ± 0.05	0.01 ± 0.06	0.05 ± 0.05
	T1	0.01 ± 0.05	0.04 ± 0.05	0.01 ± 0.06	0.04 ± 0.05	0.01 ± 0.06	0.05 ± 0.05
Overturning	Original	0.49 ± 0.04	0.00 ± 0.02	0.54 ± 0.05	-0.08 ± 0.02	0.60 ± 0.05	-0.13 ± 0.03
	T1	0.54 ± 0.05	0.00 ± 0.02	0.61 ± 0.05	-0.09 ± 0.02	0.69 ± 0.06	-0.13 ± 0.03
Horizontal (gyre)	Original	-0.12 ± 0.01	0.24 ± 0.02	-0.12 ± 0.01	0.23 ± 0.02	-0.11 ± 0.01	0.17 ± 0.01
	T1	-0.12 ± 0.01	0.25 ± 0.02	-0.12 ± 0.01	0.23 ± 0.02	-0.11 ± 0.01	0.17 ± 0.01

using a simpler model with only the velocities at the reference level and the Ekman adjustments as unknowns.

Some of the weaknesses of the inverse model are related to the accurate calculation of the geostrophic transport before the inverse model. We have assumed linear bottom topography between the deepest common level of each station to compute the transport of each bottom triangle. There are uncertainties associated to this approximation, in the order of 1 Sv, but can increase in areas of boundary currents along sloping topography (Ganachaud, 2003b; McDonagh et al., 2008; Robbins & Toole, 1997).

The Ekman transport can also be an issue when adjusting the geostrophic transport in surface layers. We believe that the geostrophic calculation of each section is balanced by the Ekman transport for the time of the cruise. There is an adjustment for the instantaneous response of this wind forcing on the upper layers. Using the Ekman transport of the time of the cruise we remove the effect of the seasonal or monthly variability in upper layers. In any case, the Ekman transport is adjusted in the inverse model.

Dianeutral estimates

Dianeutral transport, both advection velocity (ω) and diffusion coefficient ($\varkappa_{\mathrm{z}}$), were calculated in every box delimited by two sections and two neutral density surfaces. The small imbalance between horizontal mass transport within each box after the inverse model was compensated by an adjustment with a vertical transport and its associated ω across neutral density surfaces. The remaining changes in vertical heat transport are explained by diffusion processes (Hernández-Guerra & Talley, 2016; Hogg et al., 1982; Morris et al., 2001; Munk, 1966). Dianeutral diffusion coefficient $\varkappa_{\mathrm{z}}$ is not shown in this paper.

Table 2.6. Sensitivity tests for the values of transport and average salinity of Bering Strait. The results are focused on the heat and freshwater components on the section A10 (30°S). Sensitivity test T2 changes the average salinity of the Bering Strait from 32.5 to 31.5 and T3 to 33.5. Sensitivity test T4 changes the mass transport through Bering Strait from -0.8 ± 0.6 to -1.0 ± 0.5 Sv. The uncertainties associated with the property transports are part of the results of the inverse model using the Gauss-Markov estimator.

		1990-99		2000-09		2010-19	
		Heat (PW)	Freshwater (Sv)	Heat (PW)	Freshwater (Sv)	Heat (PW)	Freshwater (Sv)
Total	Original	0.37 ± 0.06	0.28 ± 0.08	0.42 ± 0.06	0.19 ± 0.07	0.49 ± 0.07	0.09 ± 0.06
	T2	0.37 ± 0.06	0.29 ± 0.10	0.42 ± 0.06	0.20 ± 0.09	0.48 ± 0.07	0.17 ± 0.08
	T3	0.37 ± 0.06	0.26 ± 0.05	0.42 ± 0.06	0.17 ± 0.05	0.48 ± 0.07	0.09 ± 0.04
	T4	0.37 ± 0.06	0.29 ± 0.08	0.42 ± 0.06	0.20 ± 0.07	0.49 ± 0.07	0.10 ± 0.06
Throughflow	Original	0.01 ± 0.05	0.04 ± 0.05	0.01 ± 0.05	0.04 ± 0.05	0.01 ± 0.06	0.05 ± 0.05
	T2	0.01 ± 0.05	0.05 ± 0.08	0.01 ± 0.05	0.06 ± 0.08	0.02 ± 0.06	0.13 ± 0.07
	T3	0.01 ± 0.05	0.02 ± 0.03	0.01 ± 0.05	0.03 ± 0.03	0.02 ± 0.06	0.05 ± 0.03
	T4	0.01 ± 0.05	0.05 ± 0.05	0.01 ± 0.05	0.06 ± 0.05	0.02 ± 0.06	0.06 ± 0.05
Overturning	Original	0.49 ± 0.04	0.00 ± 0.02	0.54 ± 0.05	-0.08 ± 0.02	0.60 ± 0.05	-0.13 ± 0.03
	T2	0.49 ± 0.04	0.00 ± 0.02	0.54 ± 0.05	-0.08 ± 0.02	0.60 ± 0.05	-0.13 ± 0.03
	T3	0.49 ± 0.04	0.00 ± 0.02	0.54 ± 0.05	-0.08 ± 0.02	0.60 ± 0.05	-0.13 ± 0.03
	T4	0.49 ± 0.04	0.00 ± 0.02	0.54 ± 0.05	-0.08 ± 0.02	0.60 ± 0.05	-0.13 ± 0.03
Horizontal (gyre)	Original	-0.12 ± 0.01	0.24 ± 0.02	-0.12 ± 0.01	0.23 ± 0.02	-0.11 ± 0.01	0.17 ± 0.01
	T2	-0.12 ± 0.01	0.24 ± 0.02	-0.12 ± 0.01	0.23 ± 0.02	-0.13 ± 0.03	0.17 ± 0.01
	T3	-0.12 ± 0.01	0.24 ± 0.02	-0.12 ± 0.01	0.23 ± 0.02	-0.11 ± 0.01	0.17 ± 0.01
	T4	-0.12 ± 0.01	0.24 ± 0.02	-0.12 ± 0.01	0.23 ± 0.02	-0.13 ± 0.03	0.17 ± 0.01

2.2.3 Sensitivity tests

Several sensitivity tests were conducted to determine the best configuration of the inverse models. The tightness of the constraints on regional and topographic features of the Southern Hemisphere were assessed by removing the constraints on section A10 (30°S). The results for each constraint are in Table 2.5. The boundary currents display some differences, but it has not been transmitted to the net heat and freshwater budget, which remain the same, and has not altered the values of the freshwater overturning.

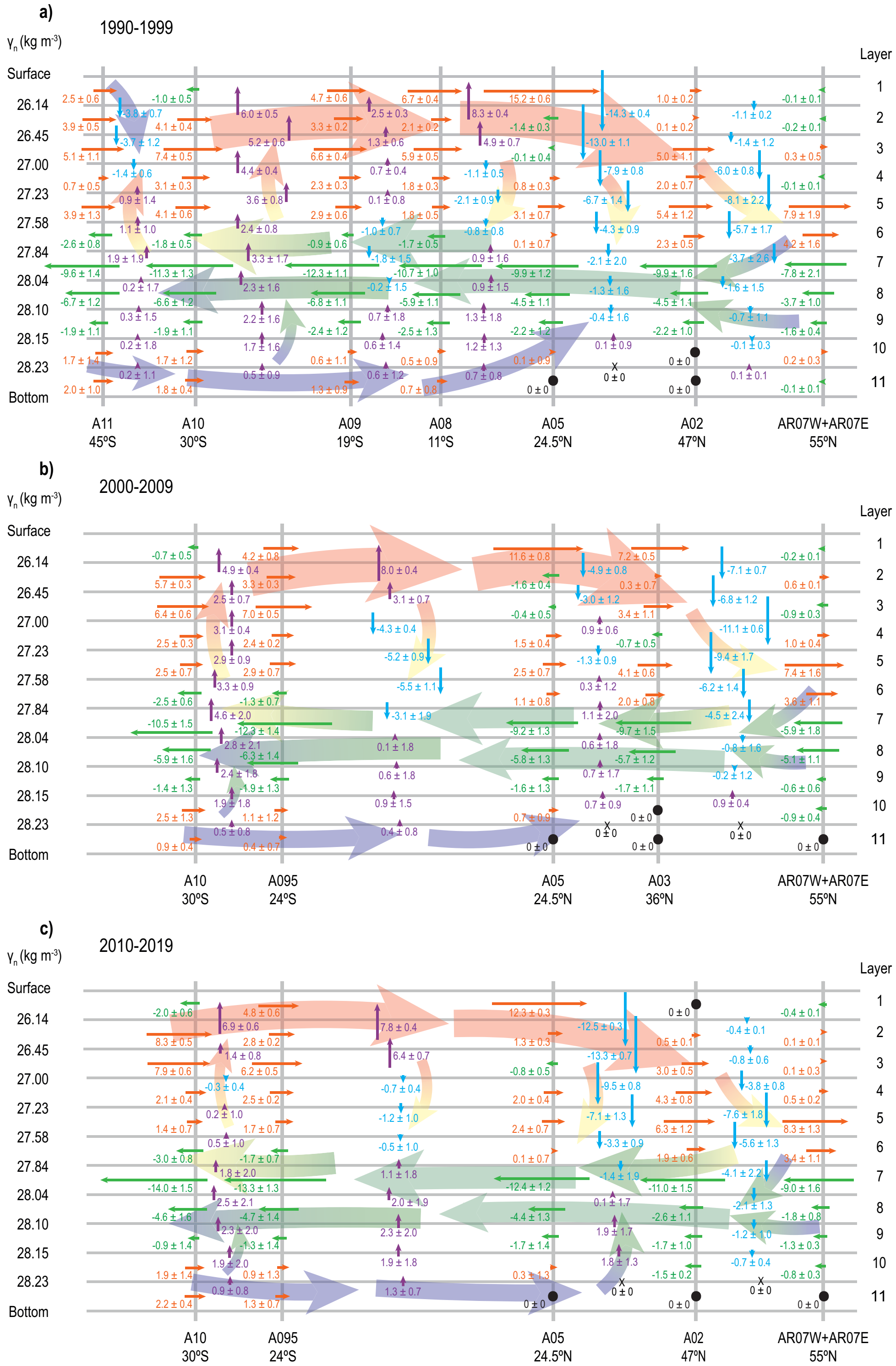
a)
1990-1999
b)
2000-2009
c)
2010-2019
γ_n (kg m^{-3})
Surface
26.14
26.45
27.00
27.23
27.58
27.84
28.04
28.10
28.15
28.23
Bottom
Layer
1
2
3
4
5
6
7
8
9
10
11
A11 45ºS
A10 30ºS
A095 24ºS
A09 19ºS
A08 11ºS
A05 24.5ºN
A03 36ºN
A02 47ºN
AR07W+AR07E 55ºN

Figure 2.2. Vertical and meridional schematic of the circulation. Grey horizontal lines mark the neutral density interphases, and grey vertical lines are the position of each zonal section at their nominal latitude for the (a) 1990-99 decade, (b) 2000-09 decade and (c) 2010-19 decade. The horizontal mass transport (Sv) is represented with horizontal arrows, in orange for northward (positive) transport and green for southward (negative) transport. The vertical transport between two sections in the interphase between two layers is represented with vertical arrows, in violet for upward (positive) transport and blue for downward (negative) transport. Black dots and crosses represent layers with no transport. Background arrows manifest the presence of two counter-rotating overturning cells across the basin.

We have also conducted sensibility tests to understand the importance of the temporal variability of the Bering Strait salinity and transport (Table 2.6). We have changed the average salinity of the Bering Strait from 31.5 to 33.5 (Woodgate & Aagaard, 2005) and the Bering Strait transport for the last two decades from -0.8 ± 0.6 to -1.0 ± 0.5 Sv (Woodgate, 2018). These changes affect basically the throughflow components, but the overturning and horizontal components are not changed.

2.3 Results and discussion

2.3.1 Meridional transport

Two counter-rotating overturning cells appear in the results of the inverse models (background arrows in Figure 2.2). The upper overturning cell is partially closed by the vertical transport of water, with downward vertical transport in the SPNA associated with entrainment of warm North Atlantic Current (NAC; McCartney & Talley 1984) and upwelling in the subtropical gyre of the South Atlantic Ocean (Figure 2.2). In the abyssal cell, part of the southward flowing NADW sinks in the Southern Ocean and then returns northward as the Antarctic Bottom Water (AABW) (Wefer et al., 1996), that then upwells on its way north to the subtropical North Atlantic. This study does not reach latitudes south enough to observe the deep-water formation in the Southern Ocean. The northward transports of upper and abyssal layers are balanced by the southward transport of deep layers (Kersalé et al., 2020). The boundaries of the deep layers lie between γ^n of 27.84 and 28.15 kg m^{-3} for the southern hemisphere and between or 27.58 and 28.15 kg m^{-3} or bottom for the northern hemisphere.

In the SPNA, the core of the warm NAC gets denser on its way northward, as seen in the sections 47°N and 55°N (Figure 2.2), with stronger northward transports between γ^n of 26.45 and 27.58 kg m^{-3} at 47°N (12.4 ± 1.8 Sv for 1990-99 and 13.7 ± 1.5 Sv for 2010-19) and between γ^n of 27.23 and 27.84kg m^{-3} at 55°N (12.1 ± 2.5 Sv for 1990-99, 11.0 ± 1.9 Sv for 2000-09 and 11.6 ± 1.7 Sv for 2010-19, where 1 Sverdrup (Sv) = 10^6 m^3 s^{-1} $\approxeq$ 10^9 kg s^{-1}). This maximum is associated with stronger downwelling values at 27.00-27.84 kg m^{-3}.

In the thermocline layers of the subtropical regions of both hemispheres (sections 24°S, 19°S, 11°S, 24.5°N and 36°N) the transport is maximum at the surface, decreasing with depth, reflecting the usual structure of a wind-driven subtropical gyre. The apparent variability in the horizontal and vertical fluxes observed in Figure 2.2 could be due to the different latitudinal extent among sections in the different decades.

2.3.2 Overturning circulation

The meridional overturning circulation is evident in the section-average net transport of northward water by the upper and abyssal layers and by the southward transport by deep layers for all latitudes (Figure 2.3).

There is no apparent change in the overturning strength amongst the diverse hydrographic realizations carried out in different decades, with no differences for the upper, deep and abyssal layers across the Atlantic Ocean. However, we have to be aware that there are some limitations associated with inverse modelling of hydrographic data. Each inverse solution could be interpreted as representative of a relatively short time interval (Fu et al., 2020) or could give information of monthly variations of the AMOC (Bryden et al., 2005b) Similarly, Ganachaud (2003b) refer to their estimates as time-average transoceanic transports with realistic uncertainties, although they acknowledge the temporal sampling problem inherent to the discrete sampling of hydrographic data.

Our results are similar to those obtained by other inverse models of the Atlantic with data of the first decade of our study (Ganachaud 2003a; Lumpkin & Pazos 2007; Macdonald 1995; Sloyan & Schröter 2001; Table 2.7). In general, the results agree, but we find more differences in upper layers and our model tends to provide smaller transports in bottom layers. A recent reconstruction of three decades of inverse models using sections north of 24.5°N (Fu et al., 2020) has also found stability in the strength of the AMOC for the SPNA.

OSNAP data products are available for 21 months, from July 2014 to March 2016 (Lozier et al., 2019b). AMOC values from OSNAP data can be compared to those of the inverse model for the last decade of the section at 55°N (West and East) but taking into account the shorter period in OSNAP data and the limitation of the inverse model solutions described before. The mass transports from the inverse model for each subbasin (1.0 ± 0.9 Sv for the West and 10.9 ± 1.7 Sv for the East) are slightly weaker than those obtained by OSNAP (2.1 ± 0.3 Sv for the West and 15.6 ± 0.8 Sv for the East). However, for the total section, the subpolar AMOC is not different (11.9 ± 2.1 Sv for the inverse model and 14.9 ± 0.9 Sv for OSNAP). Our results indicate a fairly constant weak transport in the Labrador basin over the three decades, and the Eastern basin being the major contributor to the AMOC, evidencing the OSNAP findings (Lozier et al., 2019a; Petit et al., 2020) of weak transport in the Labrador Sea between 2014 and 2016 that have persisted for the previous three decades.

AMOC estimates are also available for the RAPID program from April 2004 to August 2018 (Moat et al., 2020). Values for the 2010-19 decade are very similar between the inverse model

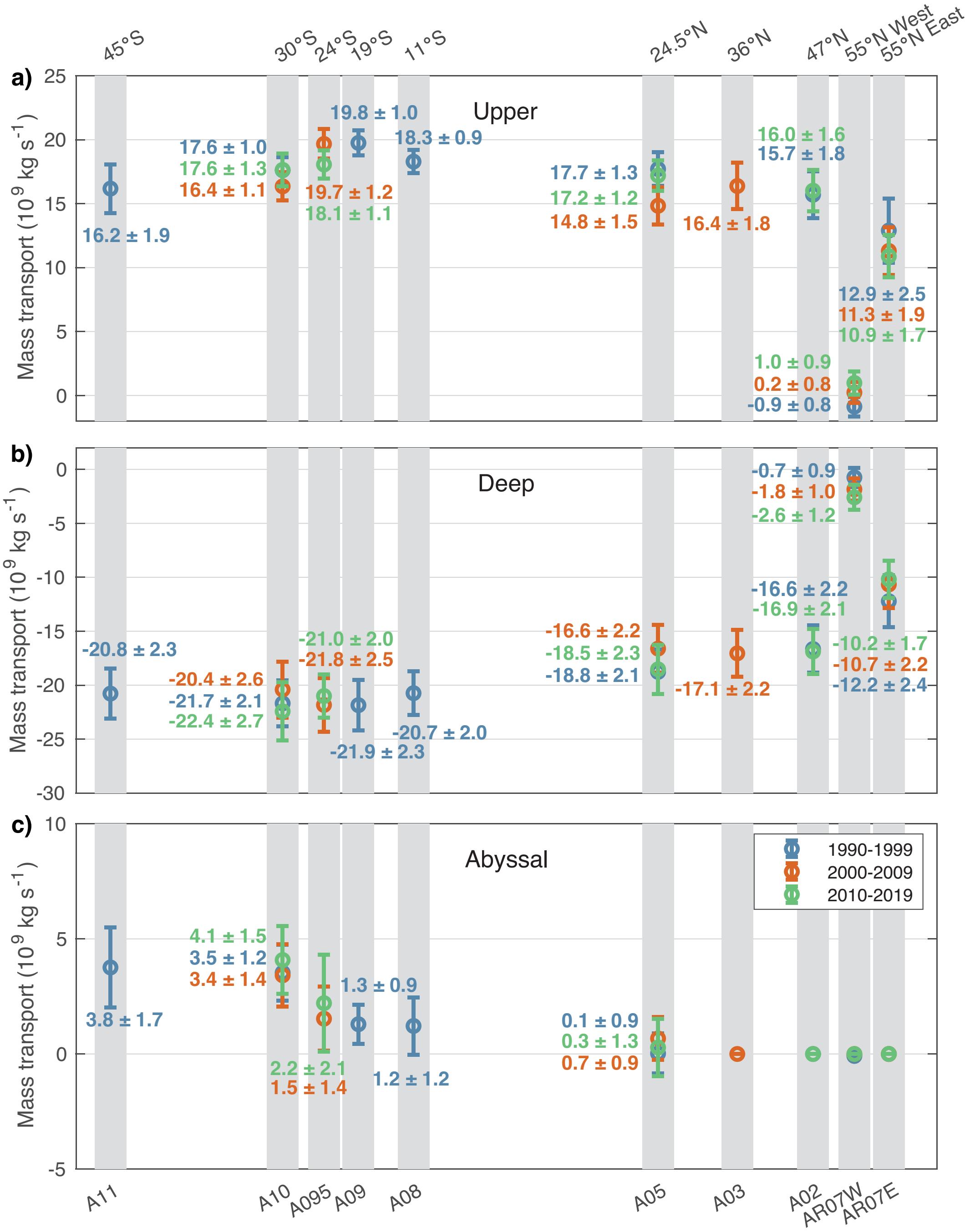

Figure 2.3. Mass transport (Sv) attending to each layer for each latitude and decade. The grey bars mark the nominal latitude of each zonal section, and the colours represent each decade, blue for 1990-99, orange for 2000-2009 and green for 2010-2019. The mass transport is divided into three layers – upper (a), deep (b) and abyssal (c).

Table 2.7. Compilation of mass transport (Sv) values for other large scale box inverse models. Notes: * only AR07E, † SAVE4, ‡ SAVE2,§ 23°S, ¶ SAVE 3 leg3 + leg4 (17°S)

Period	Layers	A11 45°S	A10 30°S	A095 24°S	A09 19°S	A08 11°S	A05 24.5°N	A03 36°N	A02 47°N	AR07W+AR07E 55°N	AR07W 53°N	AR07E 58°N
This model (decade 1990-99)												
1990-99	Upper	16.2 ± 1.9	17.6 ±1.0		19.8 ± 1.0	18.3 ± 0.9	17.7 ± 1.3		15.7 ± 1.8	12.0 ± 2.6	-0.9 ± 0.8	12.9 ± 2.5
	Deep	-20.8 ± 2.3	-21.7 ± 2.1		-21.9 ± 2.3	-20.7 ± 2.0	-18.8 ± 2.1		-16.6 ± 2.2	-12.8 ± 2.6	-0.7 ± 0.9	-12.1 ± 2.4
	Bottom	3.8 ± 1.7	3.5 ± 1.2		1.3 ± 0.9	1.2 ± 1.2	0.1 ± 0.9					
Ganachaud & Wunsch (2003)												
1990-99	Upper	8 ± 3	18 ± 3		26 ± 3	28 ± 4	14 ± 2		19 ± 2			
	Deep	-18 ± 4	-23 ± 3		-23 ± 3	-23 ± 4	-18.5 ± 2		-16 ± 2			
	Bottom	5 ± 2	6 ± 1.3		3.4 ± 1.1	3.1 ± 1.5	1 ± 1		0			
Lumpkin & Pazos (2007)												
1990-99	MOC	12.4 ± 2.6				16.2 ± 3.0	18.0 ± 2.5		16.3 ± 2.7	17.0 ± 4.3*		
Sloyan & Schröter (2001)												
1988-89	Upper		9.7 ± 0.4†		16.5± 0.6‡							
	Deep		-17.8 ± 2.1		-20.0 ± 2.4							
	Bottom		7.3 ± 1.7		5.2 ± 1.6							
Macdonald (1995)												
1981-1990	Upper			6.5 ± 0.6§	5.3 ± 0.9¶	9.9 ± 0.6	15.5 ± 0.9	10.5 ± 1.3	23.2 ± 0.8			
	Deep			-20.1 ± 1.2	-21.0 ± 3.1	-27.5 ± 1.4	-16.8 ± 1.2	-11.5 ± 1.6	-24.3 ± 1.3			
	Bottom			5.9 ± 0.9	3.1 ± 1.1	3.5 ± 1.0	0.4 ± 0.8					
Fu et al. (2020)												
1990-99	MOC						16.7 ± 2.4			15.4 ± 7.7	1.5 ± 3.3	15.8 ± 4.5
2000-09	MOC						14.8 ± 2.2			15.6 ± 3.9	0.5 ± 0.9	16.6 ± 3.3
2010-19	MOC						16.8 ± 3.1			13.4 ± 7.5	2.0 ± 3.5	14.9 ± 5.0

(24.5°N cruise in 2011) and RAPID (over 2010-2018) for upper (17.2 ± 1.2 and 16.4 ± 4.5 Sv, respectively), deep (-18.5 ± 2.3 and -17.3 ± 4.1 Sv, respectively) and abyssal (0.3 ± 1.3 and 1.1 ± 0.6 Sv, respectively) layers. The mass transports of the inverse model of the 2000-09 decade (24.5°N cruise in 2004) are weaker than RAPID values (averaged over the interval 2004-2009) for upper (14.8 ± 1.5 and 18.0 ± 4.7 Sv, respectively), deep (-16.6 ± 2.2 and -18.6 ± 4.3 Sv, respectively) and abyssal (0.7 ± 0.9 and 0.8 ± 0.6 Sv, respectively), although not different, in part due to the high uncertainties associated to RAPID data.

The question of the slowing of the AMOC or not is exceptionally important. Contrasting the results of in situ observations and reconstructions is a significant contribution to the debate. Monitoring programs enabled the observation of interannual changes in AMOC, such as the 0.5 Sv per year weakening of the AMOC at 26.5°N between 2004 and 2012, possibly explained by internal variability (Roberts et al., 2014), although recent studies using empirical analysis of hydrographic RAPID data dating back to the 1980s show no overall decline (Worthington et al., 2021). Other higher-frequency variations can be found, such as the ∼30% 2009-2010 decrease of AMOC at 26.5°N based on the previous 5 years of measurements (McCarthy et al., 2012). This decrease in strength was detected in the AMOC upper limb at 41°N but not in the deep western return limb at 16°N (Srokosz et al., 2012; Srokosz & Bryden, 2015).

The relationship between temperature and MOC enables the use of satellite sea surface temperature as a proxy for long-term reconstructions of MOC strength (Caesar et al., 2018; Manta et al., 2021), which can be compared to the estimations obtained with global climate numerical models (Caesar et al., 2018; Fraser & Cunningham, 2021). Longer-term reconstructions and projections from proxies and high-resolution climate models display a decline in the strength of the AMOC by 15% (Caesar et al., 2018) and 30% (Rahmstorf et al., 2015) since the 1950s, in the frame of a consistent weak AMOC for the last 150 years (Thornalley et al., 2018). Fraser & Cunningham (2021) have found no significant weakening trend in their reconstruction of AMOC over the last 120 years. Expendable bathythermograph (XBT) and Argo profile data enable the estimation of AMOC (Goes et al., 2020; Majumder et al., 2016), and results agree with our inverse model, especially for XBT-derived solutions, with Argo estimates being considerably higher. Monthly XBT transects could complement the study of short-term variability of the AMOC.

2.3.3 Heat transport

Total heat transport can be divided into its components attending to the mechanisms of vertical and horizontal circulation (Figure 2.4), allowing to break up the heat transport into a barotropic (throughflow), baroclinic (overturning) and horizontal (or gyre) component (Bryden & Imawaki, 2001). The throughflow component is the net transport across the section at the section-averaged temperature (Figure 2.5 a); the overturning component is the zonally averaged vertical circulation and the horizontal or gyre component is the horizontal and vertical residual heat (Bryden et al. 2011; Bryden & Imawaki 2001; McDonagh et al. 2015; Figure 2.4 a,c,e). Overall, the overturning heat transport (Figure 2.4 c), which represents changes in the meridional structure of the water column, dominates the total heat transport and increases equatorward. The horizontal or gyre component (Figure 2.4 e) comprises the result of large-scale gyre circulation and eddies, which remains fairly constant across all latitudes and through the decades of this study (McDonagh et al., 2015).

The North Atlantic subtropical gyre (24.5°N) shows a greater change in terms of overturning heat transport than in the rest of sections, with a strong decrease from a maximum value in 1990-1999 of 1.27 ± 0.06 PW to 0.97 ± 0.07 in 2000-2009 PW and a recovery to 1.10 ± 0.05 PW in 2010-19. The Labrador Sea (55°N West) net transports are almost null, with negligible contributions from the marked cyclonic gyre affecting the whole basin (Lozier et al., 2019a), vertically and horizontally. Nevertheless, in the Eastern subbasin of the northernmost section (55°N East) the overturning component majorly contributes to the total heat transport.

The RAPID-MOCHA mean heat transports of 1.3 ± 0.4 PW and 1.2 ± 0.4 PW for the decades of 2000-09 and 2010-19, respectively (Moat et al., 2016) are not significantly different than the values of the inverse model (0.97 ± 0.09 and 1.13 ± 0.07 PW, respectively) for the section 24.5°N. In the SPNA, the mean heat transport product estimated from OSNAP (Lozier et al., 2019a,b) for the Eastern subbasin at 55°N (0.38 ± 0.02 PW) is similar to the inverse model value (0.29 ± 0.06 PW). The values for the Western subbasin at 55°N are very small in both cases (0.01 ±

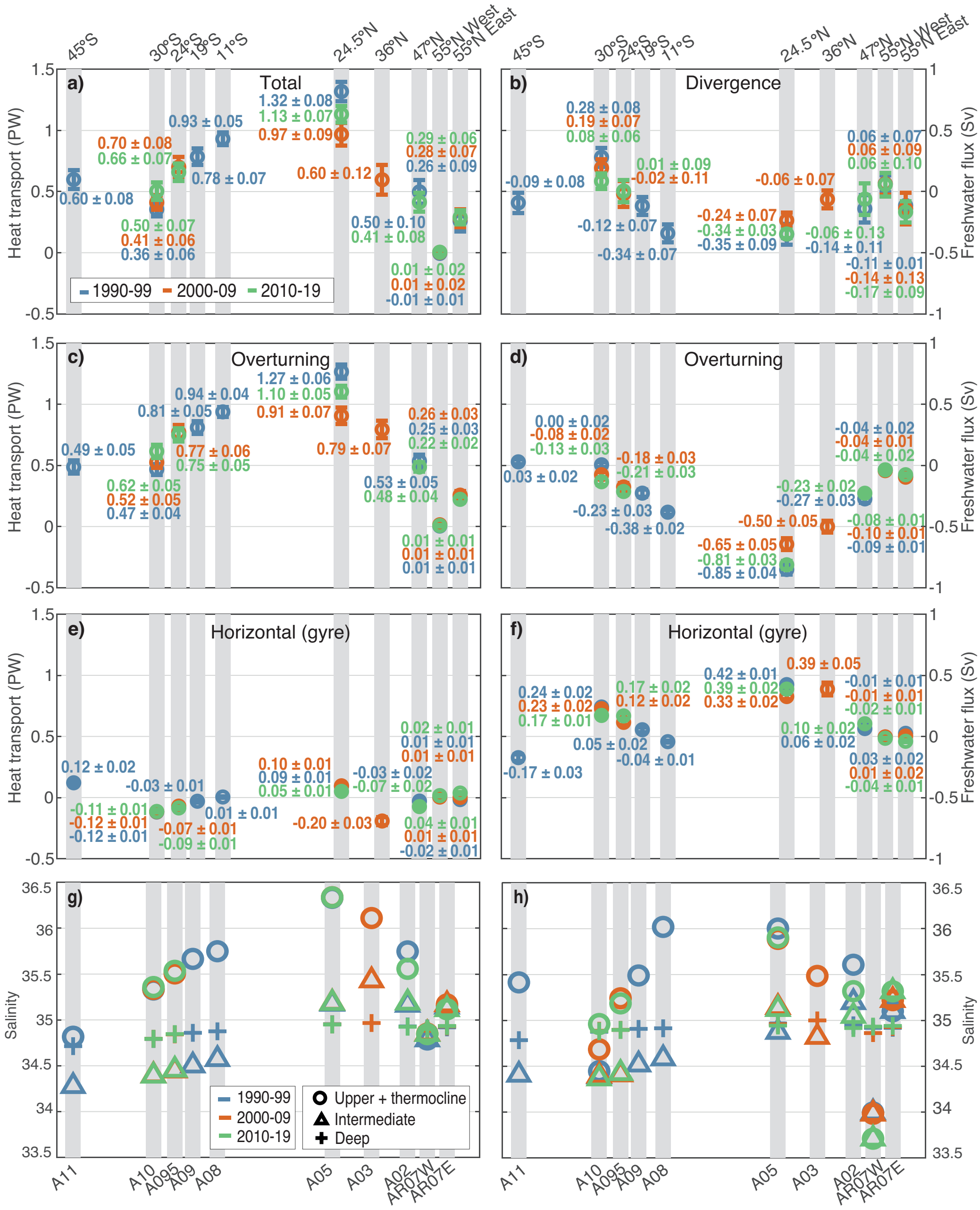

Figure 2.4. Heat and freshwater transport attending to their components and area and transport-weighted salinity for each latitude and decade. The grey bars mark the nominal latitude of each zonal section, and the colours represent each decade, blue for 1990-99, orange for 2000-2009 and green for 2010-2019. The left panels (a,c,e) are the heat transport in PW, and the panels on the right (b,d,f) are the freshwater transport in Sv. The total transport (a,b) is divided in throughflow, overturning (c,d) and horizontal or gyre (e,f). Area-weighted (g) and transport-weighted salinity (h). Each property has been divided into three water masses – upper and thermocline waters (circles), intermediate waters (triangles), and deep waters (crosses).

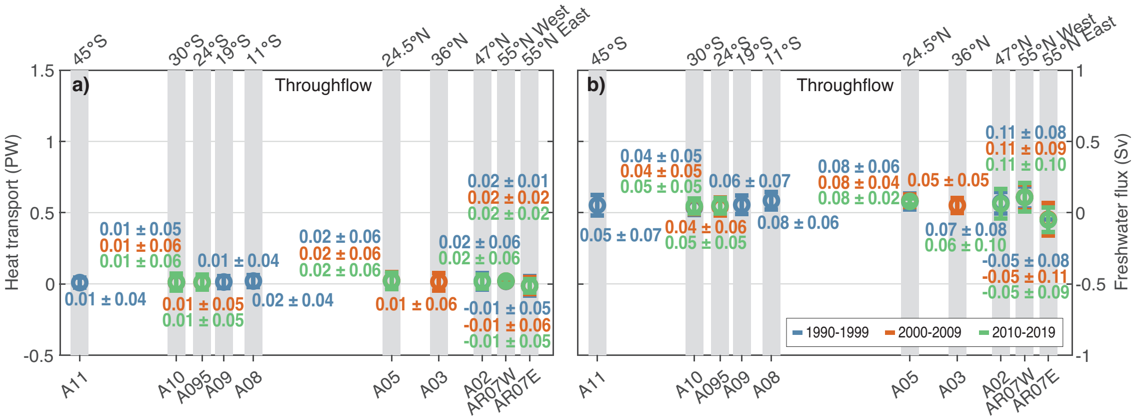

Figure 2.5. Heat (a) and freshwater (b) transport throughflow component for each latitude and decade. The gray bars mark the nominal latitude of each zonal section, and the colors represent each decade. The left panel is the heat transport in PW, and the panel on the right is the freshwater flux in Sv.

0.02 PW for the inverse model and 0.08 ± 0.004 PW for OSNAP), and the values for the whole basin are comparable (0.30 ± 0.05 PW for the inverse model and 0.46 ± 0.02 PW for OSNAP), although different, partly because OSNAP data are not available for the whole decade. These results confirm the importance of the Eastern basin (55°N East) in the export of heat from the Atlantic to the Arctic Ocean, carried by the NAC in the upper layers.

2.3.4 Freshwater transport

Oceanic freshwater transport is the non-salt part of mass transport. Its divergence can be understood as the balance of evaporation, precipitation, river runoff and ice processes. It is calculated by constraining the salt flux across each section to that across the Bering Strait. The salt flux (or non-freshwater part of the mass transport) is not affected by the strength of freshwater divergence as this happens at zero salinity. Definitions for the freshwater flux are described in Appendix C. The freshwater divergence (Figure 2.4 b,d,f) can be divided, as the heat transport, into its components. On this occasion and in contrast to the heat flux, the freshwater throughflow contributes from 5 to 35% to the total flux (Figure 2.5 b). This component represents the evolution of the section average salinity from that of the Bering Strait (a southward flow of 0.8 Sv with an average salinity of 32.5, resulting in a salinity flux of -26.0 Sv psu; McDonagh & King 2005; Woodgate & Aagaard 2005). The freshwater overturning component (Figure 2.4 d) presents a stronger southward transport in the sections close to the equator. The horizontal or gyre freshwater flux (Fig. 2.4 f) displays a higher northward freshwater flux in the sections that occupy the subtropical gyres (24.5°N and 36°N in the North Atlantic and 24°S and 30°S in the South Atlantic), with similar values for all decades.

The mean freshwater divergence transport across the whole OSNAP section (-0.32 ± 0.01 Sv; Lozier et al. 2019a,b) in the 2010-19 decade is stronger than in the inverse model (-0.11 ± 0.11 Sv). In the inverse model, there is a southward freshwater transport (-0.17 ± 0.09 Sv) in the Eastern subbasin, that is basically unaltered by the no significant northward transport in the Western subbasin (0.06 ± 0.10 Sv). OSNAP data suggest, in turn, that both subbasins contribute similarly to the southward freshwater transport across the whole section (-0.18 ± 0.01 Sv and -0.14 ± 0.01 Sv for the West and East subbasins, respectively).

The south Atlantic subtropical gyre presents low values of overturning freshwater flux at 30°S, thus being the only section with a horizontal component larger than the overturning (Mecking et al., 2016). Based on our understanding from model studies, the overturning freshwater flux at this latitude has been identified as a possible proxy for the stability of the AMOC (Bryden et al., 2011; Dijkstra, 2007; Gent, 2018; Rahmstorf, 1996; de Vries & Weber, 2005; Weber & Drijfhout, 2007; Weijer et al., 2019), potentially determining whether it is in a monostable or bistable regime. We have found a tendency towards increasingly southward values from 1990-99 (0.00 ± 0.02 Sv) to 2000-09 (-0.08 ± 0.02 Sv), and no differences within uncertainties between 2000-09 decade and the 2010-19 decade (-0.13 ± 0.03 Sv), with an overall change between 1990-99 and 2010-19. Negative values of the overturning freshwater transport at 30°S indicate that the AMOC transports freshwater southwards, and a net input of freshwater north of 30°S is necessary to maintain the salinity structure of the overturning circulation. This result is consistent with other studies relying on observational data that have found that the overturning circulation effectively carries freshwater out of the Atlantic through its southern boundary (Bryden et al., 2011; Garzoli et al., 2013; McDonagh & King, 2005; Saunders & King, 1995; Weijer et al., 1999).

The transport-weighted sensitivity of the overturning and horizontal components reflects the change in each component subtracting the effect of a change in the mass transport. The transport weighted freshwater overturning - the freshwater overturning divided by the overturning strength - at 30°S shows a systematic decrease (0.000 ± 0.001, -0.005 ± 0.001, and -0.008 ± 0.002 for each hydrographic cruise done in each decade, respectively) that reflects an increasing difference between the freshwater content in upper and lower layers. To assess the origin of this change, we have computed the transport and area-weighted salinity for upper and thermocline, intermediate, and deep layers. The area-weighted salinity (Figure 2.4 g) values for each layer fail to show changes for each decade. However, the transport-weighted salinity (Figure 2.4 h) for upper and thermocline layers presents higher variability (34.45, 34.68 and 34.96 for the realizations carried out in each decade), whereas the intermediate and deep layers remain fairly constant. Thus, this change in the freshwater overturning arises from an increase in the salinity of upper layers transported northward in the upper ocean, possibly due to higher transport of the salty waters of the Agulhas leakage from the Indian Ocean. Model simulations have indicated that there might be a Southern Hemisphere origin to the AMOC decadal variability arising from the Agulhas leakage (Biastoch et al., 2008). The strength of this variability factor decreases northward but can reach up to 0.6 Sv. On longer timescales, it has shown a correlation with the Atlantic Multidecadal Oscillation, and it has been linked to wind-driven processes (Biastoch et al., 2015). Other studies have found no significant impact on the AMOC (Weijer & van Sebille, 2014), and therefore, a discussion on this topic continues.

2.4 Conclusions

The behaviour of the AMOC and its driving mechanisms and feedbacks has received much attention in climate change scenarios due to the major climate impacts associated with a predicted slowdown. As a result, several ocean locations are being monitored to estimate the changes in the strength of the AMOC at different latitudes.

Our results from inverse models based on hydrographic data show that the Atlantic basin overturning transport displays no changes at any latitude between the different hydrographic cruises. In the SPNA, our results indicate that the major contributor to the AMOC for the three decades is the Eastern basin (55°N East) as estimated by OSNAP for the last decade.

At 30°S, an increase of southward freshwater overturning transport has been estimated over the three decades, indicating that the AMOC is possibly in a bistable state based on findings from model studies. These negative values appear when AMOC exports freshwater out of the Atlantic, equivalent to a net precipitation over the Atlantic basin. In this case, the AMOC has multiple equilibria and may collapse due to a large enough freshwater perturbation (Dijkstra, 2007; Mecking et al., 2016; Weijer et al., 2019).

Chapter 3

Horizontal circulation

This chapter is in revision for publication in *Ocean Science*:

Caínzos, V., Pérez-Hernádez, M. D., Santana-Toscano, D., Arumí-Planas, C., and Hernández-Guerra, A., (2023). Consistent picture of the horizontal circulation of the Atlantic Ocean over three decades. Ocean Science (*in revision*).

3.1 Introduction

The Atlantic Ocean is connected by its meridional overturning circulation (AMOC), which can be considered as two overturning cells that meet at deep layers. The upper cell consists of upper warm, saline waters that are transported northward and, eventually, get colder, fresher and denser and travel southward in deep layers. This cell is balanced by the lower cell of the AMOC, in which the southward deep layers are returned northward by the abyssal layers (Caínzos et al., 2022a; Kersalé et al., 2020). This proves to be a remarkable characteristic of the Atlantic Ocean, since it maintains a net northward transport of heat across all latitudes, contrasting to the southward heat transport appearing in other oceans in the subtropical gyre of the southern hemisphere (Ganachaud & Wunsch, 2003; Jayne & Marotzke, 2001; Forget & Ferreira, 2019).

The complex system of currents making up the AMOC has been often oversimplified, despite the multiple pathways connecting the different elements of the AMOC (Bower et al., 2019). Lagrangian studies have provided very useful insights of ocean currents, firstly on the surface and then for the full water column, mapping the spatial structure of the ocean circulation as they naturally drift (Bower et al., 2019; Davis et al., 1992). However, most of these measurements are currently limited to the top-most 2000 m since this is the maximum depth of the Argo profiles. Deep-Argo profilers could provide in the future a continuous quantification of the ocean below 2000 m (Foppert et al., 2021; Johnson et al., 2015, 2019a). Moreover, data from mooring arrays at key locations have provided continuous measurements over the last years and could be useful to quantify currents at these chosen latitudes (Lozier et al., 2017; Cunningham et al., 2007; Johns et al., 2011; Kanzow et al., 2006; Hummels et al., 2015; Meinen et al., 2013; Kersalé et al., 2020). A combination of these international arrays has evolved into synthetic observational time series of the AMOC (McCarthy et al., 2020). However, with the earlier starting date of these arrays being the 2000s, the time series are sometimes too short to study variability and lack the necessary spatial resolution to fully resolve the structure or variability of currents. Therefore, ship-based observing systems are the only current alternative to study the full-water column of the ocean at periodic intervals that allow us to expand back into the 1990s.

Repeat hydrographic sections have been made available since the 1950s with the efforts of the International Geophysical Year. Near the end of the twentieth century, continuous basin-scale measurements were emphasized under the World Ocean Circulation Experiment (WOCE) and, later, the Global Ocean Ship-Based Hydrographic Investigations Program (GO-SHIP; Talley et al. 2016). Full-depth water column, high-resolution measurements of temperature and salinity enable the computation of geostrophic velocity for each hydrographic station pair relative to a known level of no motion. Inverse modelling provides a useful tool in computing the absolute geostrophic velocity (Wunsch, 1996). Moreover, it enables the estimation of meridional property transports from high-resolution hydrographic data, accompanied by uncertainties obtained along the inverse solutions (Ganachaud & Wunsch, 2003; Macdonald & Wunsch, 1996; Fu et al., 2020; Lumpkin & Pazos, 2007).

Ganachaud & Wunsch (2000) have previously provided a globally consistent circulation scheme using WOCE sections for the global ocean using inverse modelling. Furthermore, they also described the regional aspects of that circulation (Ganachaud & Wunsch, 2003). Their suggested circulation in the Atlantic Ocean agrees with estimates from other global and regional studies spanning over the previous 30 years. Their solutions rely on the fact that large-scale quantities are close to the time mean. The remaining uncertainties are dominated by oceanic variability in the density and other properties, which mainly originated from a lack of measurements and large seasonality.

Caínzos et al. (2022a) have published updated estimations of the AMOC, heat and freshwater transports across the Atlantic Ocean using WOCE and GO-SHIP sections for the last thirty years. The solutions were obtained using inverse models, one for each of the last three decades – 1990 to 1999, 2000 to 2009 and 2010 to 2019. For that study, the authors focused on the possible changes of the AMOC at each latitude available in each model. The results show no changes in the AMOC for all sections analysed over the whole Atlantic for the last thirty years for either mass, transport or freshwater.

In this study, we will describe the horizontal circulation in each section and try to quantify the strength of surface, deep, and abyssal currents in the Atlantic Ocean as well as their changes over the last three decades. Additionally, we have also investigated the changes in heat and freshwater content and their transformation across latitudes. Throughout the text, we first describe the hydrographic data and the methodology applied to them, as well as the properties of the currents present for all latitudes, dividing them into surface, deep and bottom currents. These currents are discussed following the direction of their flow, from their origin to their destination to be able to compare how they might have changed on their way. However, the currents in the figures are depicted maintaining their geographical structure, from north to south.

3.2 Data and methods

3.2.1 Hydrographic data

We have compiled zonal hydrographic sections for the last three decades (1990-99, 2000-09, 2010-19) as part of WOCE and GO-SHIP programs. The selected sections span the whole Atlantic basin, from 45°S to 55°N in the first decade and from 30°S to 55°N for the last two decades (Figure 3.1). Deviations of some stations from the nominal latitude appear mostly over the western and eastern boundaries and over the platform, correcting the track line to a perpendicular angle to the main current. Only three sections appear in all three decades: 30°S, 24.5°N and the northernmost section divided into the western (53°N) and eastern (58°N) subbasins. Table 2.1

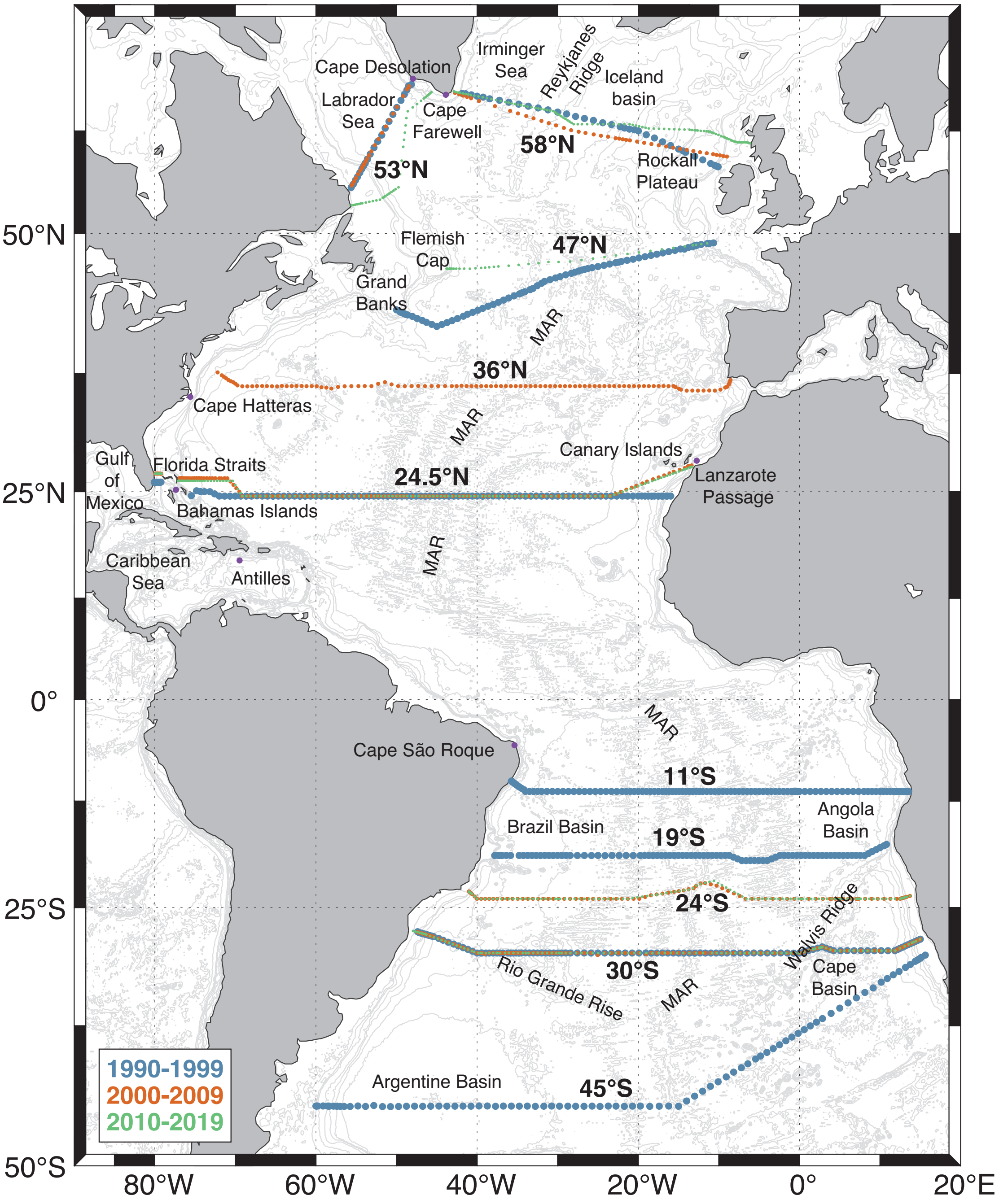

Figure 3.1. Map of the zonal sections in each decade for the inverse model. Each section is accompanied by its nominal latitude, with colours representing each decade, blue for 1990-1999, orange for 2000-2009, and green for 2010-2019. The main geographical features are included in the figure.

summarizes the chosen sections and their characteristics.

We have identified the main water masses in these sections and defined a reference level of no motion located at the interface between the southward flowing North Atlantic Deep Water (NADW) and the northward Antarctic Bottom Water (AABW), following Caínzos et al. (2022a), Hernández-Guerra et al. (2019) and McDonagh & King (2005). This neutral density (γ^n) reference layer is used in the thermal wind equation to estimate geostrophic velocities and transports. The value of the reference layer for each section is specified in Table 2.1. If any pair of stations fail to reach this value of neutral density, then the deepest common level is used instead of the reference layer. This usually happens over the continental slope, and the velocity in the triangular section below this level is taken to be constant and equal to the velocity at the lowest common level.

The water column is divided into 11 layers defined by isolines of the same neutral density selected according to the presence of different water masses (Hernández-Guerra et al., 2019; Talley, 2008). The Ekman transport is estimated using the National Center for Environmental Prediction and National Center for Atmospheric Research (NCEP–NCAR) surface winds. We compute the Ekman transport for the time of the cruise and include it in the first layer of each section. If outcropping is found at the surface, we measure the percentage of each layer at the surface and then associate these different weights to the Ekman transport for each outcropping layer.

3.2.2 Inverse model

Applying geostrophy to each pair of hydrographic stations, we obtain relative velocities referenced to a supposed level of no motion. However, in truth this reference level has a velocity different from zero. Inverse models have been widely used to determine the unknown geostrophic reference velocities for each hydrographic station pair. The most basic constraints applied to inverse models are based on the continuity equation, either in mass, heat and/or salinity content (Wunsch, 1978, 1996). The inverse model equations are represented in matrix form as:

$$\mathrm{Ab} + \mathrm{n} = -\mathrm{Y} \tag{3.1}$$

where A is a $\mathrm{M} \times \mathrm{N}$ matrix, there N is the total number of unknowns and M is the number of transport constraints (or equations), b is a column vector of length N containing the unknowns of the system, and n is a column vector of length M that includes the noise of each constraint. Y is a column vector of length M with the initial transports and externally imposed mass transports.

The inverse model used here is the same as in Caínzos et al. (2022a). For each decade, the inverse model links boxes between adjacent sections from south to north. For a single box, we have conserved mass and salinity content. Mass is conserved for the whole box for all station pairs of both sections and considers the Ekman corrections for each section included in the first layer. Regional constraints are applied to each section, despite having different station pairs and neutral density layers affected. To define the continuity of mass transport for each of the layers, conservation of each layer was imposed between both sections, with Ekman correction in the outcropping layers. In addition to mass conservation, we have also constrained the salinity content of each single section. Using salinity allows for changes in freshwater across the section while still conserving mass. The system of unknowns includes the velocities at the reference level and the adjustment of the Ekman transport in the first layer. The Gauss-Markov estimator is applied to solve this highly underdetermined system of equations (Wunsch, 1996). The same model configuration is used for each decade, so that differences in the model solution are attributable to changes in circulation. Further in-depth descriptions of the reference level, a priori estimates and uncertainties, and sensitivity tests applied to these inverse models appear in the Supporting Information of Caínzos et al. (2022a).

Using the results from the inverse model we can obtain the absolute velocity, considering adding the adjustments to the velocities at the reference level (b) to the geostrophic velocity between each pair of stations, $\mathrm{v_r}$. The adjusted mass transport ($\mathrm{T_M}$) can be computed integrating the absolute velocity over an area A defined by a certain horizontal and vertical extension:

$$\mathrm{T_M} = \int \rho \, (\mathrm{v_r} + \mathrm{b}) \, \mathrm{dA} \tag{3.2}$$

where ρ is the density. The corrected heat transport ($\mathrm{T_H}$) can be computed similarly as

$$\mathrm{T_H} = \int \mathrm{c_p} \, \Theta \, \rho \, (\mathrm{v_r} + \mathrm{b}) \, \mathrm{dA} \tag{3.3}$$

where $\mathrm{c_p}$ is the heat capacity of sea water and Θ is the potential temperature. The freshwater flux (FW) has been estimated as the freshwater divergence, which represents the difference between the total freshwater flux and the volume flux through the Bering Strait (Caínzos et al., 2022a; McDonagh et al., 2015; Bryden et al., 2011):

$$\mathrm{FW} = -\frac{\mathrm{T_i^M S'} - \iint \rho \, \mathrm{S'} \, \mathrm{v} \, \mathrm{dxd\gamma^n}}{\mathrm{S_0}} \tag{3.4}$$

3.3 Results and discussion

3.3.1 Boundary and surface currents

Malvinas Current

The Malvinas Current (MC) is a cold and nutrient-enriched current originating from a northernmost branch of the northward Antarctic Circumpolar Current (ACC) known as the Subantarctic

Table 3.1. Characteristics of each upper-layer current found at every section.

Decade	Stations	Long (°E)	Dist (km)	Layers	Depth (m)	Mass Trans (Sv)	Heat Trans (PW)	Fw Total (Sv)	TWT (°C)	TWS
Malvinas Current 45°S										
1990-99	1:5	-59.9:-58.6	109	1:7	0 to 1206	37.2 ± 2.0	0.54 ± 0.02	0.07 ± 0.01	3.66	34.265
Brazil Current 30°S										
1990-99	1:15	-47.2:-42.9	443	1:4	0 to 678	-26.7 ± 1.6	-1.63 ± 0.09	0.16 ± 0.02	15.47	35.611
2000-09	6:14	-46.3:-43.6	282	1:4	0 to 735	-22.2 ± 1.5	-1.31 ± 0.08	0.09 ± 0.02	14.96	35.558
2010-19	1:7	-47.7:-46.5	122	1:4	0 to 505	-9.5 ± 0.7	-0.64 ± 0.04	0.05 ± 0.01	16.99	35.900
Brazil Current Recirculation 30°S										
1990-99	16:20	-41.7:-40.0	180	1:4	0 to 1207	16.4 ± 1.9	0.85 ± 0.07	-0.16 ± 0.03	13.09	35.300
2000-09	15:17	-42.3:-41.7	60	1:4	0 to 1187	15.9 ± 2.0	0.80 ± 0.08	-0.14 ± 0.03	12.75	35.248
2010-19	8:10	-45.8:-45.4	49	1:4	0 to 764	13.2 ± 1.4	0.76 ± 0.07	-0.06 ± 0.02	14.54	35.271
Brazil Current 24°S										
2000-09	1:5	-41.0:-40.8	25	1:3	0 to 476	-4.7 ± 0.4	-0.39 ± 0.02	0.04 ± 0.01	21.03	36.340
2010-19	1:6	-41.0:-40.6	47	1:3	0 to 515	-12.0 ± 0.7	-0.88 ± 0.04	0.16 ± 0.01	18.64	36.066
Brazil Current Recirculation 24°S										
2000-09	6:10	-40.3:-39.0	136	1:4	0 to 719	8.9 ± 1.4	0.57 ± 0.09	-0.03 ± 0.03	16.17	35.617
2010-19	7:8	-40.3:-40.0	43	1:4	0 to 738	10.5 ± 0.9	0.70 ± 0.05	-0.07 ± 0.02	16.69	35.785
Brazil Current 19°S										
1990-99	1:4	-37.4:-37.1	37	1:6	0 to 1514	-19.7 ± 1.3	-0.79 ± 0.05	0.06 ± 0.03	10.21	35.113
Brazil Current Recirculation 19°S										
1990-99	5:6	-36.7:-36.4	25	1:6	0 to 1490	19.3 ± 2.1	0.67 ± 0.08	0.06 ± 0.04	8.79	34.863
Antarctic Circumpolar Current Front 45°S										
1990-99	51:57	-15.0:-10.1	463	1:8	0 to 3035	-55.5 ± 5.6	-1.09 ± 0.07	-0.14 ± 0.03	4.96	34.471
Benguela Current 45°S										
1990-99	72:90	2.9:15.1	1335	1:4	0 to 650	24.0 ± 2.3	1.19 ± 0.11	-0.07 ± 0.02	12.53	35.057
Benguela Current 30°S										
1990-99	99:109	11.8:14.7	304	1:4	0 to 496	12.1 ± 1.2	0.60 ± 0.05	-0.02 ± 0.01	12.66	34.998
2000-09	100:110	11.8:14.7	306	1:4	0 to 523	12.1 ± 1.2	0.61 ± 0.06	-0.02 ± 0.01	12.75	35.071
2010-19	111:119	11.3:14.5	326	1:4	0 to 528	13.5 ± 1.0	0.67 ± 0.05	-0.05 ± 0.01	12.66	35.102
Benguela Current 24°S										
2000-09	82:84	9.0:9.7	76	1:4	0 to 540	8.7 ± 1.3	0.44 ± 0.06	-0.01 ± 0.01	12.69	35.019
2010-19	103:106	8.7:9.7	108	1:4	0 to 552	4.6 ± 0.8	0.25 ± 0.04	-0.01 ± 0.01	13.94	35.096
Benguela Current 19°S										
1990-99	82:85	8.1:9.0	113	1:4	0 to 500	2.3 ± 1.2	0.13 ± 0.05	-0.01 ± 0.01	14.06	35.262
South Equatorial Current 30°S										
1990-99	57:96	-18.4:8.5	2587	1:4	0 to 696	16.9 ± 1.9	0.86 ± 0.09	0.01 ± 0.02	12.85	35.060
2000-09	57:96	-19.0:7.6	2565	1:4	0 to 736	14.6 ± 2.1	0.76 ± 0.10	0.00 ± 0.02	13.22	35.142
2010-19	58:108	-19.8:9.0	2773	1:4	0 to 727	15.9 ± 1.9	0.80 ± 0.09	-0.01 ± 0.02	12.70	35.179
South Equatorial Current 24°S										
2000-09	32:81	-24.2:7.4	3201	1:4	0 to 620	16.5 ± 1.7	1.00 ± 0.10	0.02 ± 0.03	15.35	35.451
2010-19	34:102	-26.1:7.6	3421	1:4	0 to 634	16.5 ± 1.6	1.04 ± 0.10	-0.14 ± 0.03	15.94	35.537
South Equatorial Current 19°S										
1990-99	25:81	-23.2:7.0	3181	1:4	0 to 515	9.0 ± 1.9	0.60 ± 0.11	-0.07 ± 0.04	16.90	35.644
North Brazil Current 11°S										
1990-99	1:10	-35.7:-34.7	130	1:5	0 to 937	17.0 ± 1.2	0.98 ± 0.05	-0.19 ± 0.03	14.59	35.509
Florida Current 24.5°N										
1990-99	1:10	-80.0:-79.3	68	1:6	0 to 511	34.5 ± 0.3	2.70 ± 0.02	-0.17 ± 0.01	19.84	36.120
2000-09	1:8	-79.9:-79.3	58	1:6	0 to 566	32.1 ± 0.3	2.43 ± 0.02	-0.09 ± 0.01	19.16	36.201
2010-19	1:13	-79.9:-79.2	70	1:6	0 to 592	31.3 ± 0.3	2.31 ± 0.02	-0.14 ± 0.01	18.65	36.098

Continuation from Table 3.1.

Decade	Stations	Long (°E)	Dist (km)	Layers	Depth (m)	Mass Trans (Sv)	Heat Trans (PW)	Fw Total (Sv)	TWT (°C)	TWS
Antilles Current 24.5°N										
1990-99	11:14	-75.5:-74.3	125	1:4	0 to 736	12.8 ± 1.0	0.98 ± 0.07	-0.04 ± 0.01	19.45	36.394
2000-09	10:17	-76.8:-76.4	38	1:4	0 to 758	13.2 ± 0.4	0.97 ± 0.03	-0.02 ± 0.01	18.67	36.431
2010-19	14:24	-77.1:-76.7	39	1:4	0 to 704	7.5 ± 0.3	0.56 ± 0.02	-0.02 ± 0.01	19.05	36.484
Canary Current 24.5°N										
1990-99	98:107	-20.0:-16.9	310	1:4	0 to 509	-5.1 ± 0.9	-0.34 ± 0.06	0.01 ± 0.01	16.57	36.283
2000-09	110:114	-19.5:-17.5	215	1:4	0 to 532	-6.1 ± 1.4	-0.40 ± 0.08	0.03 ± 0.01	16.59	36.313
2010-19	145:153	-19.1:-16.4	289	1:4	0 to 578	-4.8 ± 0.7	-0.32 ± 0.05	0.01 ± 0.01	16.86	36.372
Gulf Stream 36°N										
2000-09	1:10	-71.7:-69.1	256	1:6	0 to 891	74.9 ± 1.7	4.56 ± 0.11	-0.82 ± 0.04	15.42	36.014
Gulf Stream Recirculation 36°N										
2000-09	10:17	-68.5:-64.8	331	1:6	0 to 1281	-35.4 ± 3.0	-2.29 ± 0.18	0.19 ± 0.05	16.36	36.138
North Atlantic Current 47°N										
1990-99	1:14	-49.6:-44.4	444	1:6	0 to 838	33.4 ± 2.9	1.79 ± 0.14	-0.22 ± 0.04	13.53	35.722
2010-19	7:15	-42.9:-39.0	294	1:6	0 to 982	28.2 ± 1.5	1.18 ± 0.05	-0.09 ± 0.02	10.59	35.368
North Atlantic Current 58°N										
1990-99	42:53	-21.7:-14.1	496	1:6	0 to 1034	5.2 ± 3.7	0.19 ± 0.13	0.03 ± 0.02	9.12	35.290
2000-09	47:61	-22.8:-13.2	599	1:6	0 to 1010	5.4 ± 2.7	0.20 ± 0.10	0.00 ± 0.01	9.27	35.347
2010-19	93:121	-21.1:-10.1	662	1:6	0 to 947	6.7 ± 1.6	0.25 ± 0.05	-0.01 ± 0.01	9.29	35.292
East Reykjanes Ridge Current 58°N										
1990-99	40:42	-23.3:-22.2	66	1:6	0 to 1183	-3.2 ± 2.2	-0.10 ± 0.07	0.00 ± 0.01	8.14	35.131
2000-09	38:41	-31.1:-29.2	117	1:6	0 to 911	-1.8 ± 1.4	-0.06 ± 0.04	0.00 ± 0.01	8.45	35.070
2010-19	80:84	-28.5:-27.5	63	1:6	0 to 929	-2.0 ± 0.8	-0.06 ± 0.02	0.00 ± 0.01	7.79	35.082
Irminger Current 58°N										
1990-99	29:34	-36.1:-31.2	282	1:6	0 to 615	5.0 ± 2.7	0.13 ± 0.06	0.00 ± 0.01	6.37	34.991
2000-09	34:38	-34.9:-32.0	78	1:6	0 to 798	4.7 ± 1.9	0.15 ± 0.05	0.00 ± 0.01	8.12	35.105
2010-19	59:80	-35.7:-28.8	418	1:6	0 to 783	6.1 ± 1.2	0.17 ± 0.03	0.00 ± 0.01	6.91	35.019
East Greenland Current 58°N										
1990-99	22:29	-41.9:-37.2	264	1:6	0 to 194	-0.4 ± 0.6	-0.01 ± 0.01	0.00 ± 0.01	5.94	34.938
2000-09	26:34	-42.8:-35.9	408	1:6	0 to 621	-1.6 ± 1.8	-0.04 ± 0.04	0.00 ± 0.01	6.60	34.826
2010-19	40:48	-42.9:-41.4	82	1:6	0 to 579	-3.3 ± 1.0	-0.06 ± 0.02	-0.02 ± 0.01	4.42	34.560
Upper West Greenland Current 53°N										
1990-99	18:21	-49.0:-48.5	67	1:6	0 to 262	1.3 ± 0.4	0.01 + 0.01	0.01 ± 0.01	2.74	34.126
2000-09	20:25	-49.9:-48.5	164	1:6	0 to 1232	1.6 ± 1.0	0.03 ± 0.02	0.00 ± 0.01	4.62	34.857
2010-19	31:35	-47.4:-46.4	75	1:6	0 to 788	3.4 ± 1.0	0.05 ± 0.02	0.04 ± 0.01	3.57	34.332
Upper Labrador Current 53°N										
1990-99	5:7	-54.3:-54.1	26	1:6	0 to 413	-2.1 ± 0.5	0.00 ± 0.01	-0.02 ± 0.01	0.45	33.569
2000-09	4:8	-54.8:-54.1	80	1:6	0 to 418	-1.2 ± 0.4	0.00 ± 0.01	-0.01 ± 0.01	0.98	33.630
2010-19	6:12	-54.2:-52.1	151	1:6	0 to 400	-1.6 ± 0.4	0.00 ± 0.01	-0.01 ± 0.01	0.22	33.455

Front that enters the South Atlantic as part of the cold-fresher water route (Bower et al., 2019). It keeps flowing along the continental shelf of Argentina colliding at ∼ 39°S with the warmer and saltier southward Brazil Current (BrC), and then both currents turn offshore (Artana et al., 2018; Legeckis & Gordon, 1982; Garzoli, 1993; Vivier & Provost, 1999a; Goni et al., 1996). The MC is observed as a northward transport of 37.2 ± 2.0 Sv at 45°S over the platform and slope, extending 109 km from the coast to 58.6°W (Figure 3.2 l, m and Table 3.1). The current, extending from the surface up to 1200 m, flows more intensely along the layer between 27.23 and 27.58 kg m^{-3} (~650 m), carrying 19.2 ± 1.5 Sv, representing over 50% of its total strength. The MC transports equatorward 0.54 ± 0.02 PW of heat and 0.07 ± 0.01 Sv of freshwater, carrying waters with mean transport-weighted (TW) salinity of 34.265 and temperature of 3.66°C.

The mass transport estimation coincides with the 24-year mean transport of 37.1 ± 2.6 Sv at 41°S from in situ current velocity and satellite altimetry from Artana et al. (2018). They have also found no significant trend in the MC transport, with larger annual standard deviations mainly associated with smaller mean transports. Earlier estimations using direct velocity measurements at the same location also agree with these results, manifesting the high variability of the MC: 41.5 Sv with a standard deviation of 12 Sv for December 1993 to June 1995 (Vivier & Provost, 1999b) and 34.3 Sv for December 2001 to February 2003 (Spadone & Provost, 2009). Other estimations from inverse solutions using hydrographic data have found slightly larger results (42.7 ± 6.5 Sv; McDonagh & King 2005). Further south, at 51°S, the Subantarctic Front has also shown large interannual variability, carrying 32.6 Sv in 1999 while 17.9 Sv in 2010 (Pérez-Hernández et al., 2017), being the former consistent with our MC estimates.

This section is subjected to the presence of fronts designated by large-scale features of the ACC (Orsi et al., 1995; Sokolov & Rintoul, 2009). The subtropical front marks the northernmost presence of subantarctic waters and can be found at 45°S (Smythe-Wright et al., 1998) extending over 463 km between 15.0°W and 10.1°W, occupying a large part of the barotropic water column (up to ~3000 m deep). Across this front, there is a net southward mass transport of -55.5 ± 5.6 Sv, effectively removing -1.09 ± 0.07 PW of heat and -0.14 ± 0.03 Sv of freshwater out of the South Atlantic.

Brazil Current

The westward South Equatorial Current bifurcates when it reaches the continental shelf off Cape São Roque (Figure 3.1), dividing into the northward flowing North Brazil Current (NBrC) and the southward western boundary Brazil Current (BrC), carrying warm subtropical water (Stramma et al., 1990).

At 19°S (Figure 3.2 c, d and Table 3.1), the BrC transports southward -19.7 ± 1.3 Sv of water in an approximate barotropic pattern up to 27.84 kg m^{-3}, spanning down to roughly 1500 m depth, and extending 37 km from the coast to 37.1°W. The heat transport carried out by this current is -0.79 ± 0.05 PW, while maintaining a northward flux of 0.06 ± 0.03 Sv of freshwater for the 1990-99 decade. The BrC at this latitude is followed up by a narrow recirculation between 36.7°W and 36.4°W over a similar depth range, transporting northward 19.3 ± 2.1 Sv of mass transport, 0.67 ± 0.08 PW of heat transport and 0.06 ± 0.04 Sv of freshwater flux.

The BrC at 24°S (Figure 3.2 f, g and Table 3.1) is manifested as a narrow current with a recirculation of almost the same magnitude, followed by another southward flowing current occupying

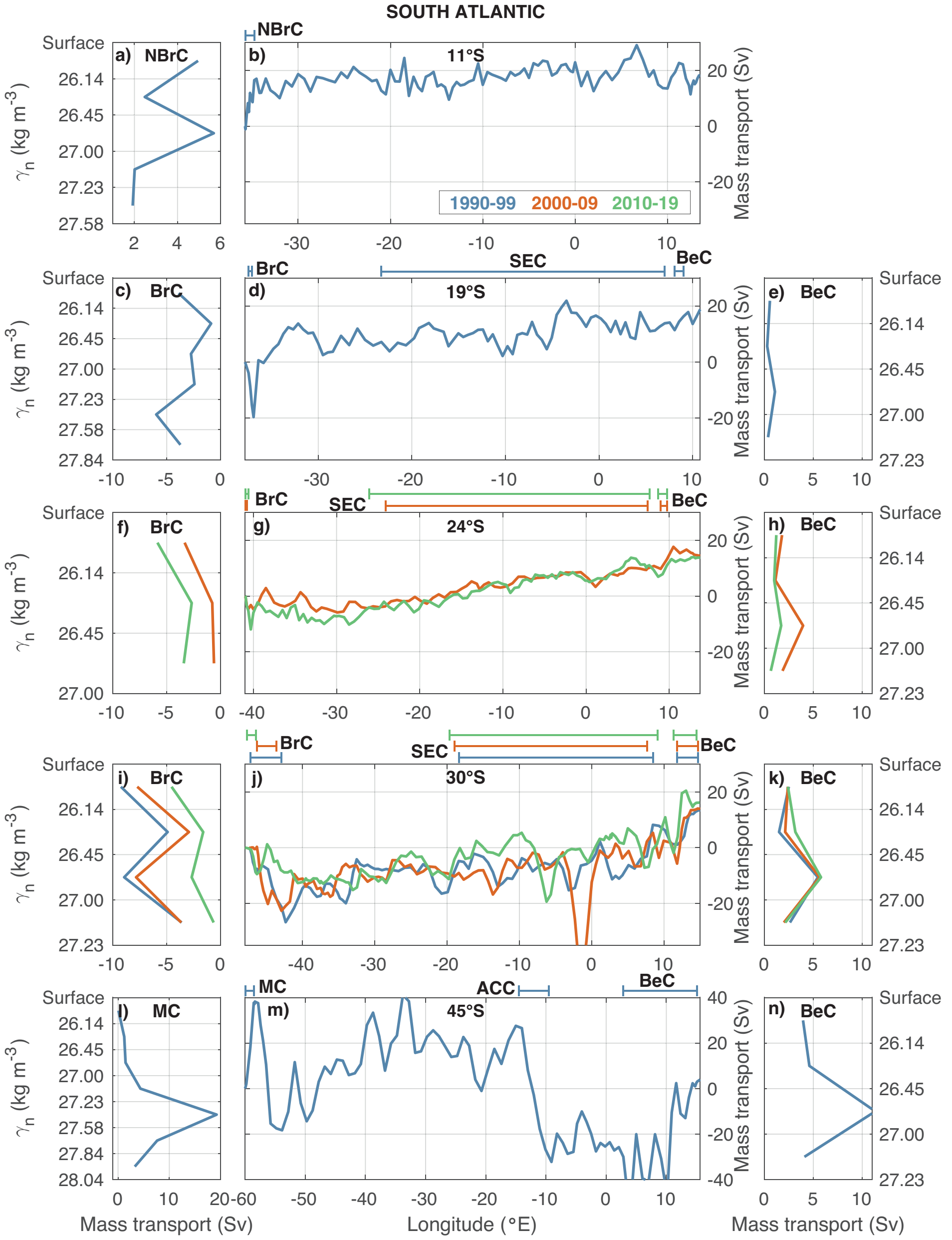

Figure 3.2. South Atlantic currents at different latitudes and decades. Net mass transport (Sv) per layer defined between neutral density interfaces for North Brazil Current (NBrC) at 11°S (a), Brazil Current (BrC) at 19°S (c), 24°S (f) and 30°S (i), for the Benguela Current System (BeC) at 19°S (e), 24°S (h), 30°S (k) and 45°S (n) and for Malvinas Current (MC) at 45°S (l). The transport per layer is computed using the stations and layers specified in Table 3.1. The longitudinal ranges of the currents at each latitude and decade appear on the top of the middle panel with different colours, in blue for 1990-1999, orange for 2000-2009, and green for 2010-2019. The middle panels show the eastward accumulated horizontal mass transport (Sv) for upper layers for the 11°S (b), 19°S (d), 24°S (g), 30°S (j) and 45°S (m) sections.

a larger horizontal extension toward the ocean interior. The BrC occupies a longitudinal extent of 25 km from the coast to 40.8°W in 2000-09 and 47 km from the coast to 40.6°W in 2010-19. The vertical extension of the BrC at 24°S is reduced, reaching the γ^n interface of 27.00 kg m^{-3} (depth of $\sim$500 m). The transports decrease compared to 19°S for mass (-4.7 ± 0.4 and -12.0 ± 0.7 Sv), heat (-0.39 ± 0.02 and -0.88 ± 0.04 PW), with no significant changes in the northward flux of freshwater (0.04 ± 0.01 and 0.16 ± 0.01 Sv) for both the 2000-09 and 2010-19 decades, respectively. These southward transports of mass are consistent with the results of -9.6 Sv, -8.6 Sv and -7.3 ± 0.9 Sv from Stramma (1989), Garzoli et al. (2013) and Arumí-Planas et al. (2023) (submitted), respectively, although a previous inverse solution at this latitude has found slightly lower values (-5.8 ± 0.1 Sv, Evans et al. 2017). At this latitude appears a recirculation 136 and 43 km eastward of the BrC, reaching depths of $\sim$700 m. This current recirculates a large part of the BrC transport, with 8.9 ± 1.4 and 10.5 ± 0.9 Sv of northward mass transport for each decade, 0.57 ± 0.09 and 0.70 ± 0.05 PW of heat transport and southward freshwater fluxes (-0.03 ± 0.03 and -0.07 ± 0.02 Sv).

The Brazil Current at 30°S gets broader, extending 443 km from the coast to 42.9°W, from 282 km from 46.3°W to 43.6°W and 122 km from the coast to 46.5°W in each decade. Moreover, the BrC deepens its lower interface (27.23 kg m^{-3}), reaching slightly larger depths for the 1990-99 and 2000-09 decades and a similar depth for the 2010-19 decade (678, 735 and 505 m). This is a pattern consistent with the behaviour of the BrC at this latitude, with similar structures for the first two decades (Figure 3.2 i, j and Table 3.1). The BrC shows a decreasing southward transport among decades, with a sharp decrease for the last one (-26.7 ± 1.6, -22.2 ± 1.5 and -9.5 ± 0.7 Sv for the 1990-99, 2000-09 and 2010-19 decades, respectively), with similar tendencies for heat transport (-1.63 ± 0.09, -1.31 ± 0.08 and -0.64 ± 0.04 PW) and freshwater flux (0.16 ± 0.02, 0.09 ± 0.02 and 0.05 ± 0.01 Sv). At this latitude, the strengthening of the BrC is counteracted by a recirculation occurring eastward of the BrC, redirecting northward over half of the current (16.4 ± 1.9, 15.9 ± 2.0 and 13.2 ± 1.4 Sv of mass transport, 0.85 ± 0.07, 0.80 ± 0.08 and 0.76 ± 0.07 PW of heat transport and -0.16 ± 0.03, -0.14 ± 0.03 and -0.06 ± 0.02 Sv of freshwater). The combination of BrC and its recirculation increased from 24°S to this latitude, agreeing with the estimations of Peterson & Stramma (1991) that indicate an intensification of 5% per 100 km south of 24°S. This southward intensification has been corroborated with results from hydrography (Stramma, 1989; Garzoli et al., 2013) and a combination of Argo floats and satellite altimetry (Schmid & Majumder, 2018). At a latitude close to 27°S, the northern branch of the intermediate circulation moves westward from the eastern boundary until it encounters the South American continental margin. At this point, the intermediate flow breaks into two branches, one veering equatorward and flowing against the BrC north of 27°S, which may result in the reduced BrC at 24°S, and the other feeding the BrC with a stronger net southward transport in intermediate layers at 30°S (Legeais et al., 2013; Boebel et al., 1999; Valla et al., 2018).

The BrC at 19°S presents TW temperatures of 10.21°C and salinities of 35.113, which increases on its way southward to 24°S (21.03 and 18.64°C for the 2000-09 and 2010-19 decades and 36.340 and 36.066). The values for the recirculation at 24°S are slightly reduced compared with BrC (16.17 and 16.69°C and 35.617 and 35.785). Properties at 30°S appear to decrease among the first decades for both TW temperature (15.47 and 14.96°C) and TW salinity (35.611 and 35.558), with an increase for the last decade on both TW temperature and salinity (16.99°C and 35.900, respectively). The recirculation at 30°S presents values lower than those of the BrC at the same latitude (TW temperatures of 13.09, 12.75 and 14.54°C and TW salinities of 35.300, 35.248 and 35.271).

Benguela Current System

The northward Benguela Current System (BeC) is the relatively strong eastern boundary current of the South Atlantic subtropical gyre, with a varying longitudinal extension (Wedepohl et al., 2000).

The BeC can be first identified at cape Agulhas (located at 34.8°S, 20.0°E) for the 45°S section (Figure 3.2 m, n and Table 3.1), extending from 2.9°E to the coast over 1335 km in the horizontal and 650 m in the vertical, up to a γ^n of 27.23 kg m^{-3}. The BeC reaches the southern tip of the African continent transporting 24.0 ± 2.3 Sv of mass, 1.19 ± 0.11 PW of heat and -0.07 ± 0.02 Sv of freshwater. At this latitude, the BeC carries water with TW temperatures of 12.53°C and TW salinities of 35.057.

The BeC at 30°S (Figure 3.2 j, k and Table 3.1) occupies narrower extensions (~310 km) from ~11.5°E to the coast, influencing the first 500 m of the water column, maintaining the same γ^n lower interface of 27.23 kg m^{-3}. The BeC carries similar mass transports of 12.1 ± 1.2, 12.1 ± 1.2, and 13.5 ± 1.0 Sv for the 1990-99, 2000-09 and 2010-19 decades, respectively, accompanied by 0.60 ± 0.05, 0.61 ± 0.06 and 0.67 ± 0.05 PW of heat transport. The freshwater flux carried southward by the BeC appears to increase for the last decade (-0.02 ± 0.01, -0.02 ± 0.01 and -0.05 ± 0.01 Sv). Garzoli & Gordon (1996) studied the time evolution of the BeC at 30°S and found large variability for the transport and velocity records due to the passage of Agulhas rings, with a mean transport of 16 Sv, comparable to our estimations.

At 24°S the BeC extends over ~90 km, from ~8.9°E to the coast (Figure 3.2 g, h and Table 3.1), while maintaining similar vertical structures from the surface up to ~550 m deep for γ^n of 27.23 kg m^{-3}. Despite the similar structure, different transports appear (8.7 ±1.3 and 4.6 ± 0.8 Sv for mass; 0.44 ± 0.06 and 0.25 ± 0.04 PW for heat), significantly weaker than those at 30°S.

Our results from 30°S and 24°S manifest the strong variability of the Benguela Current, with no clear pattern. At 19°S, the BeC presents the same narrow extension as in 24°S (113 km) from 8.1°E to the coast, whilst reaching in the vertical from the surface up to 500 m (Figure 3.2 d, e and Table 3.1). There is a slight reduction at 19°S, reaching values of 2.3 ± 1.2 Sv for mass transport, 0.13 ± 0.05 PW of heat transport and null freshwater flux, with no continuity north of 19°S.

The BeC is fed by subtropical thermocline waters from the Indian and South Atlantic Oceans, as well as saline, low-oxygen tropical Atlantic water and cooler, fresher subantarctic water (Garzoli & Gordon, 1996; Garzoli et al., 1996). Model studies have found that around most of the transport entering the South Atlantic via the Agulhas leakage carries waters from the Indonesian Throughflow and the south of Australia (Durgadoo et al., 2017). Thus, the BeC at 30°S advects waters with TW temperatures of 12.66, 12.75 and 12.66°C and TW salinities of 34.998, 35.071 and 35.102 for each decade, respectively. Similar values are maintained for the 24°S sections, with TW temperatures of 12.69 and 13.94°C and TW salinities of 35.019 and 35.096 for the last two decades. Both TW temperature and salinity increase for waters of the BeC reaching 19°S (14.06°C and 35.262, respectively).

South Equatorial Current

The South Equatorial Current (SEC) is a broad current flowing westward toward the Brazilian shelf, where it bifurcates at Cape São Roque (Figure 3.1), with one branch heading north as the North Brazil Current (NBrC) and the other, weaker, southward as the BrC.

The SEC at 30°S occupies the first ~700 m of the water column, at depths above 27.23 kg m^{-3}, occupying large extensions of ~2700 km between 18.4°W and 8.5°E in 1990-99, 19.0°W and 7.6°E in 2000-09 and 19.8°W and 9.0°E in 2010-19 (Figure 3.2 j and Table 3.1). The SEC net northward transports of mass (16.9 ± 1.9, 14.6 ± 2.1 and 15.9 ± 1.9 Sv) and heat (0.86 ± 0.09, 0.76 ± 0.10 and 0.80 ± 0.09 PW) show similar values among decades, with null values for the freshwater flux.

At 24°S the SEC has become slightly shallower, with depths of ~625 m for the 27.23 kg m^{-3} γn interface. However, on its way northwestward, it has expanded horizontally, occupying now longitudinal extensions of ~3300 km between 24.2°W and 7.4°E in 2000-09 and 26.1°W and 7.6°E in 2010-19 (Figure 3.2 g and Table 3.1). The transports associated to the SEC are similar to those at 30°S, with stable values of 16.5 ± 1.7 and 16.5 ± 1.6 Sv for mass transport, 1.00 ± 0.10 and 1.04 ± 0.10 PW for heat transport.

The values at 19°S show a SEC reaching depths of ~515 m for the same 27.23 kg m^{-3} lower interface, while maintaining a similar horizontal extent (~3200 km) over longitudes 23.2°W and 7.0°E (Figure 3.2 d and Table 3.1). The mass transport at this latitude has decreased significantly (9.0 ± 1.9 Sv), accompanied by a reduction in heat transport (0.60 ± 0.11 PW).

The salinities present in the South Atlantic are subject to the intense surface evaporation in the region between 8°S and 25°S. The SEC starts carrying waters at 30°S with TW temperatures of 12.85, 13.22 and 12.70°C and TW salinities of 35.060, 35.142 and 35.179. Those properties increase on its way northwestward, reaching at 24°S TW temperatures of 15.35 and 15.94°C and TW salinities of 35.451 and 35.537 for the last two decades. At 19°S, the SEC carries waters with TW temperature of 16.90°C and TW salinity of 35.644.

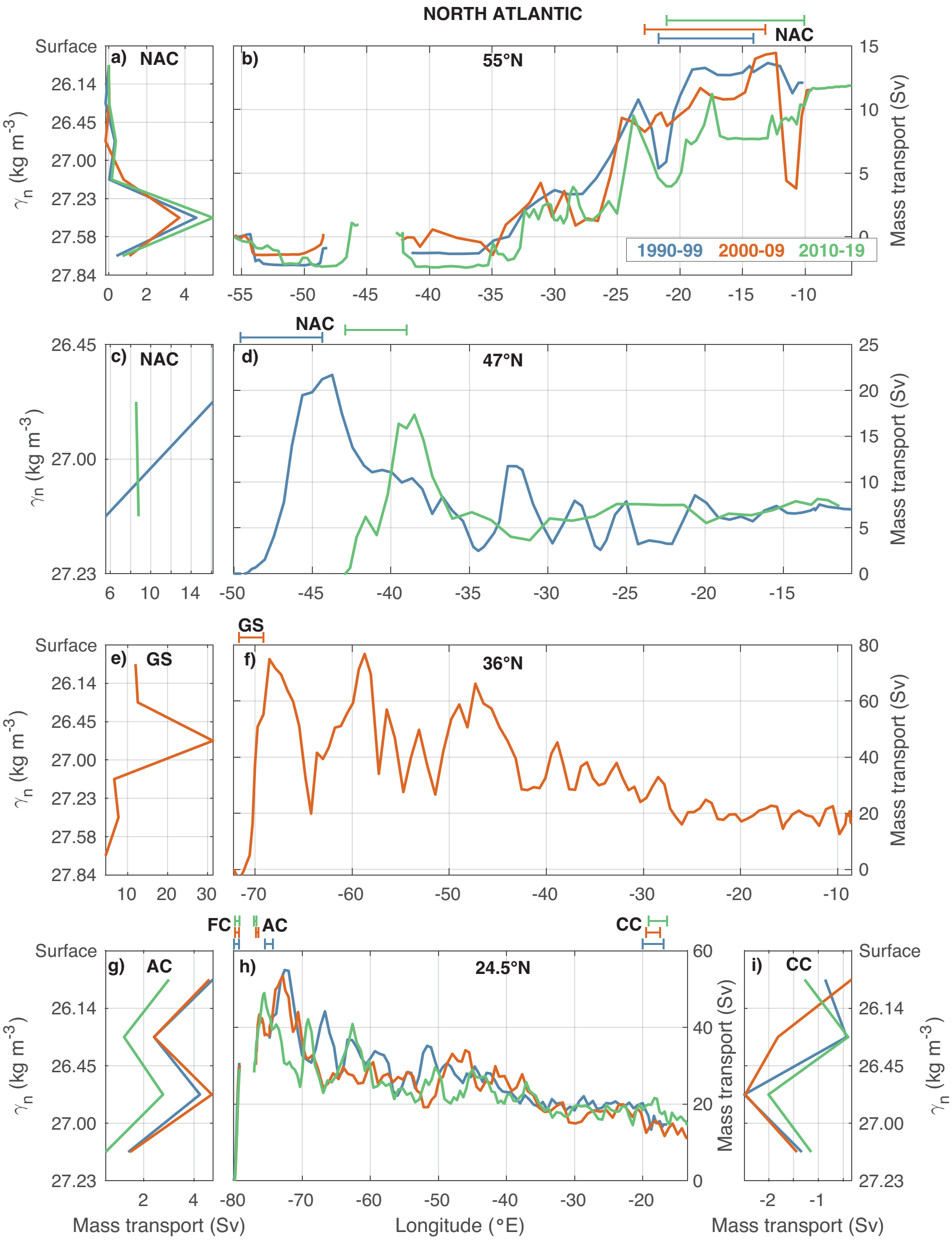

Figure 3.3. Surface currents in the north Atlantic at different latitudes and decades. Net mass transport (Sv) per layer defined between neutral density interfaces for the northward North Atlantic Current (NAC) at 47°N (a) and 55°N (c), Gulf Stream (GS) at 36°N (e), Antilles Current (AC) at 24.5°N (g) and for the southward Canary Current (CC) at 24.5°N (i). The transport per layer is computed using the stations and layers specified in Table 3.1. The longitudinal ranges of the currents at each latitude and decade appear on the top of the middle panel with different colours, in blue for 1990-1999, orange for 2000-2009, and green for 2010-2019. The right panels show the eastward accumulated horizontal mass transport (Sv) for upper layers for the 55°N (b), 47°N (d), 36°N (f) and 24.5°N (h) sections.

North Brazil Current

The northward North Brazil Current (NBrC) carries warm water from the south Atlantic along the coast of Brazil, across the equator, and into the northern hemisphere, acting as a conduit for cross-equatorial transport of upper ocean waters as part of the AMOC. This northward branch of the SEC can be found at 11°S (Figure 3.2 a, b and Table 3.1), sampled in the 1990-99 decade, extending from the coast to 34.7°W over 130 km. Its vertical structure presents two maximums in the circulation, with a surface layer from the surface to 26.14 kg m^{-3} (∼203 m) and a subsurface layer from 26.45 to 27.00 kg m^{-3} (∼400 to ∼500 m), carrying 5.0 ± 0.4 and 5.7 ± 0.3 Sv, respectively. The total equatorward transport is 17.0 ± 1.2 Sv of mass and 0.98 ± 0.05 PW of heat, associated with a southward freshwater flux of -0.19 ± 0.03 Sv. The strong current estimated agrees with the 15-month mean value of 16 ± 2 Sv obtained by Garzoli (2004) from Inverted EchoSounders (IES) and are slightly lower than the Argo-based solutions of Tuchen et al. (2022) of 21.8 Sv.

The NBrC presents higher TW temperatures (14.59°C) and salinities (35.509) than the ones found at 19°S for the BrC.

Florida Current

The Florida Current (FC) stretches over ∼70 km from the Florida Straits up to Cape Hatteras (Figure 3.1), sourcing mainly from the Loop Current coming from the Gulf of Mexico (Maul & Vukovich, 1993) and, to a lesser extent, from the Antilles Current (AC), transporting warm waters northward (Figure 3.3 h and Table 3.1) in a water column of ∼600 m deep. The FC shows different values of mass transport across decades (34.5 ± 0.3, 32.1 ± 0.3 and 31.3 ± 0.3 Sv for the 1990-99, 2000-09 and 2010-19 decades, respectively), also manifested in its heat transport (2.70 ± 0.02, 2.43 ± 0.02 and 2.31 ± 0.02 PW), combined with their TW temperature (19.84, 19.16 and 18.65°C). The freshwater flux associated to the FC, although not as important as the heat transport, also presents relatively high southward values (-0.17 ± 0.01, -0.09 ± 0.01 and -0.14 ± 0.01 Sv), associated with quite stable values of TW salinity (36.120, 36.201 and 36.098), with differences of less than 0.1.

Our results can be compared with the nearly continuous monitoring of the FC transport since 1982 at 27°N from submarine cable measurements, which yields an average transport of 31.8 ± 0.1 Sv (Piecuch, 2020). Its mean seasonal cycle has a 3.3-Sv annual periodicity, with maxima in mid-July and minima in mid-January (Atkinson et al., 2010), linking its variability to the North Atlantic Oscillation (Baringer & Larsen, 2001) coupled with a long-term weakening (Piecuch, 2020).

Antilles Current

In the western coast of the subtropical North Atlantic, the Antilles Current (AC) flows northward and then northwestward around the Bahamas Islands (Figure 3.1) before joining the FC and Gulf Stream (GS). The AC at 24.5°N occupies the first ∼700 m of the water column, from the surface to 27.23 kg m^{-3}, but presents different longitudinal extensions among decades (125 km from Cape Hatteras to74.3°W in 1990-99, and ∼38 km from Cape Hatteras to 76.4°W and 76.7°W in 2000-09 and 2010-19, respectively).

The values of mass transport for the AC show similar values for the first two decades and a sharp decrease for the 2010-19 estimation (12.8 ± 1.0, 13.2 ± 0.4 and 7.5 ± 0.3 Sv), with a similar pattern for its heat transport (0.98 ± 0.07, 0.97 ± 0.03 and 0.56 ± 0.02 PW) as shown in Figure 3.3 g, h and Table 3.1. The decreasing values in heat transport can be attributed to a combination of a reduction in mass transport as well as in TW temperature (18.59, 18.23 and 18.05°C). The freshwater flux of the AC presents low values (-0.04 ± 0.01, -0.02 ± 0.01 and -0.02 ± 0.01 Sv), associated to similar TW salinities among decades (36.258, 36.377 and 36.359).

Our results show relatively strong values for the AC, similar to the values obtained by Hernández-Guerra et al. (2014). However, historical estimations place the average AC transport in a range between 2-12 Sv (Lee et al., 1996; Olson et al., 1984; Schmitz et al., 1992; Schmitz & McCartney, 1993). More recently, a combination of different observation systems at 26.5°N from 2005 to 2015 shows a relatively weak AC of 4.7 Sv with a daily standard deviation of 7.5 Sv (Meinen et al., 2019), with transports varying between -15 and 25 Sv (Johns et al., 2008), despite presenting a rather weak seasonal component (Meinen et al., 2019).

Canary Current

The Canary Current (CC) is the relatively weak eastern boundary current of the North Atlantic subtropical gyre, linking the Azores Current with the North Equatorial Current (Pérez-Hernández et al., 2013; Casanova-Masjoan et al., 2020; Comas-Rodríguez et al., 2011). The CC is relatively shallow, flowing along the first ∼750 m of the water column from the surface to 27.23 kg m^{-3} and with a width over ∼270 km (Figure 3.3 h, i and Table 3.1). The different geographical position of the stations at this boundary for the 1990-99 prevents from obtaining values directly comparable to the other decades. At these latitudes there is a point of inflection in the accumulated mass transport denoting the start of the CC, from non-significant values to negative mass transport. This current transports southward -5.1 ± 0.9, -6.1 ± 1.4 and -4.8 ± 0.7 Sv of mass, -0.34 ± 0.06, -0.40 ± 0.08 and -0.32 ± 0.05 PW of heat and 0.01 ± 0.01, 0.03 ± 0.01 and 0.01 ± 0.01 Sv of freshwater. Moreover, this current carries waters with TW temperatures lower than its western counterpart (16.57, 16.59 and 16.86°C) and similar high TW salinities (36.283, 36.313 and 36.372).

The CC has an average transport of 3.0 ± 1.0 Sv with a seasonal amplitude of 1.4 ± 0.7 Sv (Machín et al. 2006; Pérez-Hernández et al. 2023, submitted). The CC varies seasonally not only in intensity but also in position, migrating from its easternmost position in spring to its westernmost position in fall. The transport estimations agree with the seasonal range given above and they are similar to the -5.5 Sv found for the spring (Casanova-Masjoan et al., 2020). In contrast, our estimations are slightly higher than the results obtained by Hernández-Guerra et al. (2014) of 2.1 ± 0.9 Sv for 1992 and 2.3 ± 1.1 Sv for 2011 between the eastern boundary and 20°W, or the 2.9 ± 0.8 Sv of Machín et al. (2006). Nevertheless, most of the previous CC observations have taken place in fall when the transports have been observed to be as high as 6.2 ± 0.6 Sv with a northward recirculation in the Lanzarote Passage (Pérez-Hernández et al., 2013; Hernández-Guerra et al., 2017).

East of the CC, the Lanzarote Passage presents a unique dynamic, with its own pattern of variability that has been related to the seasonal amplitude of the AMOC (Pérez-Hernández et al. 2015, 2023, submitted; Vélez-Belchí et al. 2017). Our results for the 2000-09 and 2010-19 cruises have found -1.0 ± 0.6 and -1.8 ± 0.6 Sv over ~70 km, respectively, carrying waters with similar TW temperature and salinity. These values correspond to the spring-summer estimates for the Lanzarote passage flow of -0.81± 1.48 Sv estimated with nine years of mooring data (Casanova-Masjoan et al., 2020; Fraile-Nuez et al., 2010).

Gulf Stream

The strong Gulf Stream (GS) brings warm water from the Gulf of Mexico into the North Atlantic subtropical gyre including water from the FC and AC. After the GS turns offshore from the continental shelf at Cape Hatteras, the mass transport carried by the GS nearly doubles at a rate of 8 Sv every 100 km, with large variations in space and time (Johns et al., 1995; Hogg & Johns, 1995; Frankignoul et al., 2001). The section at 36°N sampled during the 2000-09 decade can detect its strength along the coast, occupying the first ~900 m of the water column (up to 27.84 kg m^{-3}) and with a horizontal extension over ~250 km from 71.7°W to 69.1°W. The GS has a strong northward transport of 74.9 ± 1.7 Sv for mass and 4.56 ± 0.11 PW for heat, as well as strong southward freshwater flux of -0.82 ± 0.04 Sv (Figure 3.3 e, f and Table 3.1). McDonagh et al. (2010) found similar values of 67.2 ± 17.2 Sv for the GS transport at 36°N, and Rossby et al. (2014) detected no significant trends in the strength of the GS surface transport over the last 20 years using direct measurements. Almost half of the northward transport associated to the GS is recirculated southward, up to 64.8°W (387 km east to the east of the GS). This recirculation of the GS brings southward -35.4 ± 8.7 Sv of mass transport and -2.29 ± 0.18 PW of heat transport, with an opposing freshwater flux of 0.19 ± 0.05 Sv.

The GS presents high TW temperature (15.42°C), but not as high as for the FC and AC, and a similar value of TW salinity (36.014) compared with FC and AC.

North Atlantic Current

The North Atlantic Current (NAC) is a shallow, variable wind-driven body of warm water covering a large part of the eastern subpolar North Atlantic (SPNA) on its way to the Nordic Seas. The NAC represents the bulk of the GS after its branch point and subsequent separation from

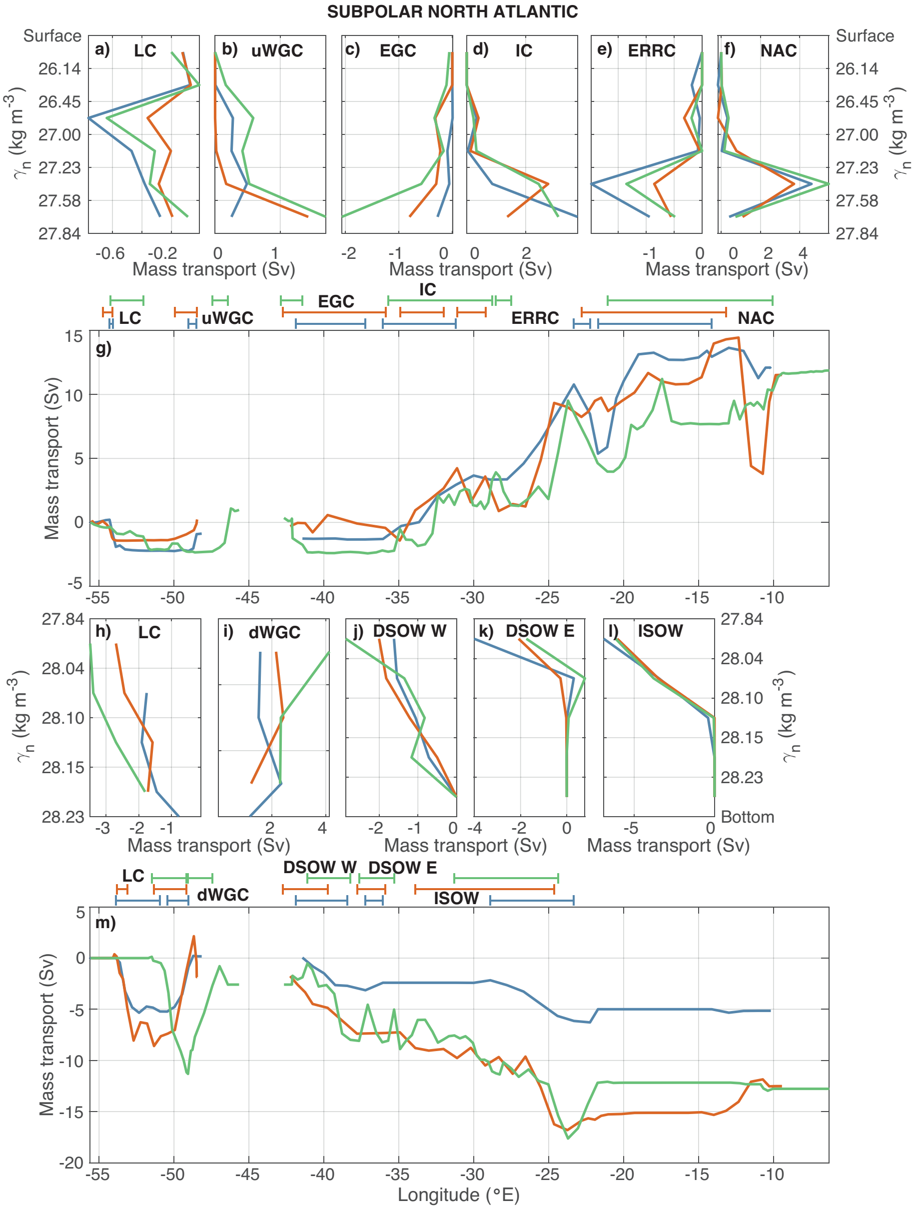

Figure 3.4. Upper and deep currents in the subpolar North Atlantic at 55°N for the three decades. Net mass transport (Sv) per layer defined between neutral density interfaces at 55°N for upper layers: upper Labrador Current (LC; a), upper West Greenland Current (uWGC; b), East Greenland Current (EGC; c) Irminger Current (IC; d), East Reykjanes Ridge Current (ERRC; e) and North Atlantic Current (NAC; f), as well as for deep layers: deep Labrador Current (LC; h), deep West Greenland Current (dWGC; i), west and east Denmark Strait Overflow Waters (DSOW; j and k) and Iceland-Scotland Overflow Waters (ISOW; l). The transport per layer is computed using the stations and layers specified in Tables 3.1 and 3.2. The longitudinal ranges of the currents at each latitude and decade appear on the top of the middle panel with different colours, in blue for 1990-1999, orange for 2000-2009, and green for 2010-2019. The panels below the vertical net transport show the eastward accumulated horizontal mass transport (Sv) at 55°N for upper (g) and deep (m) layers.

the coast. The NAC at 47°N is located between 49.6°W and 44.4°W for the 1990-99 cruise and between 42.9°W and 39.0°W for the 2010-19 cruise, due to the difference in the geometry of the two cruises, reaching similar depths of 838 and 982 m from 26.45 to 27.23 kg m^{-3}, respectively. The mass transports for NAC at 47°N are consistent with those of the net GS system after considering its recirculation, the small contribution that recirculates within the subtropical gyre (see Canary Current) and the -1.9 ± 2.3 Sv and -1.3 ± 2.1 Sv that sink between the 24.5°N and 47°N sections for each decade, respectively (Caínzos et al., 2022a). Thus, the NAC transports 33.4 ± 2.9 and 28.2 ± 1.5 Sv for the 1990-99 and 2010-19 decades, respectively (Figure 3.3 c, d and Table 3.1). The main mass transport is subsuperficial with a mass transport of 21.7 ± 2.0 and 17.3 ± 0.8 Sv in the layer between 26.45 ($\sim$200 m) and 27.23 kg m^{-3} ($\sim$400 m) in 1990-99 and 2010-19, respectively. Meinen & Watts (2000) using current meter moorings and IES attributed a much higher value of 146 ± 13 Sv for the NAC at 42°N, located close to our hydrographic section at 47°N for 1990-99. A more recent study combining altimetry and Argo data reconstructed the transports of NAC from 1993 to 2016 between 40°N and 53°N, attributing values between 35 and 50 Sv along 47°N between 45°W and 37°W (Stendardo et al., 2020). Our estimations for heat transport are lower than those of the GS (1.79 ± 0.14 and 1.18 ± 0.05 PW, respectively), due to the reduction in the TW temperature (13.53 and 10.59°C) on its way northward. The freshwater flux has also been reduced (-0.22 ± 0.04 and -0.09 ± 0.02 Sv), resulting from the lower values in TW salinity (35.722 and 35.368).

The NAC flows northeastward and reaches the section at 58°N (Figure 3.3 a, b, Figure 3.4 f and Table 3.1). At this latitude, the NAC extends longitudinally between 21.7°W and 14.1°W, 22.8°W and 13.2°W and 21.1°W and 10.1°W for the 1990-99, 2000-09 and 2010-19 decades, respectively, with a vertical extension from the surface to 27.84 kg m^{-3} ($\sim$1000 m). The strength of the current has been largely reduced at this point, with net mass transports of 5.2 ± 3.7, 5.4 ± 2.7 and 6.7 ± 1.6 Sv and heat transport of 0.19 ± 0.13, 0.20 ± 0.10 and 0.25 ± 0.05 PW. This corresponds to a 20 to 25-Sv reduction in the transport of the NAC crossing the SPNA, with near a fifth part corresponding to a sink in these latitudes (3.8 ± 3.1 Sv between 47°N and 55°N, 4.8 ± 2.7 Sv between 36°N and 55°N and 4.0 ± 2.4 Sv between 47°N and 55°N (Caínzos et al., 2022a).

Stendardo et al. (2020) found an average value of 2.5 Sv for the NAC at this latitude, which is slightly lower than our estimations. Moreover, recent glider sections from July 2014 to August 2016 along 58°N from 21°W to 15°W (Houpert et al., 2018) have provided absolute geostrophic transports for all year of 5.1 ± 1.0 Sv, with 6.7 ± 0.9 Sv for summer and 2.8 ± 1.7 Sv for winter, comparable to our estimations at 58°N.

The freshwater flux at this latitude is almost negligible (0.03 ± 0.02, 0.00 ± 0.01 and -0.01 ± 0.01 Sv). Both TW temperature and salinities have become colder and fresher, with quite stable values for both properties (9.12, 9.27 and 9.29°C for the TW temperature and 35.290, 35.347 and 35.292 for the TW salinity).

East Reykjanes Ridge Current, Irminger Current and East Greenland Current

The surface currents on the eastern part of the northernmost section, at the nominal latitude of 58°N, are an important link between the Arctic Ocean and the North Atlantic Ocean via their upper circulation (Figure 3.1). Within the Iceland Basin, the NAC flows cyclonically turning southwestward and flowing along the Reykjanes Ridge flank as the East Reykjanes Ridge Current (ERRC), that then turns anticyclonically around and across the ridge (Pollard et al., 2004). Thus, upon entering the Irminger Sea, the Irminger Current (IC) flows northward along the western flank of the Reykjanes Ridge carrying warm, saline Atlantic waters.

The ERRC runs along the eastern side of the Reykjanes Ridge and Iceland over ∼80 km, exporting waters southward in the upper layers up to 27.84 kg m^{-3} (∼1000 m deep), with relatively high values of TW temperature and salinity (Figure 3.4 e, g and Table 3.1). We have found relatively low values of mass transport for the southward flowing ERRC (-3.2 ± 2.2, -1.8 ± 1.4 and -2.0 ± 0.8 Sv for each decade, respectively). Using repeated ship-based measurements along the Greenland-Portugal OVIDE line, Daniault et al. (2016) have estimated the decadal mean circulation for the North Atlantic over 2002-2012, with values for the ERRC transport slightly larger than ours (-4.1 ± 0.6 Sv). The associated heat transport is quite small (-0.10 ± 0.07, -0.06 ± 0.04 and -0.06 ± 0.02 PW), and the freshwater flux is null (0.00 ± 0.01 Sv for all cases). The TW temperatures (8.14, 8.45 and 7.79°C) and salinities (35.131, 35.070 and 35.082) are slightly lower than those of NAC.

On the other side of the Reykjanes Ridge, the ∼300 km-wide IC transports waters from the SPNA toward the Arctic Ocean in the upper ∼700 m, with a shallowing of the 27.84 kg m^{-3} isopycnal (Figure 3.4 d, g and Table 3.1). The northward transport of mass (5.0 ± 2.7, 4.7 ± 1.9 and 6.1 ± 1.2 Sv) agrees with the result obtained by Daniault et al. (2016) of 4.8 ± 1.1 Sv and Sarafanov et al. (2012) of 5.6 ± 0.4 Sv. Casanova-Masjoan et al. (2020) obtained 3.04 ± 0.23 Sv for the Irminger current around Iceland, of which 2.24 ± 0.23 Sv flow north as part of the North Icelandic Irminger Current (NIIC). However, other studies have attributed IC transports in the range of 9-12 Sv (Våge et al., 2011; Lherminier et al., 2010; Bacon, 1997). There is also a northward transport of heat (0.13 ± 0.06, 0.15 ± 0.05 and 0.17 ± 0.03 PW), although with null values for the freshwater flux. The values of TW temperature (6.37, 8.12 and 6.91°C) and salinity (34.991, 35.105 and 35.019) are, again, slightly lower than those from the ERRC.

Flowing southward along the eastern coast of Greenland, the East Greenland Current (EGC) exports cold and fresh water from the Arctic into the SPNA. The values of net southward mass transport are small but strengthen with time (-0.4 ± 0.6, -1.6 ± 1.8 and -3.3 ± 1.0 Sv), with almost null heat transports (-0.01 ± 0.01, -0.04 ± 0.04 and -0.06 ± 0.02 PW) and null freshwater flux (Figure 3.4 c, g and Table 3.1). We have found variable transports for the EGC, relatively weaker than previous estimations (-3.8 ± 0.3 Sv from Daniault et al. 2016; -5.4 ± 0.7 from Sarafanov et al. 2012; and -3.5 ± 0.5 Sv from Le Bras et al. 2018).

The TW temperatures (5.94, 6.60 and 4.42°C) and salinities (34.938, 34.826 and 34.560) show the lower values found in the upper layers of the 58°N section.

Upper West Greenland Current and upper Labrador Current

The EGC turns northwest at the southern tip of Greenland, entering the Labrador Sea and originating the upper West Greenland Current (uWGC) at 53°N. The uWGC varies horizontally, ranging from the coast to 49.0°W (67 km), 49.9°W (164 km) and 47.4°W (75 km) for each decade, as well as vertically (from the surface to 262, 1232 and 788 m). The waters entering the Labrador Sea have a small but variable net transport for mass (1.3 ± 0.4, 1.6 ± 1.0 and 3.4 ± 1.0 Sv), with an intensification for the last decade (Figure 3.4 b, g and Table 3.1). These values are lower than the average transports of uWGC estimated previously: 3.8 ± 0.9 Sv (Myers et al., 2007) at Cape Farewell; 3.2 ± 2.3 Sv and 5.5 ± 3.9 Sv at Cape Farewell and Cape Desolation, respectively (Myers et al., 2009) and 4.6 Sv at both Cape Farewell and Cape Desolation (Gou et al., 2022). More recent estimations have situated the upper transport via the eastern basin of the Labrador Sea in 11.1 ± 5.0 Sv (Pacini et al., 2020). The values for heat (0.01 ± 0.01, 0.03 ± 0.02 and 0.05 ± 0.02 PW) and freshwater (0.01 ± 0.01, 0.00 ± 0.01 and 0.04 ± 0.01 Sv) transports are negligible except for the last decade. These values can reflect the mean value obtained from seven decades of high-resolution coupled ice-ocean model results, with mean annual fluxes between 99 and 162 mSv (Florindo-López et al., 2020). The TW temperatures (2.74, 4.62 and 3.57°C) and salinities (34.126, 34.857 and 34.332) have yet again become colder and fresher.

The net export of the water formed in the Labrador Sea is through its southwestern border, as part of the Labrador Current (LC). The net transport can be divided into the upper and deep layer, setting the interface at a neutral density of 27.84 kg m^{-3}, up to a depth of $\sim$400 m. The upper LC extends from 54.3°W to 54.1°W, 54.8°W to 54.1°W and 54.2°W to 52.1°W, occupying 26, 80 and 151 km. The upper layers of the LC transport out of the Labrador basin -2.1 ± .05, -1.2 ± 0.4 and -1.6 ± 0.4 Sv of mass transport, with null values for either heat or freshwater flux (Figure 3.4 a, g and Table 3.1). This southward export is lower than estimations from mooring data (-6.3 ± 0.2 Sv 10-year mean by Fischer et al. 2010; -8.3 ± 0.5 Sv 17-year mean by Zantopp et al. 2017) and hydrographic sections (-6.3 Sv mean over 1996-2003 by Li & Lozier 2018). The TW temperatures in this upper layer are very cold (0.45, 0.98 and 0.22°C), associated with low salinities (33.569, 33.630 and 33.455).

3.3.2 Deep currents

Iceland-Scotland Overflow Waters and Denmark Strait Overflow Waters

The deep layers of the east part of the northernmost section (at 58°N) constitute the overflow waters, divided into the Iceland-Scotland Overflow Waters (ISOW) and the Denmark Strait

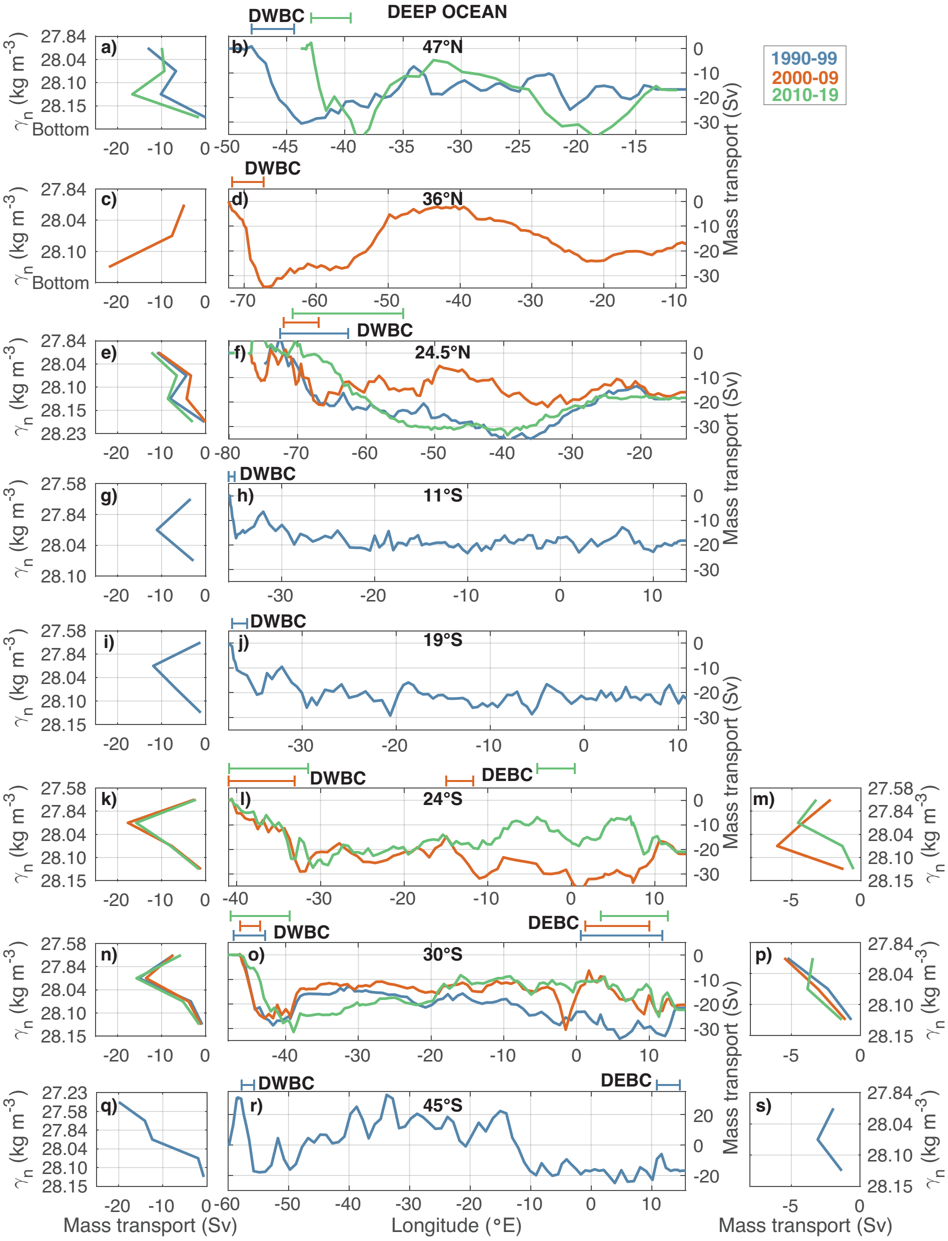

Figure 3.5. Deep boundary currents of the Atlantic at different latitudes and decades. Net mass transport (Sv) per layer defined between neutral density interfaces for Deep Western Boundary Current (DWBC) at 47°N (a), 36°N (c), 24.5°N (e), 11°S (g), 19°S (i), 24°S (k), 30°S (n) and 45°S (q) and for Deep Eastern Boundary Current (DEBC) at 24°S (m), 30°S (p) and 45°S (s). The transport per layer is computed using the stations and layers specified in Table 3.2. The longitudinal ranges of the currents at each latitude and decade appear on the top of the middle panel with different colours, in blue for 1990-1999, orange for 2000-2009, and green for 2010-2019. The middle panels show the eastward accumulated horizontal mass transport (Sv) for deep layers for the 47°N (b), 36°N (d), 24.5°N (f), 11°S (h), 19°S (j), 24°S (l), 30°S (o) and 45°S (r) sections.

Overflow Waters (DSOW). The ISOW flows between the Scottish and Icelandic platforms, exporting water from the Arctic into the Atlantic from ∼2100 m to the bottom of the water column. The longitudinal extension of the ISOW is similar for all decades (335 km from 28.9°W to 23.3°W, 567 km from 33.9°W to 24.6°W and 416 km from 31.3°W to 24.4°°W for the 1990-99, 2000-09 and 2010-19 decades, respectively). There is a net southward transport of -10.8 ± 6.5, -9.6 ± 5.3 and -10.0 ± 3.0 Sv of mass across those longitudes (Figure 3.4 l, m and Table 3.2), accompanied by a southward transport of heat (-0.13 ± 0.09, -0.11 ± 0.07 and -0.12 ±0.04 PW). Previous estimations for ISOW are considerably weaker than our results. García-Ibáñez et al. (2015) built an inverse model for the SPNA, estimating for deep layers -1.4 ± 1.0 Sv of ISOW being exported out of the eastern North Atlantic. Moreover, using an array of current meters deployed as part of the OSNAP program, Johns et al. (2021) have determined a mean southward flow of ISOW along the eastern flank of the Reykjanes Ridge of -5.3 ± 0.4 Sv between 2014-2018. The TW temperatures (3.07, 3.04 and 3.08°C) and salinities (34.943, 34.944 and 34.958) are quite stable among decades.

The DSOW has been divided into two main paths, flowing along the boundaries of the Irminger Sea. The DSOW flowing at the western side of the Reykjanes Ridge (eastern boundary of Irminger Sea) extends ∼110 km between 37.2°W and 36.1°W, 37.8°W and 35.9°W and 37.7°W and 35.3°W for the 1990-99, 2000-09 and 2010-19 decades, respectively (Figure 3.4 k, m and Table 3.2). This path of the DSOW exports between ∼2500 m and the bottom layers -3.7 ± 8.2, -2.4 ± 8.0 and -0.9 ± 4.6 Sv of mass transport per decade, with low associated heat transports (-0.05 ± 0.10, -0.03 ± 0.10 and -0.02 ± 0.06 PW). The TW temperatures are slightly higher than those of ISOW (3.28, 3.50 and 4.27°C), but with lower salinities except for the last decade (34.886, 34.908 and 34.955).

The western branch of the DSOW extends over ∼180 km from the coast and from ∼2000 m to the bottom of the water column. This current flowing along the western boundary of the Irminger Sea (Figure 3.4 j, m and Table 3.2) has a slightly stronger export of water southwards (-4.9 ± 7.8, -5.5 ± 6.8 and -6.2 ± 4.9 Sv), with similarly low values of heat transport (-0.04 ± 0.10, -0.05 ± 0.09 and -0.06 ± 0.07 PW) and null freshwater flux. The TW temperatures (2.29, 2.45 and 2.54°C) are lower than on the western boundary of the Irminger Sea, while maintaining similar TW salinities (34.904, 34.911 and 34.915). Hydrographic sections over different summers estimated 4.9 ± 0.5 Sv for the DSOW at the Denmark Strait (Brearley et al., 2012), which coincides with our downstream estimations.

The combined values for both paths of DSOW exceed the year-long mean total volume transport of DSOW upstream of our section. Hydrographic sections over different summers at the Denmark Strait (Brearley et al., 2012) yielded -4.9 ± 0.5 Sv southward, while mooring arrays at the northern part of the Denmark Strait estimated -3.54 ± 0.16 Sv (Harden et al., 2016), similar to results from downstream the sill (3.4 Sv with a standard deviation of 1.4 Sv, Jochumsen et al. 2012). This increase in DSOW southward of the Denmark Strait may respond to the entrainment of water from the Irminger Current, nearly doubling the volume transport carried by the DSOW

(Koszalka et al., 2013; Dickson et al., 2008).

Deep West Greenland Current and deep Labrador Current

Analogously to the uWGC, there is a northward deep transport entering the Labrador Sea via its eastern boundary, the deep West Greenland Current (dWGC) occupying ∼220 km from the coast to the interior of the Labrador Sea and flowing along the lower part of the water column (from ∼3500 m to the bottom). This current carries into the Labrador basin 5.4 ± 1.0, 5.8 ± 1.1 and 8.8 ± 1.5 Sv of mass transport for the 1990-99, 2000-09 and 2010-19 decades, respectively (Figure 3.4 i, m and Table 3.2). This last value is comparable with the 8.3 ± 2.8 Sv found by Pacini et al. (2020) using high-resolution moorings from 2014 to 2018 deployed as part of OSNAP. The increase in transport for the last decade is also evident for heat transport (0.04 ± 0.01, 0.04 ± 0.01 and 0.07 ± 0.01 PW), with null freshwater flux. The dWGC is slightly colder (TW temperatures of 1.84, 1.93 and 2.04°C) and saltier (TW salinities of 34.900, 34.888 and 34.908) than the uWGC, with lower temperature and salt content than the western branch of the DSOW.

Deep layers export most of the LC out of the Labrador Sea through its western boundary. It is a relatively narrow current, extending over 364, 89 and 424 km, with its upper vertical interface ranging from 2615, 1956 and 2314 m deep to the bottom for each decade. This outflow of mass transport increases with time (-5.2 ± 0.9, -8.4 ± 3.9 and -11.4 ± 6.8 Sv), although not significantly, due to the high variability associated to the deep LC, expressed with the large values of uncertainties, around half of the mean value (Figure 3.4 h, m and Table 3.2). However, other studies have found stronger deep-water transports: 26 ± 5 Sv from two years of direct current observations and moored current-meter array (Fischer et al., 2004), updated to 30 ± 3 Sv for the 10-year mean (Fischer et al., 2010) and an average of 30.2 ± 6.6 Sv over the past 17 years from moorings and shipboard station data (Zantopp et al., 2017). Heat is also exported out of the Labrador Sea via deep layers, with values of -0.04 ± 0.01, -0.07 ± 0.05 and -0.11 ± 0.09 PW for each decade, respectively. Freshwater fluxes remain almost negligible. The TW temperatures and salinities are warmer (1.92, 2.24, 2.37°C) and saltier (34.900, 34.893 and 34.911) than for upper layers, with values similar to those of the western DSOW.

Deep Western Boundary Current

The Deep Western Boundary Current (DWBC) mainly follows the western border of the Atlantic Ocean. The DWBC at 47°N lies below the neutral density of 27.84 kg m^{-3} (∼2800 m to the bottom) and occupies a similar longitudinal extension to the upper northward NAC (∼280 km) (Figure 3.5 a, b and Table 3.2). The DWBC flows southward at 47°N with a mass transport of similar magnitude (-30.1 ± 10.4 and -37.5 ± 5.7 Sv for 1990-99 and 2010-19, respectively). These values for the DWBC exceed the -17.5 Sv estimated by Fischer et al. (2015) at Grand Banks with ADCP velocities. The DWBC at this latitude also transports a southward heat transport (-0.31 ± 0.13

Table 3.2. Characteristics of each deep-layer current found at every section

Decade	Stations	Long (°E)	Dist (km)	Layers	Depth (m)	Mass Trans (Sv)	Heat Trans (PW)	Fw Total (Sv)	TWT (°C)	TWS
Iceland-Scotland Overflow Waters 58°N										
1990-99	35:41	-28.9:-23.3	335	7:11	2353 to bottom	-10.8 ± 6.5	-0.13 ± 0.09	0.00 ± 0.01	3.07	34.943
2000-09	35:46	-33.9:-24.6	567	7:11	2157 to bottom	-9.6 ± 5.3	-0.11 ± 0.07	0.00 ± 0.01	3.04	34.944
2010-19	70:89	-31.3:-24.4	416	7:11	2037 to bottom	-10.0 ± 3.0	-0.12 ± 0.04	0.01 ± 0.01	3.08	34.958
Denmark Strait Overflow Waters East 58°N										
1990-99	28:30	-37.2:-36.1	68	7:11	2413 to bottom	-3.7 ± 8.2	-0.05 ± 0.10	0.00 ± 0.01	3.28	34.886
2000-09	32:34	-37.8:-35.9	113	7:11	2521 to bottom	-2.4 ± 8.0	-0.03 ± 0.10	0.00 ± 0.01	3.50	34.908
2010-19	55:61	-37.7:-35.3	135	7:11	2511 to bottom	-0.9 ± 4.6	-0.02 ± 0.06	0.00 ± 0.01	4.27	34.955
Denmark Strait Overflow Waters West 58°N										
1990-99	22:28	-41.9:-38.4	195	7:11	2257 to bottom	-4.9 ± 7.8	-0.04 ± 0.10	-0.01 ± 0.01	2.29	34.904
2000-09	26:32	-42.8:-39.8	177	7:11	1760 to bottom	-5.5 ± 6.8	-0.05 ± 0.09	0.00 ± 0.01	2.45	34.911
2010-19	48:55	-41.1:-38.2	164	7:11	2292 to bottom	-6.2 ± 4.9	-0.06 ± 0.07	0.01 ± 0.01	2.54	34.915
Deep West Greenland Current 53°N										
1990-99	15:19	-50.5:-49.0	162	8:11	3302 to bottom	5.4 ± 1.0	0.04 ± 0.01	0.00 ± 0.01	1.84	34.900
2000-09	17:22	-51.3:-49.2	249	8:10	3981 to bottom	5.8 ± 1.1	0.04 ± 0.01	0.00 ± 0.01	1.93	34.888
2010-19	25:32	-49.1:-47.4	278	8:10	3305 to bottom	8.8 ± 1.5	0.07 ± 0.01	0.00 ± 0.01	2.04	34.908
Deep Labrador Current 53°N										
1990-99	7:15	-53.9:-50.9	364	8:11	2615 to bottom	-5.2 ± 0.9	-0.04 ± 0.01	0.00 ± 0.01	1.92	34.900
2000-09	10:14	-53.8:-53.1	89	7:10	1956 to bottom	-8.4 ± 3.9	-0.07 ± 0.05	0.00 ± 0.01	2.24	34.893
2010-19	14:25	-51.5:-49.2	424	7:10	2314 to bottom	-11.4 ± 6.8	-0.11 ± 0.09	0.06 ± 0.03	2.37	34.911
Deep Western Boundary Current 47°N										
1990-99	7:14	-48.0:-44.4	310	7:10	2859 to bottom	-30.1 ± 10.4	-0.31 ± 0.13	0.00 ± 0.01	2.64	34.922
2010-19	7:14	-42.9:-39.5	257	7:10	2820 to bottom	-37.5 ± 5.7	-0.34 ± 0.07	-0.01 ± 0.01	2.30	34.909
Deep Western Boundary Current 36°N										
2000-09	1:13	-71.7:-67.3	406	7:9	2682 to bottom	-34.5 ± 8.7	-0.29 ± 0.10	0.01 ± 0.01	2.13	34.906
Deep Western Boundary Current 24.5°N										
1990-99	16:32	-72.6:-62.7	1002	7:10	2553 to 5630	-23.8 ± 10.8	-0.27 ± 0.11	0.01 ± 0.02	2.88	34.954
2000-09	34:46	-72.0:-56.9	556	7:10	2572 to 5534	-18.3 ± 9.8	-0.22 ± 0.10	0.02 ± 0.01	3.10	34.963
2010-19	46:76	-70.7:-54.6	1624	7:10	2507 to 5741	-30.4 ± 7.3	-0.33 ± 0.07	0.01 ± 0.01	2.72	34.941
Deep Western Boundary Current Recirculation 24.5°N										
1990-99	11:16	-75.5:-73.2	237	7:10	2599 to 4979	6.8 ± 6.5	0.11 ± 0.07	-0.01 ± 0.01	4.05	35.009
2000-09	23:29	-75.3:-74.2	107	7:10	2644 to 4337	11.5 ± 3.3	0.16 ± 0.04	-0.01 ± 0.01	3.47	34.970
2010-19	22:27	-76.8:-76.4	36	7:10	2644 to 4745	6.3 ± 1.4	0.04 ± 0.02	0.01 ± 0.01	1.41	34.873
Deep Western Boundary Current 11°S										
1990-99	1:8	-35.7:-35.1	88	6:8	1323 to 2561	-17.3 ± 2.2	-0.23 ± 0.03	0.02 ± 0.01	3.39	34.902
Deep Western Boundary Current 19°S										
1990-99	1:7	-37.4:-35.8	168	6:9	1493 to 3370	-20.8 ± 7.2	-0.25 ± 0.09	0.00 ± 0.02	2.98	34.927
Deep Western Boundary Current 24°S										
2000-09	1:20	-41.0:-33.1	808	6:9	1375 to 2946	-29.0 ± 9.0	-0.33 ± 0.10	0.02 ± 0.01	2.92	34.891
2010-19	1:25	-41.0:-31.5	967	6:9	1403 to 3145	-27.5 ± 7.1	-0.32 ± 0.08	-0.02 ± 0.01	2.91	34.899
Deep Western Boundary Current 30°S										
1990-99	1:15	-47.2:-42.9	443	6:9	1336 to 2177	-26.6 ± 5.1	-0.32 ± 0.06	0.02 ± 0.01	3.06	34.820
2000-09	6:14	-46.3:-43.6	282	6:9	1674 to 2861	-25.9 ± 5.0	-0.32 ± 0.06	-0.01 ± 0.02	3.11	34.830
2010-19	1:23	-47.7:-39.5	833	6:9	1368 to 2580	-27.9 ± 1.9	-0.32 ± 0.02	0.01 ± 0.01	2.93	34.840
Deep Western Boundary Current 45°S										
1990-99	7:12	-57.8:-55.8	162	5:9	717 to 3352	-49.1 ± 7.0	-0.53 ± 0.07	-0.20 ± 0.04	2.73	34.441

Continuation from Table 3.2.

Decade	Stations	Long (°E)	Dist (km)	Layers	Depth (m)	Mass Trans (Sv)	Heat Trans (PW)	Fw Total (Sv)	TWT (°C)	TWS
Deep Eastern Boundary Current 30°S										
1990-99	83:100	0.6:11.8	1086	7:9	2502 to 3833	-8.3 ± 4.6	-0.08 ± 0.05	0.00 ± 0.01	2.48	34.828
2000-09	85:99	1.1:10.0	852	7:9	2494 to 3781	-9.7 ± 3.5	-0.09 ± 0.03	0.00 ± 0.01	2.44	34.833
2010-19	97:114	3.3:12.5	887	7:9	2544 to 3932	-8.6 ± 3.4	-0.08 ± 0.03	0.01 ± 0.01	2.31	34.852
Deep Eastern Boundary Current 45°S										
1990-99	80:87	10.9:14.6	415	7:9	2358 to 3153	-6.4 ± 6.3	-0.06 ± 0.06	0.01 ± 0.01	2.22	34.860
Deep Eastern Boundary Current 24°S										
2000-09	45:52	-15.0:11.7	348	6:9	1416 to 4141	-13.7 ± 5.5	-0.14 ± 0.05	0.00 ± 0.01	2.59	34.829
2010-19	74:85	-4.1:0.4	457	6:9	1438 to 5089	-9.7 ± 6.1	-0.12 ± 0.06	-0.01 ± 0.01	3.03	34.786

and -0.34 ± 0.07 PW) with null values of freshwater flux. The DWBC presents TW temperatures of 2.64 and 2.30°C and TW salinities of 34.922 and 34.909.

The DWBC at 36°N (Figure 3.5 c, d and Table 3.2) gets wider, occupying 406 km from the coast to 67.3°W while flowing along similar depth levels (from ~2682 m to the bottom). The net mass transport of -34.5 ± 8.7 Sv is southward, similar to the 2000-09 decade at 47°N, associated with -0.29 ± 0.10 PW of heat transport, in agreement with the 10-year mean of -29.59 ± 2.08 Sv from the mooring line W. The values for the TW properties are quite similar to those at 47°N (2.13°C for TW temperature and 34.906 for TW salinity).

The presence of Antarctic Bottom Water (AABW) at 24.5°N constitutes a deep boundary for the vertical extension of the DWBC, that is, therefore, restricted to neutral densities between 27.84 and 28.23 kg m^{-3} (from ~2500 m to ~5500 m deep). At this latitude, we find even wider (and varying) horizontal extensions of the DWBC, ranging between 1062, 601 and 1663 km for each decade, from the coast to 62.7°W, 56.9°W and 54.6°W (Figure 3.5 e, f and Table 3.2). The strength of the DWBC has decreased when it reaches this latitude, with mass transports of -23.8 ± 10.8, -18.3 ± 9.8 and -30.4 ± 7.3 Sv for the 1990-99, 2000-09 and 2010-19 decades, respectively. These values, with their relatively large uncertainties, coincide with the IES-derived transport from Meinen et al. (2004) of -25 ± 9 Sv, and with the mooring array estimations from Johns et al. (2008) of -26.5 Sv, as well as inverse solutions using hydrography from Hernández-Guerra et al. (2014) of -22.1 ± 4.2 for the 1992 cruise and -20.1 ± 3.7 Sv for the 2011 cruise. The heat transport is also reduced (-0.27 ± 0.11, -0.22 ± 0.10 and -0.33 ± 0.07 PW), while the freshwater remains negligible. The TW properties become warmer (2.88, 3.10 and 2.72°) and saltier (34.954, 34.963 and 34.941) on its way south. West of the DWBC, there is a recirculation that carries water northward at deep layers. The ratio of northward transport opposing the DWBC varies for each decade (29%, 63% and 21%), with net mass transports similar for the first and last decade and a stronger component for the 2000-09 decade (6.8 ± 6.5, 11.5 ± 3.3 and 6.3 ± 1.4 Sv). This recirculation has been previously estimated to be around 13 Sv using current metre moorings (Bryden et al., 2005a) and 8 Sv from CTD and LADCP profiles (Biló & Johns, 2020), despite the poorly defined zonal extent of the circulation.

The distribution of AABW into the South Atlantic constitutes a deep boundary for the vertical extension of the DWBC, that is shifted upwards between neutral densities of 27.58 and 28.15 kg m^{-3}. At 11°S for the 1990-99 decade, the DWBC flows as a narrow jet along the coast up to 35.1°W ($\sim$88 km wide), extending from $\sim$1323 to $\sim$2561 m in the water column. This deep southward flow transports -17.3 ± 2.2 Sv of mass, -0.23 ± 0.03 PW of heat and 0.02 ± 0.01 Sv of freshwater (Figure 3.5 g, h and Table 3.2). Hummels et al. (2015) found similar values of DWBC transport from shipboard and moored observations (-17.5 ± 1.7 Sv), while previous studies using hydrographic sections have obtained much stronger southward transports (-35.5 ± 14.7 Sv; Schott et al., 2005). While the TW temperature has increased on its way south (3.39°C), the DWBC has become fresher (TW salinity of 34.902).

The DWBC at 19°S during 1990-99 has extended horizontally to a width of 168 km (from the coast to 35.8°W) and deepened (between 1493 and 3370 m). The deep current at this latitude has increased its southward mass transport to -20.8 ± 7.2 Sv (Figure 3.5 i, j and Table 3.2), as well as heat (-0.25 ± 0.09 PW). The water mass has become colder but saltier, with a TW temperature of 2.98°C and TW salinity of 34.927.

On its way southward, the DWBC gets wider until reaching values of 808 and 967 km at 24°S for the 2000-09 and 2010-19 decades, respectively, while occupying similar vertical depths (from $\sim$1400 to $\sim$3000 m) (Figure 3.5 k, l and Table 3.2). At 24°S, the DWBC transports -29.0 ± 9.0 and -27.5 ± 7.1 Sv of mass southward for the 2000-09 and 2010-19 decades, respectively, with a more intense DWBC than in other inverse solutions (Arumí-Planas et al. 2023, submitted). This deep transport has increased with respect to 19°S, not only in mass but also in heat (-0.33 ± 0.10 and -0.32 ± 0.08 PW), with an almost null freshwater flux (0.02 ± 0.01 and -0.02 ± 0.01 Sv). At this latitude, the DWBC gets colder but also fresher, with TW temperatures of 2.92 and 2.91°C and TW salinities of 34.891 and 34.786.

When the DWBC reaches 30°S, its location presents certain variability, ranging between 443, 282 and 833 km wide, and between depths of 1336 to 2177 m, 1674 to 2861 m and 1368 to 2580 m in 1990-99, 2000-09 and 2010-19, respectively (Figure 3.5 n, o and Table 3.2). However, the strength of the southward deep current is quite similar to the values at 24°S, and they are quite stable among decades. The net mass transports of the DWBC at 30°S are -26.6 ± 5.1, -25.9 ± 5.0 and -27.9 ± 1.9 Sv for each decade, significantly higher than previous estimations of -16.1 ± 5.1 Sv using hydrography (Hernández-Guerra et al., 2019). The heat transports associated to the DWBC at this latitude are the same for every decade (-0.32 ± 0.06, -0.32 ± 0.06 and -0.32 ± 0.02 PW), with almost null freshwater fluxes (0.02 ± 0.01, -0.01 ± 0.02 and 0.01 ± 0.01 Sv). The TW temperatures have increased (3.06, 3.11 and 2.93°C), while reducing the values of the TW salinities (34.820, 34.830 and 34.840).

The southernmost section of our study, at 45°S, manifests the presence of a narrow DWBC (162 km) from 57.8°W to 55.8°W (Figure 3.5 q, r and Table 3.2), occupying a significant larger part of the water column (∼717 to ∼3352 m). There is a strong DWBC transport of -49.1 ± 7.0 Sv for mass, -0.53 ± 0.07 PW for heat and -0.20 ± 0.04 Sv for freshwater. The DWBC at this latitude has gotten colder (TW temperature of 2.73°C) and fresher (TW salinity of 34.265).

Deep Eastern Boundary Current

The change in the orientation of the Brazilian coast after Cape São Roque (Figure 3.1) results in a division of the main DWBC that originates an eastern branch that crosses the Mid Atlantic Ridge (MAR). In our hydrographic sections, the separate branch of the DWBC lies on the eastern side of the MAR at 24°S, and it has been denominated the Deep Eastern Boundary Current (DEBC; Arhan et al. 2003; Bower et al. 2019; Garzoli et al. 2015; Stramma & England 1999).

The DEBC at 24°S covers a horizontal range of ∼420 km and a vertical range between ∼1400 and ∼4100 m for the 2000-09 decade and ∼1400 and ∼5100 m for the 2010-19 decade. The mass transport carried out by the DEBC at 24°S for the 2000-09 and 2010-19 decades is quite variable, with net mass transports of -13.7 ± 5.5 and -9.7 ± 6.1 Sv, respectively (Figure 3.5 l, m and Table 3.2), not significantly different than the estimation from Arumí-Planas et al. (2023) (submitted), of -16.3 ± 4.7 Sv. The heat transport values are quite similar (-0.14 ± 0.05 and -0.12 ± 0.06 PW) despite the variable mass transports, due to the differences in the TW temperatures (2.59 and 3.03°C). The TW salinities have values of 34.829 and 34.786 with a null value of freshwater flux.

At 30°S the DEBC occupies a smaller part of the water column, between ∼2500 and ∼3800 m deep, with a horizontal extension of ∼900 km wide. This southward flow exhibits similar values of mass transport among decades (-8.3 ± 4.6, -9.7 ± 3.5 and -8.6 ± 3.4 Sv for the 1990-99, 2000-09 and 2010-19 decades, respectively; Figure 3.5 o, p and Table 3.2), reproduced for heat transport (-0.08 ± 0.05, -0.09 ± 0.03 and -0.08 ± 0.03 PW). Hernández-Guerra et al. (2019) found similar values for the 2003 and 2011 cruises (-8.2 ± 5.6 Sv and -12.7 ± 5.5 Sv, respectively), comparable with the IES reconstruction of -12 Sv from Kersalé et al. (2019). The values for the TW properties remain quite stable for all decades, for both temperature (2.48, 2.44 and 2.31°C) and salinity (34.828, 34.833 and 34.852).

The 45°S section exhibits the presence of a narrower (415 km) DEBC during the 1990-99 decade, from 10.9°E to 14.6°E (Figure 3.5 r, s and Table 3.2). There is a reduction in the southward transport of mass (-6.4 ± 6.3 Sv) and heat (-0.06 ± 0.06 PW) compared with the values at 30°S, carrying waters with TW temperature of 2.22°C and TW salinity of 34.860.

3.3.3 Bottom currents

Antarctic Bottom Water

The Antarctic Bottom Water (AABW) originates in the Southern Ocean and reaches the Atlantic Ocean as the densest water mass, distributing along the ocean bottom on its way northward.

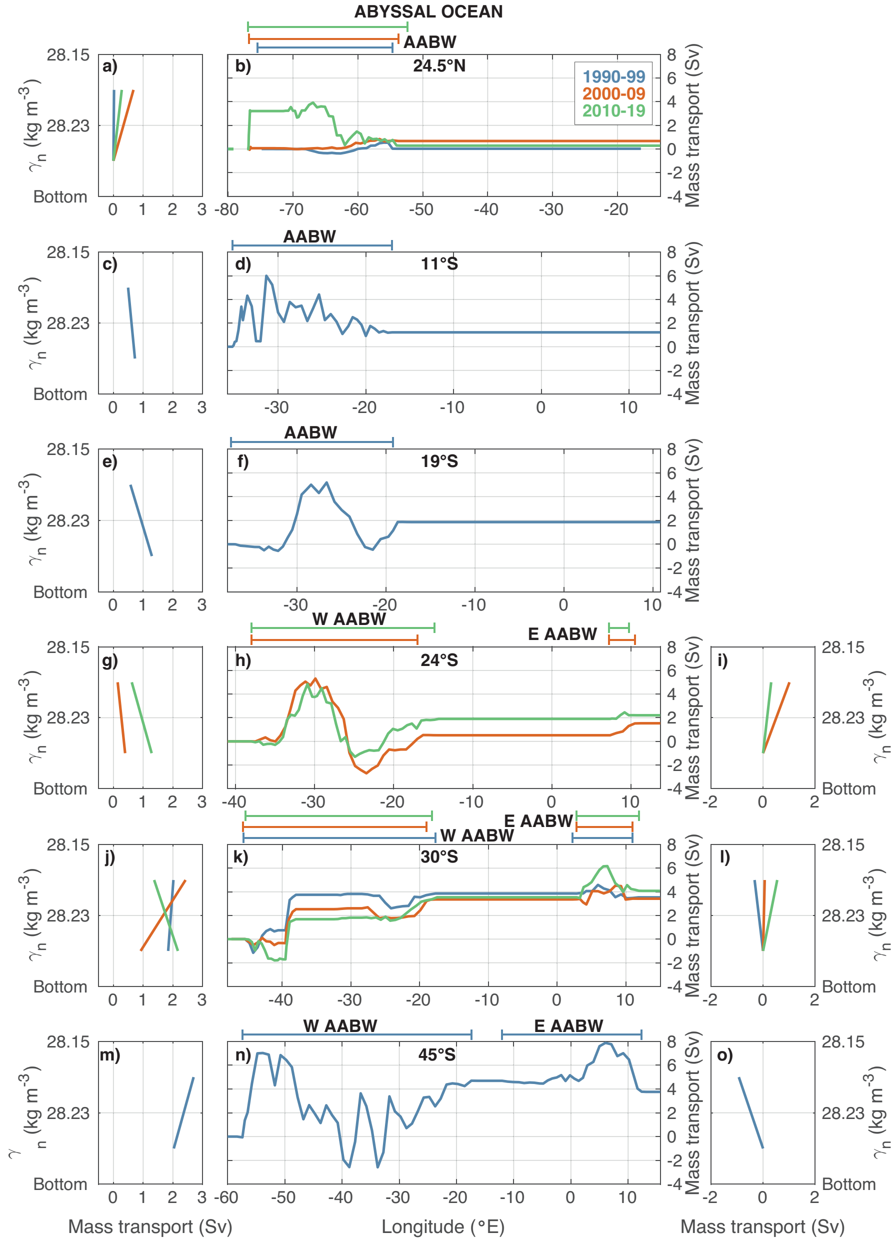

Figure 3.6. Abyssal currents in the Atlantic at different latitudes and decades. Net mass transport (Sv) per layer defined between neutral density interfaces for the Antarctic Bottom Water (AABW) West of the MAR at 24.5°N (a), 11°S (c), 19°S (e), 24°S (g), 30°S (j), and 45°S (m), and East of the MAR at 24°S (i), 30°S (l), and 45°S (o). The transport per layer is computed using the stations and layers specified in Table 3.3. The longitudinal ranges of the currents at each latitude and decade appear on the top of the middle panel with different colours, in blue for 1990-1999, orange for 2000-2009, and green for 2010-2019. The middle panels show the eastward accumulated horizontal mass transport (Sv) for upper layers for the 24.5°N (b), 11°S (d), 19°S (f), 24°S (h), 30°S (k), and 45°S (n) sections.

At 45°S, the AABW enters the Atlantic Ocean west of the MAR between 57.4°W and 17.4°W, from ∼3800 m to the bottom during the 1990-99 decade, introducing a net mass transport of 4.7 ± 1.7 Sv of cold (TW temperature of 0.41°C) and relatively fresh (TW salinity of 34.697) water (Figure 3.6 m, n and Table 3.3). No heat or freshwater transport is associated to the AABW. Previous studies using the same hydrographic section have found similar net inputs from the AABW at the Argentine Basin (5.6 ± 1.0 Sv by McDonagh & King 2005 and 5.6 ± 0.9 Sv by Naveira Garabato et al. 2014). East of the MAR, there is another contribution from the Southern Ocean to the South Atlantic basin (Figure 3.6 n, o and Table 3.3). However, including its recirculation, the net transport yields a southward -0.9 ± 1.6 Sv of water slightly warmer and saltier (TW temperature of 1.18°C and TW salinity of 34.777). Therefore, the total net transport of bottom waters at 45°S introduces 3.8 ± 1.7 Sv into the Atlantic basin.

The AABW continues its way to the north and reaches 30°S west of the MAR between 45.7°W and 17.7°W, 45.7°W and 19.0°W and 45.4°W and 18.2°W for the 1990-99, 2000-09 and 2010-19 decades, respectively (Figure 3.6 j, k and Table 3.3), occupying the water column at depths below ∼3500 m. The net strength of the Western AABW has reduced at this point, with quite stable values for all decades of mass transport (3.9 ± 1.3, 3.3 ± 1.3 and 3.5 ± 1.5 Sv). The TW temperatures (0.46, 0.71 and 0.55°C) and salinities (34.722, 34.750 and 34.730) of this water mass at this latitude west of the MAR have increased, after being mixed with the water masses above while flowing northward, with marked higher values for the 2000-09 period. The eastern AABW yields non-significant values for the mass transport at any decades (-0.3 ± 1.0, 0.1 ± 1.0 and 0.5 ± 0.9 Sv; Figure 3.6 k, l and Table 3.3), resulting in net total transport across bottom layers dominated by the western subbasin (3.5 ± 1.2, 3.4 ± 1.4 and 4.1 ± 1.5 Sv). Results from previous studies attribute similar albeit slightly stronger AABW northward transports at 30°S, with 5.4 ± 1.4 Sv (McDonagh & King, 2005) and 5.2 ± 1.1 Sv (Naveira Garabato et al., 2014) for the 1992-93 cruise and 6.5 ± 1.9 Sv and 8.3 ± 2.1 Sv for the 2003 and 2011 cruises, respectively (Hernández-Guerra et al., 2019).

The AABW at 24°S occupies smaller horizontal extensions west of the MAR, from 38.0°W to 17.0°W (2138 km) and from 38.0°W to 14.8°W (2362 km) for the 2000-09 and 2010-19 decades, respectively (Figure 3.6 g, h and Table 3.3). At this latitude, the upper level of the AABW has deepened to ∼4550 m. The values for the last two decades at 24°S show weaker AABW mass transports west of the MAR (0.5 ± 2.3 and 1.9 ± 2.0 Sv). The eastern basin shows similar values to the western basin, with inputs of 1.0 ± 2.0 and 0.3 ± 1.4 Sv (Figure 3.6 h, i and Table 3.3). The total AABW transports (1.5 ± 1.4 and 2.2 ± 1.5 Sv) yield lower results than other inverse solutions for the 2009 cruise (2.6 ± 0.5 Sv; Evans et al. 2017) and 2018 cruise (6.6 ± 1.6 Sv; Arumí-Planas et al. 2023, submitted).

Following its way northward along the South American coast, the AABW at 19°S can be found between 37.4°W and 19.2°W (1914 km wide) in the horizontal and between ∼4260 m and the bottom of the ocean (Figure 3.6 e, f and Table 3.3). At this latitude, no eastern contribution can be found and the AABW is restricted west of the MAR. The AABW at 19°S shows similar values of mass transport (1.9 ± 1.4 Sv) for the first decade to the total values at 24°S for the remaining decades.

The AABW at 11°S appears between 35.2°W and 17.0°W, occupying ~1900 km in the horizontal, and in the vertical from 4377 m to the bottom of the water column (Figure 3.6 c, d and Table 3.3). The strength of the AABW flow at 11°S remains mainly unchanged (1.2 ± 1.2 Sv of mass transport). Using a combination of shipboard measurements and mooring arrays, Schott et al. (2005) have estimated a mean northward transport of 2.7 ± 2.9 Sv over 2000-04, which yield similarly non-significant values.

The last section where we can observe the presence of the AABW is 24.5°N, with relatively large horizontal extensions (75.5°W to 54.7°W, 76.8°W to 53.7°W and 76.9°W to 52.3°W of 2103, 2322 and 2474 km wide, respectively) with very small mass transports (0.1 ± 0.9, 0.7 ± 0.9 and 0.3 ± 1.3 Sv) for the 1990-99, 2000-09 and 2010-19 decades (Figure 3.6 a, b and Table 3.3). Comparable non-significant northward mass transports are obtained by Hernández-Guerra et al. (2014) for 1992 (1.4 ± 1.8 Sv) and 2011 (1.1 ± 1.8 Sv). The combination of shipboard measurements and the

Table 3.3. Characteristics of each abyssal-layer current found at every section

Decade	Stations	Long (°E)	Dist (km)	Layers	Depth (m)	Mass Trans (Sv)	Heat Trans (PW)	Fw Total (Sv)	TWT (°C)	TWS
Antarctic Bottom Water – West MAR 45°S										
1990-99	8:50	-57.4:-17.4	3144	10:11	3838 to bottom	4.7 ± 1.5	0.01 ± 0.01	0.00 ± 0.01	0.41	34.697
Antarctic Bottom Water – East MAR 45°S										
1990-99	54:83	-12.0:12.4	2505	10:11	4560 to bottom	-0.9 ± 1.6	0.01 ± 0.01	0.00 ± 0.01	1.18	34.777
Antarctic Bottom Water – West MAR 30°S										
1990-99	9:59	-45.7:-17.7	2725	10:11	3549 to bottom	3.9 ± 1.3	0.01 ± 0.01	0.00 ± 0.01	0.46	34.722
2000-09	9:58	-45.7:-19.0	2599	10:11	3510 to bottom	3.3 ± 1.3	0.01 ± 0.01	0.00 ± 0.01	0.74	34.750
2010-19	9:61	-45.4:-18.2	2639	10:11	3683 to bottom	3.5 ± 1.5	0.01 ± 0.01	0.00 ± 0.01	0.53	34.730
Antarctic Bottom Water – East MAR 30°S										
1990-99	86:99	2.3:11.0	842	10:11	4630 to bottom	-0.3 ± 1.0	0.00 ± 0.0	0.00 ± 0.01	0.98	34.760
2000-09	88:100	2.8:11.0	788	10:11	4761 to bottom	0.1 ± 1.0	0.00 ± 0.01	0.00 ± 0.01	-1.12	34.561
2010-19	96:113	2.8:11.9	877	10:11	4723 to bottom	0.5 ± 0.9	0.00 ± 0.01	0.00 ± 0.01	0.66	34.729
Antarctic Bottom Water – West MAR 24°S										
2000-09	11:43	-38.0:-17.0	2138	10:11	4552 to bottom	0.5 ± 2.3	0.00 ± 0.01	0.00 ± 0.01	-0.87	34.568
2010-19	11:54	-38.0:-14.8	2362	10:11	4568 to bottom	1.9 ± 2.0	0.01 ± 0.01	0.00 ± 0.01	0.17	34.691
Antarctic Bottom Water – East MAR 24°S										
2000-09	79:85	7.2:10.5	331	10:11	4089 to bottom	1.0 ± 2.0	0.00 ± 0.01	0.00 ± 0.01	0.97	34.756
2010-19	99:106	7.2:9.7	253	10:11	4273 to bottom	0.3 ± 1.4	0.00 ± 0.01	0.00 ± 0.01	0.91	34.752
Antarctic Bottom Water – West MAR 19°S										
1990-99	1:31	-37.4:-19.2	1914	10:11	4259 to bottom	1.9 ± 1.4	0.00 ± 0.01	-0.02 ± 0.01	0.08	34.683
Antarctic Bottom Water – West MAR 11°S										
1990-99	6:42	-35.2:-17.0	1989	10:11	4377 to bottom	1.2 ± 1.2	0.00 ± 0.01	0.00 ± 0.01	0.08	34.682
Antarctic Bottom Water – West MAR 24.5°N										
1990-99	11:44	-75.5:-54.7	2103	10:11	5608 to bottom	0.1 ± 0.9	0.01 ± 0.01	0.00 ± 0.01	0.61	34.811
2000-09	11:64	-76.8:-53.7	2322	10:11	5198 to bottom	0.7 ± 0.9	0.00 ± 0.01	0.00 ± 0.01	1.49	34.848
2010-19	19:80	-76.9:-52.3	2474	10:11	5310 to bottom	0.3 ± 1.3	0.01 ± 0.01	0.00 ± 0.01	5.47	35.304

RAPID mooring array yield similar weak AABW transports, with mean values of 1.0 Sv (McCarthy et al., 2015) and stronger ranges of 2.2-3.7 Sv (Frajka-Williams et al., 2011).

3.4 Summary and conclusions

The complex system of currents throughout the Atlantic basin that constitute the AMOC has been described in this study using repeated hydrographic sections over the last thirty years. Inverse methods enable quantifying not only the AMOC, but also the strength and properties associated with the most significant currents flowing along the Atlantic Ocean, attending to their transports of mass, heat, and freshwater for different vertical and horizontal ranges.

Surface currents in the subtropical basins of the Atlantic Ocean describe the wind-driven gyre circulation, with stronger poleward western boundary currents compensated by equatorward flow in the ocean interior and weaker eastern boundary currents occupying a larger longitudinal extension (Figure 3.7).

Near 61 Sv of surface and intermediate water enter the Atlantic basin from the Southern and Indian Oceans at the southern boundary of our study area. The cold and fresh water route of the MC (37.2 ± 2.0 Sv) carries more water than the eastern warm and salty water route connecting the Atlantic with the Indian Ocean (24.0 ± 2.3 Sv). However, the flow of the MC retroflects and joins again the ACC east of 20°W together with a contribution from the South Atlantic subtropical gyre (-55.5 ± 5.6 Sv). The input from the Indian Ocean is divided into two nearly steady branches at 30°S, the SEC (15.8 ± 3.4 Sv on average for the whole period) and the BeC (12.5 ± 2.0 Sv on average for the whole period). Mass transports for both currents decrease on their way northward to 19°S, lowering to 2.3 ± 1.2 Sv and 9.0 ± 1.9 Sv, respectively. The complex system of currents of the South Atlantic subtropical gyre is oversimplified in Figure 3.7. All together suggests not only a northward flow of the BeC and SEC, but also a large east-to-west contribution towards the BrC (ca. 2 to 7 Sv) between 24°S and 30°S. In this location a widening of the SEC is also observed (Figure 3.7). In the 2000-2009 decade, this east-to-west contribution seems to be feeding the southward transport of the BrC at 30°S, while the circulation is harder to infer for the other decades. The 11°S section marks the end of the South Atlantic subtropical gyre where the NBrC transports northward 17.0 ± 1.2 Sv. Nearly half of the transport of this current finds its source on the northwestward SEC (9.0 ± 1.9 Sv).

In the northern hemisphere, both the FC and the AC carry northward warm waters from the equatorial area. These currents have decreased their transport ca. 4 Sv in the last decade. The GF transport increases by 29.6 ± 1.8 Sv from 24.5°N to 36°N (Figure 3.7). At 36°N, the GS carries 74.9 ± 1.7 Sv, of which -35.4 ± 3.0 Sv recirculates southward. The GS at this latitude feeds both the North Atlantic subtropical and subpolar gyres. A nearly steady transport of 5.3 ± 1.8 Sv (average transport for the three decades) recirculates southward on the CC closing the subtropical loop.

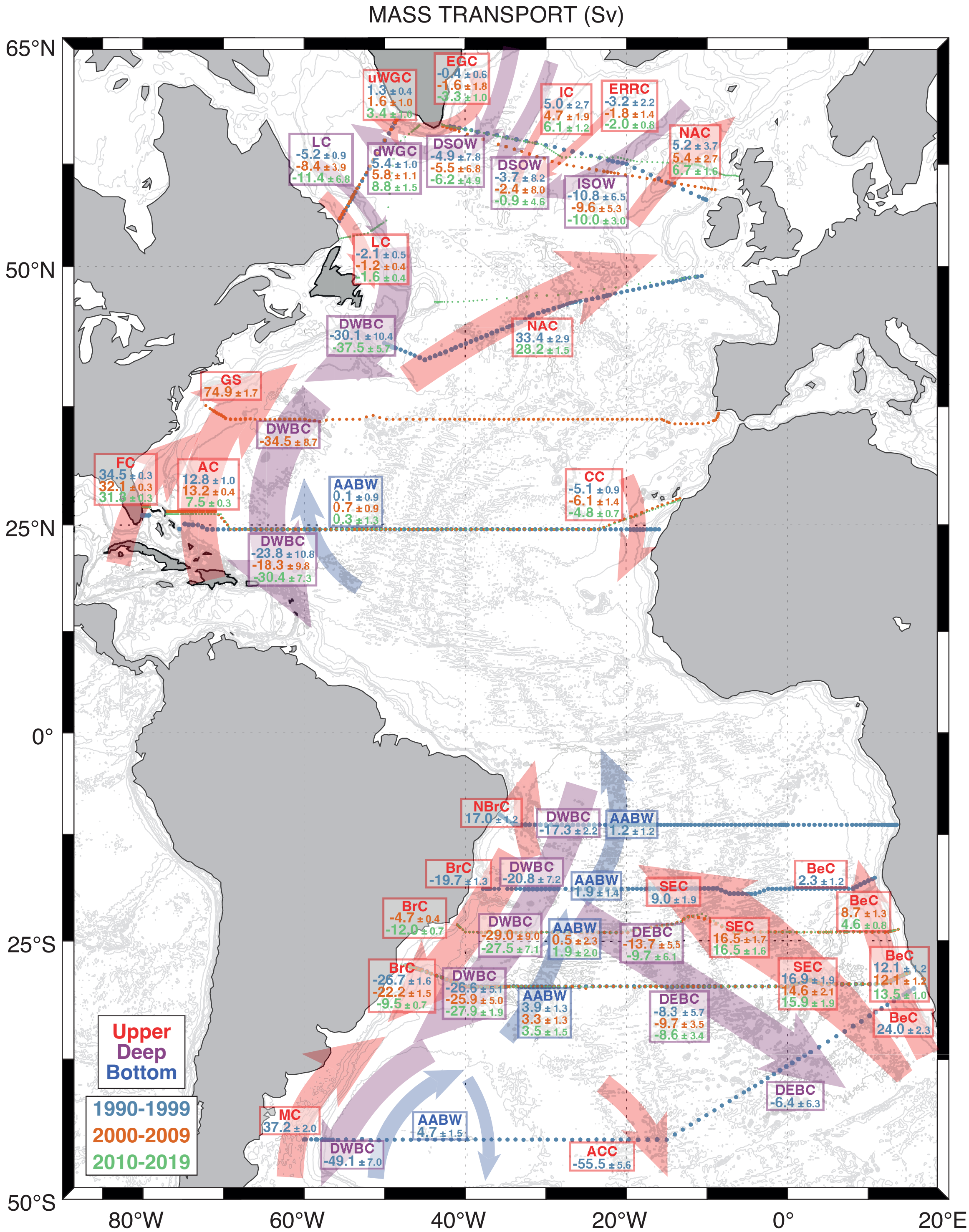
MASS TRANSPORT (Sv)
65°N
50°N
25°N
0°
25°S
50°S
80°W
60°W
40°W
20°W
0°
20°E
uWGC 1.3 ± 0.4 1.6 ± 1.0 3.4 ± 1.0
EGC -0.4 ± 0.6 -1.6 ± 1.8 -3.3 ± 1.0
IC 5.0 ± 2.7 4.7 ± 1.9 6.1 ± 1.2
ERRC -3.2 ± 2.2 -1.8 ± 1.4 -2.0 ± 0.8
LC -5.2 ± 0.9 -8.4 ± 3.9 -11.4 ± 6.8
dWGC 5.4 ± 1.0 5.8 ± 1.1 8.8 ± 1.5
DSOW -4.9 ± 7.8 -5.5 ± 6.8 -6.2 ± 4.9
DSOW -3.7 ± 8.2 -2.4 ± 8.0 -0.9 ± 4.6
ISOW -10.8 ± 6.5 -9.6 ± 5.3 -10.0 ± 3.0
NAC 5.2 ± 3.7 5.4 ± 2.7 6.7 ± 1.6
LC -2.1 ± 0.5 -1.2 ± 0.4 -1.6 ± 0.4
DWBC -30.1 ± 10.4 -37.5 ± 5.7
NAC 33.4 ± 2.9 28.2 ± 1.5
GS 74.9 ± 1.7
DWBC -34.5 ± 8.7
FC 34.5 ± 0.3 32.1 ± 0.3 31.3 ± 0.3
AC 12.8 ± 1.0 13.2 ± 0.4 7.5 ± 0.3
AABW 0.1 ± 0.9 0.7 ± 0.9 0.3 ± 1.3
CC -5.1 ± 0.9 -6.1 ± 1.4 -4.8 ± 0.7
DWBC -23.8 ± 10.8 -18.3 ± 9.8 -30.4 ± 7.3
NBrC 17.0 ± 1.2
DWBC -17.3 ± 2.2
AABW 1.2 ± 1.2
BrC -19.7 ± 1.3
DWBC -20.8 ± 7.2
AABW 1.9 ± 1.4
SEC 9.0 ± 1.9
BeC 2.3 ± 1.2
BeC 8.7 ± 1.3 4.6 ± 0.8
BrC -4.7 ± 0.4 -12.0 ± 0.7
DWBC -29.0 ± 9.0 -27.5 ± 7.1
AABW 0.5 ± 2.3 1.9 ± 2.0
DEBC -13.7 ± 5.5 -9.7 ± 6.1
SEC 16.5 ± 1.7 16.5 ± 1.6
BeC 12.1 ± 1.2 12.1 ± 1.2 13.5 ± 1.0
BrC -26.7 ± 1.6 -22.2 ± 1.5 -9.5 ± 0.7
DWBC -26.6 ± 5.1 -25.9 ± 5.0 -27.9 ± 1.9
AABW 3.9 ± 1.3 3.3 ± 1.3 3.5 ± 1.5
DEBC -8.3 ± 5.7 -9.7 ± 3.5 -8.6 ± 3.4
SEC 16.9 ± 1.9 14.6 ± 2.1 15.9 ± 1.9
BeC 24.0 ± 2.3
DEBC -6.4 ± 6.3
Upper
Deep
Bottom
1990-1999
2000-2009
2010-2019
MC 37.2 ± 2.0
AABW 4.7 ± 1.5
DWBC -49.1 ± 7.0
ACC -55.5 ± 5.6

Figure 3.7. Circulation in the upper, deep and abyssal layers in the Atlantic Ocean for mass transport (Sv). The background arrows represent the circulation of the main currents in the text, in red for surface layers, purple for deep and blue for abyssal. At each section, the mass transports (in Sv) for each current appear in a box, with values in blue for 1990-1999, orange for 2000-2009, and green for 2010-2019. Surface currents include Antilles Current (AC), Benguela Current (BeC), Antarctic Circumpolar Current (ACC), Brazil Current (BrC), Canary Current (CC), East Greenland Current (EGC), East Reykjanes Ridge Current (ERRC), Florida Current (FC), Gulf Stream (GS), Irminger Current (IC), Labrador Current (LC), Malvinas Current (MC), North Atlantic Current (NAC), North Brazil Current (NBrC), South Equatorial Current (SEC) and Upper West Greenland Current (uWGC). Deep currents are comprised of Deep Eastern Boundary Current (DEBC), Deep West Greenland Current (dWGC), Deep, Western Boundary Current (DWBC), Denmark Strait Overflow Water (DSOW), Iceland-Scotland Overflow Water (ISOW) and Labrador Current (LC). Abyssal layers are configured by the distribution of Antarctic Bottom Water (AABW).

Between 24.5°N and 55°N, there is a sink to deeper layers of over 5 Sv, with the remaining transport flowing northward on the NAC contributing to the SPNA (Caínzos et al., 2022a). Part of this flow enters on the Arctic basin through the Iceland-Scotland Ridge, of which about 2 Sv recirculates through the gyre and a roughly average of 5.3 ± 3.5 Sv contributes to the NIIC. The EGC connects the Arctic Basin surface waters with those within the SPNA. Interestingly, both the EGC and its downstream continuations on the Labrador Sea (uWGC and LC) show increasing transports that double from the first to the last decade. This behaviour supports the observations of an "Atlantification" of the Arctic Basin (Polyakov et al., 2017, 2020).

The southward flow in deep layers enters the Atlantic basin at the northernmost section via the ISOW and DSOW (Figure 3.7). The stable ISOW (10.1 ± 8.9 Sv on average) carries southward relatively more water than the combined pathways of the DSOW (8.6 ± 11.3, 7.9 ± 1.05 and 7.1 ± 6.7 Sv). The net DSOW manifest decreasing values, but the large errors mask any possible significant trend. Deep currents in the Labrador basin flow cyclonically, with a null net transport out of the Labrador Sea for the first decade and over 2.5 Sv for the 2000-09 and 2010-19 decades.

On its way south, deep layers show the continuity of the DWBC Current throughout the basin (Figure 3.7). At 47°N, the DWBC conveys an average transport of 33.8 ± 11.9 Sv southward after turning westward at Flemish Cap (Figure 3.1). The DWBC maintains similar strength at 36°N and then reduces at 24.5°N, where different values appear for each decade. There is a reduction in the 2000-09 estimation, accompanied by a strengthening of its recirculation, followed by a recuperation in 2010-19. The DWBC reaches 11°S carrying -17.3 ± 2.2 Sv southward, increasing by 17% its transport as it approaches 19°S. South of this latitude, the DWBC separates into a western branch flowing along the western boundary and an eastern branch that crosses the MAR towards the eastern basin (Figure 3.7). At 24°S, the DWBC has increased to an average value of -28.3 ± 11.4 Sv, similar to the mean transport at 30°S (-26.8 ± 7.4 Sv) This increase could be associated to an upper vertical flux from abyssal to deep layers between 24°S and 24.5°N for the 2000-09 and 2010-19 decades of 0.8 and 1.9 Sv, respectively. The export of deep transport through the western basin at 45°S rises by almost 50% to -49.1 ± 7.0 Sv. The eastern branch, the DEBC, suffers a reduction in its strength on its way south. From a mean value of -11.7 ± 8.2 Sv at 24°S, the DEBC is reduced to -8.9 ± 7.5 Sv at 30°S by 24%. The net export at 45°S via the eastern basin results in -6.4 ± 6.3 Sv (after a 28% reduction), corresponding to a 12% of the total deep outflow at the southern boundary of the Atlantic.

Abyssal layers are mainly confined to the South Atlantic, with a stronger net northward input via the western basin (Figure 3.7). East of the MAR, the northward transport of AABW is recirculated, describing a clockwise gyre in abyssal layers up to 24°S. On the western basin, the AABW flows northward, from 4.7 ± 1.5 Sv at 45°S to a mean value of 3.6 ± 2.4 Sv at 30°S, decreasing by 23%. West of the MAR at 24°S, the AABW exhibits different values in different decades with a significant reduction compared to the estimates at 30°S. The northward mass transport of 1.2 ± 1.2 Sv at 11°S reaches 24.5°N with almost negligible values (0.4 ± 1.8 Sv on average). AABW is not detected north of 24.5°N. We found no significant changes in transport. However, we can observe a warming trend with time in the TW temperature, not accompanied by freshening of the abyssal waters. Recent publications have found evidence of this increase in AABW temperature with steady and significant rates around 0.02°C decade^{-1} using different datasets and periods of time (Chidichimo et al., 2023; Johnson et al., 2020; Meinen et al., 2020; Campos et al., 2021; Zenk & Morozov, 2007; Herrford et al., 2017).

The heat transport introduced in the South Atlantic by the warm and salty water route of the Agulhas leakage is 1.19 ± 0.11 PW, distributed along the eastern basin. This heat transport is divided into the contributions for the BeC and SEC, both reducing its heat transport northward (Figure 3.8). The cold and fresh water route, instead, only transports, 0.54 ± 0.02 PW northward, with a southward heat transport toward the Southern Ocean via ACC of -1.09 ± 0.07 PW. The BrC carries heat between 19°S and 30°S along the western boundary, with higher values at 30°S. As a result, the South Atlantic exports roughly 1 PW to the northern hemisphere carried by the NBrC. The northward transport of heat in upper layers of the North Atlantic is mainly achieved by the strong heat transported by the FC (2.48 ± 0.03 PW on average) that increases to 4.56 ± 0.11 PW in the GS at 36°N. The convection processes in the SPNA result in a decrease of heat transport to 1.79 ± 0.14 and 1.18 ± 0.05 PW for the NAC at 47°N. In deep layers, the DWBC carries roughly -0.3 PW southward, starting at 47°N from the Grand banks throughout the North Atlantic and the South Atlantic up to 24°S (Figure 3.8). The DWBC continues carrying around -0.3 PW southward along the western boundary until 45°S, where the net transport of heat via deep layers increases to -0.53 ± 0.07 PW due to the strong values of the MC. At 24°S, the DEBC carries almost half of the estimate for the DWBC, introducing an average of -0.13 ± 0.08 PW into the eastern subbasin. This heat transport reduces southward, with a net export at the southernmost boundary of -0.06 ± 0.06 PW.

The freshwater flux is confined to upper layers (Figure 3.9), with a transport into the South Atlantic via the MC of 0.07 ± 0.01 Sv, counteracted by the -0.07 ± 0.02 Sv of the BeC. However, the ACC exports double of these values towards the Southern Ocean. The BrC carries freshwater northward, while the BeC shows, northward of 45°S, non-significant values of freshwater flux along the eastern boundary. In the North Atlantic, there is mainly a southward freshwater flux

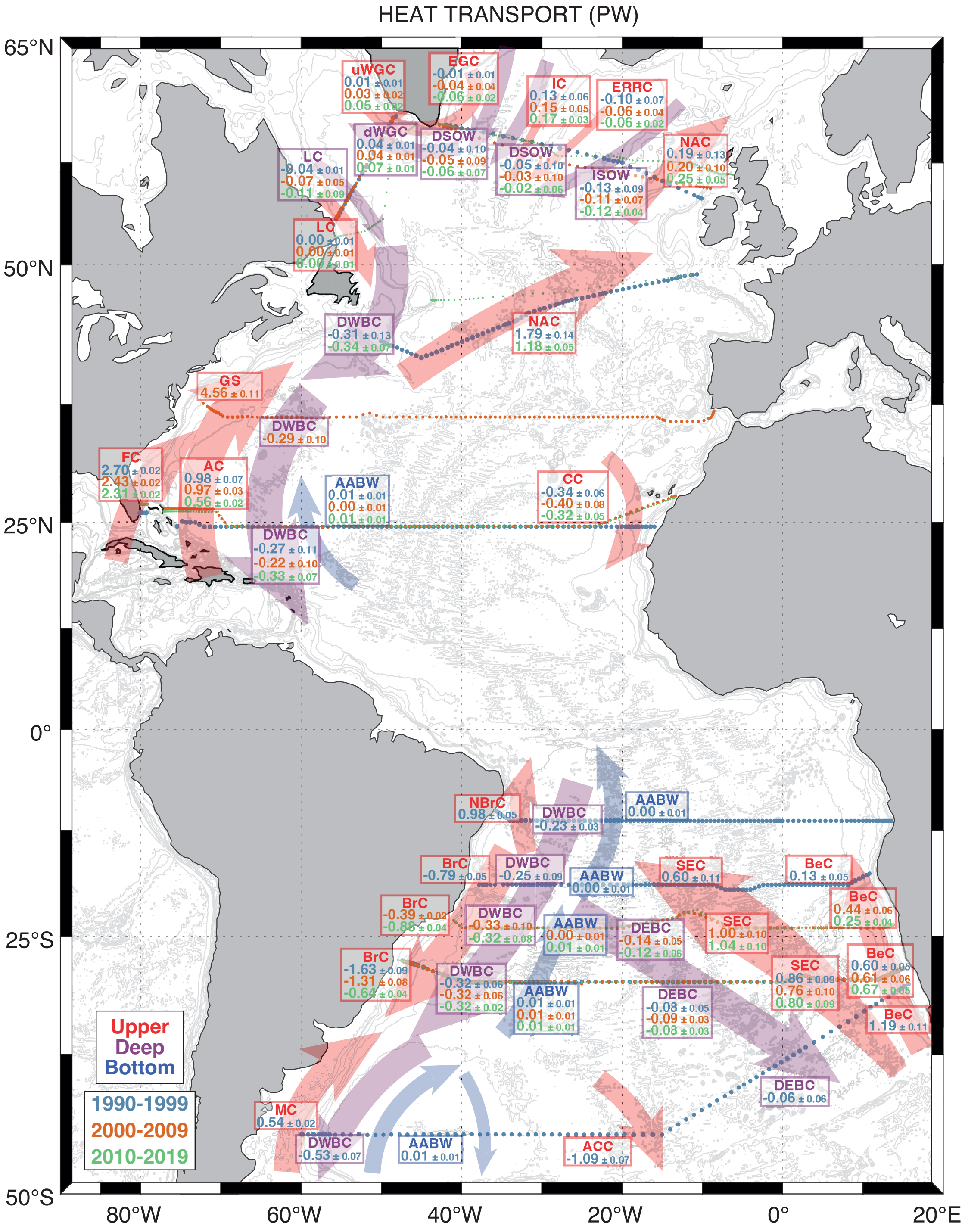

Figure 3.8. Same as Figure 3.7 but for heat transport (PW).

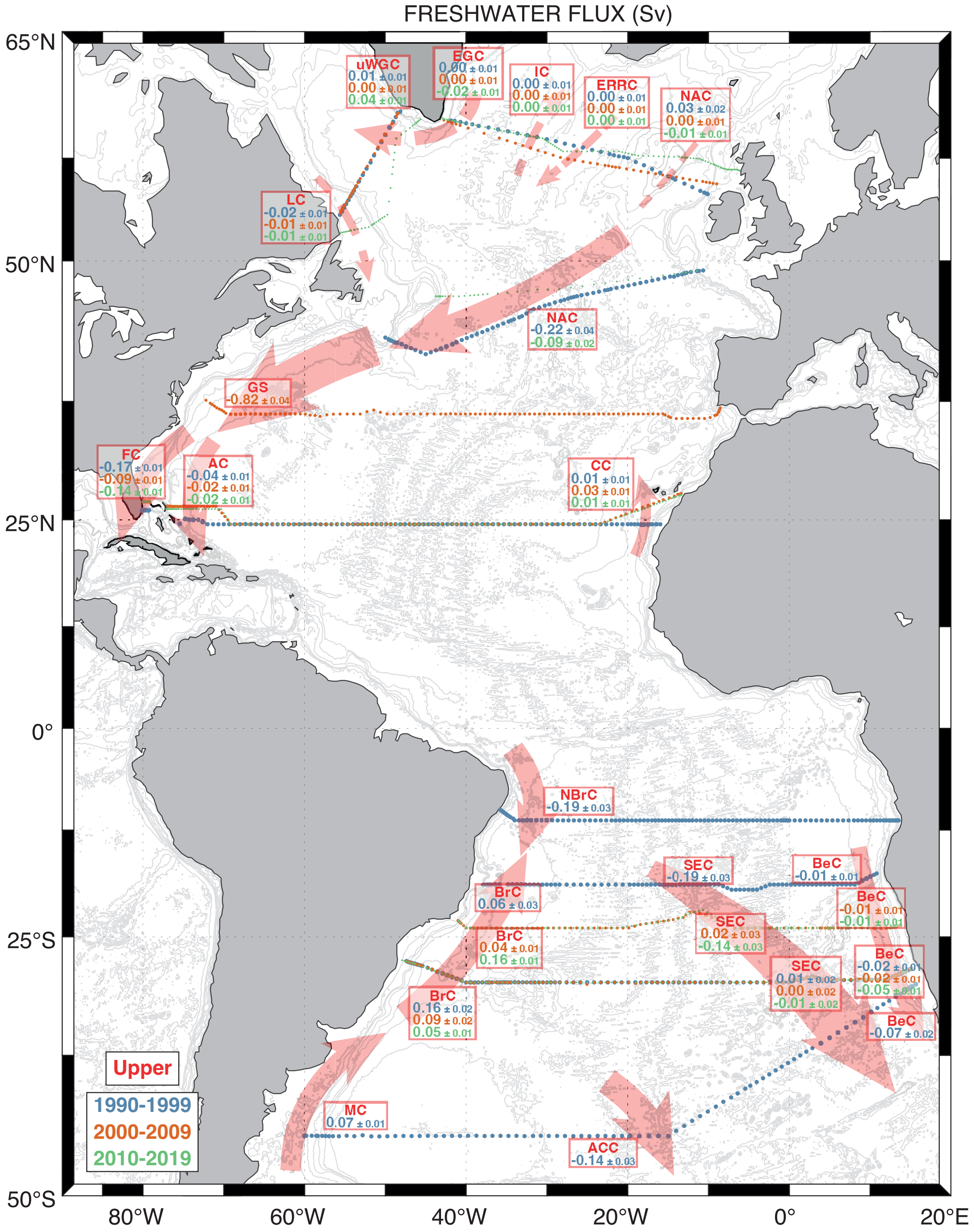

Figure 3.9. Same as Figure 3.7 but for freshwater transport (Sv) in upper layers.

along the eastern basin.

In general, we cannot find any pattern of change of strength of the currents with time, with similar estimations obtained for the different decades. No changes in TW properties have been observed either.

Chapter 4

Anthropogenic Carbon Transport Variability

This chapter has been published as:

Caínzos, V., Velo, A., Pérez, F. F., and Hernández-Guerra, A. (2022). Anthropogenic Carbon transport variability in the Atlantic Ocean over three decades. Global Biogeochemical Cycles, 36, e2022GB007475. https://doi.org/10.1029/2022GB007475.

4.1 Introduction

Human activities have dispersed 650 $\pm$ 65 Gt of carbon to the atmosphere since 1850, of which about 30% has been sequestered by the oceans (Friedlingstein et al., 2020; Gruber et al., 2019; Khatiwala et al., 2013), leading to a continuous increase in total inorganic carbon concentration (C_T). The rise in C_T has, in turn, led to a decrease in surface seawater pH of approximately 0.1 from the pre-industrial era to the present, which implies an increase of approximately 30% in hydrogen ion concentration (Doney et al., 2009; Gattuso et al., 2015). This decline in pH leads to a reduction in the saturation state of calcium carbonate and consequently a serious threat to calcareous marine organisms such as pteropods and corals (Doney et al., 2020; Guinotte et al., 2006; Pérez et al., 2018).

The increase in C_T is very small compared to its concentrations in the ocean ($<$0.1% per year), so most studies quantify the anthropogenic CO_2 (C_{anth}) storage rate rather than the C_T change (Gruber et al., 2019; Khatiwala et al., 2013; Mikaloff Fletcher et al., 2006). The largest C_{anth} water column inventories are found in the subpolar North Atlantic (SPNA; Khatiwala et al. 2013; Sabine et al. 2004). This is due to the combination of (i) convective processes that cause significant ventilation and subduction of C_{anth}-enriched surface water into the interior ocean (Sabine et al., 2004)and (ii) a large amount of C_{anth} advected by the northward currents from tropical latitudes (Brown et al., 2021; Pérez et al., 2013).

Both processes are embedded in the Atlantic Meridional Overturning Circulation (AMOC), which drives the net upper northward transport of C_{anth}-enriched waters throughout the North Atlantic, maintaining a positive correlation between the intensity of the AMOC and the C_{anth} storage rate in the subpolar North Atlantic (DeVries et al., 2017; Pérez et al., 2013; Racapé et al., 2018). Deep-ocean ventilation has been largely related to the strength of the AMOC and controls the connection between the time scales of heat uptake and carbon storage (Kersalé et al., 2020). In the tropical North Atlantic, the rise in C_{anth} concentrations in thermocline waters is the main cause of the slight increase of northward C_{anth} transport from 1992-1993 to 2010-2011, attenuated by the weakening of the circulation (Hernández-Guerra et al., 2014; Zunino et al., 2015b).

Several studies have described the North Atlantic transport, storage and uptake of C_{anth}, benefitting from monitoring projects such as the RAPID/MOCHA/WBTS array (hereafter the RAPID array; Cunningham et al. 2007; Johns et al. 2011; McCarthy et al. 2015) and OVIDE (Lherminier et al., 2010; Mercier et al., 2015). Biogeochemical observations and early estimations of C_{anth} have been combined with ocean circulation models in inverse schemes to estimate air-sea fluxes, C_{anth} storage rate and C_{anth} transport in the ocean interior (DeVries, 2014; Gruber et al., 2019; Mikaloff Fletcher et al., 2006).

However, the South Atlantic has not been subject to such an extensive study, despite representing the region of the Atlantic Ocean with a higher exchange with other ocean basins. The upper limb of the AMOC in the South Atlantic is connected via Drake Passage to the Pacific

Ocean, and via the Agulhas Current System to the Indian Ocean. Evans et al. (2017) evaluated the C_{anth} divergence in the South Atlantic and found that the C_{anth} that entered the South Atlantic through Drake Passage was then exported northwards and eastwards, associated with the Antarctic Circumpolar Current and, to a lesser extent, the Agulhas Current System. Thus, this interbasin exchange supplies the Atlantic and the Indian sector of the Southern Ocean with C_{anth}. Decadal variability in C_{anth} concentration has been studied at 30°S, with a net increase in C_{anth} concentration in Sub Antarctic Mode Waters and Antarctic Intermediate Waters, mainly west of the Mid-Atlantic Ridge (Murata et al., 2008).

In this study, we provide a detailed perspective on the transport of C_{anth}, both from observational and inverse modelling circulation data, and attending to the different components of the meridional circulation, to assess changes for the last three decades, providing a regional perspective. We have also evaluated the contribution of the different water masses that occupy the whole Atlantic basin, using the best available information for different time periods. Thus, we propose a basin solution to anthropogenic transports obtained from hydrographic observations and based on the mass transports determined with inverse models for the last thirty years of the Atlantic Ocean (Caínzos et al., 2022a).

4.2 Data and Methods

4.2.1 Hydrographic data

We have selected zonal hydrographic sections for the last thirty years and grouped them by decade (1990-99, 2000-09, 2010-19). These sections occupy the Atlantic basin, from 45°S to 55°N in the first decade and from 30°S to 55°N for the last two decades (Figure 4.1). Three sections appear in all three decades: A10 (30°S), A05 (24.5°N) and AR07W+AR07E (55°N).

Biogeochemical data for most of the cruises, including water sample values for oxygen, nutrients (nitrate, phosphate, silicate), alkalinity (A_T), C_T and pH, have been obtained from the Global Ocean Data Analysis Project version 2.2021 (GLODAPv2; Key et al. 2015; Lauvset et al. 2021; Olsen et al. 2016). The data included in GLODAPv2 are subject to primary and secondary quality control to correct the measurements. Sections A02 1993 (47°N), AR07W 1990 (55°N) and AR07E 1991 (58°N) are not available in GLODAPv2, so we have used the biogeochemical data provided by the CLIVAR and Carbon Hydrographic Data Office (CCHDO). Data for sections AR07W 2014 (55°N) and AR07E 2014 (58°N) were recovered from the British Oceanographic Data Centre (BODC) with measurement values for A_T and C_T. Variables not provided by these datasets were filled with the Bayesian neural network CANYON-B (Bittig et al., 2018), solving for nutrient concentrations (nitrate, silicate and phosphate), A_T and C_T using temperature, salinity, oxygen concentration, and geolocation data. Table 4.1 summarizes this information.

Biogeochemical samples naturally underrepresent the water column, typically with a maxi-

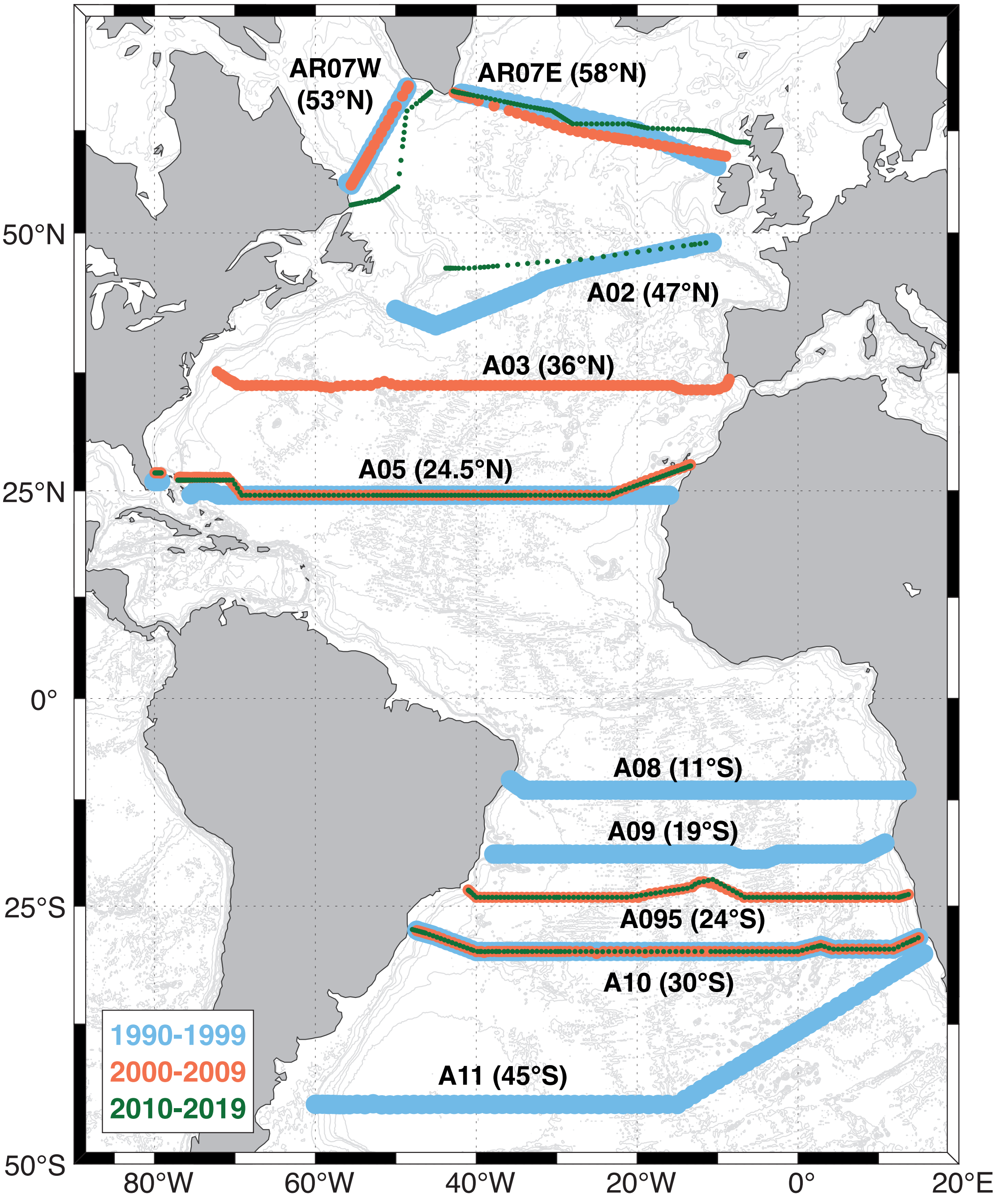

Figure 4.1. Map of the zonal sections included in each decade for the inverse model. Each section is accompanied by its world ocean circulation experiment name and its nominal latitude (between parenthesis), and the colours represent each decade, blue for 1990–99, orange for 2000–09, and green for 2010–19. Three sections have been repeated in every decade (A10 – 30°S, A05 – 24.5°N, AR07W and AR07E – 55°N).

Table 4.1. Summary of the sections used in each model and the dataset from which they were recovered.

Latitude	Section	Year	Code	Dataset	NCEI DOI	References
45°S	A11	1992	74DI19921222	GLODAPv2	10.3334/cdiac/otg.woce_a11_74di19921222	
30°S	A10	1992-93	06MT19921227	GLODAPv2	10.3334/CDIAC/otg.ndp066	Johnson et al. (1998)
19°S	A09	1991	06MT19910210	GLODAPv2	10.3334/CDIAC/otg.ndp051	Johnson et al. (1995)
11°S	A08	1994	06MT19940329	GLODAPv2	10.3334/CDIAC/otg.ndp079	Johnson et al. (2002)
24.5°N	A05	1992	29HE19920714	GLODAPv2	10.3334/CDIAC/otg.ndp074	Millero et al. (2000)
24.5°N	Florida	1992	29HE19920714	GLODAPv2	10.3334/CDIAC/otg.ndp074	Millero et al. (2000)
47°N	A02	1993	06GA19930612	CCHDO		
55°N	AR07W	1990	18DA90012	CCHDO		
55°N	AR07E	1991	74AB62	CCHDO		
30°S	A10	2003	49NZ20031106	GLODAPv2	10.25921/gjsx-gy37	Uchida et al. (2005)
24°S	A095	2009	740H20090307	GLODAPv2	10.3334/cdiac/otg.clivar_a9.5_2009	Schuster et al. (2014)
24.5°N	A05	2004	74DI20040404	GLODAPv2	10.3334/cdiac/otg.carina_74di20040404	Cunningham (2005)
24.5°N	Florida	2004	74DI20040404	GLODAPv2	10.3334/cdiac/otg.carina_74di20040404	Cunningham (2005)
36°N	A03	2005	74AB20050501	GLODAPv2	10.3334/cdiac/otg.carina_74ab20050501	McDonagh (2007)
55°N	AR07W	2005	18HU20050526	GLODAPv2	10.3334/cdiac/otg.woce_ar07w_2005	
55°N	AR07E	2007	64PE20070830	GLODAPv2	10.3334/cdiac/otg.clivar_ar07e_2007	
30°S	A10	2011	33RO20110926	GLODAPv2	10.3334/cdiac/otg.clivar_a10_2011	
24°S	A095	2018	740H20180228	GLODAPv2	10.25921/xy1r-rx06	
24.5°N	A05	2011	29AH20110128	GLODAPv2	10.3334/cdiac/otg.clivar_a05_29ah20110128	
24.5°N	Florida	2011	29AH20110128	GLODAPv2	10.3334/cdiac/otg.clivar_a05_29ah20110128	
47°N	A02	2013	06M220130509	GLODAPv2	10.25921/43nw-j564	
55°N	AR07W	2014	74JC20140606	BODC		
55°N	AR07E	2014	74JC20140606	BODC		

mum of 24 samples in the water column. We have interpolated all the available biogeochemical parameters every 2 dbar (to mirror the resolution of the hydrographic CTD casts) for each station using a 2D linear interpolation on scattered data employing a Delaunay triangulation, with a nearest extrapolation method. We have interpolated in a neutral density (γ^{n}) framework, with the computed values of γ^{n} for each 2 dbar, allowing to interpolate along the interphase of the water masses and distributing the deeper values more evenly.

4.2.2 Inverse model

The initial geostrophic estimation of mass transport for each station pair is computed assuming a null velocity at a reference level. But this level of no motion, chosen as the interphase of water masses flowing in opposite directions, has a velocity different from zero. Inverse models can solve for these velocities at the reference level for each station pair, applying constraints and uncertainties, mainly related to mass conservation (Ganachaud & Wunsch, 2000; Hernández-Guerra et al., 2019; Wunsch, 1996). Caínzos et al. (2022a) constructed three inverse models, one for each of the last decades, imposing mass conservation for each box between adjacent sections, and for each single section, mass and salinity content were conserved, on top of regional constraints of independent measurements and topographic features.

Building on their methodology, we have constructed three similar inverse models combining the sections for each decade, in which we have included constraints for the conservation of oxygen, nitrate, silicate and phosphate (Fontela et al., 2019; Maze et al., 2012). For each of these biogeochemical variables, we have applied a balance for each layer of neutral density between adjacent sections. Since these are not conservative variables and there are sources and sinks at play, we have included an input of oxygen from the atmosphere in the first layer and a consumption rate of oxygen for each layer of the water column. Therefore, using these initial estimates, the method allows for an adjustment on both the oxygen production in the surface layers and its consumption along the water column. For nitrate, phosphate and silicate, we have applied the Redfield ratio used previously in similar studies (-150 O_2 : 16 N : 1 P : 16 Si; Anderson 1995; Maze et al. 2012) to the consumption rate of oxygen for each layer of the water column.

The estimates of O_2 surface flux are computed as the average from five different Earth System Models (CESM, CCSM, MOM4, NEMO-Control and NEMO-WSTIR) and a semi-empirical dataset based on indirect observations (Morgan, 2021). For each box between two sections, we have obtained an oxygen flux for the whole area.

The concentration of dissolved oxygen and nutrients changes in the water column, affected not only by the pattern of circulation but also due to biogeochemical processes. Therefore, we have included a term to integrate the changes in tracer concentrations in time in each layer of the water column. We have used as a priori estimates the rates of oxygen consumption obtained by Stendardo & Gruber (2012) that are compatible with the model outputs from NorESMO1C and then applied the Redfield ratio to obtain the sinks and sources of nitrate, silicate and phosphate.

The combination of all these equations conforms an underdetermined system, which can be solved using the Gauss-Markov estimator. Inverse models solve the equation $\mathrm{Ax} = -\mathrm{Y}$, where A is a matrix of mass and property concentrations with size M (number of layers) by N (number of unknowns), x is a column vector of length N that contains the unknowns of the system (i.e., velocities at the reference level, Ekman transport adjustment, biogeochemical budget adjustments, …), and Y is a column vector of length M containing the initial unbalanced transports of mass and properties for each equation defined in A. This equation can be expressed in its matrix form as shown below. The matrix is a representation for a single box between two contiguous sections. Each property being conserved is represented with different colors. In this case, n is the number of pair of stations for section A; m is the number of pair of stations for section B; q is the number of layers. In the below matrix, e stands for mass and y for mass transport; s for salt and z for salt transport; f stands for oxygen and k for oxygen transport; g for nitrate and r for nitrate transport; h for silicate and t for silicate transport and, finally, j stands for phosphate and u for phosphate transport.

For each single section, we applied regional constraints to mass ($_{\mathrm{reg}}$) and, in addition to mass, we have also constraint the salinity content of each single section A and B. Using this tracer instead of mass allows for changes in freshwater across the section while still conserving mass. For each box, the net transport of mass, oxygen, nitrate, silicate and phosphate is conserved.

$$\begin{pmatrix}
e_{A_{t,1}} & \cdots & e_{A_{t,n}} & e_{B_{t,1}} & \cdots & e_{B_{t,m}} & 1 & 1 & 0 & 0 & 0 & \cdots & 0 & 0 \\
e_{A_{reg}} & \cdots & e_{A_{reg}} & 0 & \cdots & 0 & 0 & 0 & 0 & 0 & 0 & \cdots & 0 & 0 \\
0 & \cdots & 0 & e_{B_{reg}} & \cdots & e_{B_{reg}} & 0 & 0 & 0 & 0 & 0 & \cdots & 0 & 0 \\
e_{A_{1,1}} & \cdots & e_{A_{1,n}} & e_{B_{1,1}} & \cdots & e_{B_{1,m}} & 1 & 1 & 0 & 0 & 0 & \cdots & 0 & 0 \\
e_{A_{2,1}} & \cdots & e_{A_{2,n}} & e_{B_{2,1}} & \cdots & e_{B_{2,m}} & 0 & 0 & 0 & 0 & 0 & \cdots & 0 & 0 \\
\vdots & \ddots & \vdots & \vdots & \ddots & \vdots & \vdots & \vdots & \vdots & \vdots & \vdots & \ddots & \vdots & \vdots \\
e_{A_{q-1,1}} & \cdots & e_{A_{q-1,n}} & e_{B_{q-1,1}} & \cdots & e_{B_{q-1,m}} & 0 & 0 & 0 & 0 & 0 & \cdots & 0 & 0 \\
e_{A_{q,1}} & \cdots & e_{A_{q,n}} & e_{B_{q,1}} & \cdots & e_{B_{q,m}} & 0 & 0 & 0 & 0 & 0 & \cdots & 0 & 0 \\
s_{A_{t,1}} & \cdots & s_{A_{t,n}} & 0 & \cdots & 0 & \overline{\left(\frac{s_{A_1}}{e_{A_1}}\right)} & 0 & 0 & 0 & 0 & \cdots & 0 & 0 \\
0 & \cdots & 0 & s_{B_{t,1}} & \cdots & s_{B_{t,m}} & 0 & \overline{\left(\frac{s_{B_1}}{e_{B_1}}\right)} & 0 & 0 & 0 & \cdots & 0 & 0 \\
f_{A_{1,1}} & \cdots & f_{A_{1,n}} & f_{B_{1,1}} & \cdots & f_{B_{1,m}} & \overline{\left(\frac{f_{A_1}}{e_{A_1}}\right)} & \overline{\left(\frac{f_{B_1}}{e_{B_1}}\right)} & 1 & 1 & 0 & \cdots & 0 & 0 \\
f_{A_{2,1}} & \cdots & f_{A_{2,n}} & f_{B_{2,1}} & \cdots & f_{B_{2,m}} & 0 & 0 & 0 & 0 & 1 & \cdots & 0 & 0 \\
\vdots & \ddots & \vdots & \vdots & \ddots & \vdots & \vdots & \vdots & \vdots & \vdots & \vdots & \ddots & \vdots & \vdots \\
f_{A_{q-1,1}} & \cdots & f_{A_{q-1,n}} & f_{B_{q-1,1}} & \cdots & f_{B_{q-1,m}} & 0 & 0 & 0 & 0 & 0 & \cdots & 1 & 0 \\
f_{A_{q,1}} & \cdots & f_{A_{q,n}} & f_{B_{q,1}} & \cdots & f_{B_{q,m}} & 0 & 0 & 0 & 0 & 0 & \cdots & 0 & 1 \\
g_{A_{1,1}} & \cdots & g_{A_{1,n}} & g_{B_{1,1}} & \cdots & g_{B_{1,m}} & \overline{\left(\frac{g_{A_1}}{e_{A_1}}\right)} & \overline{\left(\frac{g_{B_1}}{e_{B_1}}\right)} & 0 & r_{NO} & 0 & \cdots & 0 & 0 \\
g_{A_{2,1}} & \cdots & g_{A_{2,n}} & g_{B_{2,1}} & \cdots & g_{B_{2,m}} & 0 & 0 & 0 & 0 & r_{NO} & \cdots & 0 & 0 \\
\vdots & \ddots & \vdots & \vdots & \ddots & \vdots & \vdots & \vdots & \vdots & \vdots & \vdots & \ddots & \vdots & \vdots \\
g_{A_{q-1,1}} & \cdots & g_{A_{q-1,n}} & g_{B_{q-1,1}} & \cdots & g_{B_{q-1,m}} & 0 & 0 & 0 & 0 & 0 & \cdots & r_{NO} & 0 \\
g_{A_{q,1}} & \cdots & g_{A_{q,n}} & g_{B_{q,1}} & \cdots & g_{B_{q,m}} & 0 & 0 & 0 & 0 & 0 & \cdots & 0 & r_{NO} \\
h_{A_{1,1}} & \cdots & h_{A_{1,n}} & h_{B_{1,1}} & \cdots & h_{B_{1,m}} & \overline{\left(\frac{h_{A_1}}{e_{A_1}}\right)} & \overline{\left(\frac{h_{B_1}}{e_{B_1}}\right)} & 0 & r_{SiO} & 0 & \cdots & 0 & 0 \\
h_{A_{2,1}} & \cdots & h_{A_{2,n}} & h_{B_{2,1}} & \cdots & h_{B_{2,m}} & 0 & 0 & 0 & 0 & r_{SiO} & \cdots & 0 & 0 \\
\vdots & \ddots & \vdots & \vdots & \ddots & \vdots & \vdots & \vdots & \vdots & \vdots & \vdots & \ddots & \vdots & \vdots \\
h_{A_{q-1,1}} & \cdots & h_{A_{q-1,n}} & h_{B_{q-1,1}} & \cdots & h_{B_{q-1,m}} & 0 & 0 & 0 & 0 & 0 & \cdots & r_{SiO} & 0 \\
h_{A_{q,1}} & \cdots & h_{A_{q,n}} & h_{B_{q,1}} & \cdots & h_{B_{q,m}} & 0 & 0 & 0 & 0 & 0 & \cdots & 0 & r_{SiO} \\
j_{A_{1,1}} & \cdots & j_{A_{1,n}} & j_{B_{1,1}} & \cdots & j_{B_{1,m}} & \overline{\left(\frac{j_{A_1}}{e_{A_1}}\right)} & \overline{\left(\frac{j_{B_1}}{e_{B_1}}\right)} & 0 & r_{PO} & 0 & \cdots & 0 & 0 \\
j_{A_{2,1}} & \cdots & j_{A_{2,n}} & j_{B_{2,1}} & \cdots & j_{B_{2,m}} & 0 & 0 & 0 & 0 & r_{PO} & \cdots & 0 & 0 \\
\vdots & \ddots & \vdots & \vdots & \ddots & \vdots & \vdots & \vdots & \vdots & \vdots & \vdots & \ddots & \vdots & \vdots \\
j_{A_{q-1,1}} & \cdots & j_{A_{q-1,n}} & j_{B_{q-1,1}} & \cdots & j_{B_{q-1,m}} & 0 & 0 & 0 & 0 & 0 & \cdots & r_{PO} & 0 \\
j_{A_{q,1}} & \cdots & j_{A_{q,n}} & j_{B_{q,1}} & \cdots & j_{B_{q,m}} & 0 & 0 & 0 & 0 & 0 & \cdots & 0 & r_{PO}
\end{pmatrix}$$

$$\begin{pmatrix} b_{A_1} \\ \vdots \\ b_{B_n} \\ b_{B_1} \\ \vdots \\ b_{B_m} \\ \Delta T_{A_{Ek}} \\ \Delta T_{B_{Ek}} \\ \Delta F_{a-s} \\ \Delta B_{O_{21}} \\ \Delta B_{O_{22}} \\ \vdots \\ \Delta B_{O_{2_{q-1}}} \\ \Delta B_{O_{2_q}} \end{pmatrix} = \begin{pmatrix} y_{A_t} + y_{B_t} + T_{A_{Ek}} + T_{B_{Ek}} \\ y_{A_{reg}} \\ y_{B_{reg}} \\ y_{A_1} + y_{B_1} + T_{A_{Ek}} + T_{B_{Ek}} \\ y_{A_2} + y_{B_2} \\ \vdots \\ y_{A_{q-1}} + y_{B_{q-1}} \\ y_{A_q} + y_{B_q} \\ z_{A_t} + T_{A_{Ek}} \overline{\left(\frac{S_{A_1}}{e_{A_1}}\right)} \\ z_{B_t} + T_{B_{Ek}} \overline{\left(\frac{S_{B_1}}{e_{B_1}}\right)} \\ k_{A_1} + k_{B_1} + T_{A_{Ek}} \overline{\left(\frac{f_{A_1}}{e_{A_1}}\right)} + T_{B_{Ek}} \overline{\left(\frac{f_{B_1}}{e_{B_1}}\right)} + F_{a-s} + B_{O_{21}} \\ k_{A_2} + k_{B_2} + B_{O_{22}} \\ \vdots \\ k_{A_{q-1}} + k_{B_{q-1}} + B_{O_{2_{q-1}}} \\ k_{A_q} + k_{B_q} + B_{O_{2_q}} \\ r_{A_1} + r_{B_1} + T_{A_{Ek}} \overline{\left(\frac{g_{A_1}}{e_{A_1}}\right)} + T_{B_{Ek}} \overline{\left(\frac{g_{B_1}}{e_{B_1}}\right)} + B_{O_{21}} \cdot r_{NO} \\ r_{A_2} + r_{B_2} + B_{O_{22}} \cdot r_{NO} \\ \vdots \\ r_{A_{q-1}} + r_{B_{q-1}} + B_{O_{2_{q-1}}} \cdot r_{NO} \\ r_{A_q} + r_{B_q} + B_{O_{2_q}} \cdot r_{NO} \\ t_{A_1} + t_{B_1} + T_{A_{Ek}} \overline{\left(\frac{h_{A_1}}{e_{A_1}}\right)} + T_{B_{Ek}} \overline{\left(\frac{h_{B_1}}{e_{B_1}}\right)} + B_{O_{21}} \cdot r_{SiO} \\ t_{A_2} + t_{B_2} + B_{O_{22}} \cdot r_{SiO} \\ \vdots \\ t_{A_{q-1}} + t_{B_{q-1}} + B_{O_{2_{q-1}}} \cdot r_{SiO} \\ t_{A_q} + t_{B_q} + B_{O_{2_q}} \cdot r_{SiO} \\ u_{A_1} + u_{B_1} + T_{A_{Ek}} \overline{\left(\frac{j_{A_1}}{e_{A_1}}\right)} + T_{B_{Ek}} \overline{\left(\frac{j_{B_1}}{e_{B_1}}\right)} + B_{O_{21}} \cdot r_{PO} \\ u_{A_2} + u_{B_2} + B_{O_{22}} \cdot r_{PO} \\ \vdots \\ u_{A_{q-1}} + u_{B_{q-1}} + B_{O_{2_{q-1}}} \cdot r_{PO} \\ u_{A_q} + u_{B_q} + B_{O_{2_q}} \cdot r_{PO} \end{pmatrix}$$

The inverse solutions provide the velocities at the reference level (b) for each pair station of each section. Ekman transport ($\mathrm{T_{Ek}}$) is applied for the equations of all properties balancing the net transport among both sections and the transport across the first layer of a single section. Its adjustment ($\Delta\mathrm{T_{Ek}}$) is part of the unknowns solved for each section. The oxygen influx from the air-sea interphase is included in the first layer of oxygen conservation ($\mathrm{F_{a-s}}$), and its adjustment included as part of the solutions ($\Delta\mathrm{F_{a-s}}$). To allow changes in the water column due to the non-conservative sources and sinks of oxygen we have added the term $\mathrm{B_{O_2}}$, that reflects the changes in oxygen in the water column and estimated its adjustment $\Delta\mathrm{B_{O_2}}$. We have associated changes in oxygen with those for nitrate, silicate and phosphate with the Redfield ratio ($\mathrm{r_{NO}}$, $\mathrm{r_{SiO}}$ and $\mathrm{r_{PO}}$ for nitrate, silicate and phosphate, respectively).

This method provides an estimate from all the possible solutions of the system that minimizes the error with the real value using the initial and noise information. It also gives a measure of the uncertainties for the solution and the noise (Wunsch, 1996). The Gauss-Markov method solves this system of equations with a minimum error variance solution from the initial estimates of the unknowns (the velocities at the reference level, b, the corrections to the Ekman transport, $\Delta\mathrm{T_{Ek}}$, the input of O_2 from the atmosphere, $\mathrm{F_{a-s}}$, and the rate of oxygen consumption along the water column, $\mathrm{B_{O_2}}$; Wunsch 1996).

To solve it, we first need a priori estimates and uncertainties that give an initial approximation to the actual value. The preliminary variance of the adjusted velocity at the reference level is 8 cm^2 s^{-2} for the station pairs closer to coast, where shear is stronger and 4 cm^2 s^{-2} in the deepest stations. The initial estimates for the mass transport are 9 Sv^2 for the net mass transport between two sections, therefore allowing for compensation within each box. The a priori biogeochemical imbalances for each box are zero, with a priori uncertainties of (500 kmol $s^{-1})^2$ for oxygen, (100 kmol $s^{-1})^2$ for nitrate and silicate, and (10 kmol kmol $s^{-1})^2$ for phosphate.

For layer conservation, the variance is between 13 and 1 Sv^2, decreasing towards deeper layers. The salinity uncertainties are computed as the square of the uncertainty of the Bering Strait transport (0.6 Sv) times the square of the ration between the total salt transport and the mass transport of each section.

Despite obtaining similar results, this study provides smaller uncertainties than other global inverse solutions (Ganachaud, 2003a) and decadal studies (Fu et al., 2020). This was achieved by using physical constraints with a simpler model with only the velocities at the reference level and the Ekman adjustments as unknowns. Moreover, adding the biogeochemical equations has helped reduced these uncertainties by incorporating more information to the matrix without increasing its rank.

The storage rates provided by (Gruber et al., 2019) are computed between 1994 and 2007. Therefore, the increase rate of 1.9% per decade is valid for this period. We have extended this rate also for the last decade, assuming a tendency in storing more C_{anth} into the ocean interior. However, recent studies are challenging this assumption, finding for the 2004-2014 decreasing rates in the storage of C_{anth} in the North Atlantic (Müller et al., 2022). To accommodate these discrepancies, we have decided to increase the uncertainties associated to the storage rates of C_{anth} for the last decade, without surpassing 15% of the mean value.

Sensitivity tests were also carried out to determine the effect of different parameters in the configuration of the inverse model and the concentration of C_{anth} at the surface. The physical constraints in the model have been assessed previously by (Caínzos et al., 2022a), where the initial physical-only configuration of the model is described.

For that model, several sensitivity tests were conducted to determine the best configuration of the inverse models. The tightness of the constraints on regional and topographic features

Table 4.2. Net values for each section of different parameters for different configurations of the inverse model for 1990-99 and the values before the adjustments of the inverse model (initial). The inverse solution applying only mass and salt conservation is noted as IM phys, and IM bgq represents the inverse solution with the added biogeochemical constraints. Positive values of MT (mass transport, in Sv), OHC (ocean heat content, in PW) and FW (freshwater flux, in Sv) indicate a northward transport, with negative values for a southward transport. For each variable, the 'TRedf' label indicates a sensitivity tests with a 20% variation of the values of the original Redfield ratio using a 100 repetition Montecarlo experiment. The values indicate the mean of the magnitude and the mean of the uncertainty, whereas the values within parenthesis indicate the standard deviation of the mean and uncertainty, multiplied by 10^3. The 'near int' and 'prs int' labels indicate sensitivity tests to compare the results after using different interpolation methods: the former by using a nearest interpolation method instead of linear, and the latter by replacing the neutral density framework by pressure.

	A11	A10	A09	A08	A05	A02	A07
	55°S	30°S	19°S	11°S	24.5°N	47°N	55°N
MT initial	10.2	25.0	43.9	13.1	16.3	6.1	6.7
MT IM phys	-0.8 ± 3.5	-0.5 ± 2.7	-0.8 ± 2.7	-1.2 ± 2.5	-1.0 ± 2.6	-0.9 ± 2.8	-0.9 ± 3.5
MT IM bgq	-0.8 ± 2.7	-0.6 ± 2.3	-0.7 ± 2.2	-1.1 ± 2.1	-0.9 ± 2.1	-0.9 ± 2.4	-1.0 ± 2.6
MT TRedf	-0.8 ± 2.7	-0.6 ± 2.3	-0.7 ± 2.2	-1.1 ± 2.1	-0.9 ± 2.1	-1.0 ± 2.4	-1.0 ± 2.6
	(1.54 ± 0.07)	(2.34 ± 0.03)	(0.63 ± 0.09)	(2.08 ± 0.26)	(2.54 ± 0.19)	(1.89 ± 0.34)	(0.02 ± 0.32)
MT near int	-0.8 ± 2.6	-0.5 ± 2.3	-0.8 ± 2.0	-1.1 ± 2.3	-1.0 ± 2.4	-0.9 ± 2.6	-1.0 ± 3.2
MT prs int	-0.6 ± 2.4	-0.5 ± 2.2	-0.7 ± 2.4	-1.2 ± 2.3	-0.9 ± 2.4	-0.9 ± 2.5	-0.9 ± 2.6
OHC initial	0.74	0.90	2.00	1.73	1.63	0.77	0.40
OHC IM phys	0.58 ± 0.08	0.36 ± 0.06	0.78 ± 0.07	0.93 ± 0.05	1.30 ± 0.08	0.48 ± 0.10	0.25 ± 0.09
OHC IM bgq	0.52 ± 0.07	0.35 ± 0.05	0.74 ± 0.05	0.94 ± 0.05	1.18 ± 0.07	0.41 ± 0.08	0.20 ± 0.07
OHC TRedf	0.53 ± 0.07	0.35 ± 0.05	0.74 ± 0.05	0.94 ± 0.05	1.18 ± 0.07	0.42 ± 0.08	0.21 ± 0.07
	(0.411 ± 0.001)	(0.144 ± 0.001)	(0.187 ± 0.007)	(0.441 ± 0.010)	(0.671 ± 0.042)	(0.397 ± 0.007)	(0.295 ± 0.006)
OHC near int	0.52 ± 0.07	0.38 ± 0.05	0.71 ± 0.06	0.95 ± 0.05	1.20 ± 0.08	0.44 ± 0.09	0.21 ± 0.07
OHC prs int	0.42 ± 0.07	0.32 ± 0.05	0.74 ± 0.06	0.94 ± 0.05	1.16 ± 0.07	0.42 ± 0.08	0.21 ± 0.07
FW initial	-0.85	-1.36	-3.29	-1.64	-1.34	-0.73	-0.65
FW IM phys	-0.09 ± 0.08	0.28 ± 0.08	-0.12 ± 0.07	-0.34 ± 0.07	-0.34 ± 0.09	-0.14 ± 0.11	-0.05 ± 0.07
FW IM bgq	-0.03 ± 0.07	0.27 ± 0.07	-0.10 ± 0.06	-0.36 ± 0.07	-0.25 ± 0.07	-0.07 ± 0.09	-0.02 ± 0.07
FW TRedf	-0.03 ± 0.07	0.27 ± 0.07	-0.10 ± 0.06	-0.36 ± 0.07	-0.26 ± 0.07	-0.08 ± 0.09	-0.01 ± 0.07
	(0.289 ± 0.002)	(0.120 ± 0.001)	(0.191 ± 0.004)	(0.032 ± 0.012)	(0.045 ± 0.050)	(0.213 ± 0.007)	(0.177 ± 0.001)
FW near int	-0.03 ± 0.07	0.27 ± 0.07	-0.06 ± 0.06	-0.35 ± 0.07	-0.27 ± 0.08	-0.10 ± 0.10	-0.01 ± 0.07
FW near int	0.01 ± 0.07	0.28 ± 0.07	-0.08 ± 0.07	-0.35 ± 0.07	-0.25 ± 0.08	-0.08 ± 0.09	-0.01 ± 0.07

Table 4.3. Same as Table 4.2 but for the 2000-2009 period.

	A10 30°S	A095 24°S	A05 24.5°N	A03 36°N	A07 55°N
MT initial	18.0	39.3	19.1	31.3	-6.4
MT IM phys	-0.6 ± 3.1	-0.6 ± 3.1	-1.1 ± 2.8	-0.7 ± 2.8	-1.0 ± 3.0
MT IM bgq	-0.6 ± 2.7	-0.6 ± 2.5	-1.0 ± 2.3	-0.6 ± 2.4	-1.1 ± 2.5
MT TRedf	-0.6 ± 2.7	-0.6 ± 2.5	-1.0 ± 2.3	-0.6 ± 2.4	-1.1 ± 2.5
	(1.07 ± 0.15)	(5.09 ± 0.36)	(2.68 ± 0.10)	(1.52 ± 0.05)	(0.21 ± 0.13)
MT near int	-0.6 ± 2.7	-0.7 ± 2.5	-1.0 ± 2.3	-0.6 ± 2.4	-1.0 ± 2.5
MT prs int	-0.6 ± 2.9	-0.6 ± 2.8	-1.1 ± 2.6	-0.6 ± 2.5	-1.0 ± 2.5
OHC initial	0.77	1.74	1.13	1.57	0.20
OHC IM phys	0.41 ± 0.06	0.70 ± 0.08	0.97 ± 0.09	0.59 ± 0.12	0.28 ± 0.07
OHC IM bgq	0.43 ± 0.05	0.67 ± 0.06	0.99 ± 0.08	0.53 ± 0.10	0.26 ± 0.06
OHC TRedf	0.43 ± 0.05	0.67 ± 0.06	0.98 ± 0.08	0.53 ± 0.10	0.26 ± 0.06
	(0.338 ± 0.003)	(1.956 ± 0.060)	(0.367 ± 0.031)	(0.315 ± 0.003)	(0.219 ± 0.005)
OHC near int	0.42 ± 0.06	0.72 ± 0.07	0.93 ± 0.08	0.60 ± 0.11	0.21 ± 0.07
OHC prs int	0.43 ± 0.06	0.73 ± 0.06	0.97 ± 0.08	0.54 ± 0.10	0.25 ± 0.06
FW initial	-1.04	-2.76	-1.31	-2.29	0.33
FW IM phys	0.19 ± 0.07	-0.01 ± 0.11	-0.24 ± 0.07	-0.05 ± 0.07	-0.08 ± 0.16
FW IM bgq	0.19 ± 0.07	-0.01 ± 0.08	-0.25 ± 0.06	-0.02 ± 0.06	-0.05 ± 0.13
FW TRedf	0.19 ± 0.07	-0.01 ± 0.08	-0.25 ± 0.06	0.02 ± 0.06	-0.05 ± 0.13
	(0.277 ± 0.003)	(1.844 ± 0.088)	(0.062 ± 0.013)	(0.178 ± 0.002)	(0.167 ± 0.010)
FW near int	0.20 ± 0.07	-0.05 ± 0.09	-0.22 ± 0.06	-0.09 ± 0.07	-0.03 ± 0.13
FW prs int	0.19 ± 0.07	-0.05 ± 0.07	-0.23 ± 0.06	-0.04 ± 0.06	-0.05 ± 0.13

of the Southern Hemisphere were assessed by removing the constraints on section A10 (30°S). The boundary currents display some differences, but it has not been transmitted to the net heat and freshwater budget, which remain the same, and has not altered the values of the freshwater overturning. Changing the average salinity of the Bering Strait from 31.5 to 33.5 (Woodgate & Aagaard, 2005) and the Bering Strait transport for the last two decades from -0.8 ± 0.6 to -1.0 ± 0.5 Sv (Woodgate, 2018), only the throughflow component of the freshwater was affected, but not the overturning and horizontal components.

The methodology of interpolation of biogeochemical data in the water column is a very important step in the computation of concentration and transports for each section. The selected methodology has been compared against several other methods before choosing the linear interpolation in a neutral density framework with a nearest neighbour extrapolation every 2 dbar. Linear interpolation avoids data appearing in a stair-like manner and nearest extrapolation prevents extreme values from appearing at the surface and bottom. Using a neutral density framework helps redistribute the importance of surface and deep layers in the water column, adjusting the levels by its density than rather just by its position in the water column, which

Table 4.4. Same as Table 4.2 but for the 2010-2019 period.

	A10	A095	A05	A02	A07
	30°S	24°S	24.5°N	47°N	55°N
MT initial	25.22	30.5	25.8	2.9	2.4
MT IM phys	-0.7 ± 3.3	-0.8 ± 3.1	-1.0 ± 2.9	-0.9 ± 2.6	-0.9 ± 2.6
MT IM bgq	-0.7 ± 2.7	-1.1 ± 2.5	-0.9 ± 2.3	-0.9 ± 2.2	-1.0 ± 2.1
MT TRedf	-0.7 ± 2.7	-1.1 ± 2.5	-0.9 ± 2.3	-0.9 ± 2.2	-1.0 ± 2.1
	(1.25 ± 0.13)	(11.18 ± 0.29)	(4.72 ± 0.10)	(1.73 ± 0.35)	(0.06 ± 0.26)
MT near int	-0.7 ± 3.1	-1.1 ± 2.9	-1.0 ± 2.7	-1.0 ± 2.4	-0.9 ± 2.2
MT prs int	-0.8 ± 3.1	-1.2 ± 2.8	-1.0 ± 2.6	-0.9 ± 2.3	-0.9 ± 2.1
OHC initial	0.99	1.36	1.34	0.69	0.33
OHC IM phys	0.52 ± 0.07	0.66 ± 0.07	1.13 ± 0.07	0.40 ± 0.08	0.29 ± 0.06
OHC IM bgq	0.63 ± 0.07	0.64 ± 0.06	1.15 ± 0.06	0.33 ± 0.07	0.27 ± 0.05
OHC TRedf	0.63 ± 0.07	0.64 ± 0.06	1.15 ± 0.06	0.33 ± 0.07	0.27 ± 0.05
	(0.846 ± 0.001)	(1.639 ± 0.068)	(0.427 ± 0.030)	(0.281 ± 0.009)	(0.154 ± 0.006)
OHC near int	0.67 ± 0.07	0.66 ± 0.06	1.16 ± 0.06	0.34 ± 0.07	0.26 ± 0.06
OHC prs int	0.62 ± 0.07	0.66 ± 0.06	1.17 ± 0.06	0.33 ± 0.07	0.26 ± 0.05
FW initial	-1.58	-2.11	-1.72	-0.44	-0.35
FW IM phys	0.07 ± 0.06	0.01 ± 0.09	-0.34 ± 0.03	-0.05 ± 0.13	-0.11 ± 0.13
FW IM bgq	0.01 ± 0.06	0.05 ± 0.07	-0.37 ± 0.03	-0.01 ± 0.11	-0.08 ± 0.12
FW TRedf	0.01 ± 0.06	0.05 ± 0.07	-0.37 ± 0.03	-0.01 ± 0.11	-0.08 ± 0.12
	(0.605 ± 0.001)	(1.552 ± 0.108)	(0.277 ± 0.029)	(0.117 ± 0.016)	(0.059 ± 0.005)
FW near int	-0.02 ± 0.06	0.02 ± 0.08	-0.38 ± 0.03	-0.01 ± 0.12	-0.08 ± 0.12
FW prs int	0.01 ± 0.06	0.03 ± 0.08	-0.38 ± 0.03	-0.01 ± 0.11	-0.08 ± 0.12

would naturally underrepresent the upper layers. For comparison, we have included results for two different set of interpolation methods: the first one uses a nearest interpolation method instead of linear, and the second one replaces the neutral density framework for a pressure framework. The resulting values are included in Tables 4.2, 4.3, 4.4, 4.5, 4.6 and 4.7 under the names ‘near int’ and ‘prs int’, respectively. As could be expected, the physical parameters in Tables 4.2, 4.3 and 4.4 show non-significant variations in either mass, heat or freshwater transports (with differences of $\sim$0.1 Sv, $\sim$0.03 PW and 0.03 Sv, respectively) for both interpolation tests. However, we can see differences for each box in the balance of oxygen, nutrients and C_T (Tables 4.5, 4.6 and 4.7). Nearest interpolation imposes large changes in the balance for each box, with a mean of 1100% change for oxygen, 665% for nitrate, 165% for silicate, 504% for phosphate and 8700% for total carbon. These values reduce for the interpolation in a pressure vertical framework, with changes of 378% for oxygen, 548% for nitrate, 103% for silicate, 263% for phosphate and 94% for total carbon.

The Redfield ratio chosen is consistent with a similar study from Maze et al. (2012), that uses the Redfield ratio reported by Anderson (1995). The inverse models are not very sensible to the

Table 4.5. Net values within each box of different parameters and properties for different configurations of the inverse model for 1990-99 and the values before the adjustments of the inverse model (initial). The inverse solution applying only mass and salt conservation is noted as IM phys, and IM bgq represents the inverse solution with the added biogeochemical constraints. Positive values of air-sea O_2 fluxes (FO_2; in kmol s^{-1}) indicate an oceanic gain of O_2 within the box, with negative values expressing a loss of O_2 to the atmosphere within the box of contiguous sections. The consumption rate of O_2 in the whole water column for each box (BO_2; in kmol s^{-1}) is positive for oxygen production and negative for oxygen consumption. The net transport of oxygen (kmol s^{-1}), nitrate (kmol s^{-1}), silicate (kmol s^{-1}), phosphate (kmol s^{-1}) and total carbon (PgC yr^{-1}) is computed as the balance among the transports at the boundaries of the box, integrated vertically. For each variable, the TRedf label indicates a sensitivity test with a 20% variation of the values of the original Redfield ratio using a 100 repetition Montecarlo experiment. The values indicate the mean of the magnitude and the mean of the uncertainty, whereas the values within parenthesis indicate the standard deviation of the mean and uncertainty, multiplied by 10^3. The 'near int' and 'prs int' labels indicate sensitivity tests to compare the results after using different interpolation methods: the former by using a nearest interpolation method instead of linear, and the latter by replacing the neutral density framework by pressure.

	A11-A10 55°S-30°S	A10-A09 30°S-19°S	A09-A08 19°S-11°S	A08-A05 11°S-24.5°N	A05-A02 24.5°N-47°N	A02-A07 47°N-55°N
FO_2 air-sea	259 ± 74	130 ± 39	150 ± 33	479 ± 146	-393 ± 71	-226 ± 105
FO_2 TRedf	284 ± 75	153 ± 40	135 ± 33	558 ± 166	-330 ± 73	-430 ± 119
	(22.45 ± 0.01)	(4.40 ± 0.01)	6.24 ± 0.01)	(227.22 ± 0.58)	(55.13 ± 0.02)	(4.68 ± 0.01)
FO_2 near int	279 ± 75	150 ± 40	133 ± 33	547 ± 166	-327 ± 73	-432 ± 119
FO_2 prs int	284 ± 75	153 ± 40	135 ± 33	531 ± 166	-335 ± 73	-437 ± 119
BO_2	291 ± 117	234 ± 92	170 ± 68	486 ± 265	596 ± 173	89 ± 51
BO_2 TRedf	303 ± 118	233 ± 92	166 ± 68	695 ± 282	466 ± 176	97 ± 51
	(757 ± 206)	(71 ± 63)	(148 ± 29)	(8571 ± 1993)	(4396 ± 594)	(353 ± 45)
BO_2 near int	315 ± 119	226 ± 92	162 ± 68	699 ± 284	467 ± 177	96 ± 51
BO_2 prs int	309 ± 118	228 ± 92	167 ± 68	614 ± 282	461 ± 176	96 ± 51
O_2 initial	-4407	2330	6233	-461	418	796
O_2 IM phys	-1040 ± 1077	-1668 ± 920	100 ± 979	-821 ± 1028	-1822 ± 1072	271 ± 1263
O_2 IM bgq	-967 ± 874	-1608 ± 758	-126 ± 779	-1125 ± 794	-1923 ± 839	174 ± 981
O_2 TRedf	-967 ± 873	-1608 ± 758	-125 ± 779	-1125 ± 794	-1923 ± 839	174 ± 981
	(323 ± 24)	(4381 ± 13)	(1455 ± 56)	(6071 ± 61)	(6601 ± 87)	(97 ± 146)
O_2 near int	-1112 ± 973	585 ± 958	730 ± 996	-1308 ± 1106	-1105 ± 1093	232 ± 1126
O_2 prs int	-1396 ± 817	-455 ± 719	-260 ± 718	-766 ± 721	-801 ± 793	-754 ± 997
NO_3 initial	-378	390	976	374	193	15
NO_3 IM phys	-64 ± 118	64 ± 102	257 ± 101	301 ± 123	2 ± 112	-4 ± 69
NO_3 IM bgq	-9 ± 94	77 ± 84	234 ± 80	294 ± 97	19 ± 89	-16 ± 55
NO_3 TRedf	-9 ± 94	77 ± 84	234 ± 80	294 ± 97	19 ± 89	-16 ± 55
	(661 ± 3)	(796 ± 5)	(2403 ± 14)	(5031 ± 48)	(3232 ± 40)	(118 ± 7)
NO_3 near int	117 ± 113	239 ± 105	91 ± 113	258 ± 142	192 ± 113	-39 ± 82
NO_3 prs int	-85 ± 102	32 ± 200	105 ± 146	61 ± 92	-53 ± 101	-43 ± 90
SiO_4 initial	-839	412	992	-36	77	24
SiO_4 IM phys	-219 ± 344	-145 ± 282	63 ± 243	247 ± 213	-49 ± 160	43 ± 78
SiO_4 IM bgq	-41 ± 245	-72 ± 203	59 ± 181	246 ± 155	-57 ± 116	43 ± 65
SiO_4 TRedf	-41 ± 244	-72 ± 203	59 ± 181	246 ± 154	-57 ± 116	43 ± 65
	(2330 ± 20)	(2532 ± 17)	(3035 ± 23)	(6125 ± 53)	(4232 ± 49)	(16 ± 2)
SiO_4 near int	-90 ± 234	147 ± 197	-82 ± 195	131 ± 192	49 ± 138	29 ± 72
SiO_4 prs int	-48 ± 261	-14 ± 182	29 ± 156	44 ± 154	15 ± 99	-15 ± 83

Continuation from Table 4.5.

	A11-A10 55°S-30°S	A10-A09 30°S-19°S	A09-A08 19°S-11°S	A08-A05 11°S-24.5°N	A05-A02 24.5°N-47°N	A02-A07 47°N-55°N
PO_4 initial	-18.8	28.7	52.6	5.1	9.7	0.4
PO_4 IM phys	-1.5 ± 10.9	2.4 ± 7.8	5.9 ± 6.8	1.8 ± 6.6	-5.3 ± 5.6	-1.0 ± 4.6
PO_4 IM bgq	3.1 ± 9.1	4.2 ± 6.6	4.5 ± 5.4	3.5 ± 5.4	-2.5 ± 4.6	-1.7 ± 3.6
PO_4 TRedf	3.1 ± 9.1	4.2 ± 6.6	4.5 ± 5.4	3.5 ± 5.4	-2.5 ± 4.6	-1.7 ± 3.6
	(54.0 ± 0.3)	(53.2 ± 0.2)	(141.7 ± 0.8)	(239.1 ± 1.0)	(135.8 ± 0.3)	(8.0 ± 0.5)
PO_4 near int	6.4 ± 10.3	9.5 ± 8.2	7.5 ± 9.2	14.5 ± 11.4	9.8 ± 8.3	-3.0 ± 5.4
PO_4 prs int	2.6 ± 9.0	4.1 ± 7.4	0.4 ± 7.1	-3.9 ± 9.1	-2.8 ± 7.1	-3.6 ± 5.2
C_T initial	-11.30	16.85	23.25	0.46	7.56	-0.67
C_T IM phys	1.16 ± 1.29	1.80 ± 0.71	-1.78 ± 0.80	-1.98 ± 0.74	-0.80 ± 0.76	-0.97 ± 0.67
C_T IM bgq	1.25 ± 1.26	1.72 ± 0.70	-1.82 ± 0.80	-2.25 ± 0.73	-0.83 ± 0.76	-0.92 ± 0.67
C_T TRedf	1.25 ± 1.26	1.72 ± 0.70	-1.82 ± 0.80	-2.25 ± 0.73	-0.83 ± 0.76	-0.92 ± 0.67
	(6.41 ± 0.02)	(6.62 ± 0.03)	(6.06 ± 0.05)	(19.27 ± 0.04)	(17.02 ± 0.05)	(1.08 ± 0.09)
C_T near int	9.24 ± 1.21	4.44 ± 0.61	-13.41 ± 0.63	-1.44 ± 0.46	7.98 ± 0.59	-1.40 ± 0.50
C_T prs int	0.29 ± 1.25	0.80 ± 0.68	1.04 ± 0.76	0.24 ± 0.70	-0.08 ± 0.74	0.13 ± 0.66

Redfield ratios applied, as it has been set to modulate the weights of the equations, with larger weight applied to physical constraints.

To try to assess the effect of the choice of Redfield ratio in the results, we have computed some sensitivity tests in the form of a Montecarlo experiment with 100 replicas changing the Redfield ratios randomly within 20% of its mean value. Afterwards, the 100 replicas were averaged, and are presented for comparison in Tables 4.2, 4.3, 4.4 for the physical parameters and Tables 4.5, 4.6, 4.7 for the biogeochemical parameters under the name 'TRedf'. We can see that the physical properties (net mass transport, ocean heat content and freshwater flux) for each section are mostly unchanged, and the variance found after the 100 replicas is quite small (with differences of less than 0.1 Sv of mass transport, less than 0.01 PW for heat transport and 0.01 Sv for the net freshwater flux). The mean variances of the mean value of the Montecarlo test over the Atlantic are 0.003 Sv for mass, 0.0007 PW for heat and 0.0005 Sv for freshwater. The biogeochemical properties applied to the model (oxygen, nitrate, silicate and phosphate) show more variability, with differences with respect to the mean of less than 5%, so that the values after the model are within the uncertainties and they have scarcely influenced the DIC budget. The mean variances for the mean value are 7.4 kmol s^{-1} for oxygen, 2.5 kmol s^{-1} for nitrate, 4.1 kmol s^{-1} for silicate, 0.17 kmol s^{-1} for phosphate and 0.01 kmol s^{-1} for total carbon.

Uncertainties for C_{anth} transports are obtained after the inverse model results, applying the correction in the velocities at the reference level that modify the mass transport. No Carbon species has been constrained in the model, so any changes in the surface layer are not inherently reproduced in the model-derived uncertainties.

We have tried to investigate how different values in the surface would affect the net C_{anth}

Table 4.6. Same as Table 4.5 but for the 2000-2009 period.

	A10-A095	A095-A05	A05-A03	A03-A07
	30°S-24°S	24°S-24.5°N	24.5°N-36°N	36°N-55°N
FO$_2$ air-sea	118 ± 29	671 ± 223	-131 ± 33	-379 ± 239
FO$_2$ TRedf	117 ± 29	670 ± 223	-130 ± 33	-379 ± 239
	(12.80 ± 0.01)	(768.25 ± 10.02)	(10.22 ± 0.01)	(13.41 ± 0.02)
FO$_2$ near int	116 ± 29	576 ± 223	-133 ± 33	-397 ± 239
FO$_2$ prs int	118 ± 29	562 ± 223	-134 ± 33	-374 ± 239
BO$_2$	134 ± 53	958 ± 380	275 ± 108	252 ± 117
BO$_2$ TRedf	134 ± 53	956 ± 379	275 ± 108	251 ± 117
	(89 ± 12)	(3408 ± 4599)	(1342 ± 124)	(2876 ± 344)
BO$_2$ near int	134 ± 53	909 ± 381	266 ± 108	262 ± 118
BO$_2$ prs int	134 ± 53	720 ± 378	273 ± 108	246 ± 117
O$_2$ initial	-4257	-6352	-4032	-7202
O$_2$ IM phys	167 ± 1086	-2644 ± 1070	-1661 ± 1017	1531 ± 1119
O$_2$ IM bgq	-2 ± 887	-2783 ± 851	-1833 ± 821	791 ± 904
O$_2$ TRedf	-4 ± 887	-2832 ± 851	-1878 ± 821	793 ± 904
	(5529 ± 46)	(15890 ± 43)	(8389 ± 23)	(798 ± 65)
O$_2$ near int	-257 ± 1128	-2051 ± 948	412 ± 948	-133 ± 1078
O$_2$ prs int	662 ± 919	-568 ± 852	-547 ± 872	-823 ± 942
NO$_3$ initial	-414	-339	-117	-524
NO$_3$ IM phys	12 ± 116	112 ± 131	-20 ± 115	69 ± 78
NO$_3$ IM bgq	-3 ± 95	99 ± 100	-27 ± 87	20 ± 67
NO$_3$ TRedf	-3 ± 95	98 ± 99	-27 ± 87	19 ± 67
	(2322 ± 25)	(5209 ± 46)	(2792 ± 30)	(417 ± 1)
NO$_3$ near int	-46 ± 143	-254 ± 113	-261 ± 99	64 ± 100
NO$_3$ prs int	-72 ± 80	-67 ± 79	4 ± 97	-10 ± 73
SiO$_4$ initial	-468	-631	195	-299
SiO$_4$ IM phys	103 ± 285	121 ± 246	-114 ± 170	7 ± 90
SiO$_4$ IM bgq	59 ± 218	142 ± 182	-111 ± 128	-23 ± 72
SiO$_4$ TRedf	58 ± 218	142 ± 182	-111 ± 128	-22 ± 72
	(4353 ± 85)	(9102 ± 97)	(3698 ± 30)	(297 ± 3)
SiO$_4$ near int	-81 ± 253	3 ± 196	-190 ± 139	16 ± 105
SiO$_4$ prs int	21 ± 194	19 ± 207	28 ± 164	-3 ± 158
PO$_4$ initial	-24.1	-20.4	-5.7	-30.9
PO$_4$ IM phys	2.0 ± 10.5	8.3 ± 12.0	-2.5 ± 10.2	2.7 ± 6.7
PO$_4$ IM bgq	0.8 ± 8.8	6.5 ± 9.6	-4.4 ± 8.4	0.6 ± 6.0
PO$_4$ TRedf	0.8 ± 8.8	6.5 ± 9.6	-4.2 ± 8.4	0.6 ± 6.0
	(164.9 ± 1.4)	(389.3 ± 2.6)	(223.0 ± 1.9)	(37.0 ± 0.3)
PO$_4$ near int	6.3 ± 11.3	-5.8 ± 9.0	-34.2 ± 7.8	-11.9 ± 8.2
PO$_4$ prs int	2.7 ± 10.5	3.4 ± 10.3	-2.4 ± 9.7	-5.1 ± 11.9
C$_T$ initial	-17.83	-17.37	-10.58	-24.92
C$_T$ IM phys	-0.81 ± 0.81	-1.43 ± 0.71	-1.21 ± 11.6	5.45 ± 1.10
C$_T$ IM bgq	-0.87 ± 0.80	-0.87 ± 0.70	-0.91 ± 1.16	4.19 ± 1.10
C$_T$ TRedf	-0.87 ± 0.80	-0.88 ± 0.70	-0.91 ± 1.16	4.19 ± 1.11
	(4.88 ± 0.50)	(20.99 ± 0.66)	(13.93 ± 0.08)	(0.62 ± 0.04)
C$_T$ near int	19.3 ± 0.24	-2.41 ± 0.53	13.39 ± 0.79	14.14 ± 0.63
C$_T$ prs int	-0.42 ± 0.76	-0.98 ± 0.88	-1.03 ± 1.15	-0.41 ± 1.09

Table 4.7. Same as Table 4.5 but for the 2010-2019 period.

	A10-A095 30°S-24°S	A095-A05 24°S-24.5°N	A05-A02 24.5°N-47°N	A02-A07 47°N-55°N
FO_2 air-sea	153 ± 36	-32 ± 205	-519 ± 70	-345 ± 133
FO_2 TRedf	149 ± 36	347 ± 265	-340 ± 74	-511 ± 166
	(4.51 ± 0.01)	(753.38 ± 21.61)	(18.40 ± 0.01)	(0.38 ± 0.01)
FO_2 near int	151 ± 36	724 ± 265	-332 ± 74	-612 ± 166
FO_2 prs int	149 ± 36	582 ± 265	-347 ± 74	-612 ± 166
BO_2	138 ± 53	801 ± 342	655 ± 178	59 ± 37
BO_2 TRedf	135 ± 53	987 ± 380	475 ± 181	67 ± 37
	(79 ± 12)	(8705 ± 4528)	(7723 ± 682)	(91 ± 17)
BO_2 near int	134 ± 53	900 ± 384	482 ± 182	68 ± 37
BO_2 prs int	135 ± 53	794 ± 379	488 ± 181	67 ± 37
O_2 initial	-518	-1946	5365	1604
O_2 IM phys	611 ± 1089	-1906 ± 1048	-636 ± 1024	1469 ± 1038
O_2 IM bgq	768 ± 881	-1914 ± 820	-1221 ± 815	1069 ± 851
O_2 TRedf	770 ± 881	-1909 ± 820	-1219 ± 815	1069 ± 851
	(11994 ± 48)	(22627 ± 57)	(7503 ± 105)	(1368 ± 134)
O_2 near int	-466 ± 1069	-2139 ± 994	-2175 ± 945	-332 ± 1000
O_2 prs int	675 ± 978	-436 ± 859	-384 ± 839	-333 ± 905
NO_3 initial	-60	-35	493	29
NO_3 IM phys	39 ± 125	90 ± 114	-29 ± 89	14 ± 59
NO_3 IM bgq	-19 ± 102	105 ± 91	-5 ± 73	17 ± 49
NO_3 TRedf	-19 ± 102	104 ± 91	-5 ± 73	17 ± 49
	(2421 ± 24)	(4769 ± 40)	(1930 ± 18)	(62 ± 6)
NO_3 near int	-134 ± 166	40 ± 150	106 ± 112	-50 ± 62
NO_3 prs int	27 ± 131	128 ± 147	102 ± 138	-48 ± 59
SiO_4 initial	-24	-330	538	-37
SiO_4 IM phys	139 ± 291	-35 ± 248	-331 ± 166	-98 ± 85
SiO_4 IM bgq	10 ± 193	84 ± 156	-342 ± 109	-76 ± 63
SiO_4 TRedf	30 ± 219	83 ± 178	-215 ± 122	-42 ± 68
	(4582 ± 57)	(8949 ± 83)	(3410 ± 35)	(35 ± 2)
SiO_4 near int	-53 ± 268	32 ± 210	-36 ± 132	-39 ± 71
SiO_4 prs int	41 ± 156	53 ± 180	47 ± 159	-16 ± 84
PO_4 initial	-2.9	-3.0	31.8	1.1
PO_4 IM phys	-2.1 ± 10.6	0.0 ± 10.6	-5.6 ± 6.5	-0.5 ± 3.9
PO_4 IM bgq	-3.0 ± 8.4	2.9 ± 8.6	-5.0 ± 5.5	-0.4 ± 3.2
PO_4 TRedf	-3.1 ± 8.4	2.8 ± 8.6	-5.0 ± 5.5	-0.5 ± 3.2
	(226.7 ± 2.7)	(348.4 ± 3.1)	(94.5 ± 0.7)	(4.5 ± 0.4)
PO_4 near int	-5.5 ± 11.0	5.7 ± 11.3	3.3 ± 8.5	-4.8 ± 4.1
PO_4 prs int	2.1 ± 12.4	8.3 ± 13.2	7.5 ± 9.6	-3.5 ± 7.9
C_T initial	-3.95	-4.52	18.25	-2.13
C_T IM phys	1.06 ± 0.77	-0.63 ± 0.62	-0.77 ± 0.6	-1.70 ± 0.53
C_T IM bgq	1.22 ± 0.77	0.02 ± 0.62	-0.47 ± 0.63	-1.77 ± 0.52
C_T TRedf	1.22 ± 0.77	0.01 ± 0.62	-0.47 ± 0.63	-1.77 ± 0.52
	(14.73 ± 0.04)	(23.47 ± 0.10)	(8.40 ± 0.08)	(1.56 ± 0.03)
C_T near int	8.13 ± 0.55	19.03 ± 0.39	15.52 ± 0.40	-1.40 ± 0.43
C_T prs int	0.55 ± 0.74	0.08 ± 0.60	-0.03 ± 0.63	-0.14 ± 0.52

Table 4.8. Values of net transport of standard C_{anth} (in PgC yr^{-1}) for each section for the 1990-99 decade per layer (upper, deep and abyssal) comparing the values obtained by the model and the sensitivity test performed using a Montecarlo variation of 20% of the mean C_{anth} concentration at surface. The values indicate the mean of the magnitude and the mean of the uncertainty, whereas the values within parenthesis indicate the standard deviation of the mean and uncertainty, multiplied by 10^3.

	A11	A10	A09	A08	A05	A02	A07
	55°S	30°S	19°S	11°S	24.5°N	47°N	55°N
Upper	0.209 ± 0.021	0.208 ± 0.015	0.234 ± 0.013	0.253 ± 0.011	0.206 ± 0.015	0.160 ± 0.025	0.153 ± 0.029
Upper mod	0.209 ± 0.021	0.207 ± 0.015	0.231 ± 0.013	0.249 ± 0.011	0.206 ± 0.015	0.160 ± 0.026	0.153 ± 0.029
	(0.8 ± 1.3)	(8.2 ± 1.7)	(29.6 ± 1.2)	(33.0 ± 0.9)	(3.7 ± 1.4)	(3.8 ± 0.1)	(0.8 ± 0.1)
Deep	-0.055 ± 0.009	-0.041 ± 0.011	-0.075 ± 0.017	-0.076 ± 0.013	-0.077 ± 0.021	-0.082 ± 0.014	-0.066 ± 0.025
Deep mod	-0.055 ± 0.009	-0.041 ± 0.011	-0.075 ± 0.017	-0.076 ± 0.013	-0.077 ± 0.021	-0.082 ± 0.014	-0.066 ± 0.025
	(0 ± 0)	(0 ± 0)	(0 ± 0)	(0 ± 0)	(0 ± 0)	(0 ± 0)	(0 ± 0)
Abyssal	0.016 ± 0.006	0.008 ± 0.005	0.012 ± 0.004	0.006 ± 0.004	0.001 ± 0.004	0 ± 0	0 ± 0
Abyssal mod	0.016 ± 0.006	0.008 ± 0.005	0.012 ± 0.004	0.006 ± 0.004	0.001 ± 0.004	0 ± 0	0 ± 0
	(0 ± 0)	(0 ± 0)	(0 ± 0)	(0 ± 0)	(0 ± 0)	(0 ± 0)	(0 ± 0)

Table 4.9. Same as Table 4.8 but for the 2000-2009 period.

	A10	A095	A05	A03	A07
	30°S	24°S	24.5°N	36°N	55°N
Upper	0.252 ± 0.016	0.336 ± 0.020	0.216 ± 0.019	0.119 ± 0.029	0.204 ± 0.031
Upper mod	0.252 ± 0.016	0.337 ± 0.020	0.190 ± 0.020	0.120 ± 0.029	0.204 ± 0.031
	(3.8 ± 1.8)	(35.1 ± 2.7)	(9.9 ± 2.4)	(12.5 ± 1.8)	(0.2 ± 0.1)
Deep	-0.063 ± 0.010	-0.093 ± 0.018	-0.089 ± 0.025	-0.062 ± 0.022	-0.116 ± 0.022
Deep mod	-0.063 ± 0.010	-0.094 ± 0.018	-0.095 ± 0.025	-0.062 ± 0.022	-0.116 ± 0.022
	(0 ± 0)	(0 ± 0)	(0 ± 0)	(0 ± 0)	(0 ± 0)
Abyssal	0.008 ± 0.004	-0.002 ± 0.007	0.001 ± 0.004	0 ± 0	0 ± 0
Abyssal mod	0.008 ± 0.004	-0.002 ± 0.007	0.002 ± 0.004	0 ± 0	0 ± 0
	(0 ± 0)	(0 ± 0)	(0 ± 0)	(0 ± 0)	(0 ± 0)

transports, and therefore have computed other Montecarlo experiment that modifies the surface (depth less than 100 m) C_{anth} concentration randomly by 20% and then obtained the net values of C_{anth} transport per layer for each section, shown in Tables 4.8, 4.9 and 4.10. We can see mainly changes in the upper layer, with very small differences reaching 0.005 PgC yr^{-1}. With these results we feel that we have proved that changes in the surface concentration of C_{anth} are not affecting significantly to the overall transport of C_{anth}.

The results for mass, heat and freshwater transports are not different compared to the results from the previous inverse model without considering the biogeochemical equations (Caínzos et al., 2022a). However, the conservations of oxygen, nitrate, silicate and phosphate provide adjusted values after the model that are in balance. As a consequence, these added biogeochemical equations improve the determination of the biological pump, constraining the flux of

Table 4.10. Same as Table 4.8 but for the 2010-2019 period.

	A10	A095	A05	A02	A07
	30°S	24°S	24.5°N	47°N	55°N
Upper	0.404 ± 0.023	0.400 ± 0.019	0.337 ± 0.016	0.258 ± 0.030	0.263 ± 0.031
Upper mod	0.404 ± 0.023	0.399 ± 0.019	0.334 ± 0.016	0.258 ± 0.030	0.263 ± 0.031
	(1.3 ± 2.6)	(20.4 ± 2.3)	(8.7 ± 0.9)	(0 ± 0)	(0 ± 0)
Deep	-0.081 ± 0.011	-0.084 ± 0.012	-0.118 ± 0.017	-0.154 ± 0.018	-0.148 ± 0.028
Deep mod	-0.081 ± 0.011	-0.084 ± 0.012	-0.114 ± 0.017	-0.154 ± 0.018	-0.148 ± 0.028
	(0 ± 0)	(0 ± 0)	(0 ± 0)	(0 ± 0)	(0 ± 0)
Abyssal	0.011 ± 0.005	0.004 ± 0.005	0.003 ± 0.003	0 ± 0	0 ± 0
Abyssal mod	0.011 ± 0.005	0.004 ± 0.005	0.003 ± 0.003	0 ± 0	0 ± 0
	(0 ± 0)	(0 ± 0)	(0 ± 0)	(0 ± 0)	(0 ± 0)

C_T, and, therefore, of C_{anth}. One of the main issues when obtaining results from inverse models with multiple sections is how accurately they represent the average circulation of the decade. Composing box models with several hydrographic sections result in circulation schemes that can help average out the local and small-scale variability that is found on a single hydrographic section (Ganachaud & Wunsch, 2000; Lumpkin & Pazos, 2007; Macdonald & Wunsch, 1996; Reid, 1989, 1994).

4.2.3 C_{anth} estimations

C_{anth} concentration

C_{anth} concentration cannot be measured in the ocean, thus being derived from other direct water sample values. There are several methods of C_{anth} computation, all based on two different techniques. These methods rely on the assumption that the ocean is in steady state. The first is based on back calculation, with methodologies such as ΔC^* (Gruber et al., 1996), tracer combining oxygen, inorganic carbon and total alkalinity (TrOCA; Touratier et al. 2007) or φC_T^0 (Pérez et al., 2008; Vázquez-Rodríguez et al., 2009b). The second technique is based on transit time distributions (TTDs; Waugh et al. 2006).

In this study, we have computed C_{anth} using the back-calculation φC_T^0 method (Guallart et al., 2015; Pérez et al., 2008; Ríos et al., 2012; Vázquez-Rodríguez et al., 2012, 2009b,a), with an overall uncertainty of ± 5.2 μmol kg^{-1}. This method is based on the same principles as the ΔC^* method (Gruber et al., 1996) with some improvements. To determine the amount of C_{anth} in a parcel of water, the method back-calculates the C_T of a water sample to its initial (or preformed) C_T concentration when it was last at the surface layer, based on the changes in A_T, apparent oxygen utilization (AOU), salinity and potential temperature.

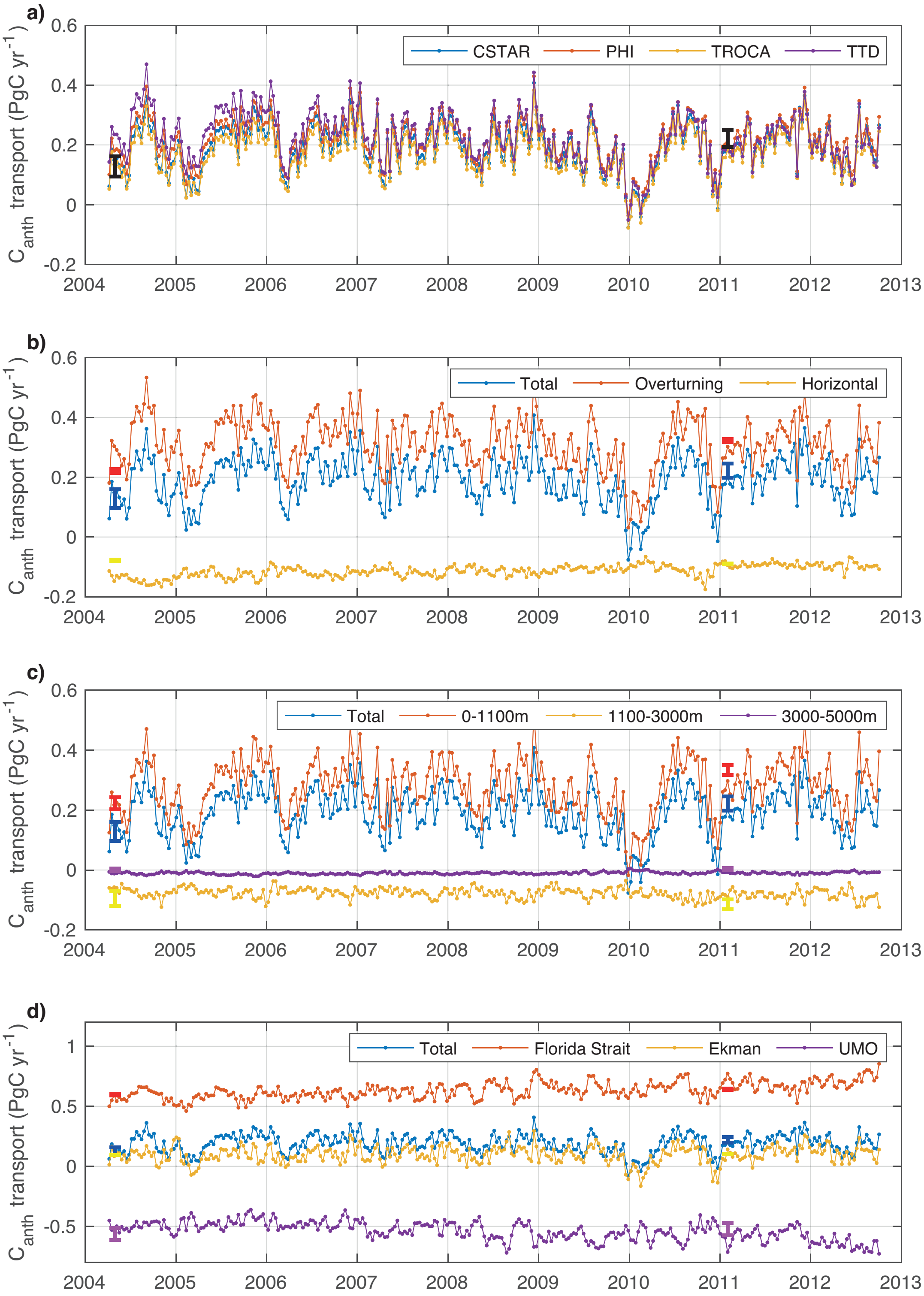
a)
b)
c)
d)
C_{anth} transport (PgC yr^{-1})
CSTAR
PHI
TROCA
TTD
Total
Overturning
Horizontal
Total
0-1100m
1100-3000m
3000-5000m
Total
Florida Strait
Ekman
UMO
0.6
0.4
0.2
0
-0.2
1
0.5
0
-0.5
2004
2005
2006
2007
2008
2009
2010
2011
2012
2013

Figure 4.2. Comparison of C_{anth} transport for section 24.5°N of the continuous values from the time series of Brown et al. (2021) from 2004 to 2012 with the inverse solution of this study for 24.5°N cruises in 2004 and 2011. The comparisons are made attending to different components of the transport (in kmol s^{-1}): a) net C_{anth} transport across 24.5°N compared with time series of C_{anth} transport obtained with different methodologies of computation of C_{anth} concentration (TTD-methods, and other backcalculation methods as Cstar, TROCA and φC_T^0); b) division of C_{anth} into its components – overturning and horizontal; c) division into layers attending to the water masses – 0 to 1100 m for upper and thermocline layers, 1100 to 3000 m for deep layers and 3000 to 5000 m for bottom layers; and d) the importance of Florida Straits and Ekman transport to the total C_{anth} transport.

This method, contrarily to the ΔC^* method, considers the temporal variation of the CO_2 air-sea disequilibrium, and uses sub-surface layer data of the Atlantic as the reference for its parameterizations (Matear et al., 2003; Thomas & Ittekkot, 2001), removing the seasonality present on the surface layer, thus making these parameterizations more representative of the water mass formation conditions. This approach delivers better results in areas of cold waters subject to strong and complex mixing processes. The back-calculation φC_T^0 method has been widely used to compute C_{anth} and has provided consistent results with other back-calculation methods (Brown et al. 2021; Guallart et al. 2015; Vázquez-Rodríguez et al. 2009b; see also Figure 4.2 a).

Transport of C_{anth}

The transport of any property (T_{Prop}) is computed for each pair of consecutive hydrographic stations and between two neutral density interphases as

$$T_{Prop} = \iint C_{Prop}\ \rho\ \mathrm{vel}\ \mathrm{dx}\mathrm{d}\gamma^{n} \tag{4.1}$$

where C_{Prop} is the property concentration, ρ is the in-situ density, vel is the velocity perpendicular to the section and $\mathrm{dxd}\gamma^n$ is the area over which the computation occurs, considering the distance between stations and the width of each vertical level, respectively.

This initial transport of C_{anth} is adjusted with the velocities at the reference level for each station pair obtained from the inverse model solution. Positive values of meridional transport refer to northward fluxes and negative to southward. In a vertical framework, positive values are upward (or towards the atmosphere, release or efflux) and negative values are downward (towards the ocean, uptake).

To understand the underlying variability in C_{anth} concentration and remove the effect of the variation in mass transport, we have computed the transport-weighted (TW) C_{anth} concentration (in μmol kg^{-1}). For water masses flowing in the same direction, we can obtain TW C_{anth} as the ratio between C_{anth} and mass transport.

The vertical transport resulting from the diffusion of C_{anth} was computed using a diffusion coefficient of 1.1 cm^2 s^{-1} for the whole basin and all depths, obtained as the average value at the interphase between upper and deep layers from the diffusion coefficients ($\varkappa_z$) computed for each box between adjacent sections. The diffusion processes included in $\varkappa_z$ are the remaining changes in vertical heat transport after compensating the horizontal imbalance in mass with a vertical transport associated to mass advection (Caínzos et al., 2022a; Hernández-Guerra & Talley, 2016; Talley et al., 2016; Hogg et al., 1982; Morris et al., 2001; Munk, 1966). This diffusion coefficient was then multiplied by the area and by the vertical derivative at the interphase between different layers of the C_{anth} concentration times density.

Storage rate of C_{anth}

To determine the amount of C_{anth} stored in PgC yr^{-1} (or kmol s^{-1}) in each cell between adjacent sections and each two neutral density interphases, we have used, primarily, the storage rates of Gruber et al. (2019), supplemented with the inventories of Sabine et al. (2004). Both datasets have quantified the oceanic sink for C_{anth} over the period 1994 to 2007 for the former and 1800 to 1994 for the latter.

The storage rates were normalized by the volume of each box and then the value for each decade was computed. Tanhua et al. (2006) found that C_{anth} is in a transient steady state (TSS) in the North Atlantic by comparing observed changes in C_T and CFC fields with those predicted from an eddy-permitting ocean circulation model. This implies that the increase of C_{anth} concentration with time is related to the surface concentration. Changes in C_{anth} for a given time period can be calculated by applying the exponential expression $\mathrm{C_t^0 = Ae^{\lambda t}}$, that reconstructs the history of atmospheric CO_2 and C_{anth} since the Industrial Revolution. The rate of change of C_{anth} is included in the factor λ (yr^{-1}), with an annual increase of 1.9%, based on a 28% increase between 1994 and 2007 (Gruber et al., 2019). The concentrations or the storage rate can be rescaled to the average year for each decade following the expression (Gruber et al., 2019; Steinfeldt et al., 2009):

$$\mathrm{C_{anth_{t2}} = C_{anth_{t1}}\, e^{\lambda(t2-t1)} = C_{anth_{t1}}(1+0.019)^{t2-t1}} \tag{4.2}$$

where $\mathrm{t1}$ is the reference year and $\mathrm{t2}$ corresponds to the midpoint year for each decade (1995, 2005 and 2015). This expression can also be applied to C_{anth} transports by obtaining the C_{anth} concentration for the desired time and combining it with the mass transport estimates. The storage rates of Gruber et al. (2019) are referred to a $\mathrm{t1 = 2000.5}$ (the midpoint of the 1994-2007 inventory change).

Using the inventory of Sabine et al. (2004) for 1994 and the change in C_{anth} concentration of Gruber et al. (2019) between 1994 and 2007, we can obtain the storage rate for 2007 following the expression:

$$\mathrm{Storage\ Rate\ C_{anth_{2007}} = 0.019\ (C_{anth_{1994}} + \Delta C_{anth_{2007-1994}})} \tag{4.3}$$

Then, the storage rates can be normalized to the middle of each decade using the TSS expression (eq.4.2), with 2007 as reference year.

In general, we have used values from the Gruber estimate (equation 4.2), but we have introduced some adjustments due to the difficulties associated to the methodology of $\Delta\mathrm{C}^{*}\mathrm{MLR}$ to detect small changes in deep waters (Gruber et al., 2019). We have computed values from the combined inventory of Gruber et al. (2019) and Sabine et al. (2004) for 2007 (equation 4.3), and then normalized to the midpoint of each decade using TSS (equation 4.2). If the storage rate from Gruber et al. (2019) exceeded over 50% the combined storage rate, it was replaced by the combined estimation. That is the case of the cells marked with an asterisk in Figure 4.3. Most of the cells achieved a better $\mathrm{C}_{\mathrm{anth}}$ balance between advection and storage with this replacement.

$\mathrm{C}_{\mathrm{anth}}$ uptake

The net budget of $\mathrm{C}_{\mathrm{anth}}$ within each cell, defined between two sections and two neutral density interphases, is the balance between the lateral advection of the meridional $\mathrm{C}_{\mathrm{anth}}$ transport across each section, the storage of $\mathrm{C}_{\mathrm{anth}}$ within the cell and the vertical fluxes of $\mathrm{C}_{\mathrm{anth}}$ (Brown et al., 2021; Pérez et al., 2013; Racapé et al., 2018; Zunino et al., 2015b). This vertical flux in the air-sea interphase is the uptake from the atmosphere. We have computed the $\mathrm{C}_{\mathrm{anth}}$ uptake indirectly, inferring it from the other two terms of the balance in each cell.

$\mathrm{C}_{\mathrm{anth}}$ components

The total transport of $\mathrm{C}_{\mathrm{anth}}$ can be divided into its components, analogous to methods applied to heat and freshwater transport, attending to the mechanisms of vertical and meridional circulation (Brown et al., 2021; Bryden & Imawaki, 2001; Caínzos et al., 2022a; McDonagh et al., 2015). Any property can be defined as a sum of their components, distinguishing between mechanisms of horizontal circulation and vertical overturning. For a zonal transoceanic section, a property P is expressed as:

$$\mathrm{P} = \mathrm{P}_0 + \mathrm{P}'(\mathrm{x},\gamma^{\mathrm{n}}) = \mathrm{P}_0 + \langle \mathrm{P} \rangle(\gamma^{\mathrm{n}}) + \mathrm{P}''(\mathrm{x},\gamma^{\mathrm{n}}) \tag{4.4}$$

where $\mathrm{P}_0 = \frac{\iint \mathrm{P}(\mathrm{x},\gamma^{\mathrm{n}})\ \mathrm{dx}\mathrm{d}\gamma^{\mathrm{n}}}{\iint \mathrm{dx}\mathrm{d}\gamma^{\mathrm{n}}}$ is the area-weighted section average, $\mathrm{P}'(\mathrm{x},\gamma^{\mathrm{n}}) = \mathrm{P}(\mathrm{x},\gamma^{\mathrm{n}}) - \mathrm{P}_0$ is the property anomaly, $\langle \mathrm{P} \rangle(\gamma^{\mathrm{n}}) = \frac{\int (\mathrm{P}(\mathrm{x},\gamma^{\mathrm{n}}) - \mathrm{P}_0)\ \mathrm{dx}}{\int \mathrm{dx}}$ are the area-weighted zonally averaged deviations from the property average P_0, and $\mathrm{P}''(\mathrm{x},\gamma^{\mathrm{n}}) = \mathrm{P} - \mathrm{P}_0 - \langle \mathrm{P} \rangle(\gamma^{\mathrm{n}})$ are the deviations from the zonal and section averages (the residual values). The last two terms are included in the anomaly term, so that $\mathrm{P}'(\mathrm{x},\gamma^{\mathrm{n}}) = \langle \mathrm{P} \rangle(\gamma^{\mathrm{n}}) + \mathrm{P}''(\mathrm{x},\gamma^{\mathrm{n}}) - \mathrm{P}_0$. The x and γ^{n} coordinates refer to the zonal and vertical extent of the section, respectively.

The transport of this property can be broken up into its corresponding components, related to those of the property:

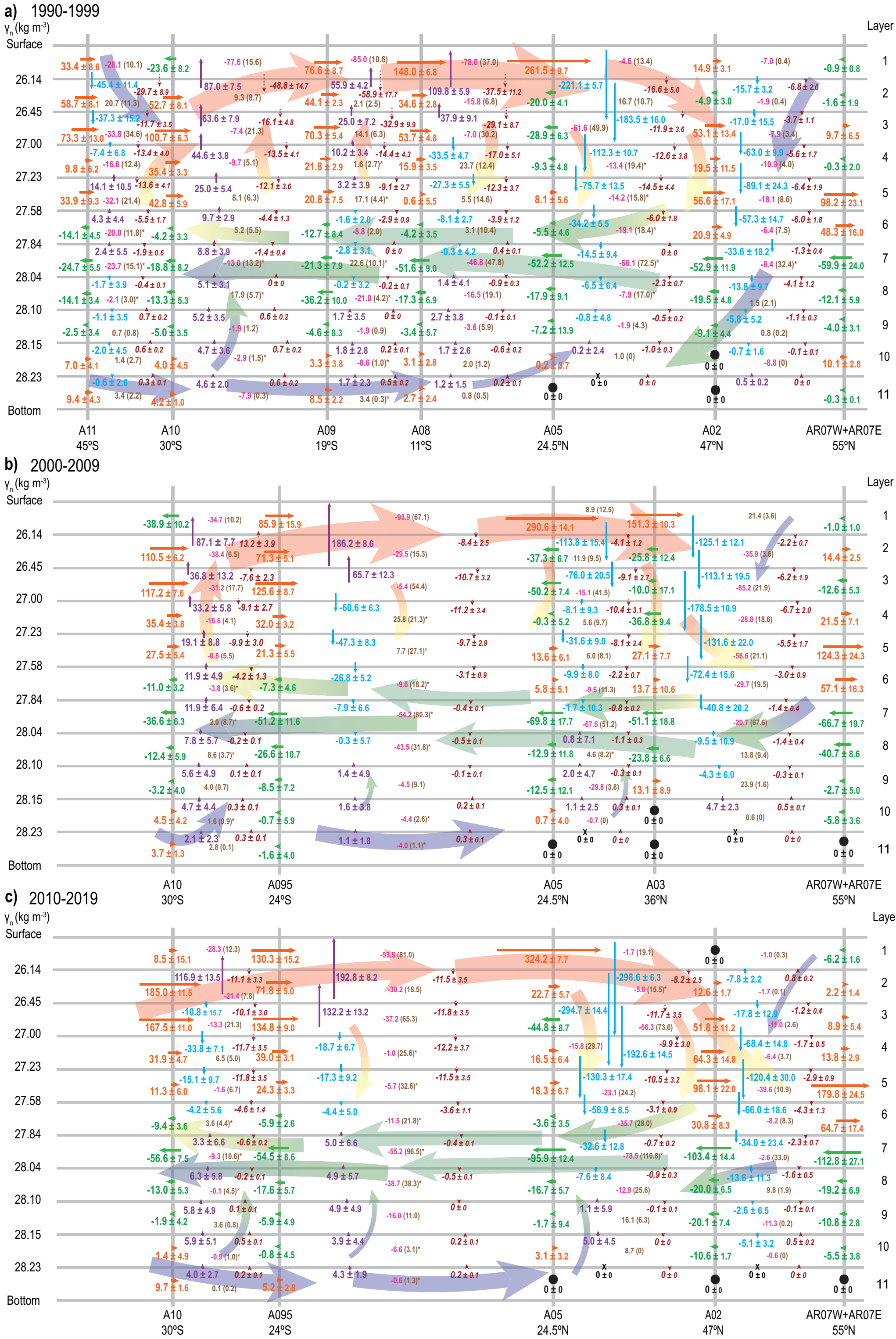
a) 1990-1999
γn (kg m-3)
Surface
26.14
26.45
27.00
27.23
27.58
27.84
28.04
28.10
28.15
28.23
Bottom
Layer
1
2
3
4
5
6
7
8
9
10
11
A11
45ºS
A10
30ºS
A09
19ºS
A08
11ºS
A05
24.5ºN
A02
47ºN
AR07W+AR07E
55ºN
b) 2000-2009
γn (kg m-3)
Surface
Layer
A10
30ºS
A095
24ºS
A05
24.5ºN
A03
36ºN
AR07W+AR07E
55ºN
c) 2010-2019
γn (kg m-3)
Surface
Layer
Bottom
A10
30ºS
A095
24ºS
A05
24.5ºN
A02
47ºN
AR07W+AR07E
55ºN

Figure 4.3. Vertical and meridional schematic of C_{anth} circulation in the Atlantic Ocean for each decade. The gray horizontal lines mark the neutral density interphases, and the gray vertical lines are the position of each zonal section at their nominal latitude for the (a) 1990–99 decade, (b) 2000–09 decade, and (c) 2010–19 decade. The meridional C_{anth} transport (PgC yr^{-1}) is represented with horizontal arrows, in orange for northward (positive) transport and green for southward (negative) transport. The vertical transport due to the advection of mass between two sections in the interphase between two layers is represented with vertical arrows, in violet for upward (positive) transport and blue for downward (negative) transport. Black dots and crosses represent layers with no transport. The vertical transport due to the diffusion of C_{anth} appears with dashed brown arrows and values, with positive for upward diffusive transport and negative for downward diffusion. For each cell, the values within parenthesis indicate the storage of C_{anth} as computed from Gruber et al. (2019). Asterisks mark the cells where the modification from Sabine et al. (2004) had to be included. The numbers outside of the parenthesis indicate the imbalance within each cell, in ocre for a (positive) gain of C_{anth} and pink for a (negative) loss of C_{anth}. Background arrows manifest the presence of two counter-rotating overturning cells across the basin.

1. The barotropic component, which represents the net transport across the section at the section averaged property concentration. This term has been called ‘throughflow’ (McDonagh et al., 2015) and ‘leakage’ (Wijffels, 2001):

$$\mathrm{P_{throughflow}} = \mathrm{T_{BS}} + (\mathrm{P_{BS}} - \mathrm{P_0}) \tag{4.5}$$

   where $\mathrm{T_{BS}}$=-0.8 Sv is the interbasin mass transport, and $\mathrm{P_{BS}}$ is the average Bering Strait property value.

2. The baroclinic transport, due to zonally averaged vertical-meridional circulation, and associated with the overturning circulation across the section. This term is called ‘overturning’:

$$\mathrm{P_{overturning}} = \iint \rho \, \langle \mathrm{P} \rangle \, \langle \mathrm{vel} \rangle \, \mathrm{dxd}\gamma^{\mathrm{n}} \tag{4.6}$$

3. The horizontal transport, due to the large-scale gyre circulation and smaller-scale eddies, which reflects correlations between residual velocity and property fields. This term is referred to as ‘horizontal’ or ‘gyre’:

$$\mathrm{P_{horizontal}} = \iint \rho \, \mathrm{P}'' \, \mathrm{vel}'' \, \mathrm{dxd}\gamma^{\mathrm{n}} \tag{4.7}$$

Applying these expressions to C_{anth} transport, we found negligible values for the throughflow component (with an average southward transport of -0.002 PgC yr^{-1}) and therefore are not shown.

4.3 Results

4.3.1 Meridional overturning circulation and C_{anth} components

The meridional circulation in the Atlantic follows two-counter rotating cells (Caínzos et al., 2022a; Kersalé et al., 2020). The balance in these cells involves northward transports of upper and abyssal layers, compensated by southward-flowing North Atlantic Deep Water (NADW) in between. The meridional advection of C_{anth} transport follows a similar pattern (Figure 4.3).

For the South Atlantic, there is a layer of northward transport with stronger values between the surface and 27.00 kg m^{-3} for all decades. There is a subsurface maximum transport of C_{anth} associated with modal or central waters flowing between 26.45 and 27.00 kg m^{-3} at 30 and 24°S and distributed more evenly on its way equatorward (sections 19 and 11°S in 1990-99). At 24.5°N there is a shallowing of the northward transport of C_{anth}, delimited to the first layer, and, more specifically, to the Florida Straits Current, that dominates the upper flux (Figure 4.3). This transport is opposed by a southward normalized transport for the upper mid-ocean, computed as the upper transport discounting the Florida Straits transport (UMO; -0.333 $\pm$ 0.015, -0.376 $\pm$ 0.019 and -0.309 $\pm$ 0.016 PgC yr^{-1}, for 1990-99, 2000-09 and 2010-19, respectively) between 26.14 and 27.84 kg m^{-3} (Figure 4.3). In the SPNA (at 47 and 55°N) the core of the NAC (North Atlantic Current) gets $\sim$4% denser on its way northward (Caínzos et al., 2022a), with stronger C_{anth} transports between 27.23 and 27.58 kg m^{-3}. Deep water formation in the Nordic and Labrador Seas offers a return southward flow of C_{anth} transport with stronger values in the upper limb of the NADW, between 27.84 and 28.04 kg m^{-3}, a pattern that is maintained as it is advected southward, despite decreasing its strength.

The division into components of C_{anth} transport reflects the importance of each component in the total transport (Figure 4.4). The total transport is a balance between the barotropic or throughflow component (which remains mainly unchanged), and the baroclinic (overturning) and horizontal (or gyre) transports. The overturning component of the C_{anth} transport provides the vertical circulation across the section, representing changes in the meridional structure of the water column. This is the principal component of the total C_{anth} transport, determining the importance of the vertical circulation in the distribution of C_{anth}, with a northward transport for the whole basin, carrying waters with high concentration of C_{anth} by the upper branch of the AMOC, contrasting with the southward transport of waters by the lower branch of the AMOC with lower concentration of C_{anth}. This overturning increases equatorward, following the increase in AMOC and heat transport, corroborated by the correlation between C_{anth} overturning transport and heat overturning transport (Figure 4.5). The slopes show a relationship between C_{anth} and heat increasing in time (0.183, 0.273 and 0.331 gC W^{-1} yr^{-1} for each decade, respectively), which persist, albeit slightly reduced, even when normalized (0.229, 0.268 and 0.287 gC W^{-1} yr^{-1}, respectively, with an average value of 0.261 $\pm$ 0.030 gC W^{-1} yr^{-1}). As a result, for the same overturning

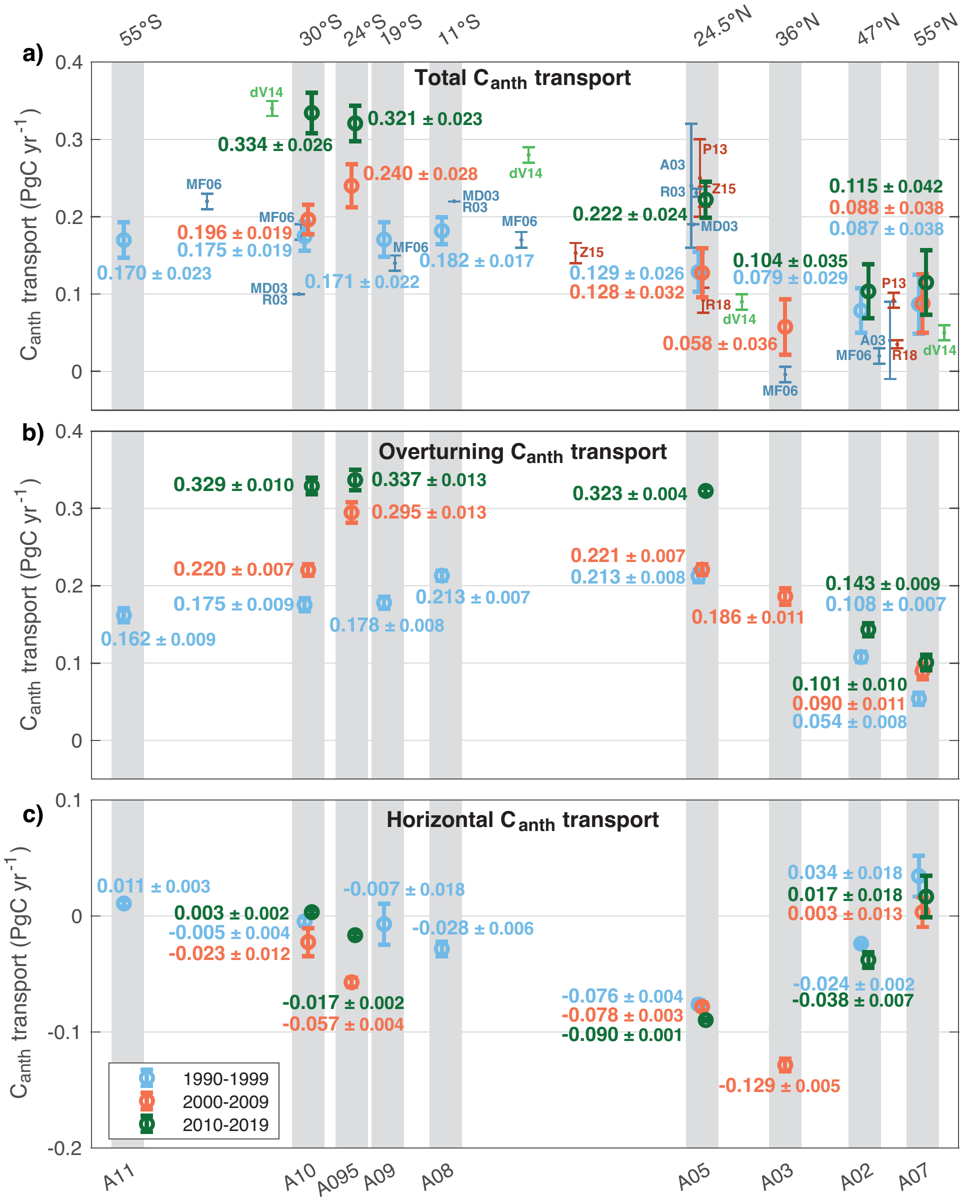

Figure 4.4. C_{anth} transport attending to its division into components (in PgC yr^{-1}). The grey bars mark the nominal latitude of each zonal section, and the colours represent each decade, blue for 1990–99, orange for 2000–09, and green for 2010–19. The total transport (a) is mainly divided into its principal components: overturning (b) and horizontal or gyre (c). The total C_{anth} transport is similar to the overturning transport, as the horizontal component is quite small. The uncertainties associated with the C_{anth} transports are part of the results of the inverse model solved using the Gauss-Markov estimator. Literature values (Figure 4.10 and Table 4.11) are added for comparison to the total C_{anth} transport: A03 (Álvarez et al., 2003), dV14 (DeVries, 2014), MD03 (Macdonald et al., 2003), MF06 (Mikaloff Fletcher et al., 2006), P13 (Pérez et al., 2013), R18 (Racapé et al., 2018), R03 (Rosón, 2003), Z15 (Zunino et al., 2015a).

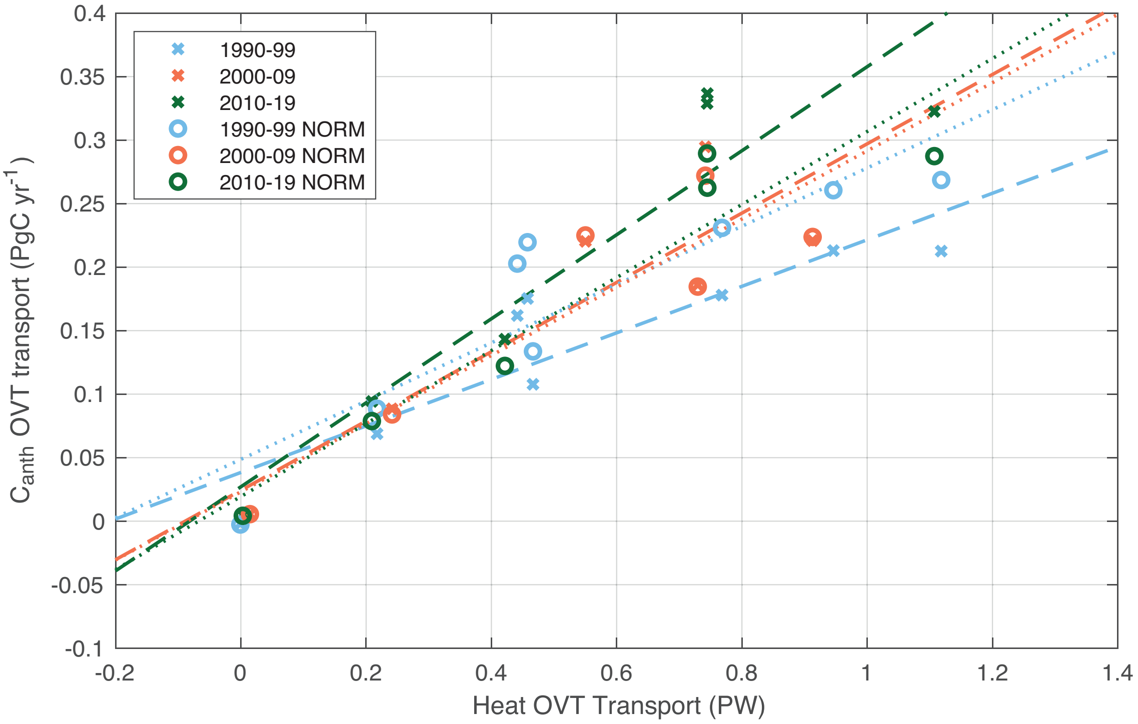

Figure 4.5. Relationship between the overturning components of heat (PW) and C_{anth} transport (PgC yr^{-1}). Scatter plots of heat overturning transport against C_{anth} overturning transport, represented with their standard values (crosses) and normalized to 2005 (open circles), for each section and for the three decades. Each colour represents a decade: blue for 1990–99, orange for 2000–09, and green for 2010–19. Linear regressions were fitted for each decade in the coloured dashed lines for the normal transport, and dotted lines represent the regressions using normalized C_{anth} transport.

heat transport, the amount of C_{anth} transport carried by the overturning has been increasing (by $\sim$0.0074 $\pm$ 0.0030 gC W^{-1} yr^{-1}). In the overturning C_{anth} transport, there is a leap between the first two decades and the last one in the subtropical gyres, with values between 1990-99 and 2010-19 around 50% larger at 30°S and 24.5°N and $\sim$15% larger between 2000-09 and 2010-19 at 24°S. Moreover, in the SPNA, there is a slight increase between 1990-99 and 2010-19 at 47 and 55°N.

The horizontal or gyre component gives information of the role of large-scale gyre circulation and eddies, including the differences in the circulation along the section, both vertically and horizontally. The values are rather small and with low variability for the whole basin, with averages for all sections of -0.014 $\pm$ 0.027, -0.057 $\pm$ 0.019 and -0.025 $\pm$ 0.019 PgC yr^{-1} for each decade, respectively. Of the total 17 sections, only the three cruises at 24.5°N and the one at 36°N show large negative values due to an eastern current transporting C_{anth}-enriched waters southwards. The contribution of the overturning and horizontal components to the transport of C_{anth} varies with latitude. An increase in the overturning would imply a stronger vertical pattern in the water column, so that the residuals along the section are lower and therefore, so is the horizontal component of the circulation. In the South Atlantic, the horizontal transport of C_{anth} represents less than 20% of the absolute overturning transport, whereas for 24.5°N, the percentages vary with the decades (36, 35 and 28%, respectively for each decade), with a related large percentage for 36°N in 2003 (69%) and a relatively high impact of the SPNA at 47°N (22 and 27%). There is an increase in the horizontal component for the 2000-09 decade over the Atlantic, strengthening the southward horizontal transport at 30°S, 24°S, 24.5°N and 36°N. This increase is counteracted by a reduction in the horizontal northward transport at 55°N, contributing only 4% of the overturning component. This could be associated with the reduction in the AMOC for this period at 24.5°N, due to an increase in the opposing upper mid-ocean (UMO) transport (Worthington et al., 2021).

4.3.2 Vertical distribution of C_{anth} transports

Our results allow the study of the Atlantic Ocean from 45°S to 55°N in 1990-99 and from 30°S to 55°N in 2000-09 and 2010-19. Attending to our repeating sections we can form two superboxes – 30°S to 24.5°N and 24.5°N to 55°N that can be compared for the three decades. The former includes the South Atlantic subtropical gyre, the Intertropical convergence Zone (ITCZ) and the North Atlantic equatorial region. The latter includes the North Atlantic subtropical gyre and the Subpolar North Atlantic (SPNA). We have computed the meridional transport, storage and air-sea influx of C_{anth} in PgC yr^{-1} within each box for the total depth, as well as for the division into upper and lower layers (Figure 4.6). With this division, the upper AMOC encompasses the northward upper layers of thermocline and intermediate waters, and the lower layer includes the combination of the deep southward layer and the northward abyssal layer of AMOC.

At 30°S, the net transport increases in time (0.175 $\pm$ 0.019, 0.197 $\pm$ 0.019 and 0.334 $\pm$ 0.026 PgC yr^{-1}, for each decade, respectively; Figure 4.6), with a large leap for the last decade, resulting from the $\sim$55% strengthening of the second and third layers of surface and modal waters (Figure 4.3). This increase in the strength of the circulation in time is also evident in the northward transport of upper layers (0.208 $\pm$ 0.015, 0.252 $\pm$ 0.016 and 0.404 $\pm$ 0.023 PgC yr^{-1}, respectively per decade) and, to a lesser extent, in the southward lower layers (-0.033 $\pm$ 0.012, -0.055 $\pm$ 0.011 and -0.070 $\pm$ 0.012 PgC yr^{-1}, for each decade). To remove the effects of the expected marine C_{anth} increase assuming TSS (Tanhua et al., 2006), we have normalized C_{anth} transports to the same year (2005). The upper layers show similar values for the first decades ($\sim$0.26 PgC yr^{-1}), with an increase of 40% over the expected for the last decade.

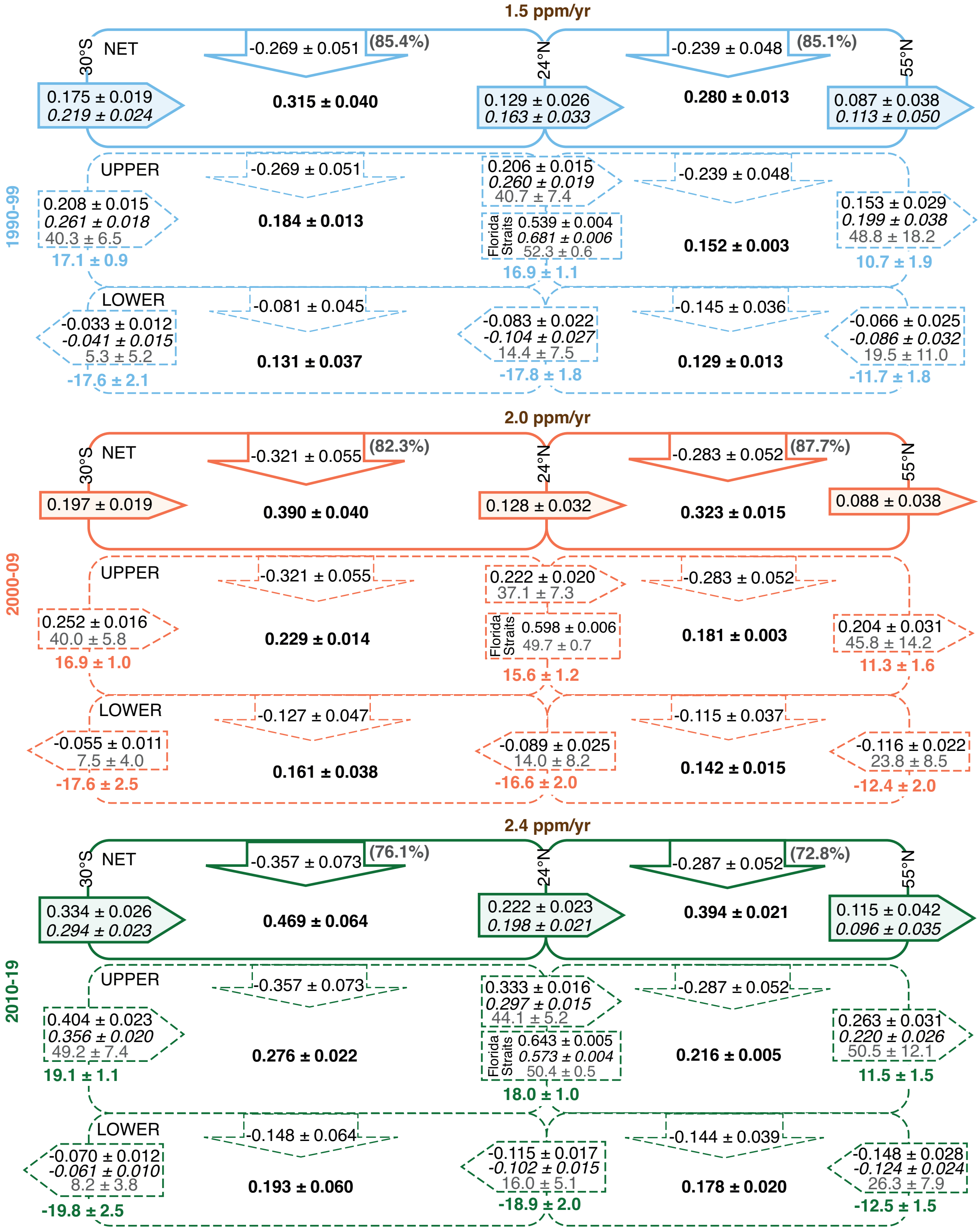
1.5 ppm/yr
1990-99
30°S
24°N
55°N
NET
-0.269 ± 0.051
(85.4%)
-0.239 ± 0.048
(85.1%)
0.175 ± 0.019
0.219 ± 0.024
0.315 ± 0.040
0.129 ± 0.026
0.163 ± 0.033
0.280 ± 0.013
0.087 ± 0.038
0.113 ± 0.050
UPPER
-0.269 ± 0.051
0.206 ± 0.015
0.260 ± 0.019
40.7 ± 7.4
-0.239 ± 0.048
0.208 ± 0.015
0.261 ± 0.018
40.3 ± 6.5
0.184 ± 0.013
Florida Straits
0.539 ± 0.004
0.681 ± 0.006
52.3 ± 0.6
0.153 ± 0.029
0.199 ± 0.038
48.8 ± 18.2
0.152 ± 0.003
17.1 ± 0.9
16.9 ± 1.1
10.7 ± 1.9
LOWER
-0.081 ± 0.045
-0.145 ± 0.036
-0.033 ± 0.012
-0.041 ± 0.015
5.3 ± 5.2
-0.083 ± 0.022
-0.104 ± 0.027
14.4 ± 7.5
-0.066 ± 0.025
-0.086 ± 0.032
19.5 ± 11.0
0.131 ± 0.037
0.129 ± 0.013
-17.6 ± 2.1
-17.8 ± 1.8
-11.7 ± 1.8
2.0 ppm/yr
2000-09
30°S
24°N
55°N
NET
-0.321 ± 0.055
(82.3%)
-0.283 ± 0.052
(87.7%)
0.197 ± 0.019
0.390 ± 0.040
0.128 ± 0.032
0.323 ± 0.015
0.088 ± 0.038
UPPER
-0.321 ± 0.055
0.222 ± 0.020
37.1 ± 7.3
-0.283 ± 0.052
0.252 ± 0.016
40.0 ± 5.8
0.229 ± 0.014
Florida Straits
0.598 ± 0.006
49.7 ± 0.7
0.181 ± 0.003
0.204 ± 0.031
45.8 ± 14.2
16.9 ± 1.0
15.6 ± 1.2
11.3 ± 1.6
LOWER
-0.127 ± 0.047
-0.115 ± 0.037
-0.055 ± 0.011
7.5 ± 4.0
-0.089 ± 0.025
14.0 ± 8.2
-0.116 ± 0.022
23.8 ± 8.5
0.161 ± 0.038
0.142 ± 0.015
-17.6 ± 2.5
-16.6 ± 2.0
-12.4 ± 2.0
2.4 ppm/yr
2010-19
30°S
24°N
55°N
NET
-0.357 ± 0.073
(76.1%)
-0.287 ± 0.052
(72.8%)
0.334 ± 0.026
0.294 ± 0.023
0.469 ± 0.064
0.222 ± 0.023
0.198 ± 0.021
0.394 ± 0.021
0.115 ± 0.042
0.096 ± 0.035
UPPER
-0.357 ± 0.073
0.333 ± 0.016
0.297 ± 0.015
44.1 ± 5.2
-0.287 ± 0.052
0.404 ± 0.023
0.356 ± 0.020
49.2 ± 7.4
0.276 ± 0.022
Florida Straits
0.643 ± 0.005
0.573 ± 0.004
50.4 ± 0.5
0.216 ± 0.005
0.263 ± 0.031
0.220 ± 0.026
50.5 ± 12.1
19.1 ± 1.1
18.0 ± 1.0
11.5 ± 1.5
LOWER
-0.148 ± 0.064
-0.144 ± 0.039
-0.070 ± 0.012
-0.061 ± 0.010
8.2 ± 3.8
-0.115 ± 0.017
-0.102 ± 0.015
16.0 ± 5.1
-0.148 ± 0.028
-0.124 ± 0.024
26.3 ± 7.9
0.193 ± 0.060
0.178 ± 0.020
-19.8 ± 2.5
-18.9 ± 2.0
-12.5 ± 1.5

Figure 4.6. C_{anth} budget in the Atlantic Ocean for two superboxes – 30°S to 24.5°N and 24.5° to 55°N for each decade, represented by different colours (blue for 1990–99, orange for 2000–09, and green for 2010–19). For each decade, the upper boxes, with continuous lines, represent the net values for the whole water column, whereas the dashed boxes represent the division into the upper and lower branches of the AMOC. Each box is delimited on either side by the meridional transport across the section, specifying the transport of different properties: C_{anth} transport (PgC yr^{-1}) appears with black regular values, normalized C_{anth} transport (PgC yr^{-1}) are the black italic values, and the mass transport (Sv) are the coloured bold values outside the arrow. Moreover, the normalized transport-weighted C_{anth} (μmol kg^{-1}) concentration is also included as the grey values. At 24.5°N, there is an extra meridional transport box for the values associated to the Florida Straits. Within each cell there is a bold black value that determines the C_{anth} storage (PgC yr^{-1}) as obtained from Gruber et al. (2019) and Sabine et al. (2004) and normalized to the middle of each decade (1995, 2005 and 2015). The vertical arrows at the top of each box are the vertical influx of C_{anth} (PgC yr^{-1}), namely the atmospheric input for the upper boxes. The bold grey values in parenthesis represent the percentage of uptake to the net storage of each box. The bold brown values at the top of each decade specifies the rate of increase of atmospheric CO_2 for each decade.

However, the lower branch of the AMOC slightly increases with very similar transports. Values for the 2005-normalized transport-weighted (TW) C_{anth} for upper layers (40.3 ± 6.5, 40.0 ± 5.8 and 49.2 ± 7.4 μmol kg^{-1}, respectively per decade; grey values in Figure 4.6) are comparable. The lower branch of the AMOC maintains a marginal increasing tendency with time (5.3 ± 5.2, 7.5 ± 4.0 and 8.2 ± 3.8 μmol kg^{-1}, respectively) with values slightly higher than those expected following TSS, although within uncertainties and therefore maybe not significant. Therefore, the change in the net transport is dominated by the transport of the upper layer, that in 2010-19 has increased its mass transport and its TW-C_{anth} concentration, resulting in the large value of C_{anth} transport.

The net flux for the whole water column of the meridional C_{anth} transport consistently decreases northward, with a reduction of 26, 54 and 34% between 30°S and 24.5°N for the decades 1990-99, 2000-09, and 2010-19, respectively. The lower branch of the AMOC at 24.5°N show relatively consistent values with time (-0.083 ± 0.022, -0.089 ± 0.025 and -0.115 ± 0.017 PgC yr^{-1}, respectively). Considering TSS, the 2005-normalized TW C_{anth} for the lower branch are 14.4 ± 7.5, 14.0 ± 8.2 and 16.0 ± 5.1 μmol kg^{-1} per decade, which are relatively stable and almost double the concentrations at 30°S. The pattern of circulation at 24.5°N between decades shows similar values in transport and TW C_{anth} concentration between 1990-99 and 2000-09, with a later recovery between 2000-09 and 2010-19 (0.129 ± 0.026, 0.128 ± 0.032 and 0.222 ± 0.023 PgC yr^{-1}, respectively), resulting from the low increase in the upper branch of the AMOC in 2000-09 (0.206 ± 0.015, 0.222 ± 0.020 and 0.333 ± 0.016 PgC yr^{-1}, respectively). The higher northward upper transport for the first decade is associated with a larger value of the normalized Florida Strait (FS) transport (0.681 ± 0.006, 0.598 ± 0.006 and 0.573 ± 0.004 PgC yr^{-1}, respectively). This upper flux at 24.5°N is dominated by the FS transport in the first layer (Figure 4.3), with southward normalized transport for the UMO (-0.420 ± 0.020, -0.376 ± 0.020 and -0.272 ± 0.015 PgC yr^{-1}, for 1990-99, 2000-09 and 2010-19, respectively). This transport of C_{anth} by UMO partially reduces the net C_{anth} transport of the total upper layer, although the decreasing trend is not apparent in the upper layer transport, dominated by the transport across the FS.

The northernmost section available, at 55°N, is composed by two subsections: the western one determining the transport across the Labrador Sea and the eastern one reflecting the northward transport by the NAC and the southward transport of the newly subducted deep waters in the sills and Nordic Seas. There is a weakening in the net C_{anth} transport northward, with a reduction over the whole basin between 30°S and 55°N of 50%, 55% and 66% for the decades 1990-99, 2000-09, and 2010-19, respectively. This pattern resembles that from the lower branch of the AMOC, with a steady South-North increasing gradient in C_{anth} transport (-0.066 $\pm$ 0.025, -0.116 $\pm$ 0.022 and -0.148 $\pm$ 0.028 PgC yr^{-1} for each decade at 55°N, respectively) maintained through the decades, with around 50% more at 55°N than at 30°S. The normalized TW C_{anth} show C_{anth}-enriched waters at 55°N (19.5 $\pm$ 11.0, 23.8 $\pm$ 8.5 and 26.3 $\pm$ 7.9 μmol kg^{-1}, per decade) that arrive at the south Atlantic subtropical gyre with ~30% of the original concentration. In the 2000-09 and 2010-19 decades, this southward decrease is also evident on the standard and normalized meridional transport, with a rather low C_{anth} transport for the 1990-99 decade. The upper AMOC transports central and intermediate waters with similar TW C_{anth} concentration for the whole period (48.8 $\pm$ 18.2, 45.8 $\pm$ 14.2 and 50.5 $\pm$ 12.1 μmol kg^{-1}, respectively). However, the

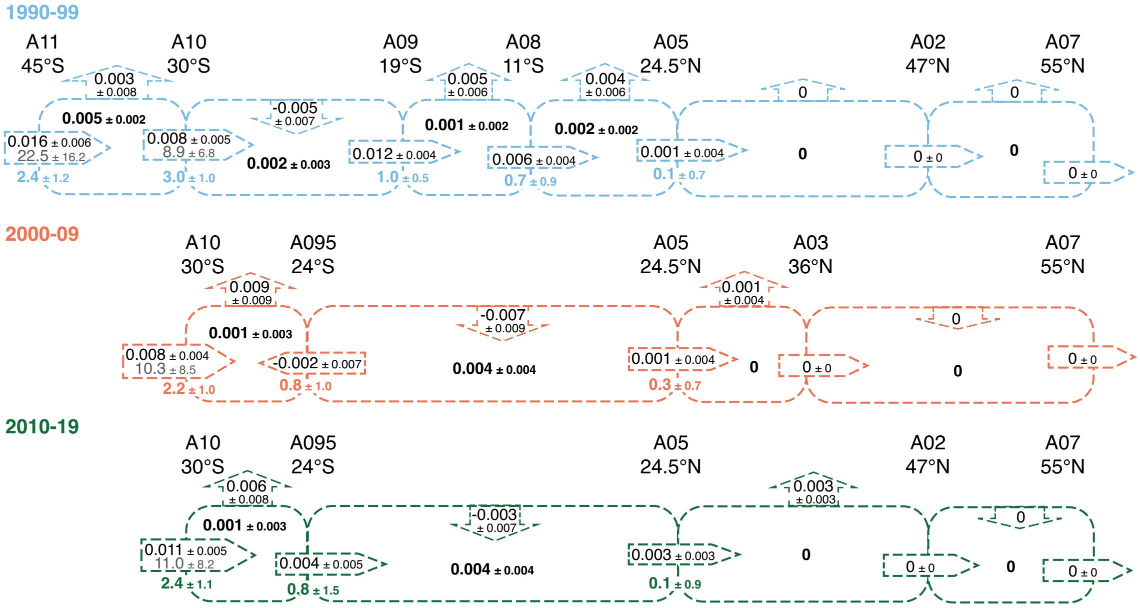

Figure 4.7. C_{anth} budget for abyssal layers in the Atlantic Ocean for each box between adjacent sections for each decade, represented by different colors (blue for 1990–99, orange for 2000–09, and green for 2010–19). Each box is delimited on either side by the horizontal C_{anth} transport (PgC yr^{-1}) across the section with black regular values, and the mass transport (Sv) are the colored bold values outside the arrow. Moreover, the normalized transport-weighted C_{anth} (μmol kg^{-1}) concentration is also included as the grey values. Within each cell there is a bold black value that determines the C_{anth} storage (PgC yr^{-1}) as obtained from Gruber et al. (2019) and Sabine et al. (2004) normalized to the middle of each decade (1995, 2005 and 2015). The vertical arrows at the top of each box are the vertical influx of C_{anth} (PgC yr^{-1}).

normalized upper C_{anth} transports experience a very slight increase in the last decade (0.199 $\pm$ 0.038, 0.204 $\pm$ 0.031 and 0.220 $\pm$ 0.026 PgC yr^{-1}, respectively).

The northward transport of the Antarctic Bottom Water (AABW) appears in the southernmost sections (namely, 45°S for the 1990-1999 decade and 30°S for the 2000-2009 and 2010-2019 decades). There is a consistent pattern of reduction of northward C_{anth} transport as the water masses travel north (Figure 4.7) for the three decades, accompanied by a decrease in the TW C_{anth} concentration from 45°S (22.5 $\pm$ 16.2 μmol kg^{-1}) to 30°S (8.9 $\pm$ 6.8 μmol kg^{-1}) in the first decade. Despite observing similar transports of C_{anth} at 30°S (0.008 $\pm$ 0.005, 0.008 $\pm$ 0.004 and 0.011 $\pm$ 0.005 PgC yr^{-1}, respectively), their normalized TW C_{anth} concentration increase in time (8.9 $\pm$ 6.8, 10.3 $\pm$ 8.5 and 11.0 $\pm$ 8.2 μmol kg^{-1}, respectively), although not significantly due to the large uncertainties. The divergence of transports between adjacent sections is the major component of the vertical flux of C_{anth}, which is mainly exported upwards to deep layers. Therefore, there is an enrichment of C_{anth} by the abyssal branch of the AMOC to the deep layers with

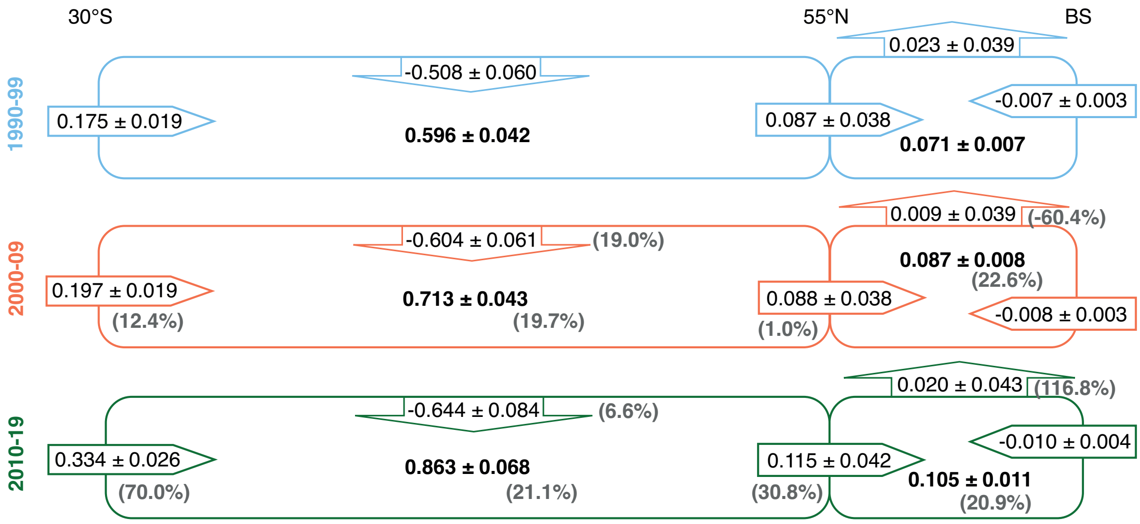

Figure 4.8. C_{anth} budget for the Atlantic Ocean box and for the box north of 55°N for each decade represented by different colors (blue for 1990–99, orange for 2000–09, and green for 2010–19). Each box is delimited on either side by the horizontal C_{anth} transport (PgC yr^{-1}) across the section with black regular values. In the cells of the Atlantic box the bold black values determine the C_{anth} storage (PgC yr^{-1}) as obtained from Gruber et al. (2019) and Sabine et al. (2004) normalized to the middle of each decade (1995, 2005 and 2015). North of 55°N, the C_{anth} storage is the combination of the estimations from Gruber et al. (2019) and Sabine et al. (2004) between 55°N and the Sills (63-66°N), and the values of 0.018 $\pm$ 0.04 PgC yr^{-1} in the Nordic Seas between 63-66 and 78°N (Jeansson et al., 2011) and 0.043 $\pm$ 0.04 PgC yr^{-1} in the Arctic Seas between 78°N and the Bering Strait (Tanhua et al., 2009), normalized to 2005. The vertical arrows at the top of each box are the vertical influx of C_{anth} (PgC yr^{-1}). The grey numbers within parenthesis represent the percentage of change between the 2000-09 and 1990-99 decades for the ones in the middle panel for the horizontal transport, storage and air-sea flux, and the change between the 2010-19 and 2000-09 decades for the bottom panel.

nearly depleted C_{anth}, generating a deep ventilation of C_{anth}. This signal can be found in the South Atlantic, with a significant transport up to 11°S (in 1990-99) and non-significant values at 24.5°N.

Defining the Atlantic basin with boundaries at 30°S and 55°N for all decades, we can detect an overall divergence over the basin, with a total storage and uptake from the atmosphere (Figures 4.6 and 4.8). This divergence in the transport at the boundaries of the Atlantic box results in an accumulation in the storage of C_{anth} over the whole basin, due to a change at 30°S significantly larger than the relatively low transports at 55°N. The storage rate supplied by this divergence is 14.7%, 15.3% and 25.3% per decade, with the increase in the last decade due to a $\sim$13% stronger overturning at 30°S.

4.3.3 Vertical fluxes of C_{anth}

In the North Atlantic the downward vertical mass transport between upper and deep layers (-6.1 ± 2.5, -4.2 ± 2.7 and -6.4 ± 2.4 Sv for each decade, respectively; Figure 4.9) represents a large part (57%, 37% and 56%) of the meridional transport across 24.5°N, manifesting the significance of the vertical overturning within the box between 24 and 55°N, with the remaining of the overturning north of 55°N.

The study of the balance of mass within each cell allows the estimation of the vertical transport of C_{anth} due to the vertical advection of mass. Accordingly, in the North Atlantic box (24.5°N – 55°N), the C_{anth} transports across the interphases between upper and deep layers show consistent relatively large values for a downward transport of C_{anth} to deep layers (-0.033. ± 0.014, -0.025 ± 0.016, -0.050 ± 0.019 PgC yr^{-1} for each decade, respectively).

In the South Atlantic, the upwelling of the recently ventilated AABW from the Southern Ocean results in an upward advection of C_{anth} transport from abyssal to deep layers. However, the vertical transport in the South Atlantic is dominated by the diffusive transport of C_{anth}, that appears due to the change at the interphase between layers from the vertical gradient of C_{anth} concentration along the water column. The larger concentration difference between upper and deep layers result in a larger diffusion transport at this interphase (-0.086 ± 0.026, -0.092 ± 0.028 and -0.119 ± 0.036 PgC yr^{-1} for each decade for the South Atlantic box, and -0.072 ± 0.021, -0.087 ± 0.026 and -0.094 ± 0.028 PgC yr^{-1} for the North Atlantic Box), with values around 40-47% of the storage of the upper layer. Normalizing to the year 2005, we can find similar values among decades, for both the South Atlantic (-0.109 ± 0.033, -0.094 ± 0.028 and -0.105 ± 0.032 PgC yr^{-1}) and North Atlantic (-0.090, -0.089 and -0.083 PgC yr^{-1}), supporting that these results follow the TSS in both boxes.

In the deep layers, there is a similar contribution from the north entrance of the AMOC and from the vertical fluxes from upper to deep layers (Figure 4.9). In the South Atlantic, the values are rather stable for all decades between the southward transport at the north boundary of the box at 24.5°N and the vertical fluxes due to the combination of vertical advection and diffusion caused by a vertical gradient in concentration of C_{anth} (-0.077 $\pm$ 0.021 and -0.086 $\pm$ 0.026, -0.095 $\pm$ 0.025 and -0.092 $\pm$ 0.028, and -0.114 $\pm$ 0.017 and -0.119 $\pm$ 0.036 PgC yr^{-1} for the horizonal deep transport and the vertical flux, respectively, for each decade). In the North Atlantic, these values are similar between the meridional deep transport and the total vertical flux (-0.066 $\pm$ 0.025 and -0.105 $\pm$ 0.025, -0.116 $\pm$ 0.022 and -0.112 $\pm$ 0.017, and -0.148 $\pm$ 0.028 and -0.144 $\pm$ 0.034 PgC yr^{-1}, respectively, for each decade) except for the first decade, when a weaker entrance from deep layers of the AMOC is overshadowed by the vertical input from the upper layers. Moreover, in the South Atlantic the main component of the vertical flux is the diffusion, and in the North Atlantic it accounts for $\sim$70% to 50% of the total vertical flux.

4.3.4 Storage and air-sea flux of C_{anth}

The storages within each box obtained from the inventories of Gruber et al. (2019) and Sabine et al. (2004) are stable for the South Atlantic (24% and 20% increase between 1990-99 and 2000-09 and between 2000-09 and 2010-19, respectively), whereas they have increased for the North Atlantic (15% and 22%; Figure 4.6). The values for the upper branch of the AMOC remain stable, and we can find the deceleration with respect to TSS between the first two decades and the relative acceleration between the last two in the lower branch of the AMOC in the North Atlantic (10% and 25%, respectively).

Generally, the storage for the whole column is greater in the box occupying the South Atlantic, due to its larger volume. However, the changes in concentrations are lower in the South Atlantic (164 $\pm$ 8, 201 $\pm$ 9 and 243 $\pm$ 9 μmol m^{-3} yr^{-1}, respectively per decade) than in the North Atlantic (317 $\pm$ 6, 372 $\pm$ 7 and 450 $\pm$ 6 μmol m^{-3} yr^{-1}, respectively).

The storage of upper layers contributes to $\sim$59% of the net storage between 30°S and 24.5°N and 55-56% between 24.5°N and 55°N, manifesting the importance of deep layers in the storage of C_{anth}, although involved in processes occurring on longer timescales. For the whole region studied, the ratio between net uptake and storage is high ($>$70%), indicating that the storage of C_{anth} happens mostly as a result of the gain of C_{anth} from the atmosphere (Figure 4.6). Part of the uptake arriving to upper layers propagates downward and contributes significantly to the storage by deep layers. The vertical advection in the North Atlantic driven by the AMOC also provides to the storage in deep waters. The values in the South Atlantic increase with time, responding to the increase in the atmospheric pCO_2 which causes larger values of C_{anth} storage.

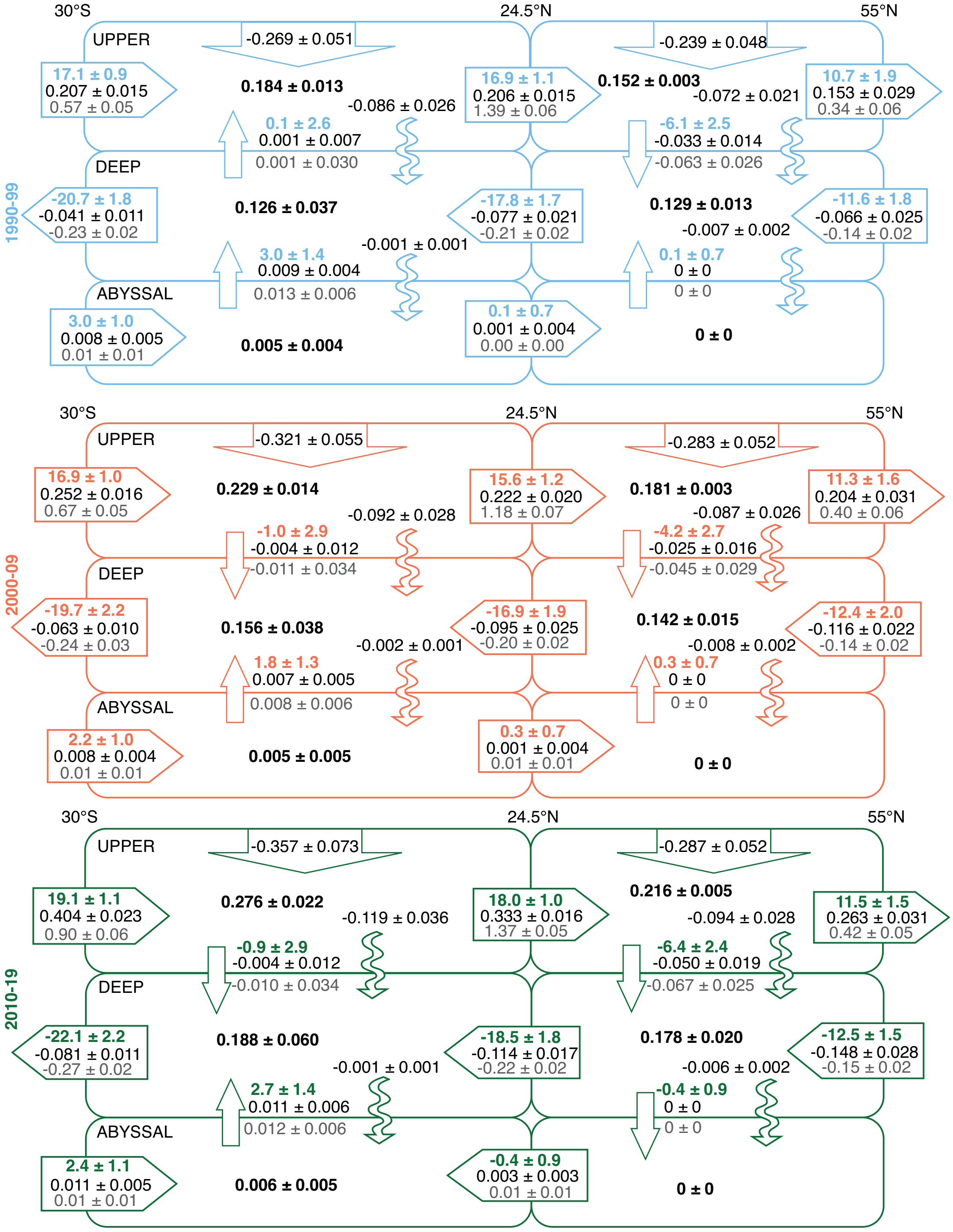
30°S
24.5°N
55°N
UPPER
-0.269 ± 0.051
-0.239 ± 0.048
17.1 ± 0.9
0.207 ± 0.015
0.57 ± 0.05
0.184 ± 0.013
-0.086 ± 0.026
16.9 ± 1.1
0.206 ± 0.015
1.39 ± 0.06
0.152 ± 0.003
-0.072 ± 0.021
10.7 ± 1.9
0.153 ± 0.029
0.34 ± 0.06
0.1 ± 2.6
0.001 ± 0.007
0.001 ± 0.030
-6.1 ± 2.5
-0.033 ± 0.014
-0.063 ± 0.026
DEEP
1990-99
-20.7 ± 1.8
-0.041 ± 0.011
-0.23 ± 0.02
0.126 ± 0.037
-17.8 ± 1.7
-0.077 ± 0.021
-0.21 ± 0.02
0.129 ± 0.013
-0.007 ± 0.002
-11.6 ± 1.8
-0.066 ± 0.025
-0.14 ± 0.02
-0.001 ± 0.001
3.0 ± 1.4
0.009 ± 0.004
0.013 ± 0.006
0.1 ± 0.7
0 ± 0
0 ± 0
ABYSSAL
3.0 ± 1.0
0.008 ± 0.005
0.01 ± 0.01
0.005 ± 0.004
0.1 ± 0.7
0.001 ± 0.004
0.00 ± 0.00
0 ± 0
30°S
24.5°N
55°N
UPPER
-0.321 ± 0.055
-0.283 ± 0.052
16.9 ± 1.0
0.252 ± 0.016
0.67 ± 0.05
0.229 ± 0.014
15.6 ± 1.2
0.222 ± 0.020
1.18 ± 0.07
0.181 ± 0.003
11.3 ± 1.6
0.204 ± 0.031
0.40 ± 0.06
-0.092 ± 0.028
-0.087 ± 0.026
-1.0 ± 2.9
-0.004 ± 0.012
-0.011 ± 0.034
-4.2 ± 2.7
-0.025 ± 0.016
-0.045 ± 0.029
DEEP
2000-09
-19.7 ± 2.2
-0.063 ± 0.010
-0.24 ± 0.03
0.156 ± 0.038
-16.9 ± 1.9
-0.095 ± 0.025
-0.20 ± 0.02
0.142 ± 0.015
-12.4 ± 2.0
-0.116 ± 0.022
-0.14 ± 0.02
-0.002 ± 0.001
-0.008 ± 0.002
1.8 ± 1.3
0.007 ± 0.005
0.008 ± 0.006
0.3 ± 0.7
0 ± 0
0 ± 0
ABYSSAL
2.2 ± 1.0
0.008 ± 0.004
0.01 ± 0.01
0.005 ± 0.005
0.3 ± 0.7
0.001 ± 0.004
0.01 ± 0.01
0 ± 0
30°S
24.5°N
55°N
UPPER
-0.357 ± 0.073
-0.287 ± 0.052
19.1 ± 1.1
0.404 ± 0.023
0.90 ± 0.06
0.276 ± 0.022
-0.119 ± 0.036
18.0 ± 1.0
0.333 ± 0.016
1.37 ± 0.05
0.216 ± 0.005
-0.094 ± 0.028
11.5 ± 1.5
0.263 ± 0.031
0.42 ± 0.05
-0.9 ± 2.9
-0.004 ± 0.012
-0.010 ± 0.034
-6.4 ± 2.4
-0.050 ± 0.019
-0.067 ± 0.025
DEEP
2010-19
-22.1 ± 2.2
-0.081 ± 0.011
-0.27 ± 0.02
0.188 ± 0.060
-18.5 ± 1.8
-0.114 ± 0.017
-0.22 ± 0.02
0.178 ± 0.020
-12.5 ± 1.5
-0.148 ± 0.028
-0.15 ± 0.02
-0.001 ± 0.001
-0.006 ± 0.002
2.7 ± 1.4
0.011 ± 0.006
0.012 ± 0.006
-0.4 ± 0.9
0 ± 0
0 ± 0
ABYSSAL
2.4 ± 1.1
0.011 ± 0.005
0.01 ± 0.01
0.006 ± 0.005
-0.4 ± 0.9
0.003 ± 0.003
0.01 ± 0.01
0 ± 0

Figure 4.9. C_{anth} budget in the Atlantic Ocean for two superboxes – 30°S to 24.5°N and 24.5°N to 55°N for each decade, represented by different colors (blue for 1990–99, orange for 2000–09, and green for 2010–19). For each decade, the upper boxes, represent the values for the upper layer, the middle boxes the deep layers and the bottom boxes represent the abyssal layers. Each box is delimited on either side by the horizontal transport across the section, specifying the transport of different properties: C_{anth} transport (PgC yr^{-1}) appears with black regular values, heat transport (PW) are the grey regular values, and the mass transport (Sv) are the colored bold values. The strait arrows at the interphase between upper and deep and deep and abyssal layers represent the exchange due to the vertical advection of mass across the layers. The properties associated to this vertical advection are the same as for the horizontal transport. The wiggly arrows correspond to the vertical diffusion across the interphase due to differences in the vertical derivative of C_{anth} concentration, with the values for C_{anth} diffusion transport in black regular font. Within each cell there is a bold black value that determines the C_{anth} storage (PgC yr^{-1}) as obtained from Gruber et al. (2019) and Sabine et al. (2004) normalized to middle of each decade (1995, 2005 and 2015). The vertical arrows at the top of the upper box are the vertical influx of C_{anth} (PgC yr^{-1}), namely the atmospheric input for the net and upper boxes.

4.4 Discussion

4.4.1 South Atlantic box

A net C_{anth} transport of 0.10 PgC yr^{-1} entering the South Atlantic across 30°S has been reported from hydrographic data for 1993 (Holfort et al. 1998; Macdonald et al. 2003; Figures 4.4 and 4.10). Our results for the same cruise are substantially larger (0.175 $\pm$ 0.019 PgC yr^{-1}), consistently increasing for the following decades. These values can be evaluated against model results that have yielded comparably similar (0.18 $\pm$ 0.01 for 1995; Mikaloff Fletcher et al. 2006) and larger estimates (0.34 $\pm$ 0.01 at 35°S for 2012; DeVries 2014). These values reflect the northward transport of C_{anth} from the recently formed central and intermediate waters from the Southern Ocean, decreasing in strength on its way northward.

Our results for the South Atlantic C_{anth} storage are like other estimates for a similar latitudinal extension for the 1990-99 decade (0.31 $\pm$ 0.02 PgC yr^{-1} from 30°S to 18°N, Mikaloff Fletcher et al. 2006; 0.250 PgC yr^{-1} from 30°S to 25°N, Macdonald et al. 2003; 0.265 $\pm$ 0.011 PgC yr^{-1}, Rosón 2003, and agree with the value from DeVries (2014) for 2012 from 30°S to 30°N (0.460 PgC yr^{-1}).

Moreover, the weaker value at 30°S from Holfort et al. (1998) creates a negative divergence within the South Atlantic box, with stronger meridional transports at 24.5°N, turning into an intensified uptake from the atmosphere (-0.340 PgC yr^{-1}, Macdonald et al. 2003; -0.394 $\pm$ 0.107 PgC yr^{-1}, Rosón 2003). However, sections with a decreasing northward transport and positive divergence present a consistent weaker uptake from the atmosphere (-0.160 $\pm$ 0.017 PgC yr^{-1}, Mikaloff Fletcher et al. 2006; -0.220 PgC yr^{-1}, DeVries 2014). Therefore, the strength of the meridional transport across the southern boundary of the Atlantic Ocean is an important factor in determining the role of meridional advection in the budget of C_{anth} in the South Atlantic.

Evans et al. (2017), using hydrographic sections from 2008-2009, have found a net northward

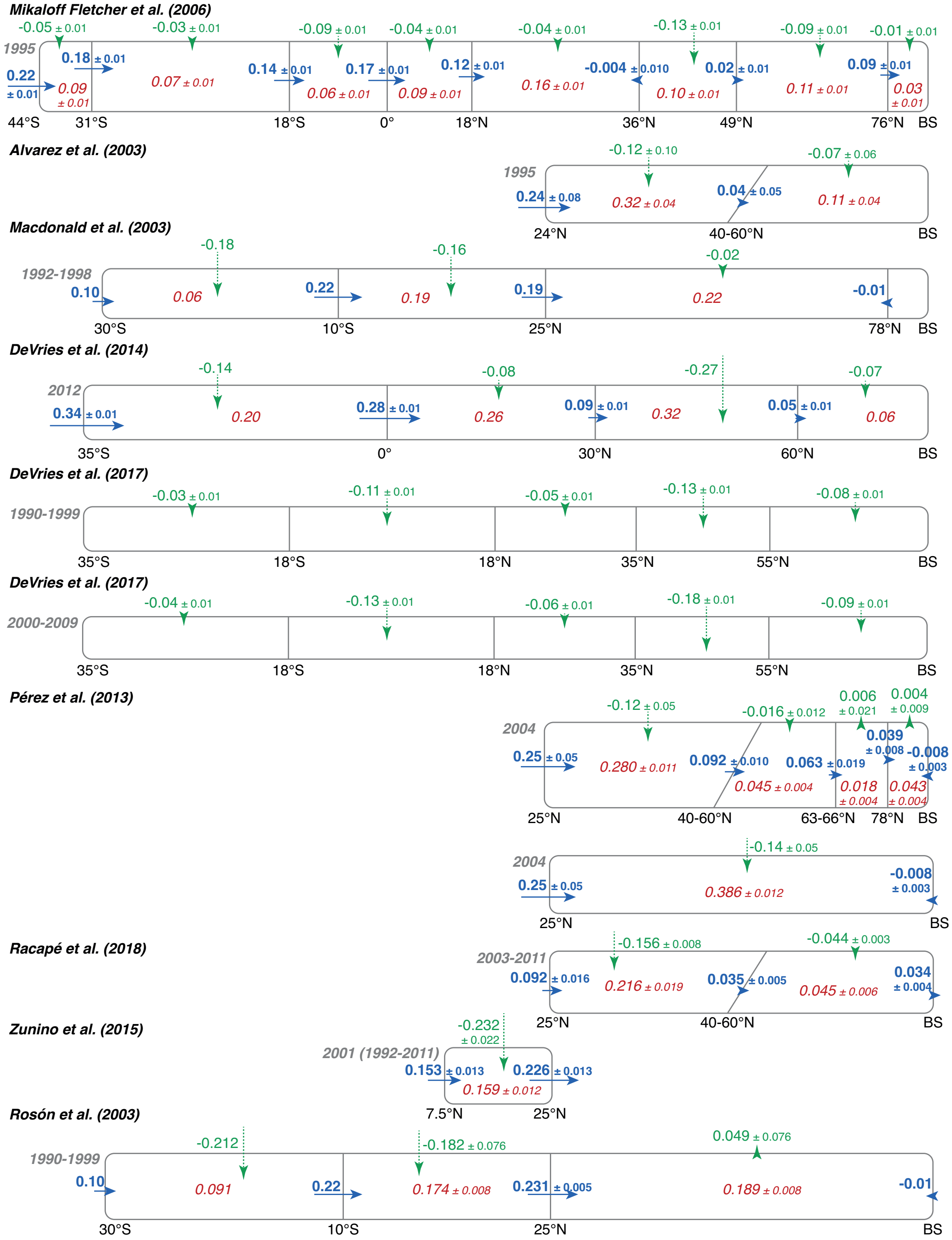

Figure 4.10. Horizontal transports (blue), storages (red) and vertical fluxes (green) of C_{anth} obtained from the literature, with reference to the years in grey at the top left of the box.

C_{anth} transport at 24°S of 0.28 ± 0.16 PgC yr^{-1} that is similar to our results at the same latitude in 2000-09 of a net northward transport of 0.24 ± 0.03 PgC yr^{-1}. This northward transport coming from surface, intermediate and abyssal layers arrive to the South Atlantic from the surface Agulhas Leakage and the whole-column input from Drake Passage, increasing the C_{anth} concentration at upper and abyssal layers (Figure 4.6 and 4.7).

Deep ventilation in the South Atlantic assimilates C_{anth}-enriched waters to abyssal depths. The northward flow of AABW transports a part of the C_{anth} air-sea uptake happening in the Southern Ocean, estimated as a 40% of the global uptake (Khatiwala et al., 2009). Complementing the decrease in mass transport on its way northward, the AABW also gets mixed with the low-TW C_{anth} NADW above and decreases its concentration. The Atlantic sector of the Southern Ocean presents moderately high concentrations of C_{anth} in deep waters ($\sim$10 µmol kg^{-1}), with similar concentrations reported below 4000 m between 30 and 50°S (Ríos et al., 2010) in 1994, which coincide with the TW C_{anth} estimates at 30°S for all decades, with a slightly larger value at 45°S for the first decade (Figure 4.7). The rate of increase for AABW determined by Ríos et al. (2012) of 0.15 ± 0.05 µmol kg^{-1} yr^{-1} agrees with the change in TW C_{anth} for the abyssal layer at 30°S between the first two decades, with 1.4 ± 10.8 µmol kg^{-1} difference between both cruises, although our values present large uncertainties arising from mass transport-weighted averaging. We have also found a non-significant slowing in the trend between 2000-09 and 2010-19, with a net change in concentration of 0.7 ± 11.8 µmol kg^{-1}. Orsi et al. (2002) determined a 21-Sv flow out of the Southern Ocean by the upper and lower Circumpolar Deep Waters and the AABW. Knowing that our contribution to the abyssal Atlantic basin is only 11% of this estimation for the whole basin (2.4 ± 1.2 Sv), the transport of C_{anth} by abyssal layers results in 0.011 PgC yr^{-1}, a value like our estimations at 45° and 30°S.

4.4.2 North Atlantic box

C_{anth} transports at 24.5°N present similar strengths for the 1990-99 and 2000-09 periods, that then recuperate in the last decade. The value in the 2004 cruise at 24.5°N is lower than expected, coinciding with a period of strong UMO (Worthington et al., 2021) as estimated by empirical models using observational data. This strong southward UMO, in turn, reduces the strength of the AMOC for this period, with stable values for the Florida Strait, Ekman, and deep layer transports. Therefore, the low C_{anth} transport at 24.5°N can be a result of a strengthening in the opposing southward transport carried by the UMO, accompanied by a reduction in the weighted C_{anth} concentration, as shown by the relatively low, although not significantly, values of TW C_{anth} for this period.

Brown et al. (2021) have published a time series reconstruction of C_{anth} transports across 24.5°N using data from the RAPID/MOCHA/WBTS mooring array and hydrographic observations. In the upper limb of the AMOC, decreasing northward mass transports were compensated by increasing C_{anth} concentration, resulting in a compensated northward C_{anth} transport for the 8.5-year period. We have compared our included cruises for 2000-09 and 2010-19 decades to the time series, and we have found similar values at the time of the cruise for each of the decompositions of the transport. The overturning C_{anth} transport (Figure 4.2 b) dominates the mean and variability of the total C_{anth} transport, with consistent negative values for the horizontal component for all the time series. Similarly, the upper layer of the water column, above 1100 m, holds this variability (Figure 4.2 c), with small values for deep and abyssal transports, the latter almost negligible. The increasing trend in our results is also present in the 8.5-yr time-series, that can be attributed to the increase in the Florida Straits C_{anth} transport, while there is a stabilization in the Ekman transport across the section, resulting in the decrease of transport of the UMO.

The North Atlantic has been closely monitored, especially at the centre of the subtropical gyre at 24.5°N and at the OVIDE section in the SPNA (Figures 4.4 a and 4.10). We have found meridional transports at 24.5°N similar to the estimates by ocean inversions that combine C_{anth} observations with results from general circulation models (0.12 ± 0.01 PgC yr^{-1} at 18°N for 1995, Mikaloff Fletcher et al. 2006; 0.09 ± 0.01 PgC yr^{-1} at 30°N for 2012, DeVries 2014), and by results from global biogeochemical ocean general circulation models (0.092 ± 0.016 PgC yr^{-1} at 25°N for 2003-2011, Racapé et al. 2018). Solutions from hydrographic data for 24.5°N present stronger meridional transports (0.19 PgC yr^{-1} for 1992-1998, Macdonald et al. 2003; 0.23 ± 0.01 PgC yr^{-1} for 1990-1999, Rosón 2003; 0.24 ± 0.08 PgC yr^{-1} for 1995, Álvarez et al. 2003; 0.23 ± 0.01 PgC yr^{-1} for 2001, Zunino et al. 2015b; 0.25 ± 0.05 PgC yr^{-1} for 2004, Pérez et al. 2013).

For our northernmost sections, at 55°N, we are closer to the estimations supporting strong lateral transports at these latitudes (0.09 PgC yr^{-1} at 76°N for 1995, Mikaloff Fletcher et al. 2006; 0.063 ± 0.019 PgC yr^{-1} at 63-66°N for 2004, Pérez et al. 2013), marking a strong overturning that carries C_{anth} into the Nordic Seas via the deep convection taking place in this region.

The estimated amount of C_{anth} stored in the North Atlantic is quite similar to other studies, but we can find differences in the value of C_{anth} acquired from the atmosphere (Table 4.11), with low values for results from ocean general circulation models (Racapé et al., 2018), ocean inversions (DeVries et al., 2017) and hydrographic estimations (Álvarez et al., 2003; Macdonald et al., 2003; Pérez et al., 2013; Rosón, 2003).

4.4.3 C_{anth} in the Atlantic basin and connection to the Arctic Ocean

Using the estimations from Pérez et al. (2013) of -0.008 ± 0.003 PgC yr^{-1} of C_{anth} transport referenced to 2004 for the Bering Strait we have constructed a box between 55°N and the Bering Strait. The storages for this box were divided into the box between 55°N and the Greenland-Iceland-Scotland Sills (∼63-66°N), and the combined results north of the Sills from Pérez et al. (2013). North of the Sills the values comprised 0.018 ± 0.04 PgC yr^{-1} in the Nordic Seas between

Table 4.11. Literature values of C_{anth} uptake from the atmosphere in the North Atlantic, referenced to the year from the study and normalized to 2005 assuming TSS.

	Latitudes	Reference year	Uptake (Pgc yr^{-1})	Uptake (norm 2005; Pgc yr^{-1})
OGCM				
Mikaloff Fletcher et al. (2006)	44 - 31°S	1995	-0.05 ± 0.01	-0.06 ± 0.01
	31 - 18°S	1995	-0.03 ± 0.01	-0.04 ± 0.01
	18°S - 0°	1995	-0.09 ± 0.01	-0.11 ± 0.01
	0° - 18°N	1995	-0.04 ± 0.01	-0.05 ± 0.01
	18 - 36°N	1995	-0.04 ± 0.01	-0.05 ± 0.01
	36 - 49°N	1995	-0.13 ± 0.01	-0.16 ± 0.01
	49 - 76°N	1995	-0.09 ± 0.01	-0.11 ± 0.01
	76°N - BS	1995	-0.01 ± 0.01	-0.01 ± 0.01
Racapé et al. (2018)	25 - 40/60°N	2003-2011	-0.156 ± 0.008	-0.150 ± 0.008
	40/60°N - BS	2003-2011	-0.044 ± 0.003	-0.042 ± 0.003
OCIM				
DeVries (2014)	35°S - 0°	2012	-0.14	-0.12
	0° - 30°N	2012	-0.08	-0.07
	30 - 60°N	2012	-0.27	-0.24
	60°N - BS	2012	-0.07	-0.06
DeVries et al. (2017)	35 - 18°S	1990-1999	-0.03 ± 0.01	-0.04 ± 0.01
	18°S - 18°N	1990-1999	-0.11 ± 0.01	-0.13 ± 0.01
	18 - 35°N	1990-1999	-0.05 ± 0.01	-0.06 ± 0.01
	35 - 55°N	1990-1999	-0.13 ± 0.01	-0.16 ± 0.01
	55°N - BS	1990-1999	-0.08 ± 0.01	-0.10 ± 0.01
	35 - 18°S	2000-2009	-0.04 ± 0.01	-0.04 ± 0.01
	18°S - 18°N	2000-2009	-0.13 ± 0.01	-0.13 ± 0.01
	18 - 35°N	2000-2009	-0.06 ± 0.01	-0.06 ± 0.01
	35 - 55°N	2000-2009	-0.18 ± 0.01	-0.18 ± 0.01
	55°N - BS	2000-2009	-0.09 ± 0.01	-0.09 ± 0.01
Hydrographic estimations				
Álvarez et al. (2003)	24 - 40/60°N	1995	-0.12 ± 0.10	-0.14 ± 0.12
	40/60°N - BS	1995	-0.07 ± 0.06	-0.08 ± 0.07
Macdonald et al. (2003)	30 - 10°S	1992-1998	-0.18	-0.22
	10°S - 25°N	1992-1998	-0.16	-0.19
	25 - 78°N	1992-1998	-0.02	-0.02
Pérez et al. (2013)	25 - 40/60°N	2004	-0.12 ± 0.05	-0.12 ± 0.05
	40/60 – 63/66°N	2004	-0.016 ± 0.012	-0.016 ± 0.012
	63/66 - 78°N	2004	0.006 ± 0.021	0.006 ± 0.021
	78°N - BS	2004	0.004 ± 0.009	0.004 ± 0.009
	25°N - BS	2004	-0.14 ± 0.05	-0.14 ± 0.05
Rosón (2003)	30 - 10°S	1990-1999	-0.212	-0.258
	10°S - 25°N	1990-1999	-0.182	-0.222
	25°N - BS	1990-1999	0.049	0.060
Zunino et al. (2015b)	7.5 - 25°N	1992 - 2011	-0.232 ± 0.022	-0.248 ± 0.023

63-66 and 78°N (Jeansson et al., 2011) and 0.043 ± 0.04 PgC yr^{-1} in the Arctic Seas between 78°N and the Bering Strait (Tanhua et al., 2009). The storages for each decade within the box between 55°N and the Sills were computed following the same methodology applied to the rest of the Atlantic, using the storage rates of Gruber et al. (2019) and the inventories of Sabine et al. (2004), and then normalized to 2005 assuming TSS (Figure 4.8).

Contrary to the Atlantic basin, where there is an uptake of C_{anth} throughout the basin, north of the SPNA there is a small loss of C_{anth} to the atmosphere, as the upper water masses are carrying large amounts of C_{anth} that become saturated as they cool during their northward transport. These estimations agree with the values north of the sills in Pérez et al. (2013), in boxes where the meridional divergence of C_{anth} transport dominates over its storage. The selection of transport from the Bering Strait influences on the net divergence in the box and, therefore on the sign of the atmospheric uptake and whether gain or loss towards the atmosphere is happening.

These values are relatively small, comparable to the negligible uptake of C_{anth} from the atmosphere in the Nordic Seas from Jeansson et al. (2011). However, the overturning circulation occurring at these latitudes redistributes the C_{anth} in the region and returns the upper layers of C_{anth}-enriched waters to the deep ocean. In turn, they then go back to the North Atlantic as the part of the dense overflows, with a lower layer representing a 43%, 57% and 56% of the transport in upper layers at 55°N for each decade, respectively (Figure 4.6).

4.4.4 Vertical transport of C_{anth}

The Atlantic Ocean is, proportionally, the basin accumulating more C_{anth} in the whole column (12.5 gC m^{-2} yr^{-1} in the Atlantic and 6.9 gC m^{-2} yr^{-1} in the Pacific), and, especially, the basin accumulating more C_{anth} below 1000 m, over four times the C_{anth} stored in the Pacific (6.5 gC m^{-2} yr^{-1} in the Atlantic versus 1.5 gC m^{-2} yr^{-1} in the Pacific; Gruber et al. 2019). The vertical transport of C_{anth} has been often overlooked or restricted to the upper layers of the water column. However, we have seen that vertical advection and diffusion take part in the redistribution of C_{anth} in the ocean interior. Exporting more C_{anth} from the surface to the bottom and at a higher rate favors a larger future uptake of C_{anth}.

Figure 4.9 shows both overturning and diffusive mixing playing an important role in the transfer of C_{anth} from the atmosphere to deep layers. These vertical processes contribute to a considerable percentage of the net uptake of C_{anth} from the atmosphere (51%, 53% and 64% per decade, respectively), redistributing the newly gained C_{anth} to deep layers. From the net uptake in the Atlantic Ocean (-0.508 ± 0.060, -0.604 ± 0.061 and -0.644 ± 0.084 PgC yr^{-1}), the overturning north of 55°N supplies the C_{anth} sequestered by the overflow waters (-0.066 ± 0.025, -0.116 ± 0.022 and -0.148 ± 0.028 PgC yr^{-1} for each decade, respectively). In the north Atlantic box, there is also downward flux of mass associated with the overturning, advecting C_{anth} with it to deep layers (-0.033 ± 0.014, -0.025 ± 0.016 and -0.050 ± 0.019 PgC yr^{-1}). Over the whole basin (30°S to

55°N), mixing diffuses C_{anth} from upper to deep layers (-0.158 ± 0.033, -0.179 ± 0.029 and -0.213 ± 0.046 PgC yr^{-1}).

Both advection and diffusion, involved in vertical transfer of properties, contribute almost equally to the interior storage of C_{anth}. These processes have not been described nor evaluated and are new parameters to include in the models. This could be relevant in the future to the simulations using different IPCC scenarios. Holzer et al. (2021) have highlighted the importance of diffusion transports in the control of Pacific carbon and nutrient storage.

DeVries et al. (2017) have previously manifested the importance of the changes in the strength of the overturning in the uptake of CO_2 by the ocean. They modeled the stronger and weaker overturning in the upper ocean for the 1990s and 2000s, respectively, and found that an intense AMOC results in and increased outgassing of natural CO_2, while the uptake of C_{anth} by the ocean also grew. However, with a weaker overturning in the 2000s, both gas exchanges decline and there appear a reduced outgassing of natural CO_2 and reduced uptake of C_{anth}. The vertical transport of mass to deep layers (>1000 m) found by DeVries et al. (2017) shows strong export to deep layers in the Nordic Seas, north of 55°N, with a small contribution from the SPNA of 2 ± 1 Sv for the 1980s and 1990s and stronger for the 2000s (7 ± 1 Sv). The latter estimation is more similar to our vertical advection of mass between 24.5°N and 55°N (Figure 4.9; -6.1 ± 2.5, -4.2 ± 2.7 and -6.4 ± 2.4 Sv for each decade, respectively). Racapé et al. (2018) also evaluated the vertical transfer of C_{anth} from surface to deep waters and found that it occurred mainly north of the OVIDE section (40-60°N), with -0.097 ± 0.028 PgC yr^{-1} exported to deep layers between 1959 and 1994 and -0.175 ± 0.021 PgC yr^{-1} between 1996 and 2011.

4.5 Conclusions

This study has evaluated the meridional and vertical transports of C_{anth} in the Atlantic Ocean for the whole water column, assessing the importance of the deep and bottom layers in the redistribution of C_{anth}. We have obtained our results from three inverse models for the last three decades combining continuity equations of mass and biogeochemical tracers for boxes bounded by contiguous across-ocean zonal sections.

Our results for the South Atlantic reflect the northward transport of C_{anth} from the water masses recently formed in the Southern Ocean, with increasing values with time. At 24.5°N, we have detected the lower-than-expected values in the overturning for the 2004 cruise, possibly due to a strengthening of the UMO at the time, and thus increasing the southward horizontal component of the C_{anth} transport. In general, changes in the net transport of C_{anth} appear due to differences in the upper layer, with values for the lower branch of the AMOC more consistent with time.

We have included not only the meridional transports, but also the vertical transfers between upper and deep and deep and abyssal layers, evaluating the contribution of these processes in the net uptake of C_{anth}. The overturning in the North Atlantic, and especially in the SPNA and Nordic Seas, plays an important role in the redistribution of the newly gained C_{anth} from the atmosphere, with relatively large fluxes exporting C_{anth} to deep layers. In the South Atlantic, the abyssal layers play a role in the introduction of C_{anth} from the AABW into the water column, and as a result provide an upward flux of C_{anth} from abyssal to deep layers. Mixing by diffusion processes occurs over the whole Atlantic, mainly in the interphase between upper and deep layers, where a stronger gradient is present, and is the main process exporting C_{anth} from upper to deep layers in the South Atlantic.

Chapter 5

Conclusions and further research

5.1 Conclusions

In summary, this thesis has successfully obtained a comprehensive picture of the Atlantic Meridional Overturning Circulation (AMOC) across the Atlantic basin over the last thirty years in terms of mass, heat, freshwater and anthropogenic carbon applying inverse methods to hydrographic data.

Firstly, we have studied the net transports of mass, heat and freshwater by the AMOC at the available hydrographic zonal sections between 45°S and 55°N. These transports are the solutions obtained from three inverse models, each one containing sections within 1990-99, 2000-09 and 2010-19. The main results from this study are:

- The presence of two counter-rotating overturning cells in the Atlantic conform the meridional structure of the AMOC and have persisted for the last thirty years. The upper overturning cell is partially closed by the vertical transport of water. A consistent circulation through the decades is observed, with upwelling in the southern subtropical gyre and downwelling in the northern subtropical gyre and the subpolar North Atlantic.
- No apparent change in the overturning strength among the diverse hydrographic realizations carried out in different decades is registered, with no differences observed for the upper, deep, and abyssal layers across the Atlantic Ocean. The values of intensity of the AMOC are in the range of 16-20 Sv between 45°S and 47°N and around 12 Sv at 55°N.
- In the northernmost section, at 55°N, where deep water formation occurs, the eastern basin is the main contributor to the AMOC, with the western basin (Labrador Sea) supplying a fairly constant weak transport, supporting the findings by the OSNAP and OVIDE observing programs.
- The overturning heat transport, which represents changes in the meridional structure of the water column, dominates the total heat transport and increases equatorward. This heat component remains constant in the Atlantic except in certain latitudes, manifesting changes at 24.5°N and a net increase between the first and the last decade at 30°S. The horizontal or gyre component presents constant values across all latitudes and through the decades of this study.
- The freshwater overturning component presents a stronger southward transport in the sections close to the equator. Most of the sections fail to show changes with time, but at 24.5°N the 2000-09 decade yields a lower value of freshwater overturning and at 30°S there is a net increase in the southward freshwater overturning between the first and last decade, with values close to zero. The horizontal or gyre freshwater flux displays a higher northward value in the sections that occupy the subtropical gyres, with similar values for all decades.

- Interestingly, this tendency towards stronger southward freshwater overturning at 30°S between 1990-99 and 2010-19 shows that the AMOC effectively exports freshwater out of the Atlantic. These results indicate that the AMOC may be in a bistable state. According to model studies, the overturning freshwater flux at this latitude has been identified as a possible proxy for the stability of the AMOC, potentially determining whether it is in a monostable or bistable regime.

Using the solutions from the same inverse models, we have studied the horizontal circulation in the Atlantic Ocean attending to the main meridional currents that take part in the AMOC. The wind-driven gyre circulation in the Atlantic is described by surface currents in subtropical basins, with stronger poleward western boundary currents compensated by weaker eastern boundary currents and equatorward flow in the ocean interior occupying a broader longitudinal extent. In general, no trends in time appear for any current strength, with consistent estimates found for the three different decades. The main results obtained for the upper, deep and abyssal circulation are as follows:

- Of the net 61 Sv entering the South Atlantic at 45°S, 61% belong to the cold and fresh waters of the Malvinas Current and 39% to the warmer and saltier water from the Benguela and South Equatorial Currents.
- In the North Atlantic, the Gulf Stream feeds the subtropical and subpolar gyres, with warm water from the Florida and Antilles Currents. Between 24.5°N and 55°N, there is a sink to deeper layers of over 5 Sv, with the remaining transport flowing northward on the North Atlantic Current contributing to the subpolar North Atlantic.
- The newly formed deep water enters the Atlantic basin via the Iceland-Scotland Overflow Waters and Denmark Strait Overflow Waters, with a stronger contribution from the Iceland-Scotland Overflow Waters.
- The Deep Western Boundary Current shows continuity on its way south, until reaching south of about 19°S, where it bifurcates into a western branch and an eastern branch that crosses the Mid-Atlantic Ridge.
- Abyssal waters are mainly confined to the South Atlantic, reaching up to 24.5°N, with a net northward input via the western basin.
- The heat transport introduced in the South Atlantic by the warm and salty waters of the Agulhas leakage is distributed along the eastern basin. This heat transport is divided into the contributions for the Benguela Current and South Equatorial Current, both reducing its heat transport northward. The cold and fresh waters of the Malvinas Current introduce only half of the transport found on the eastern basin, with a southward heat export toward the Southern Ocean of around 1 PW.

- The northward transport of heat in the upper layers of the North Atlantic is mainly achieved by the strong heat transported by the Florida Current that increases in the Gulf Stream at 36°N. The convection processes in the subpolar North Atlantic result in a decrease of heat transport for the North Atlantic Current at 47°N.
- In deep layers, the Deep Western Boundary Current carries roughly -0.3 PW southward, starting at 47°N from the Grand Banks throughout the North Atlantic and the South Atlantic up to 24°S.
- The freshwater flux is confined to the upper layers, with a transport into the South Atlantic via the Malvinas Current, counteracted by the Benguela Current.
- In the North Atlantic, there is mainly a southward freshwater flux along the western basin.

Finally, we have incorporated not only the transports of mass, heat and freshwater, but also the study of the budget of anthropogenic carbon (C_{anth}) in the Atlantic Ocean. We have successfully incorporated biogeochemical equations into the inverse model, constraining the conservation of oxygen, nitrate, silicate and phosphate to further define the carbon pump in the water column. The introduction of these variables in our study enables us to find the following conclusions:

- The change in the net transport of C_{anth} appears from the variability in the upper layers.
- There is a northward transport of C_{anth} from the recently formed central and intermediate waters from the Southern Ocean, decreasing in strength on its way northward.
- C_{anth} transports at 24.5°N presents a value lower than expected for the 2000-09 decade, related to a weaker overturning strength. This value coincides with a period of strong upper mid-ocean as estimated by empirical models using observational data. This low C_{anth} transport at 24.5°N can be a result of a strengthening in the opposing southward transport carried by the upper mid-ocean, accompanied by a reduction in the weighted C_{anth} concentration.
- For our northernmost sections, at 55°N, we are closer to the estimations supporting strong lateral transports at these latitudes, marking a strong overturning that carries C_{anth} into the Nordic Seas via the deep convection taking place in this region.
- The overturning in the North Atlantic, and especially in the subpolar North Atlantic and Nordic Seas, plays an important role in the redistribution of the newly gained C_{anth} from the atmosphere, with relatively large fluxes exporting C_{anth} to deep layers.
- In the South Atlantic, the abyssal layers play a role in the introduction of C_{anth} into the water column through the Antarctic Bottom Water, and provide, consequently, an upward flux of C_{anth} from abyssal to deep layers.

- Mixing by diffusion processes occurs over the whole Atlantic, mainly in the interphase between upper and deep layers, where a stronger gradient is present, and is the main process exporting C_{anth} from upper to deep layers in the South Atlantic.

5.2 Further research

The behaviour of the AMOC and its driving mechanisms and feedbacks has received much attention in climate change scenarios due to the major climate impacts associated with a predicted slowdown. In this regard, this thesis has produced new results using a similar approach to the global inverse solutions obtained in the 1990s with WOCE sections for both horizontal and vertical transport (Ganachaud & Wunsch, 2000; Ganachaud, 2003b; Ganachaud & Wunsch, 2003). One of the main questions arising is whether these values are representative of the time series of the AMOC at each latitude.

We cannot assume that the estimations from inverse models correspond to the time-average values. Several studies have understood inverse solutions obtained from hydrographic sections as snapshots of the circulation at the time of the cruise. This limitation prevents us from determining the trends of the AMOC through decades, and we can only estimate that, for each hydrographic section, the AMOC is unchanged between the different realizations. We have been working on understanding the adjustment of the inverse model on the use of single or multiple sections, and whether those solutions can represent the time of the cruise or a longer period. The results from this study are currently under revision in *Geophysical Research Letters*. We have used all available hydrographic zonal sections at 24.5°N and 30°S over the last thirty years to infer that single section inverse models agree with monthly outputs from the ocean general circulation model MOM (Modular Ocean Model) at the time of the cruise. In contrast, inverse models using multiple sections at different latitudes and times of the year for each of the last three decades are more consistent with decadal averages from MOM. In conclusion, we have observed that the solutions of inverse models with single sections are affected by aliasing and represent the state of the ocean at the time of the cruise. However, aliasing is greatly reduced when using multiple sections to assess low-frequency variability.

Moreover, we have included the estimations of vertical fluxes of mass and anthropogenic carbon in the Atlantic Ocean between two sections at the interphase between different layers of neutral density. Further work could be aimed to investigate the relative role of advection and mixing processes in the overturning in areas of strong convection and in the ocean interior.

Finally, there are still many unknowns and challenges in the South Atlantic despite the presence of a monitoring array at 34.5°S. The South Atlantic acts as the area of exchange with the Pacific, Indian and Southern Oceans, and therefore can influence the properties of the water masses in the whole Atlantic Ocean. Thus, analyses of the meridional coherence of the AMOC should rely on a stronger effort in determining longer, higher-resolution estimates of the reconstructions, present state and projections of the intensity of the AMOC.

Appendix A

Vertical sections

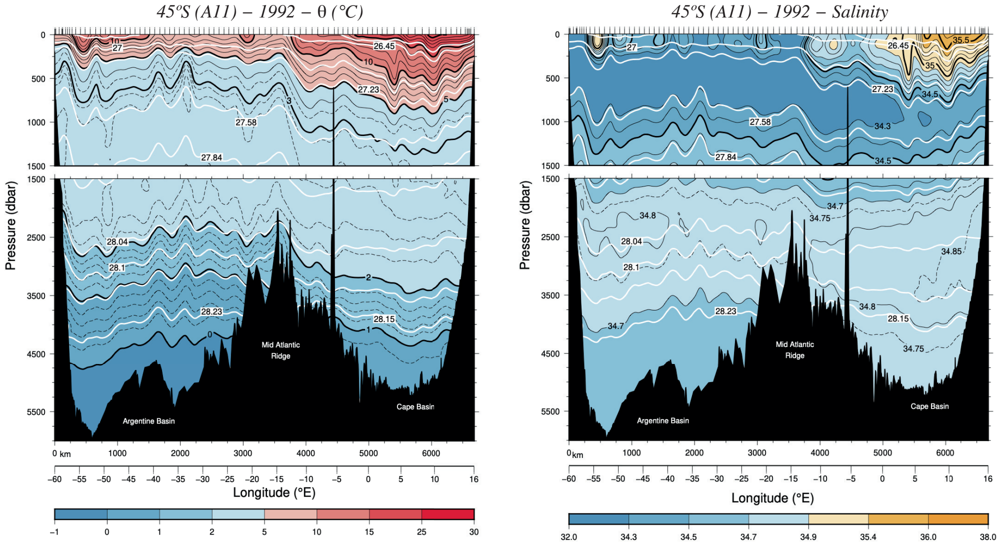

Figure A.1. Vertical sections of potential temperature (°C) on the left panel and salinity on the right panel at 45°S for 1992. Black lines represent the values of potential temperature or salinity, and white lines are the interphases of neutral density that divide each layer of the inverse model.

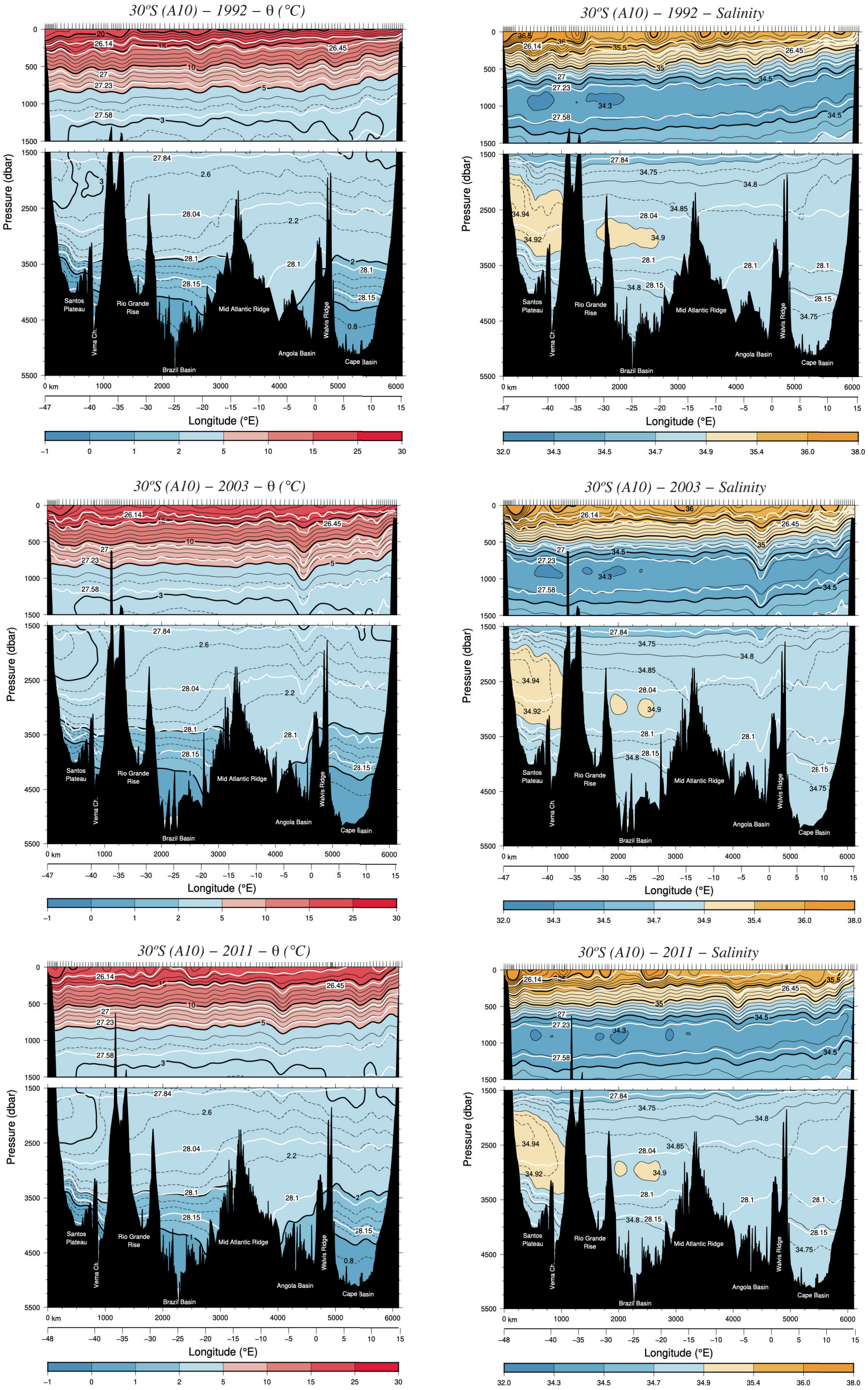

Figure A.2. Vertical sections of potential temperature (°C) on the left panels and salinity on the right panels at 30°S for 1992 (top), 2003 (middle) and 2011 (bottom). Black lines represent the values of potential temperature or salinity, and white lines are the interphases of neutral density that divide each layer of the inverse model.

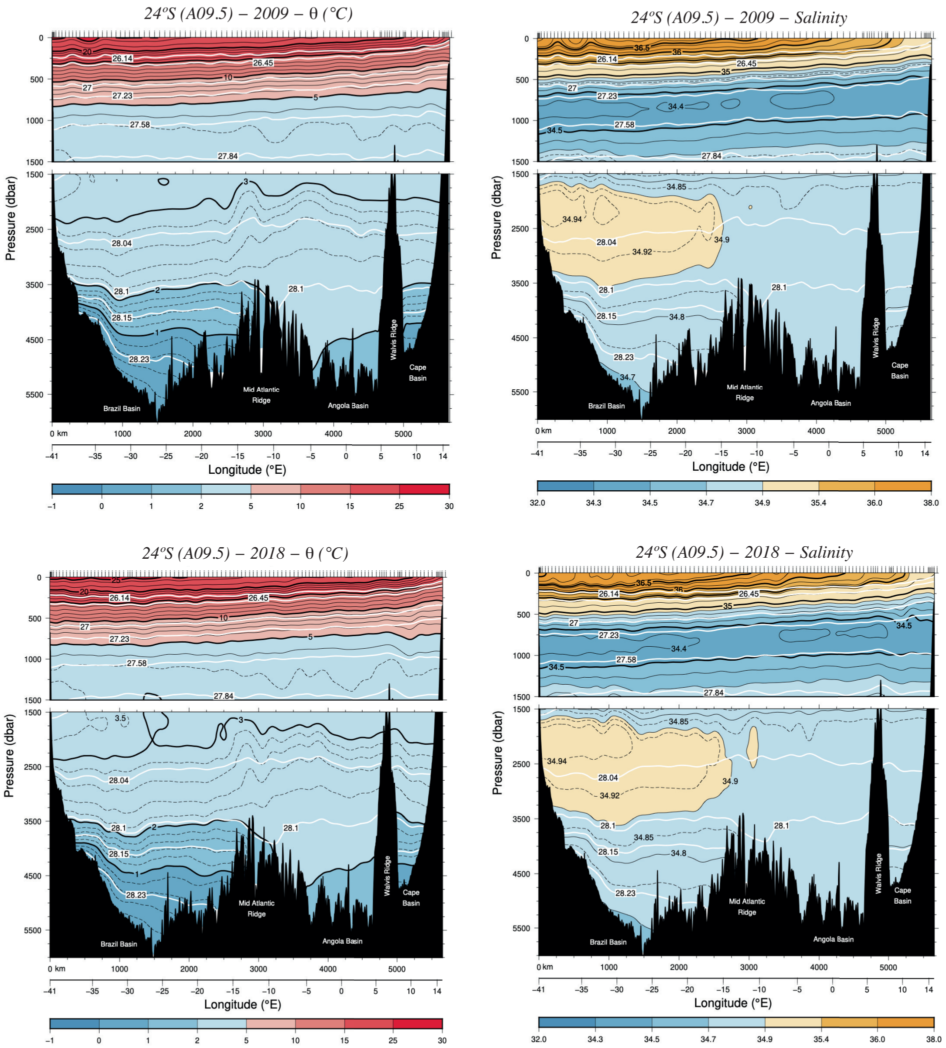

Figure A.3. Vertical sections of potential temperature (°C) on the left panels and salinity on the right panels at 24°S for 2009 (top) and 2018 (bottom). Black lines represent the values of potential temperature or salinity, and white lines are the interphases of neutral density that divide each layer of the inverse model.

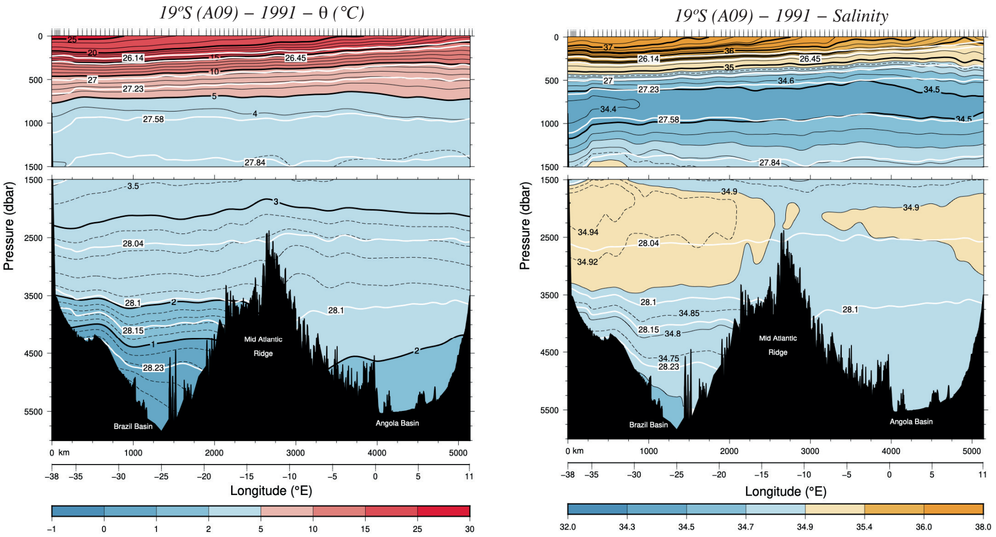

Figure A.4. Vertical sections of potential temperature (°C) on the left panel and salinity on the right panel at 19°S for 1991. Black lines represent the values of potential temperature or salinity, and white lines are the interphases of neutral density that divide each layer of the inverse model.

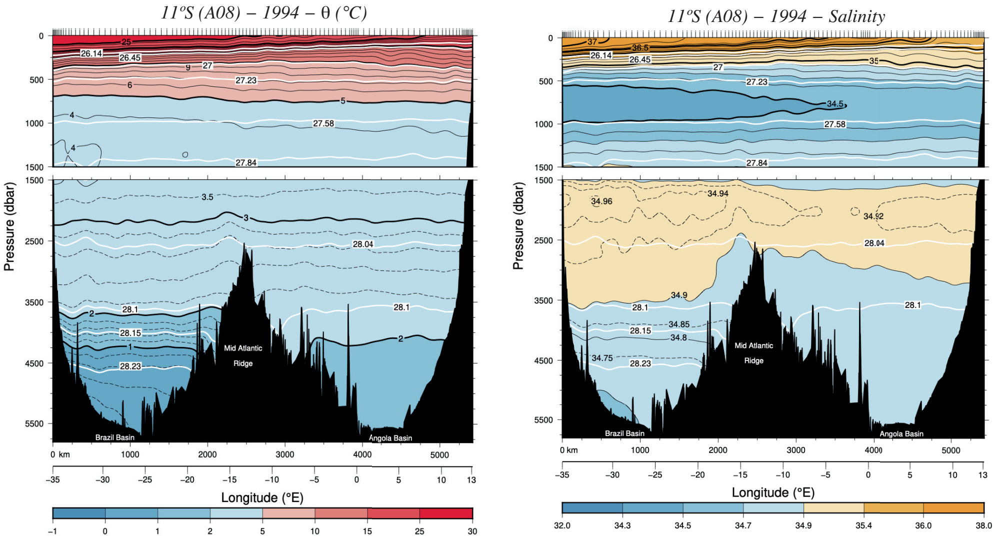

Figure A.5. Vertical sections of potential temperature (°C) on the left panel and salinity on the right panel at 11°S for 1994. Black lines represent the values of potential temperature or salinity, and white lines are the interphases of neutral density that divide each layer of the inverse model.

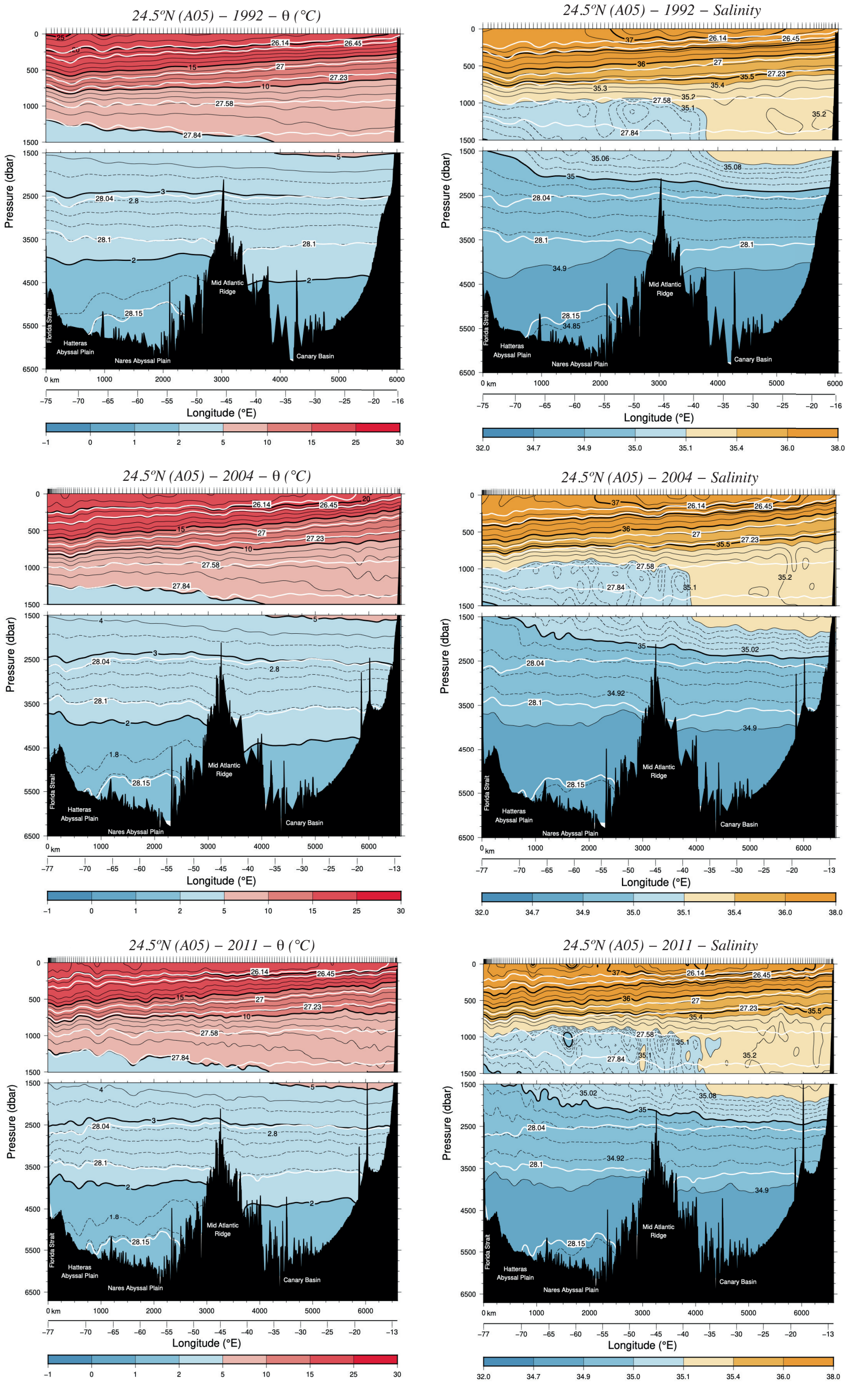

Figure A.6. Vertical sections of potential temperature (°C) on the left panels and salinity on the right panels at 24.5°N for 1992 (top), 2004 (middle) and 2011 (bottom). Black lines represent the values of potential temperature or salinity, and white lines are the interphases of neutral density that divide each layer of the inverse model.

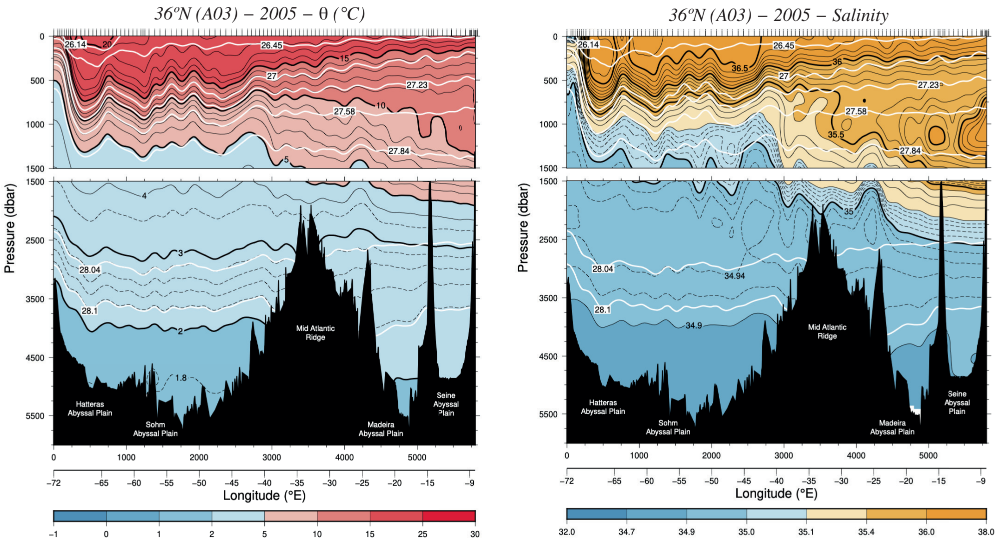

Figure A.7. Vertical sections of potential temperature (°C) on the left panel and salinity on the right panel at 36°N for 2005. Black lines represent the values of potential temperature or salinity, and white lines are the interphases of neutral density that divide each layer of the inverse model.

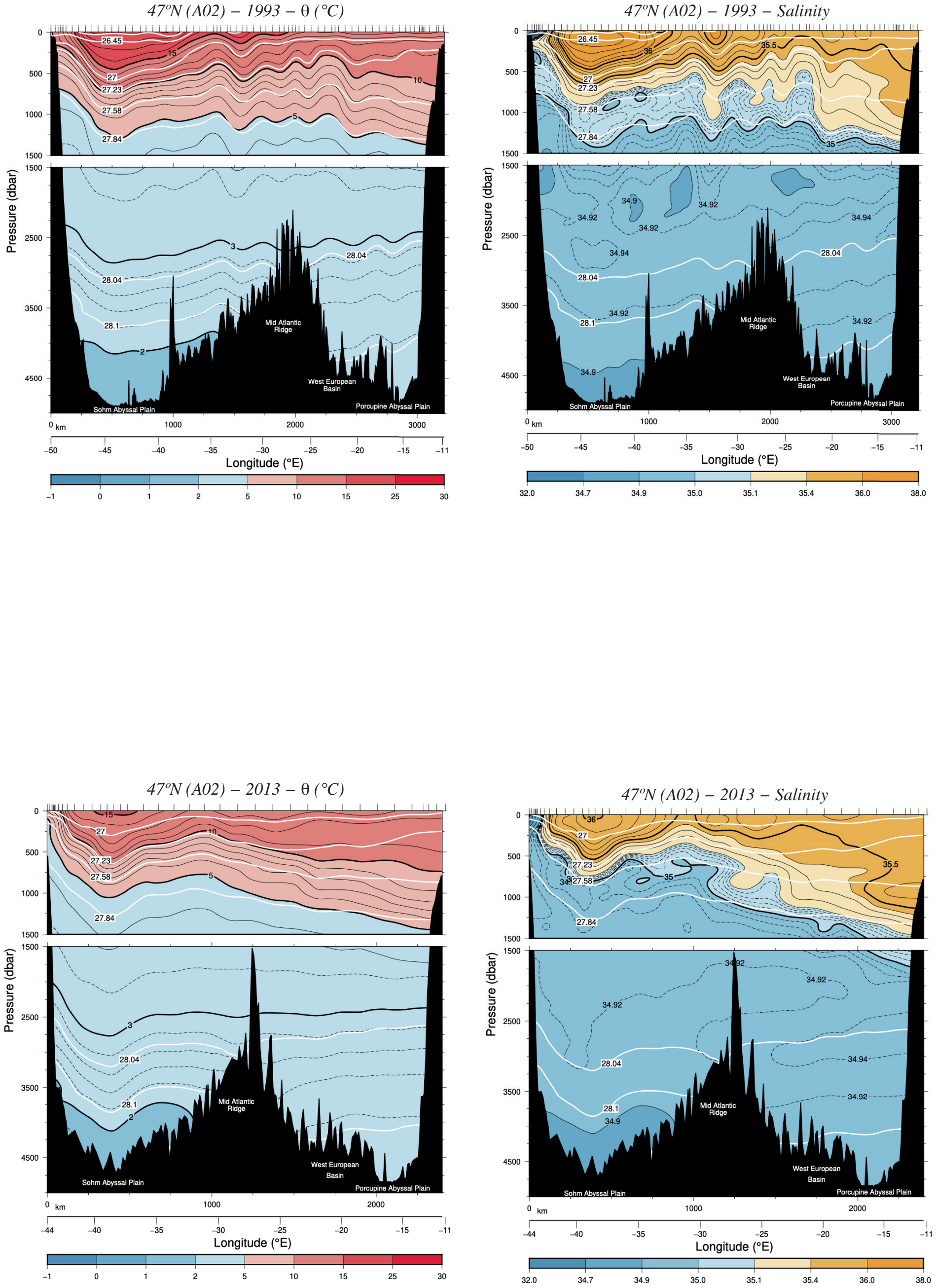

Figure A.8. Vertical sections of potential temperature (°C) on the left panels and salinity on the right panels at 47°N for 1993 (top) and 2013 (bottom). Black lines represent the values of potential temperature or salinity, and white lines are the interphases of neutral density that divide each layer of the inverse model.

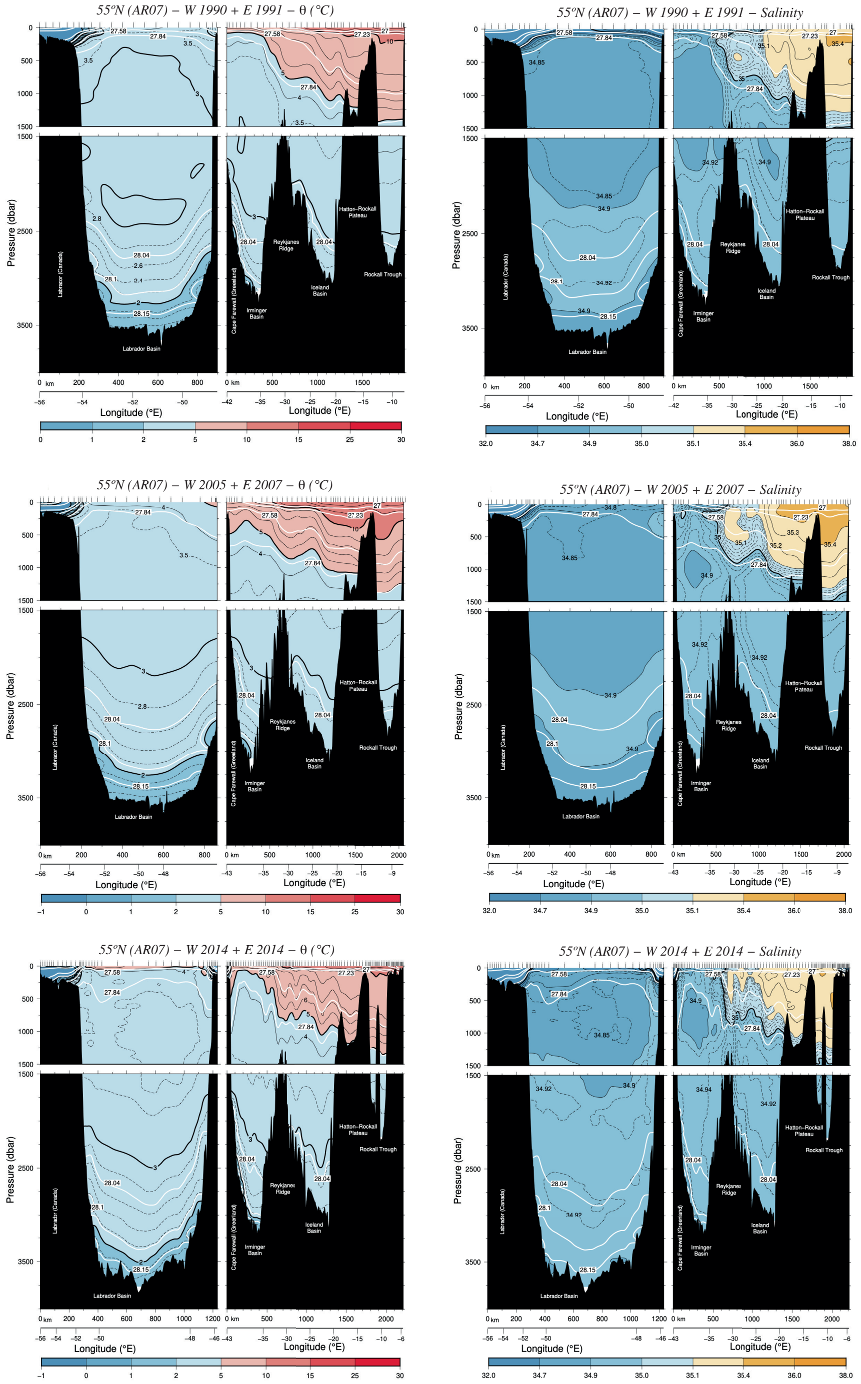

55°N (AR07) − W 1990 + E 1991 − θ (°C)

55°N (AR07) − W 1990 + E 1991 − Salinity

55°N (AR07) − W 2005 + E 2007 − θ (°C)

55°N (AR07) − W 2005 + E 2007 − Salinity

55°N (AR07) − W 2014 + E 2014 − θ (°C)

55°N (AR07) − W 2014 + E 2014 − Salinity

Figure A.9. Vertical sections of potential temperature (°C) on the left panels and salinity on the right panels at 53°N + 58°N for 1990 and 1991, respectively (top), 2005 and 2007, respectively, (middle) and 2014 (bottom). Black lines represent the values of potential temperature or salinity, and white lines are the interphases of neutral density that divide each layer of the inverse model.

Appendix B

Inverse model

To compute the velocity between stations, we can apply the thermal wind equations, which allow us to characterize the vertical shear of the horizontal velocity, but with a limitation – preventing the determination of the absolute geostrophic velocity.

$$\frac{\partial \mathrm{v}}{\partial \mathrm{z}} = -\frac{\mathrm{g}}{\rho_0 \mathrm{f}} \frac{\partial \mathrm{p}}{\partial \mathrm{x}} \tag{B.1}$$

$$\frac{\partial \mathrm{u}}{\partial \mathrm{z}} = \frac{\mathrm{g}}{\rho_0 \mathrm{f}} \frac{\partial \mathrm{p}}{\partial \mathrm{y}} \tag{B.2}$$

If we zonally integrate the equation B.1, we obtain a solution with two main components: one baroclinic, which can be estimated using hydrographic data, and another one which is constant with depth, known as the velocity at the reference level:

$$\mathrm{v_g}(\mathrm{x}, \mathrm{z}) = -\frac{\mathrm{g}}{\rho_0 \mathrm{f}} \int_{\mathrm{z_0(x)}}^{\mathrm{z}} \frac{\partial \mathrm{p}}{\partial \mathrm{x}}\, \mathrm{dz} + \mathrm{b(x)} \tag{B.3}$$

This velocity at the reference level can be estimated through inverse models, assuming geostrophy and conservation of mass and other properties.

The net amount of fluid moving int and out of this enclosed surface may be expressed as:

$$\iint_{\mathrm{S}} \rho \vec{\mathrm{v_g}} \cdot \mathrm{d}\vec{\mathrm{S}} = 0 \tag{B.4}$$

With ρ as the density (kg m^{-3}) of the water cell flowing with a geostrophic velocity ($\vec{\mathrm{v_g}}$) (m s^{-1}) and $\rho\vec{\mathrm{v_g}}$ is the mass flux (kg m^{-2} s-$^{-1}$) through an infinitesimal area dS (m^{2}), represented by its unit vector $\mathrm{d}\vec{\mathrm{S}}$.

Considering equation B.4 as the sum two components – one baroclinic ($\mathrm{v_r}$) and other on the reference level (b), that expression could be rewritten as:

$$\iint_{\mathrm{S}} \rho(\mathrm{x},\mathrm{z})\ (\mathrm{v_r}(\mathrm{x},\mathrm{z}) + \mathrm{b}(\mathrm{x}))\ \mathrm{dS}(\mathrm{x},\mathrm{z}) = 0 \tag{B.5}$$

where the component of the velocity parallel to the vector $\mathrm{d}\vec{\mathrm{S}}$ is used on a zonal section. The baroclinic component of the velocity can be obtained with the thermal wind equations (equations B.1 and B.2). Having measurements only on defined $\mathrm{N}+1$ stations, and dividing the water column in Q layers, equation B.5 can be written as:

$$\sum_{\mathrm{j}=1}^{\mathrm{N}} \sum_{\mathrm{q}=1}^{\mathrm{Q}} \rho_{\mathrm{jq}}\ (\mathrm{v_{r_{jq}}} + \mathrm{b_j})\ \Delta \mathrm{a_{jq}} \approxeq 0 \tag{B.6}$$

With subindex j denoting the station pair and q the layer, with Q the total number of layers. The result of this double sum is not exactly zero as a result of noise due to the presence of mesoscale eddies, internal waves, aliasing, … Rewriting equation B.6, taking into account that b is constant with depth:

$$\sum_{\mathrm{j}=1}^{\mathrm{N}} \sum_{\mathrm{q}=1}^{\mathrm{Q}} \rho_{\mathrm{jq}}\ \mathrm{b_j}\ \Delta \mathrm{a_{jq}} \approxeq \sum_{\mathrm{j}=1}^{\mathrm{N}} \sum_{\mathrm{q}=1}^{\mathrm{Q}} \rho_{\mathrm{jq}}\ \mathrm{v_{r_{jq}}}\ \Delta \mathrm{a_{jq}} \tag{B.7}$$

That for each layer can be written as:

$$\sum_{\mathrm{j}=1}^{\mathrm{N}} \rho_{\mathrm{jq}}\ \mathrm{b_j}\ \Delta \mathrm{a_{jq}} \approxeq -\sum_{\mathrm{j}=1}^{\mathrm{N}} \rho_{\mathrm{jq}}\ \mathrm{v_{r_{jq}}}\ \Delta \mathrm{a_{jq}} \tag{B.8}$$

The only unknowns in this expression are the velocities at the reference level bj, so that equation B.8 for each layer is expressed as follows:

$$\sum_{\mathrm{j}=1}^{\mathrm{N}} \mathrm{e_{jq}}\ \mathrm{b_j} + \mathrm{n_q} = \mathrm{y_q} \tag{B.9}$$

Being:

- $\mathrm{e_{jq}} = \rho_{\mathrm{jq}}\ \Delta \mathrm{a_{jq}}$
- $\mathrm{y_q} = \sum_{\mathrm{j}=1}^{\mathrm{N}}\ \rho_{\mathrm{jq}}\ \mathrm{v_{r_{jq}}}\ \Delta \mathrm{a_{jq}}$
- $\mathrm{n_q}$, the error due to noise in each layer

It can be expressed in matrix form as in equation B.10, where E represents the matrix coefficients,

x is the system unknowns, n is the noise and y is the baroclinic component in each layer.

$$\begin{aligned} &\mathbf{E}\,\mathbf{x} + \mathbf{n} = \mathbf{y} \\ \text{with } \mathbf{x} = &\begin{cases} \{\mathrm{b_i}\}_{\mathrm{i=1,N_{pair}}} \\ \Delta\mathrm{T_{Ek}} \end{cases} \end{aligned} \tag{B.10}$$

The system unknowns include the velocities at the reference level and the adjustment to the Ekman transport.

Appendix C

Freshwater flux definitions

Salinity Definitions

Salinity can be defined as a sum of their components, distinguishing between mechanisms of horizontal circulation and vertical overturning. For a zonal transoceanic section, salinity is expressed as:

$$\mathrm{S} = \mathrm{S}_0 + \mathrm{S}'(\mathrm{x}, \gamma^{\mathrm{n}}) = \mathrm{S}_0 + \langle \mathrm{S} \rangle(\gamma^{\mathrm{n}}) + \mathrm{S}''(\mathrm{x}, \gamma^{\mathrm{n}}) \tag{C.1}$$

where:

- $\mathrm{S}_0 = \frac{\iint \mathrm{S}(\mathrm{x},\gamma^{\mathrm{n}})\ \mathrm{dx d}\gamma^{\mathrm{n}}}{\iint \mathrm{dx d}\gamma^{\mathrm{n}}}$ is the area-weighted section average.
- $\mathrm{S}'(\mathrm{x}, \gamma^{\mathrm{n}}) = \mathrm{S}(\mathrm{x}, \gamma^{\mathrm{n}}) - \mathrm{S}_0$ is the salinity anomaly.
- $\langle \mathrm{S} \rangle(\gamma^{\mathrm{n}}) = \frac{\int (\mathrm{S}(\mathrm{x},\gamma^{\mathrm{n}}) - \mathrm{S}_0)\ \mathrm{dx}}{\int \mathrm{dx}}$ are the area-weighted zonally averaged deviations from the salinity average S_0.
- $\mathrm{S}''(\mathrm{x}, \gamma^{\mathrm{n}}) = \mathrm{S}(\mathrm{x}, \gamma^{\mathrm{n}}) - \mathrm{S}_0 - \langle \mathrm{S} \rangle$ are the deviations from the zonal and section averages (the residual values).

The last two terms are included in the anomaly term, so that $\mathrm{S}'(\mathrm{x}, \gamma^{\mathrm{n}}) = \langle \mathrm{S} \rangle(\gamma^{\mathrm{n}}) + \mathrm{S}''(\mathrm{x}, \gamma^{\mathrm{n}})$. The decompositions for velocity and potential temperature are analogous to that of salinity.

Freshwater flux definitions

The freshwater flux is the portion of mass transport that is not salt. It is defined by McDonagh et al. (2015) as the volume flux added to the section-averaged salinity so that it yields a net salinity flux equivalent to that of the Bering Strait ($\mathrm{T_BS\ S_BS} = -0.8 \times 32.5 = -26\mathrm{Sv}$).

The most important part of the total freshwater flux is the freshwater divergence, which represents the difference between the total freshwater flux and the volume flux through the

Bering Strait:

$$\mathrm{FWflux} = \mathrm{FWdiv} + \mathrm{T_iBS} = \mathrm{FWdiv} - 0.8 \tag{C.2}$$

Furthermore, the freshwater divergence can be broken up into its corresponding components, related to those of salinity (Bryden & Imawaki, 2001; Bryden et al., 2011; McDonagh et al., 2015):

- The barotropic component, which represents the total salt transport associated with the interbasin exchange (change in salinity of the Bering Strait throughflow, for the Atlantic, between the Bering Strait and the zonal section studied). This term is called 'throughflow' by McDonagh et al. (2015) and 'leakage' by Wijffels (2001).

  $$\mathrm{FWthroughfloworLeakage} = \frac{\mathrm{T_i^M\ S'}}{\mathrm{S_0}} = \frac{\mathrm{T_{BS}\ (S_{BS} - S_0)}}{\mathrm{S_0}} \tag{C.3}$$

  where $\mathrm{T_BS} = -0.8\mathrm{Sv}$ is the interbasin mass transport, and the average Bering Strait salinity is $\mathrm{S_BS} = 32.5$.

- The baroclinic transport, due to zonally averaged vertical-meridional circulation. This term is associated with the overturning circulation across the section.

  $$\mathrm{FWoverturning} = -\frac{\iint \rho\ \langle \mathrm{S} \rangle\ \mathrm{v\ dxd}\gamma^{\mathrm{n}}}{\mathrm{S_0}} \tag{C.4}$$

- The horizontal transport, due to the large-scale gyre circulation and the smaller-scale eddies, which reflects correlations in the residual velocity and salinity fields.

  $$\mathrm{FWhorizontal} = \frac{\iint \rho\ \mathrm{S''}\ \mathrm{v\ dxd}\gamma^{\mathrm{n}}}{\mathrm{S_0}} \tag{C.5}$$

The sum of the overturning and horizontal freshwater transport can be understood as the corrections of salinity and velocity across the section, which is the same expression as in Joyce et al. (2001), where the freshwater transport is attributed to the salinity anomaly $\mathrm{S'(x, \gamma^n)}$:

$$\frac{\sum_{\mathrm{i}} \sum_{\mathrm{j}} \mathrm{T_{ij}\ S'_{ij}}}{\mathrm{S_0}} = \frac{\iint \rho\ \mathrm{S'\ v\ dxd}\gamma^{\mathrm{n}}}{\mathrm{S_0}} = \frac{\iint \rho\ \langle \mathrm{S} \rangle\ \mathrm{v\ dxd}\gamma^{\mathrm{n}}}{\mathrm{S_0}} + \frac{\iint \rho\ \mathrm{S''\ v\ dxd}\gamma^{\mathrm{n}}}{\mathrm{S_0}} \tag{C.6}$$

Freshwater: development of mathematical expressions

Following Joyce et al. (2001), the freshwater flux is defined as excess of evaporation over precipitation plus runoff:

$$\mathrm{FW} = \mathrm{P} - \mathrm{E} + \mathrm{R} \tag{C.7}$$

And the mass conservation as:

$$\sum_i \sum_j T_{ij} + n_1 = -FW \tag{C.8}$$

And the conservation of salt as:

$$\sum_i \sum_j T_{ij}\, S_{ij} + n_2 = 0 \tag{C.9}$$

Defining S_0 as the mean salinity and $S'_{ij} = S_{ij} - S_0$ as the salinity anomaly, we can rewrite the salt conservation as (taking into account that $S_{ij} = S_0 + S'_{ij}$):

$$\sum_i \sum_j T_{ij}\, (S_0 + S'_{ij}) + n_2 = 0 \tag{C.10}$$

And considering that

$$\sum_i \sum_j T_{ij} = -FW - n_1 \tag{C.11}$$

The equation can be rewritten as:

$$\sum_i \sum_j T_{ij}\, S'_{ij} - (FW + n_1)\, S_0 + n_2 = 0 \tag{C.12}$$

So that we can obtain FW:

$$FW = \frac{\sum_i \sum_j T_{ij}\, S'_{ij} - n_1\, S_0 + n_2}{S_0} \tag{C.13}$$

And considering $\langle n_1 \rangle = \langle n_2 \rangle = 0$

$$FW = \frac{\sum_i \sum_j T_{ij}\, S'_{ij}}{S_0} \tag{C.14}$$

Wijffels (2001) defines the salt conservation in a volume enclosed by a hydrographic line as:

$$\iint \rho\, S\, v\, dxd\gamma^n = T_i^S \tag{C.15}$$

which is the total transport associated with an exchange between a certain section and the inflow or outflow of freshwater between different basins (such as Bering Strait (BS) or the Indonesian throughflow), hence the name interbasin salinity transport. Similarly, the interbasin mass transport can be also defined, which includes freshwater fluxes due to evaporation, precipitation and river runoff.

$$\iint \rho\, v\, dxd\gamma^n + [P - E + R] = \iint \rho\, v\, dxd\gamma^n + FW = T_i^M \tag{C.16}$$

The pure water part of the above total mass transport can be computed as the difference between the salt and mass interbasin transports:

$$\iint \rho \, \mathrm{v} \, \mathrm{dxd}\gamma^{\mathrm{n}} + \mathrm{FW} - \iint \rho \, \mathrm{S} \, \mathrm{v} \, \mathrm{dxd}\gamma^{\mathrm{n}} = \mathrm{T}_{\mathrm{i}}^{\mathrm{M}} - \mathrm{T}_{\mathrm{i}}^{\mathrm{s}} \tag{C.17}$$

Using the definitions of S_0 and S', and the assumption that the interbasin flux of salt occurs at a known salinity $\mathrm{T}_{\mathrm{i}}^{\mathrm{S}} = \mathrm{S}_{\mathrm{i}} \, \mathrm{T}_{\mathrm{i}}^{\mathrm{M}}$, the expression of FW can be obtained.

$$\mathrm{FW} + \iint \rho \, \mathrm{v} \, \mathrm{dxd}\gamma^{\mathrm{n}} - \iint \rho \, \mathrm{S} \, \mathrm{v} \, \mathrm{dxd}\gamma^{\mathrm{n}} = \mathrm{T}_{\mathrm{i}}^{\mathrm{M}} - \mathrm{S}_{\mathrm{i}} \, \mathrm{T}_{\mathrm{i}}^{\mathrm{M}}$$

$$\mathrm{FW} + \iint \rho \, \mathrm{v} \, \mathrm{dxd}\gamma^{\mathrm{n}} - \iint \rho \, (\mathrm{S}_0 + \mathrm{S}') \, \mathrm{v} \, \mathrm{dxd}\gamma^{\mathrm{n}} = \mathrm{T}_{\mathrm{i}}^{\mathrm{M}} - (\mathrm{S}_0 + \mathrm{S}') \, \mathrm{T}_{\mathrm{i}}^{\mathrm{M}}$$

$$\mathrm{FW} + \iint \rho \, \mathrm{v} \, \mathrm{dxd}\gamma^{\mathrm{n}} - \iint \rho \, \mathrm{S}_0 \, \mathrm{v} \, \mathrm{dxd}\gamma^{\mathrm{n}} - \iint \rho \, \mathrm{S}' \, \mathrm{v} \, \mathrm{dxd}\gamma^{\mathrm{n}} = \mathrm{T}_{\mathrm{i}}^{\mathrm{M}} \, (1 - \mathrm{S}_0 + \mathrm{S}')$$

$$\mathrm{FW} + (1 - \mathrm{S}_0) \iint \rho \, \mathrm{v} \, \mathrm{dxd}\gamma^{\mathrm{n}} - \iint \rho \, \mathrm{S}' \, \mathrm{v} \, \mathrm{dxd}\gamma^{\mathrm{n}} = \mathrm{T}_{\mathrm{i}}^{\mathrm{M}} \, (1 - \mathrm{S}_0) - \mathrm{T}_{\mathrm{i}}^{\mathrm{M}} \, \mathrm{S}'$$

$$\mathrm{FW} = \mathrm{T}_{\mathrm{i}}^{\mathrm{M}} \, (1 - \mathrm{S}_0) - \mathrm{T}_{\mathrm{i}}^{\mathrm{M}} \, \mathrm{S}' - (1 - \mathrm{S}_0) \iint \rho \, \mathrm{v} \, \mathrm{dxd}\gamma^{\mathrm{n}} + \iint \rho \, \mathrm{S}' \, \mathrm{v} \, \mathrm{dxd}\gamma^{\mathrm{n}}$$

$$-\mathrm{FW} = -\mathrm{T}_{\mathrm{i}}^{\mathrm{M}} \, (1 - \mathrm{S}_0) - \mathrm{T}_{\mathrm{i}}^{\mathrm{M}} \, \mathrm{S}' + (1 - \mathrm{S}_0) \iint \rho \, \mathrm{v} \, \mathrm{dxd}\gamma^{\mathrm{n}} - \iint \rho \, \mathrm{S}' \, \mathrm{v} \, \mathrm{dxd}\gamma^{\mathrm{n}}$$

$$-\mathrm{FW} = \mathrm{T}_{\mathrm{i}}^{\mathrm{M}} \, \mathrm{S}' - (1 - \mathrm{S}_0) \left(\mathrm{T}_{\mathrm{i}}^{\mathrm{M}} - \iint \rho \, \mathrm{v} \, \mathrm{dxd}\gamma^{\mathrm{n}} \right) - \iint \rho \, \mathrm{S}' \, \mathrm{v} \, \mathrm{dxd}\gamma^{\mathrm{n}}$$

$$-\mathrm{FW} = \mathrm{T}_{\mathrm{i}}^{\mathrm{M}} \, \mathrm{S}' - (1 - \mathrm{S}_0) \left(\iint \rho \, \mathrm{v} \, \mathrm{dxd}\gamma^{\mathrm{n}} + \mathrm{FW} - \iint \rho \, \mathrm{v} \, \mathrm{dxd}\gamma^{\mathrm{n}} \right) - \iint \rho \, \mathrm{S}' \, \mathrm{v} \, \mathrm{dxd}\gamma^{\mathrm{n}}$$

$$-\mathrm{FW} = \mathrm{T}_{\mathrm{i}}^{\mathrm{M}} \, \mathrm{S}' - (1 - \mathrm{S}_0) \, \mathrm{FW} - \iint \rho \, \mathrm{S}' \, \mathrm{v} \, \mathrm{dxd}\gamma^{\mathrm{n}}$$

$$-\mathrm{FW} + (1 - \mathrm{S}_0) \, \mathrm{FW} = \mathrm{T}_{\mathrm{i}}^{\mathrm{M}} \, \mathrm{S}' - \iint \rho \, \mathrm{S}' \, \mathrm{v} \, \mathrm{dxd}\gamma^{\mathrm{n}}$$

$$-\mathrm{S}_0 \, \mathrm{FW} = \mathrm{T}_{\mathrm{i}}^{\mathrm{M}} \, \mathrm{S}' - \iint \rho \, \mathrm{S}' \, \mathrm{v} \, \mathrm{dxd}\gamma^{\mathrm{n}}$$

$$\mathrm{FW} = -\frac{\mathrm{T}_{\mathrm{i}}^{\mathrm{M}} \, \mathrm{S}' - \iint \rho \, \mathrm{S}' \, \mathrm{v} \, \mathrm{dxd}\gamma^{\mathrm{n}}}{\mathrm{S}_0}$$

where the first term of the right-hand side represents the leakage associated to Bering Strait:

$$\mathrm{Leakage} = \frac{\mathrm{T}_{\mathrm{i}}^{\mathrm{M}} \, \mathrm{S}'}{\mathrm{S}_0} = \frac{\mathrm{T}_{\mathrm{BS}} \, (\mathrm{S}_{\mathrm{BS}} - \mathrm{S}_0)}{\mathrm{S}_0} \tag{C.18}$$

where $\mathrm{T}_{\mathrm{BS}} = -0.8\mathrm{Sv}$, and $\mathrm{S}_{\mathrm{BS}} = 32.5$, which is analogous to the throughflow defined by McDonagh et al. (2015).

The second term collects the corrections of salinity and velocity across the section, which is the same expression as in Joyce et al. (2001), and is the sum of the two components defined by McDonagh et al. (2015):

$$\frac{\sum_{i}\sum_{j} T_{ij}\, S'_{ij}}{S_0} = \frac{\iint \varrho\, S'\, v\, dxd\gamma^{n}}{S_0} = \frac{\iint \varrho\, \langle S \rangle\, v\, dxd\gamma^{n}}{S_0} + \frac{\iint \varrho\, S''\, v\, dxd\gamma^{n}}{S_0}$$

Appendix D

Data Availability

Hydrographic data were collected from the CCHDO website (https://cchdo.ucsd.edu) in the frame of International WOCE and GO-SHIP projects and from the BODC databases for each cruise: A11 1992 (https://cchdo.ucsd.edu/cruise/74DI199_1), A10 1992 (https://cchdo.ucsd.edu/cruise/06MT22_5), A09 1991 (https://cchdo.ucsd.edu/cruise/06MT15_3), A08 1994 (https://cchdo.ucsd.edu/cruise/06MT28_1), A05 1992 (https://cchdo.ucsd.edu/cruise/29HE06_1), A02 1993 (https://cchdo.ucsd.edu/cruise/06GA226_2), AR07W 1990 (https://cchdo.ucsd.edu/cruise/18DA90012_1), AR07E 1991 (https://cchdo.ucsd.edu/cruise/74AB62_1), A10 2003 (https://cchdo.ucsd.edu/cruise/49NZ20031106), A095 2009 (https://cchdo.ucsd.edu/cruise/740H20090307), A05 2004 (https://cchdo.ucsd.edu/cruise/74DI20040404), A03 2005 (https://www.bodc.ac.uk/data/bodc_database/ctd/search/, searching for 36 North under ‘Project’), AR07W 2005 (https://cchdo.ucsd.edu/cruise/18HU20050526), AR07E 2007 (https://cchdo.ucsd.edu/cruise/64PE20070830), A10 2011 (https://cchdo.ucsd.edu/cruise/33RO20110926), A095 2018 (https://cchdo.ucsd.edu/cruise/740H20180228), A05 2011 (https://cchdo.ucsd.edu/cruise/29AH20110128), A02 2013 (https://cchdo.ucsd.edu/cruise/06M220130509), AR07 W 2014 (https://cchdo.ucsd.edu/cruise/74JC20140606) and AR07E 2014 (https://cchdo.ucsd.edu/cruise/74JC20140606).

OSNAP data were collected and made freely available by the OSNAP project and all the national programs that contribute to it (https://www.o-snap.org/). Data from the full OSNAP array for the first 21 months (31-Jul-2014 to 20-Apr-2016) have been used to produce the 30-day mean MOC, MHT, and MFT time series across the whole section, as well as the gridded property fields, and are available at https://doi.org/10.35090/wa93-m688.

Data from the RAPID-MOCHA program are funded by the U.S. National Science Foundation and UK Natural Environment Research Council. MOC data from the RAPID-MOCHA are freely available at https://rapid.ac.uk/rapidmoc/rapid_data/datadl.php (doi:https://doi.org/10/d3z4) and heat transports at https://mocha.rsmas.miami.edu/mocha/results/index.html(doi:https:

//doi.org/10/gwqg).

The Florida Current cable and section data are made freely available on the Atlantic Oceanographic and Meteorological Laboratory web page (https://www.aoml.noaa.gov/phod/floridacurrent/) and are funded by the DOC-NOAA Climate Program Office - Ocean Observing and Monitoring Division. Florida Current daily mean transport from year 2000 until present is available at https://www.aoml.noaa.gov/phod/floridacurrent/data_access.php and historical data from 1982 to 1998 at https://www.aoml.noaa.gov/phod/floridacurrent/historical_data.php, of which we have used the used data from 1990 to 1998.

The daily mean u and v-wind components of NCEP/NCAR reanalysis winds were collected from https://psl.noaa.gov/data/gridded/data.ncep.reanalysis.pressure.html.

GLODAPv2.2021 is available via https://www.glodap.info/index.php/merged-and-adjusted-data-product-v22021/.

The cruises obtained from GLODAPv2 have the following DOIs: A11 1992 (https://doi.org/10.3334/cdiac/otg.woce_a11_74di19921222), A10 1992 (https://doi.org/10.3334/CDIAC/otg.ndp066), A09 1991 (https://doi.org/10.3334/CDIAC/otg.ndp051), A08 1994 (https://doi.org/10.3334/CDIAC/otg.ndp079), A05 1992 (https://doi.org/10.3334/CDIAC/otg.ndp074), A10 2003 (https://doi.org/10.25921/gjsx-gy37), A095 2009 (https://doi.org/10.3334/cdiac/otg.clivar_a9.5_2009), A05 2004 (https://doi.org/10.3334/cdiac/otg.carina_74di20040404), A03 2005 (https://doi.org/10.3334/cdiac/otg.carina_74ab20050501), AR07W 2005 (https://doi.org/10.3334/cdiac/otg.woce_ar07w_2005), AR07E 2007 (https://doi.org/10.3334/cdiac/otg.clivar_ar07e_2007), A10 2011 (https://doi.org/10.3334/cdiac/otg.clivar_a10_2011), A095 2018 (https://doi.org/10.25921/xy1r-rx06), A05 2011 (https://doi.org/10.3334/cdiac/otg.clivar_a05_29ah20110128) and A02 2013 (https://doi.org/10.25921/43nw-j564).

The carbon transport data that support the findings of Brown et al. (2021) are available from the British Oceanographic Data Centre at http://doi.org/10/fn4j.

The carbon concentrations for the 2014 AR07W and AR07E cruises of Tynan et al. (2016) are available from the British Oceanographic Data Centre at http://doi.org/10/bb3f.

The anthropogenic CO_2 estimates reported in Gruber et al. (2019) can be obtained through NCEI's Ocean Carbon Data System: https://www.ncei.noaa.gov/access/ocean-carbon-acidification-data-system/oceans/ndp_100/ndp100.html.

The anthropogenic CO_2 estimates reported in Sabine et al. (2004) can be also accessed via NCEI's Ocean Carbon Data System: Sabine, Christopher L.; Feely, Richard A.; Key, Robert M.; Wanninkhof, Rik; Millero, Frank J.; Kozyr, Alex (2019). GLobal Ocean Data Analysis Project (GLODAP) version 1.1 (NCEI Accession 0001644). NOAA National Centers for Environmental Information. Dataset. https://doi.org/10.25921/pkjs-5w29. Accessed [2022-09-13].

Matlab and R code for CANYON-B are available at https://github.com/HCBScienceProducts/.

Matlab code for C_{anth} estimation using φC_T^0 method is available at http://oceano.iim.csic.es/_media/cantphict0_toolbox_20190213.zip.

Datasets for the monthly average air-sea fluxes of O_2, CO_2, and N_2 from Earth System Models are available at https://doi.org/10.5281/zenodo.4716840 (Morgan, 2021).

Appendix E

Institutional Acknowledgments

This thesis has been completed as part of Verónica Caínzos work at IOCAG, in the doctoral program in Oceanography and Global Change, as well as the Unidad Océano y Clima from Universidad de Las Palmas de Gran Canaria, an R&D&i CSIC-associate unit. This study was supported by the SAGA project (RTI2018-100844-B-C31) funded by the Ministerio de Ciencia, Innovación y Universidades of the Spanish Government.

Verónica Caínzos acknowledges the Agencia Canaria de Investigación, Innovación y Sociedad de la Información (ACIISI) grant program of “Apoyo al personal investigador en formación” TESIS2019010015. The research stay at NORCE Norwegian Research Centre and the Bjerknes Centre for Climate Research in Bergen (Norway) was supported by the Agencia Canaria de Investigación, Innovación y Sociedad de la Información (ACIISI) grant for ”Estancias Breves en España y en el Extranjero 2019” EST2019010010. The research stay at the Atlantic Oceanographic and Meteorological Laboratory (AOML-NOAA) and University of Miami in Miami (United States) was supported by the Agencia Canaria de Investigación, Innovación y Sociedad de la Información (ACIISI) grant for ”Estancias Breves en España y en el Extranjero 2022” EST2022010018.

We would like to thank the chief scientists and teams that collected all the data for the zonal sections: P. Saunders, T. Müller, G. Siedler, G. Parrilla, A. Sy, J. Lazier, M. Bersch, Y. Yoshikawa, B. King, S. Cunningham, G. Harrison, G.-J. Brummer, M. Baringer, A. Macdonald, D. Kieke and P. Holliday.

Appendix F

Resumen en castellano

Introducción

El océano Atlántico se caracteriza por su transporte neto de calor hacia el norte a través de toda la cuenca, logrado principalmente por la Circulación Latitudinal de Retorno del Atlántico (AMOC, por sus siglas en inglés *Atlantic Meridional Overturning Circulation*). Se trata de uno de los principales mecanismos de redistribución del calor en el océano, junto con la masa, la sal, el carbono, los nutrientes y otras propiedades biogeoquímicas (Chidichimo et al., 2023; Kersalé et al., 2020; McCarthy et al., 2020; Steinfeldt et al., 2009). La AMOC está compuesta por un sistema de vías tridimensionales complejas e irregulares que transportan masas de agua en capas superficiales, intermedias, profundas y abisales, transformando estas masas de agua en su camino (Cessi, 2019).

La circulación de retorno aparece en forma de dos celdas que giran en sentido contrario (Figura 1.1). En la celda superior, un flujo neto hacia el norte transporta las aguas cálidas de la termoclina y capas intermedias que ocupan el primer kilómetro de la columna de agua. En su camino hacia el norte, estas aguas pierden flotabilidad debido al fuerte enfriamiento en el Atlántico Norte subpolar (SPNA, por sus siglas en inglés *subpolar North Atlantic*), creando el Agua Profunda del Atlántico Norte (NADW, por sus siglas en inglés *North Atlantic Deep Water*) que fluye hacia el sur por toda la cuenca a través de capas profundas. La presencia de redes de vigilancia en esta frontera septentrional del Océano Atlántico permite cuantificar esta transformación de la masa de agua. Los resultados de la sección OVIDE (*Observatoire de la Variabilité Interannuelle à DEcennale*) han puesto de manifiesto el complejo giro subpolar oriental responsable de la mayor parte de la formación de masa de agua en el SPNA (Lherminier et al., 2010; Mercier et al., 2015). Estudios recientes que se benefician del sistema de monitorización del programa OSNAP (*Overturning in the Subpolar North Atlantic Program*) han demostrado que la capa profunda de la AMOC incluye, principalmente, aguas de las cuencas de Irminger e Islandia y de los mares nórdicos, mientras que la cuenca del Labrador contribuye mínimamente al total de la AMOC (Lozier et al., 2019a).

Esta celda superior se cierra principalmente por la ganancia de flotabilidad en el Océano Austral debido a los fuertes vientos del oeste que impulsan un transporte de Ekman que favorece el afloramiento (Figura 1.1). La mezcla diapicna impulsada por el viento en el océano interior también puede contribuir a la transformación del agua de las capas inferiores a las superiores (Johnson et al., 2019b).

En la celda inferior, el transporte hacia el sur que fluye a lo largo de las capas profundas se equilibra con el flujo hacia el norte de la masa de agua profunda más densa, el (AABW, por sus siglas en inglés *Antarctic Bottom Water*, Figura 1.1). El AABW se forma por el hundimiento de aguas más frías formadas en el océano Antártico, particularmente en el mar de Weddell (McCarthy et al., 2020; Talley, 2013). Sin embargo, la extensión hacia el norte de la AABW está restringida por la topografía, confinada principalmente a la cuenca occidental debido a la presencia de la dorsal del Atlántico Medio (MAR) en la cuenca oriental que bloquea su avance hacia el norte.

Objetivos

Estimar la evolución de la AMOC es excepcionalmente importante. Las reconstrucciones de modelos y los datos de observaciones directas han arrojado resultados opuestos en cuanto a su estabilidad. Evaluar cómo ha cambiado la AMOC en los últimos treinta años puede ayudar a comprender el papel de la AMOC en el clima del Atlántico Norte y a definir las previsiones sobre la AMOC en el futuro.

La utilización de datos in situ, al igual que los programas de vigilancia, permitió observar los cambios interanuales de la AMOC. El sistema de monitorización subtropical RAPID en 26,5°N sugiere un debilitamiento de la AMOC entre 2004 y 2012 de 0,5 Sv/año (Roberts et al., 2014; Smeed et al., 2014). Sin embargo, la existencia de una recuperación hasta 2018 evita que se observe ninguna disminución significativa de la AMOC (Moat et al., 2020). Además, estudios recientes que utilizan el análisis empírico de datos hidrográficos RAPID que se remontan a la década de 1980 no muestran ningún descenso general (Worthington et al., 2021). En el Atlántico Norte subpolar, el registro OSNAP es aún demasiado corto para determinar cambios a largo plazo. De forma similar, en el Atlántico Sur, el programa SAMBA (*South Atlantic MOC Basin-wide Array*) estima la fuerza de la AMOC a 34,5°S. Sin embargo, su registro sigue siendo limitado, y la variabilidad principal aparece en el intervalo de días a semanas (Kersalé et al., 2020). Estas redes de vigilancia han revolucionado la forma de estudiar la AMOC. Sin embargo, dado que los primeros datos datan de la década de 2000, todavía tenemos que basarnos en otros tipos de conjuntos de datos in situ para observar la AMOC en la década anterior.

Esta tesis trata de responder a la pregunta subyacente de si existen diferencias en la intensidad de la AMOC en determinadas latitudes realizadas entre 1990-99, 2000-09 y 2010-19. Los datos hidrográficos proporcionan observaciones directas de alta resolución, de toda la columna de agua y de baja incertidumbre con resoluciones temporales de 5-10 años. Así pues, las secciones hidrográficas repetidas permiten determinar la circulación en un intervalo de tiempo considerablemente más largo que las observaciones de sistemas de monitorización. Esta investigación ha aprovechado estos conjuntos de datos para investigar la distribución meridional de la AMOC durante los últimos treinta años en términos de masa, calor y agua dulce. También hemos intentado comprender la importancia relativa del aumento de la presión parcial de COC_2 en la interfase aire-mar y los cambios en el transporte de masa en el transporte neto de carbono antropogénico (C_{anth}).

Esquema de la tesis

Esta tesis describe los resultados de tres modelos inversos del océano Atlántico para tres décadas: 1990-99, 2000-09 y 2010-19. Proponemos nuevas perspectivas sobre algunas de las cuestiones que han surgido desde el estudio de Ganachaud & Wunsch (2000) para la década 1990-99. La evolución y variabilidad de la AMOC ha sido ampliamente discutida en nuestra área de estudio, comparando los resultados de los datos hidrográficos y las salidas de los modelos. Así pues, el manuscrito se ha dividido en tres capítulos principales, en los que se abordan distintos aspectos de la AMOC. Dentro de cada capítulo, hay una introducción específica, una descripción de los datos y la metodología empleados, y una discusión de los resultados obtenidos.

El Capítulo 2 examina la intensidad de la AMOC durante los últimos treinta años utilizando datos hidrográficos en el marco de un método inverso, publicado en *Geophysical Research Letters* (Caínzos et al., 2022a). Hemos estimado la fuerza de la AMOC a lo largo de estas tres décadas, proporcionando una herramienta para evaluar la variabilidad de la circulación latitudinal de retorno del Océano Atlántico utilizando datos hidrográficos. Hemos diagnosticado el transporte de masa, calor y agua dulce, y presentamos un resumen de toda la cuenca a partir del gran esfuerzo de muestreo del océano desde la década de 1990.

Además, aprovechando estas estimaciones, hemos analizado la circulación regional en la cuenca atlántica en el Capítulo 3, cuantificando la contribución de cada corriente principal que fluye a lo largo de las secciones en términos de transporte de masa, calor y agua dulce. Ello ayuda a dibujar una imagen de la circulación en la cuenca atlántica para toda la columna de agua, coherente con las representaciones lagrangianas de este complejo sistema de corrientes. Este capítulo está siendo considerado para su publicación en *Ocean Science* (Caínzos et al. 2023, en revisión).

Las mediciones biogeoquímicas se utilizan en el Capítulo 4 para estimar el presupuesto de C_{anth} en el Océano Atlántico y cómo ha cambiado en los últimos treinta años. Hemos proporcionado nuevos resultados que evalúan la variabilidad del C_{anth} asociada a la circulación latitudinal de retorno del Atlántico utilizando datos hidrográficos. Combinando resultados físicos con variables biogeoquímicas, hemos podido evaluar la importancia de los flujos horizontales y verticales a lo largo de toda la cuenca atlántica. Estos resultados se han publicado en *Global Biogeochemical Cycles* (Caínzos et al., 2022b).

Finalmente, el Capítulo 5 ofrece un resumen general con las principales observaciones concluyentes, y perspectivas para futuros trabajos.

Conclusiones generales

En resumen, esta tesis ha logrado obtener una imagen completa de la Circulación Latitudinal de Retorno del Atlántico a través de la cuenca atlántica durante los últimos treinta años en términos de masa, calor, agua dulce y carbono antropogénico aplicando métodos inversos a datos hidrográficos.

En primer lugar, hemos estudiado los transportes netos de masa, calor y agua dulce por la AMOC en las secciones zonales hidrográficas disponibles entre 45°S y 55°N. Estos transportes son las soluciones obtenidas a partir de tres modelos inversos, cada uno de los cuales contiene secciones comprendidas entre 1990-99, 2000-09 y 2010-19. Los principales resultados de este estudio son:

- La presencia en el Atlántico de dos celdas de retorno que giran en sentido contrario conforma la estructura meridional de la AMOC y ha persistido durante los últimos treinta años. La celda superior está parcialmente cerrada por el transporte vertical de agua. Se observa una circulación constante a lo largo de las décadas, con afloramiento en el giro subtropical meridional y descenso en el giro subtropical septentrional y el Atlántico Norte subpolar.

- No existen cambios aparentes en la intensidad de la AMOC entre las diversas realizaciones hidrográficas llevadas a cabo en diferentes décadas, sin que se observen diferencias para las capas superiores, profundas y abisales a lo largo del océano Atlántico. Los valores de intensidad de la AMOC se sitúan en el rango de 16-20 Sv entre 45°S y 47°N y en torno a 12 Sv en 55°N.

- En la sección más septentrional, en 55°N, donde se produce la formación de aguas profundas, la cuenca oriental es la principal contribuyente a la AMOC, mientras que la cuenca occidental (Mar del Labrador) aporta un transporte débil bastante constante, lo que corrobora los resultados de los programas de observación OSNAP y OVIDE.

- El transporte de calor de retorno, que representa los cambios en la estructura vertical de la columna de agua, domina el transporte total de calor y aumenta hacia el ecuador. Este componente de calor permanece constante en el Atlántico excepto en ciertas latitudes, manifestando cambios en 24,5°N y un aumento neto entre la primera y la última década en 30°S. La componente horizontal o de giro presenta valores constantes en todas las latitudes y a lo largo de las décadas de este estudio.

- La componente de retorno de agua dulce presenta un transporte más fuerte hacia el sur en las secciones cercanas al ecuador. La mayoría de las secciones no muestran cambios con el tiempo, pero en 24,5°N la década 2000-09 arroja un valor más bajo y en 30°S hay un aumento neto hacia el sur entre la primera y la última década, con valores cercanos a cero. El flujo horizontal o de giro de agua dulce muestra un valor más alto hacia el norte en las secciones que ocupan los giros subtropicales, con valores similares para todas las décadas.

- Curiosamente, esta tendencia hacia un mayor retorno de agua dulce hacia el sur en 30°S entre 1990-99 y 2010-19 muestra que la AMOC efectivamente exporta agua dulce fuera del Atlántico. Estos resultados indican que la AMOC puede encontrarse en un estado biestable. Según estudios de modelos, el flujo de agua dulce de retorno en esta latitud se ha identificado como un posible indicador indirecto de la estabilidad de la AMOC, que podría determinar si se encuentra en un régimen monoestable o biestable.

Utilizando las soluciones de los mismos modelos inversos, hemos estudiado la circulación horizontal en el Océano Atlántico atendiendo a las principales corrientes latitudinales que participan en la AMOC. El giro oceánico impulsado por el viento está representado por corrientes superficiales en cuencas subtropicales, con corrientes de contorno occidental más intensas hacia el polo, compensadas por el flujo hacia el ecuador en el interior del océano y corrientes de contorno oriental más débiles que ocupan una extensión longitudinal más amplia. En general, no aparecen tendencias en el tiempo para ninguna corriente, encontrándose estimaciones coherentes para diferentes décadas. Los principales resultados obtenidos para la circulación superior, profunda y abisal son los siguientes:

- De los 61 Sv netos que entran en el Atlántico Sur en 45°S, el 61% pertenecen a las aguas frías y dulces de la Corriente de las Malvinas (MC, por sus siglas en inglés *Malvinas Current*) y el 39% a las aguas más cálidas y saladas de las Corrientes de Benguela (BeC, por sus siglas en inglés *Benguela Current*) y Ecuatorial del Sur (SEC, por sus siglas en inglés *South Equatorial Current*).

- En el Atlántico Norte, la Corriente del Golfo (GS, por sus siglas en inglés *Gulf Stream*) alimenta los giros subtropical y subpolar, con aguas cálidas procedentes de las Corrientes de Florida (FC, por sus siglas en inglés *Florida Current*) y de las Antillas (AC, por sus siglas en inglés *Antilles Current*). Entre 24,5°N y 55°N, se produce un hundimiento hacia capas más profundas de más de 5 Sv, y el transporte restante fluye hacia el norte en la Corriente del Atlántico Norte (NAC, por sus siglas en inglés *North Atlantic Current*) contribuyendo al Atlántico Norte subpolar.

- El agua profunda recién formada entra en la cuenca atlántica a través de las Aguas de Desbordamiento de Islandia-Escocia (ISOW, por sus siglas en inglés *Iceland-Scotland Overflow Waters*) y las Aguas de Desbordamiento del Estrecho de Dinamarca (DSOW, por sus siglas en inglés *Denmark Strait Overflow Waters*), con una mayor contribución de las Aguas de Desbordamiento de Islandia-Escocia.
- La Corriente Profunda de Borde Occidental (DWBC, por sus siglas en inglés *Deep Western Boundary Current*) muestra continuidad en su camino hacia el sur, hasta llegar al sur de aproximadamente 19°S, donde se bifurca en una rama occidental y otra oriental que atraviesa la dorsal Atlántica.
- Las aguas abisales se limitan principalmente al Atlántico Sur, llegando hasta los 24,5°N, con una entrada neta hacia el norte a través de la cuenca occidental.
- El transporte de calor introducido en el Atlántico Sur por las aguas cálidas y saladas del escape de Agulhas (en inglés *Agulhas Leakage*) se distribuye a lo largo de la cuenca oriental. Este transporte de calor se divide en las contribuciones para las Corrientes de Benguela y Ecuatorial del Sur, ambas reduciendo su transporte de calor hacia el norte. Las aguas frías y dulces de la Corriente de las Malvinas introducen sólo la mitad del transporte que se encuentra en la cuenca oriental, con una exportación de calor hacia el sur, hacia el Océano Austral, de alrededor de 1 PW.
- El transporte de calor hacia el norte en las capas superiores del Atlántico Norte se debe principalmente al fuerte calor transportado por la Corriente de Florida que aumenta en la Corriente del Golfo a 36°N. Los procesos de convección en el Atlántico Norte subpolar provocan una disminución del transporte de calor por la Corriente del Atlántico Norte a 47°N.
- En capas profundas, la Corriente Profunda de Borde Occidental transporta aproximadamente -0,3 PW hacia el sur, a partir de 47°N desde los Grandes Bancos (en inglés *Grand Banks*) por todo el Atlántico Norte y el Atlántico Sur hasta 24°S.
- El flujo de agua dulce se limita a las capas superiores, con un transporte hacia el Atlántico Sur a través de la Corriente de las Malvinas, contrarrestado por la Corriente de Benguela.

- En el Atlántico Norte, se produce principalmente un flujo de agua dulce hacia el sur a lo largo de la cuenca occidental.

Por último, hemos incorporado no sólo los transportes de masa, calor y agua dulce, sino también el estudio del presupuesto de carbono antropogénico (C_{anth}) en el océano Atlántico. Hemos incorporado con éxito ecuaciones biogeoquímicas al modelo inverso, restringiendo la conservación de oxígeno, nitrato, silicato y fosfato para definir mejor la bomba de carbono en la columna de agua. La introducción de estas variables en nuestro estudio nos permite extraer las siguientes conclusiones:

- El cambio en el transporte neto de C_{anth} aparece a partir de la variabilidad en las capas superiores.
- Existe un transporte de C_{anth} hacia el norte procedente de las aguas centrales e intermedias recién formadas del Océano Austral, cuya fuerza disminuye en su camino hacia el norte.
- El transporte de C_{anth} a 24,5°N presenta un valor inferior al esperado para la década 2000-09, relacionado con una fuerza de vuelco más débil. Este valor coincide con un periodo de mayor intensidad en la parte superior del océano interior, según las estimaciones de los modelos empíricos que utilizan datos observacionales. Este bajo transporte de C_{anth} a 24,5°N puede ser el resultado de un refuerzo en el transporte opuesto hacia el sur transportado por el océano interior superior, acompañado de una reducción en la concentración ponderada de C_{anth}.
- Para nuestras secciones más septentrionales, a 55°N, nos acercamos más a las estimaciones que apoyan fuertes transportes laterales en estas latitudes, marcando un fuerte retorno que transporta C_{anth} hacia los mares nórdicos a través de la convección profunda que tiene lugar en esta región.
- El retorno en el Atlántico Norte, y especialmente en el Atlántico Norte subpolar y los mares nórdicos, desempeña un papel importante en la redistribución del C_{anth} recién obtenido de la atmósfera, con flujos relativamente grandes que exportan C_{anth} a capas profundas.
- En el Atlántico Sur, las capas abisales desempeñan un papel en la introducción de C_{anth} en la columna de agua a través del Agua de Fondo Antártica, y proporcionan, en consecuencia, un flujo ascendente de C_{anth} desde las capas abisales a las profundas.
- La mezcla mediante procesos de difusión se produce en todo el Atlántico, principalmente en la interfase entre las capas superiores y profundas, donde existe un gradiente más fuerte, y es el principal proceso de exportación de C_{anth} desde las capas superiores a las profundas en el Atlántico Sur.

Bibliography

Álvarez, M., Ríos, A. F., Pérez, F. F., Bryden, H. L., & Rosón, G. (2003). Transports and budgets of total inorganic carbon in the subpolar and temperate North Atlantic. *Global Biogeochemical Cycles*, 17(1), 1–21. https://doi.org/10.1029/2002GB001881

Anderson, L. A. (1995). On the hydrogen and oxygen content of marine phytoplankton. *Deep Sea Research, Part I*, 42(9), 1675–1680.

Arhan, M., Mercier, H., & Park, Y. H. (2003). On the deep water circulation of the eastern South Atlantic Ocean. *Deep-Sea Research Part I: Oceanographic Research Papers*, 50(7), 889–916. https://doi.org/10.1016/S0967-0637(03)00072-4

Artana, C., Ferrari, R., Koenig, Z., Sennéchael, N., Saraceno, M., Piola, A. R., & Provost, C. (2018). Malvinas current volume transport at 41° S: A 24 yearlong time series consistent with mooring data from 3 decades and satellite altimetry. *Journal of Geophysical Research: Oceans*, 123(1), 378–398. https://doi.org/10.1002/2017JC013600

Arumí-Planas, C., Hernández-Guerra, A., Pelegrí, J. L., Vélez-Belchí, P., Emelianov, M., Caínzos, V., Cana, L., Firing, Y. L., García-Weil, L., Pérez-Hernández, M. D., & Santana-Toscano, D. (2023). The South Atlantic Circulation between 34.5ºS, 24ºS and above the Mid-Atlantic Ridge from an Inverse Box Model. *Journal of Geophysical Research: Oceans*, Submitted.

Atkinson, C. P., Bryden, H. L., Hirschi, J. J., & Kanzow, T. (2010). On the seasonal cycles and variability of Florida Straits, Ekman and Sverdrup transports at 26° N in the Atlantic Ocean. *Ocean Science*, 6(4), 837–859. https://doi.org/10.5194/os-6-837-2010

Bacon, S. (1997). Circulation and fluxes in the North Atlantic between Greenland and Ireland. *Journal of Physical Oceanography*, 27(7), 1420–1435. https://doi.org/10.1175/1520-0485(1997)027⟨1420:cafitn⟩2.0.co;2

Baringer, M. O. & Larsen, J. C. (2001). Sixteen years of Florida current transport at 27° N. *Geophysical Research Letters*, 28(16), 3179–3182. https://doi.org/10.1029/2001GL013246

Baringer, M. O. & Molinari, R. (1999). Atlantic ocean baroclinic heat flux at 24 to 26° N. *Geophysical Research Letters*, 26(3), 353–356.

Bersch, M., Yashayaev, I., & Koltermann, K. P. (2007). Recent changes of the thermohaline circulation in the subpolar North Atlantic. *Ocean Dynamics*, 57(3), 223–235. https://doi.org/10.1007/s10236-007-0104-7

Biastoch, A., Böning, C. W., & Lutjeharms, J. R. E. (2008). Agulhas leakage dynamics affects decadal variability in Atlantic overturning circulation. *Nature*, 456(7221), 489–492. https://doi.org/10.1038/nature07426

Biastoch, A., Durgadoo, J. V., Morrison, A. K., van Sebille, E., Weijer, W., & Griffies, S. M. (2015). Atlantic multi-decadal oscillation covaries with Agulhas leakage. *Nature Communications*, 6(1), 10082. https://doi.org/10.1038/ncomms10082

Biló, T. C. & Johns, W. E. (2020). The Deep Western Boundary Current and Adjacent Interior Circulation at 24°–30° N: Mean Structure and Mesoscale Variability. *Journal of Physical Oceanography*, 50(9), 2735–2758. https://doi.org/10.1175/JPO-D-20-0094.1

Bittig, H., Steinhoff, T., Claustre, H., Fiedler, B., Williams, N., Sauzède, R., Körtzinger, A., & Gattuso, J.-P. (2018). An Alternative to Static Climatologies: Robust Estimation of Open Ocean CO2 Variables and Nutrient Concentrations From T, S, and O2 Data Using Bayesian Neural Networks. *Frontiers in Marine Science*, 5(SEP), 1–29. https://doi.org/10.3389/fmars.2018.00328

Boebel, O., Davis, R. E., Ollitrault, M., Peterson, R. G., Richardson, P. L., Schmid, C., & Zenk, W. (1999). The intermediate depth circulation of the western South Atlantic. *Geophysical Research Letters*, 26(21), 3329–3332. https://doi.org/10.1029/1999GL002355

Bower, A., Lozier, S., Biastoch, A., Drouin, K., Foukal, N., Furey, H., Lankhorst, M., Rühs, S., & Zou, S. (2019). Lagrangian Views of the Pathways of the Atlantic Meridional Overturning Circulation. *Journal of Geophysical Research: Oceans*, 124(8), 5313–5335. https://doi.org/10.1029/2019JC015014

Brearley, J. A., Pickart, R. S., Valdimarsson, H., Jonsson, S., Schmitt, R. W., & Haine, T. W. (2012). The East Greenland boundary current system south of Denmark Strait. *Deep Sea Research Part I: Oceanographic Research Papers*, 63, 1–19. https://doi.org/10.1016/j.dsr.2012.01.001

Brown, P. J., McDonagh, E. L., Sanders, R., Watson, A. J., Wanninkhof, R., King, B. A., Smeed, D. A., Baringer, M. O., Meinen, C. S., Schuster, U., Yool, A., & Messias, M.-J. (2021). Circulation-driven variability of Atlantic anthropogenic carbon transports and uptake. *Nature Geoscience*. https://doi.org/10.1038/s41561-021-00774-5

Bryden, H. L. & Imawaki, S. (2001). Chapter 6.1 Ocean heat transport. *Ocean Circulation & Climate: Observing and Modelling the Global Ocean*, (Chapter 6.1, 455–474). Academic Press. https://doi.org/10.1016/S0074-6142(01)80134-0

Bryden, H. L., Johns, W. E., & Saunders, P. M. (2005a). Deep western boundary current east of Abaco: Mean structure and transport. *Journal of Marine Research*, 63(1), 35–57. https://doi.org/10.1357/0022240053693806

Bryden, H. L., King, B. A., & McCarthy, G. D. (2011). South Atlantic overturning circulation at 24°S. *Journal of Marine Research*, 69(1), 39–56. https://doi.org/10.1357/002224011798147633

Bryden, H. L., Longworth, H. R., & Cunningham, S. A. (2005b). Slowing of the Atlantic meridional overturning circulation at 25° N. *Nature*, 438, 655–657. https://doi.org/10.1038/nature04385

Buckley, M. W. & Marshall, J. (2016). Observations, inferences, and mechanisms of the Atlantic Meridional Overturning Circulation: A review. *Reviews of Geophysics*, 54(1), 5–63. https://doi.org/10.1002/2015RG000493

Caesar, L., McCarthy, G. D., Thornalley, D. J. R., Cahill, N., & Rahmstorf, S. (2021). Current Atlantic Meridional Overturning Circulation weakest in last millennium. *Nature Geoscience*, 14(3), 118–120. https://doi.org/10.1038/s41561-021-00699-z

Caesar, L., Rahmstorf, S., Robinson, A., Feulner, G., & Saba, V. (2018). Observed fingerprint of a weakening Atlantic Ocean overturning circulation. *Nature*, 556(7700), 191–196. https://doi.org/10.1038/s41586-018-0006-5

Caínzos, V., Hernández-Guerra, A., McCarthy, G. D., McDonagh, E. L., Cubas Armas, M., & Pérez-Hernández, M. D. (2022a). Thirty Years of GOSHIP and WOCE Data: Atlantic Overturning of Mass, Heat, and Freshwater Transport. *Geophysical Research Letters*, 49(4). https://doi.org/10.1029/2021GL096527

Caínzos, V., Pérez-Hernández, M. D., Santana-Toscano, D., Arumí-Planas, C., & Hernández-Guerra, A. (2023). Consistent picture of the horizontal circulation of the Atlantic Ocean over three decades. *EGUsphere*, Preprint(February). https://doi.org/10.5194/egusphere-2023-136

Caínzos, V., Velo, A., Pérez, F. F., & Hernández-Guerra, A. (2022b). Anthropogenic Carbon Transport Variability in the Atlantic Ocean Over Three Decades. *Global Biogeochemical Cycles*, 36(11). https://doi.org/10.1029/2022GB007475

Campos, E. J. D., van Caspel, M. C., Zenk, W., Morozov, E. G., Frey, D. I., Piola, A. R., Meinen, C. S., Sato, O. T., Perez, R. C., & Dong, S. (2021). Warming Trend in Antarctic Bottom Water in the Vema Channel in the South Atlantic. *Geophysical Research Letters*, 48(19), 1–7. https://doi.org/10.1029/2021GL094709

Casanova-Masjoan, M., Pérez-Hernández, M. D., Vélez-Belchí, P., Cana, L., & Hernández-Guerra, A. (2020). Variability of the Canary Current diagnosed by inverse box models. *Journal of Geophysical Research: Oceans*, 125(8), e2020JC016199. https://doi.org/10.1029/2020JC016199

Casanova-Masjoan, M., Pérez-Hernández, M. D., Pickart, R. S., Valdimarsson, H., Ólafsdóttir, S. R., Macrander, A., Grisolía-Santos, D., Torres, D. J., Jónsson, S., Våge, K., Lin, P., & Hernández-Guerra, A. (2020). Along-Stream, Seasonal, and Interannual Variability of the North Icelandic Irminger Current and East Icelandic Current Around Iceland. *Journal of Geophysical Research: Oceans*, 125(9), 1–24. https://doi.org/10.1029/2020JC016283

Cessi, P. (2019). The Global Overturning Circulation. *Annual Review of Marine Science*, 11(1), 249–270. https://doi.org/10.1146/annurev-marine-010318-095241

Cheng, W., Chiang, J. C. H., & Zhang, D. (2013). Atlantic Meridional Overturning Circulation (AMOC) in CMIP5 Models: RCP and Historical Simulations. *Journal of Climate*, 26(18), 7187–7197. https://doi.org/10.1175/JCLI-D-12-00496.1

Chidichimo, M. P., Perez, R. C., Speich, S., Kersalé, M., Sprintall, J., Dong, S., Lamont, T., Sato, O. T., Chereskin, T. K., Hummels, R., & Schmid, C. (2023). Energetic overturning flows, dynamic interocean exchanges, and ocean warming observed in the South Atlantic. *Communications Earth & Environment*, 4(1), 10. https://doi.org/10.1038/s43247-022-00644-x

Comas-Rodríguez, I., Hernández-Guerra, A., Fraile-Nuez, E., Martínez-Marrero, A., Benítez-Barrios, V. M., Pérez-Hernández, M. D., & Vélez-Belchí, P. (2011). The Azores Current System from a meridional section at 24.5°W. *Journal of Geophysical Research*, 116(C9), C09021. https://doi.org/10.1029/2011JC007129

Cunningham, S. A. (2005). RRS "Discovery" Cruise D279, 04 Apr - 10 May 2004. A Transatlantic hydrography section at 24.5N. Technical Report 54, National Oceanography Centre Southampton, Southampton, UK.

Cunningham, S. A., Kanzow, T., Rayner, D., Baringer, M. O., Johns, W. E., Marotzke, J., Longworth, H. R., Grant, E. M., Hirschi, J. J. M., Beal, L. M., Meinen, C. S., & Bryden, H. L. (2007). Temporal variability of the Atlantic meridional overturning circulation at 26.5°N. *Science*, 317, 935–938. https://doi.org/10.1126/science.1141304

Curry, B., Lee, C. M., Petrie, B., Moritz, R. E., & Kwok, R. (2014). Multiyear volume, liquid freshwater, and sea ice transports through Davis Strait, 2004–10. *Journal of Physical Oceanography*, 44(4), 1244–1266. https://doi.org/10.1175/jpo-d-13-0177.1

Daniault, N., Mercier, H., Lherminier, P., Sarafanov, A., Falina, A., Zunino, P., Pérez, F. F., Ríos, A. F., Ferron, B., Huck, T., Thierry, V., & Gladyshev, S. (2016). The northern North Atlantic Ocean mean circulation in the early 21st century. *Progress in Oceanography*, 146, 142–158. https://doi.org/10.1016/j.pocean.2016.06.007

Davis, R. E., Regier, L. A., Dufour, J., & Webb, D. C. (1992). The Autonomous Lagrangian Circulation Explorer (ALACE). *Journal of Atmospheric and Oceanic Technology*, 9(3), 264–285. https://doi.org/10.1175/1520-0426(1992)009⟨0264:TALCE⟩2.0.CO;2

de Vries, P. & Weber, S. L. (2005). The Atlantic freshwater budget as a diagnostic for the existence of a stable shut down of the meridional overturning circulation. *Geophysical Research Letters*, 32(9), L09606. https://doi.org/10.1029/2004GL021450

Desbruyères, D. G., Mercier, H., Maze, G., & Daniault, N. (2019). Surface predictor of overturning circulation and heat content change in the subpolar North Atlantic. *Ocean Science*, 15(3), 809–817. https://doi.org/10.5194/os-15-809-2019

DeVries, T. (2014). The oceanic anthropogenic CO2 sink: Storage, air-sea fluxes, and transports over the industrial era. *Global Biogeochemical Cycles*, 28(7), 631–647. https://doi.org/10.1002/2013GB004739

DeVries, T., Holzer, M., & Primeau, F. (2017). Recent increase in oceanic carbon uptake driven by weaker upper-ocean overturning. *Nature*, 542(7640), 215–218. https://doi.org/10.1038/nature21068

Dickson, B., Dye, S., Jónsson, S., Köhl, A., Macrander, A., Marnela, M., Meincke, J., Olsen, S., Rudels, B., Valdimarsson, H., & Voet, G. (2008). The Overflow Flux West of Iceland: Variability, Origins and Forcing. *Arctic–Subarctic Ocean Fluxes*, 443–474. Springer Netherlands. https://doi.org/10.1007/978-1-4020-6774-7_20

Dijkstra, H. A. (2007). Characterization of the multiple equilibria regime in a global ocean model. *Tellus*, 59A, 695–705. https://doi.org/10.1111/j.1600-0870.2007.00267.x

Doney, S. C., Busch, D. S., Cooley, S. R., & Kroeker, K. J. (2020). The Impacts of Ocean Acidification on Marine Ecosystems and Reliant Human Communities. *Annual Review of Environment and Resources*, 45(1), 83–112. https://doi.org/10.1146/annurev-environ-012320-083019

Doney, S. C., Fabry, V. J., Feely, R. A., & Kleypas, J. A. (2009). Ocean Acidification: The Other CO2 Problem. *Annual Review of Marine Science*, 1(1), 169–192. https://doi.org/10.1146/annurev.marine.010908.163834

Donners, J. & Drijfhout, S. S. (2004). The Lagrangian view of South Atlantic interocean exchange in a global ocean model compared with inverse model results. *Journal of Physical Oceanography*, 34(5), 1019–1035. https://doi.org/10.1175/1520-0485(2004)034⟨1019:TLVOSA⟩2.0.CO;2

Durgadoo, J. V., Rühs, S., Biastoch, A., & Böning, C. W. B. (2017). Indian Ocean sources of Agulhas leakage. *Journal of Geophysical Research: Oceans*, 122(4), 3481–3499. https://doi.org/10.1002/2016JC012676

Evans, G. R., McDonagh, E. L., King, B. A., Bryden, H. L., Bakker, D. C. E., Brown, P. J., Schuster, U., Speer, K. G., & van Heuven, S. M. A. C. (2017). South Atlantic interbasin exchanges of mass, heat, salt and anthropogenic carbon. *Progress in Oceanography*, 151, 62–82. https://doi.org/10.1016/j.pocean.2016.11.005

Fischer, J., Karstensen, J., Zantopp, R., Visbeck, M., Biastoch, A., Behrens, E., Böning, C., Quadfasel, D., Jochumsen, K., Valdimarsson, H., Jónsson, S., Bacon, S., Holliday, N., Dye, S., Rhein, M., & Mertens, C. (2015). Intra-seasonal variability of the DWBC in the western subpolar North Atlantic. *Progress in Oceanography*, 132, 233–249. https://doi.org/10.1016/j.pocean.2014.04.002

Fischer, J., Schott, F. A., & Dengler, M. (2004). Boundary Circulation at the Exit of the Labrador Sea. *Journal of Physical Oceanography*, 34(7), 1548–1570. https://doi.org/10.1175/1520-0485(2004)034⟨1548:BCATEO⟩2.0.CO;2

Fischer, J., Visbeck, M., Zantopp, R., & Nunes, N. (2010). Interannual to decadal variability of outflow from the Labrador Sea. *Geophysical Research Letters*, 37(24). https://doi.org/10.1029/2010GL045321

Florindo-López, C., Bacon, S., Aksenov, Y., Chafik, L., Colbourne, E., & Holliday, N. P. (2020). Arctic Ocean and Hudson Bay freshwater exports: new estimates from seven decades of hydrographic surveys on the Labrador Shelf. *Journal of Climate*, 33(20), 8849–8868. https://doi.org/10.1175/JCLI-D-19-0083.1

Fontela, M., Mercier, H., & Pérez, F. F. (2019). Long-term integrated biogeochemical budget driven by circulation in the eastern subpolar North Atlantic. *Progress in Oceanography*, 173(September 2018), 51–65. https://doi.org/10.1016/j.pocean.2019.02.004

Foppert, A., Rintoul, S. R., Purkey, S. G., Zilberman, N., Kobayashi, T., Sallèe, J., Wijk, E. M., & Wallace, L. O. (2021). Deep Argo Reveals Bottom Water Properties and Pathways in the Australian-Antarctic Basin. *Journal of Geophysical Research: Oceans*, 126(12), 1–18. https://doi.org/10.1029/2021JC017935

Forget, G. & Ferreira, D. (2019). Global ocean heat transport dominated by heat export from the tropical Pacific. *Nature Geoscience*, 12(5), 351–354. https://doi.org/10.1038/s41561-019-0333-7

Fraile-Nuez, E., Machín, F., Vélez-Belchí, P., López-Laatzen, F., Borges, R., Benítez-Barrios, V. M., & Hernández-Guerra, A. (2010). Nine years of mass transport data in the eastern boundary of the North Atlantic Subtropical Gyre. *Journal of Geophysical Research*, 115(C9), C09009. https://doi.org/10.1029/2010JC006161

Frajka-Williams, E. (2019). Topographic eddies. *Encyclopedia of Ocean Sciences*, number June 2018, 158–168. Elsevier, (3 ed.). https://doi.org/10.1016/B978-0-12-409548-9.10852-8

Frajka-Williams, E., Cunningham, S. A., Bryden, H. L., & King, B. A. (2011). Variability of Antarctic Bottom Water at 24.5°N in the Atlantic. *Journal of Geophysical Research*, 116(C11), C11026. https://doi.org/10.1029/2011JC007168

Frankignoul, C., de Coëtlogon, G., Joyce, T. M., & Dong, S. (2001). Gulf Stream Variability and Ocean–Atmosphere Interactions. *Journal of Physical Oceanography*, 31(12), 3516–3529. https://doi.org/10.1175/1520-0485(2002)031⟨3516:GSVAOA⟩2.0.CO;2

Fraser, N. J. & Cunningham, S. A. (2021). 120 Years of AMOC Variability Reconstructed From Observations Using the Bernoulli Inverse. *Geophysical Research Letters*, 48(18). https://doi.org/10.1029/2021GL093893

Friedlingstein, P., O'Sullivan, M., Jones, M. W., Andrew, R. M., Hauck, J., Olsen, A., Peters, G. P., Peters, W., Pongratz, J., Sitch, S., Le Quéré, C., Canadell, J. G., Ciais, P., Jackson, R. B., Alin, S., Aragão, L. E. O. C., Arneth, A., Arora, V., Bates, N. R., Becker, M., Benoit-Cattin, A., Bittig, H. C., Bopp, L., Bultan, S., Chandra, N., Chevallier, F., Chini, L. P., Evans, W., Florentie, L., Forster, P. M., Gasser, T., Gehlen, M., Gilfillan, D., Gkritzalis, T., Gregor, L., Gruber, N., Harris, I., Hartung, K., Haverd, V., Houghton, R. A., Ilyina, T., Jain, A. K., Joetzjer, E., Kadono, K., Kato, E., Kitidis, V., Korsbakken, J. I., Landschützer, P., Lefèvre, N., Lenton, A., Lienert, S., Liu, Z., Lombardozzi, D., Marland, G., Metzl, N., Munro, D. R., Nabel, J. E. M. S., Nakaoka, S.-I., Niwa, Y., O'Brien, K., Ono, T., Palmer, P. I., Pierrot, D., Poulter, B., Resplandy, L., Robertson, E., Rödenbeck, C., Schwinger, J., Séférian, R., Skjelvan, I., Smith, A. J. P., Sutton, A. J., Tanhua, T., Tans, P. P., Tian, H., Tilbrook, B., van der Werf, G., Vuichard, N., Walker, A. P., Wanninkhof, R., Watson, A. J., Willis, D., Wiltshire, A. J., Yuan, W., Yue, X., & Zaehle, S. (2020). Global Carbon Budget 2020. *Earth System Science Data*, 12(4), 3269–3340. https://doi.org/10.5194/essd-12-3269-2020

Fu, Y., Karstensen, J., & Brandt, P. (2018). Atlantic Meridional Overturning Circulation at 14.5° N in 1989 and 2013 and 24.5° N in 1992 and 2015: volume, heat, and freshwater transports. *Ocean Science*, 14(4), 589–616. https://doi.org/10.5194/os-14-589-2018

Fu, Y., Li, F., Karstensen, J., & Wang, C. (2020). A stable Atlantic Meridional Overturning Circulation in a changing North Atlantic Ocean since the 1990s. *Science Advances*, 6(48), eabc7836. https://doi.org/10.1126/sciadv.abc7836

Ganachaud, A. S. (1999). *Large scale oceanic circulation and fluxes of freshwater, heat, nutrients and oxygen*. Massachusetts Institute of Technology and Woods Hole Oceanographic Institution. https://doi.org/10.1575/1912/4130

Ganachaud, A. S. (2003a). Error budget of inverse box models: The North Atlantic. *Journal of Atmospheric and Oceanic Technology*, 20(11), 1641–1655. https://doi.org/10.1175/1520-0426(2003)020⟨1641:EBOIBM⟩2.0.CO;2

Ganachaud, A. S. (2003b). Large-scale mass transports, water mass formation, and diffusivities estimated from World Ocean Circulation Experiment (WOCE) hydrographic data. *Journal of Geophysical Research*, 108(C7). https://doi.org/10.1029/2002jc001565

Ganachaud, A. S. & Wunsch, C. (2000). Improved estimates of global ocean circulation, heat transport and mixing from hydrographic data. *Nature*, 408, 453–456.

Ganachaud, A. S. & Wunsch, C. (2003). Large-scale ocean heat and freshwater transports during the World Ocean Circulation Experiment. *Journal of Climate*, 16, 696–705. https://doi.org/10.1175/1520-0442(2003)016⟨0696:LSOHAF⟩2.0.CO;2

García-Ibáñez, M. I., Pardo, P. C., Carracedo, L. I., Mercier, H., Lherminier, P., Ríos, A. F., & Pérez, F. F. (2015). Structure, transports and transformations of the water masses in the Atlantic Subpolar Gyre. *Progress in Oceanography*, 135, 18–36. https://doi.org/10.1016/j.pocean.2015.03.009

Garzoli, S. L. (1993). Geostrophic velocity and transport variability in the Brazil-Malvinas Confluence. *Deep Sea Research Part I: Oceanographic Research Papers*, 40(7), 1379–1403. https://doi.org/10.1016/0967-0637(93)90118-M

Garzoli, S. L. (2004). North Brazil Current retroflection and transports. *Journal of Geophysical Research*, 109(C1), C01013. https://doi.org/10.1029/2003JC001775

Garzoli, S. L., Baringer, M. O., Dong, S., Perez, R. C., & Yao, Q. (2013). South Atlantic meridional fluxes. *Deep-Sea Research Part I: Oceanographic Research Papers*, 71, 21–32. https://doi.org/10.1016/j.dsr.2012.09.003

Garzoli, S. L., Dong, S., Fine, R., Meinen, C. S., Perez, R. C., Schmid, C., van Sebille, E., & Yao, Q. (2015). The fate of the Deep Western Boundary Current in the South Atlantic. *Deep Sea Research Part I: Oceanographic Research Papers*, 103, 125–136. https://doi.org/10.1016/j.dsr.2015.05.008

Garzoli, S. L. & Gordon, A. L. (1996). Origins and variability of the Benguela Current. *Journal of Geophysical Research: Oceans*, 101(C1), 897–906. https://doi.org/10.1029/95JC03221

Garzoli, S. L., Gordon, A. L., Kamenkovich, V., Pillsbury, D., & Duncombe-Rae, C. (1996). Variability and sources of the southeastern Atlantic circulation. *Journal of Marine Research*, 54(6), 1039–1071. https://doi.org/10.1357/0022240963213763

Gattuso, J.-P., Magnan, A., Billé, R., Cheung, W. W. L., Howes, E. L., Joos, F., Allemand, D., Bopp, L., Cooley, S. R., Eakin, C. M., Hoegh-Guldberg, O., Kelly, R. P., Pörtner, H.-O., Rogers, A. D., Baxter,

J. M., Laffoley, D., Osborn, D., Rankovic, A., Rochette, J., Sumaila, U. R., Treyer, S., & Turley, C. (2015). Contrasting futures for ocean and society from different anthropogenic CO2 emissions scenarios. *Science*, 349(6243). https://doi.org/10.1126/science.aac4722

Gent, P. R. (2018). A commentary on the Atlantic meridional overturning circulation stability in climate models. *Ocean Modelling*, 122(June), 57–66. https://doi.org/10.1016/j.ocemod.2017.12.006

Goes, M., Goni, G., Dong, S., Boyer, T., & Baringer, M. (2020). The Complementary Value of XBT and Argo Observations to Monitor Ocean Boundary Currents and Meridional Heat and Volume Transports: A Case Study in the Atlantic Ocean. *Journal of Atmospheric and Oceanic Technology*, 37(12), 2267–2282. https://doi.org/10.1175/JTECH-D-20-0027.1

Goni, G., Kamholz, S., Garzoli, S., & Olson, D. (1996). Dynamics of the Brazil-Malvinas Confluence based on inverted echo sounders and altimetry. *Journal of Geophysical Research: Oceans*, 101(C7), 16273–16289. https://doi.org/10.1029/96JC01146

Gordon, A. L. & Greengrove, C. L. (1986). Geostrophic circulation of the Brazil-Falkland confluence. *Deep Sea Research Part A. Oceanographic Research Papers*, 33(5), 573–585. https://doi.org/10.1016/0198-0149(86)90054-3

Gou, R., Pennelly, C., & Myers, P. G. (2022). The Changing Behavior of the West Greenland Current System in a Very High-Resolution Model. *Journal of Geophysical Research: Oceans*, 127(8), 1–15. https://doi.org/10.1029/2022JC018404

Gruber, N., Clement, D., Carter, B. R., Feely, R. A., van Heuven, S., Hoppema, M., Ishii, M., Key, R. M., Kozyr, A., Lauvset, S. K., Lo Monaco, C., Mathis, J. T., Murata, A., Olsen, A., Perez, F. F., Sabine, C. L., Tanhua, T., & Wanninkhof, R. (2019). The oceanic sink for anthropogenic CO2 from 1994 to 2007. *Science*, 363(6432), 1193–1199. https://doi.org/10.1126/science.aau5153

Gruber, N., Sarmiento, J. L., & Stocker, T. F. (1996). An improved method for detecting anthropogenic CO2 in the oceans. *Global Biogeochemical Cycles*, 10(4), 809–837. https://doi.org/10.1029/96GB01608

Guallart, E. F., Schuster, U., Fajar, N. M., Legge, O., Brown, P., Pelejero, C., Messias, M.-J., Calvo, E., Watson, A., Ríos, A. F., & Pérez, F. F. (2015). Trends in anthropogenic CO2 in water masses of the Subtropical North Atlantic Ocean. *Progress in Oceanography*, 131, 21–32. https://doi.org/10.1016/j.pocean.2014.11.006

Guinotte, J. M., Orr, J., Cairns, S., Freiwald, A., Morgan, L., & George, R. (2006). Will human-induced changes in seawater chemistry alter the distribution of deep-sea scleractinian corals? *Frontiers in Ecology and the Environment*, 4(3), 141–146. https://doi.org/https://doi.org/10.1890/1540-9295(2006)004[0141:WHCISC]2.0.CO;2

Harden, B. E., Pickart, R. S., Valdimarsson, H., Våge, K., de Steur, L., Richards, C., Bahr, F., Torres, D., Børve, E., Jónsson, S., Macrander, A., Østerhus, S., Håvik, L., & Hattermann, T. (2016). Upstream sources of the Denmark Strait Overflow: Observations from a high-resolution mooring array. *Deep-Sea Research Part I: Oceanographic Research Papers*, 112, 94–112. https://doi.org/10.1016/j.dsr.2016.02.007

Hernández-Guerra, A., Espino-Falcón, E., Vélez-Belchí, P., Dolores Pérez-Hernández, M., Martínez-Marrero, A., & Cana, L. (2017). Recirculation of the Canary Current in fall 2014. *Journal of Marine Systems*, 174, 25–39. https://doi.org/10.1016/j.jmarsys.2017.04.002

Hernández-Guerra, A., Pelegrí, J. L., Fraile-Nuez, E., Benítez-Barrios, V. M., Emelianov, M., Pérez-Hernández, M. D., & Vélez-Belchí, P. (2014). Meridional overturning transports at 7.5N and 24.5N in the Atlantic Ocean during 1992–93 and 2010–11. *Progress in Oceanography*, 128, 98–114. https://doi.org/10.1016/j.pocean.2014.08.016

Hernández-Guerra, A. & Talley, L. D. (2016). Meridional overturning transports at 30°S in the Indian and Pacific Oceans in 2002–2003 and 2009. *Progress in Oceanography*, 146, 89–120. https://doi.org/10.1016/j.pocean.2016.06.005

Hernández-Guerra, A., Talley, L. D., Pelegrí, J. L., Vélez-Belchí, P., Baringer, M. O., Macdonald, A. M., & McDonagh, E. L. (2019). The upper, deep, abyssal and overturning circulation in the Atlantic Ocean at 30°S in 2003 and 2011. *Progress in Oceanography*, 176(102136). https://doi.org/10.1016/j.pocean.2019.102136

Herrford, J., Brandt, P., & Zenk, W. (2017). Property changes of deep and bottom waters in the Western Tropical Atlantic. *Deep Sea Research Part I: Oceanographic Research Papers*, 124(April), 103–125. https://doi.org/10.1016/j.dsr.2017.04.007

Hogg, N., Biscaye, P., Gardner, W., & Schmitz, W. J. (1982). On the transport and modification of Antarctic Bottom Water in the Vema Channel. *Journal of Marine Research*, 40(Supplement), 231–263.

Hogg, N. G. & Johns, W. E. (1995). Western boundary currents. *Reviews of Geophysics*, 33(S2), 1311–1334. https://doi.org/10.1029/95RG00491

Hogg, N. G. & Owens, W. B. (1999). Direct measurement of the deep circulation within the Brazil Basin. *Deep Sea Research Part II: Topical Studies in Oceanography*, 46(1-2), 335–353. https://doi.org/10.1016/S0967-0645(98)00097-6

Holfort, J., Johnson, K. M., Schneider, B., Siedler, G., & Wallace, D. W. R. (1998). Meridional transport of dissolved inorganic carbon in the South Atlantic Ocean. *Global Biogeochemical Cycles*, 12(3), 479–499. https://doi.org/10.1029/98GB01533

Holliday, N. P., Bacon, S., Cunningham, S. A., Gary, S. F., Karstensen, J., King, B. A., Li, F., & Mcdonagh, E. L. (2018). Subpolar North Atlantic Overturning and Gyre-Scale Circulation in the Summers of 2014 and 2016. *Journal of Geophysical Research: Oceans*, 123(7), 4538–4559. https://doi.org/10.1029/2018JC013841

Holzer, M., DeVries, T., & de Lavergne, C. (2021). Diffusion controls the ventilation of a Pacific Shadow Zone above abyssal overturning. *Nature Communications*, 12(1), 4348. https://doi.org/10.1038/s41467-021-24648-x

Houpert, L., Inall, M. E., Dumont, E., Gary, S., Johnson, C., Porter, M., Johns, W. E., & Cunningham, S. A. (2018). Structure and transport of the North Atlantic Current in the Eastern Subpolar Gyre from sustained glider observations. *Journal of Geophysical Research: Oceans*, 123(8), 6019–6038. https://doi.org/10.1029/2018JC014162

Hummels, R., Brandt, P., Dengler, M., Fischer, J., Araujo, M., Veleda, D., & Durgadoo, J. V. (2015). Interannual to decadal changes in the western boundary circulation in the Atlantic at 11°S. *Geophysical Research Letters*, 42(18), 7615–7622. https://doi.org/10.1002/2015GL065254

Jackett, D. R. & McDougall, T. J. (1997). A neutral density variable for the World's Oceans. *Journal of Physical Oceanography*, 27(2), 237–263. https://doi.org/10.1175/1520-0485(1997)027⟨0237:ANDVFT⟩2.0.CO;2

Jackson, L. C., Biastoch, A., Buckley, M. W., Desbruyères, D. G., Frajka-Williams, E., Moat, B., & Robson, J. (2022). The evolution of the North Atlantic Meridional Overturning Circulation since 1980. *Nature Reviews Earth & Environment*, 0123456789. https://doi.org/10.1038/s43017-022-00263-2

Jackson, L. C., Kahana, R., Graham, T., Ringer, M. A., Woollings, T., Mecking, J. V., & Wood, R. A. (2015). Global and European climate impacts of a slowdown of the AMOC in a high resolution GCM. *Climate Dynamics*, 45(11-12), 3299–3316. https://doi.org/10.1007/s00382-015-2540-2

Jayne, S. R. & Marotzke, J. (2001). The dynamics of ocean heat transport variability. *Reviews of Geophysics*, 39(3), 385–411. https://doi.org/10.1029/2000RG000084

Jeansson, E., Olsen, A., Eldevik, T., Skjelvan, I., Omar, A. M., Lauvset, S. K., Nilsen, J. E. Ø., Bellerby, R. G. J., Johannessen, T., & Falck, E. (2011). The Nordic Seas carbon budget: Sources, sinks, and uncertainties. *Global Biogeochemical Cycles*, 25(4), GB4010. https://doi.org/10.1029/2010GB003961

Jochumsen, K., Quadfasel, D., Valdimarsson, H., & Jónsson, S. (2012). Variability of the Denmark Strait overflow: Moored time series from 1996-2011. *Journal of Geophysical Research: Oceans*, 117(C12). https://doi.org/10.1029/2012JC008244

Johns, W. E., Baringer, M. O., Beal, L. M., Cunningham, S. A., Kanzow, T., Bryden, H. L., Hirschi, J. J. M., Marotzke, J., Meinen, C. S., Shaw, B., & Curry, R. (2011). Continuous, array-based estimates of Atlantic Ocean heat transport at 26.5° N. *Journal of Climate*, 24, 2429–2449. https://doi.org/10.1175/2010JCLI3997.1

Johns, W. E., Beal, L. M., Baringer, M. O., Molina, J. R., Cunningham, S. A., Kanzow, T., & Rayner, D. (2008). Variability of Shallow and Deep Western Boundary Currents off the Bahamas during 2004–05: Results from the 26° N RAPID–MOC Array. *Journal of Physical Oceanography*, 38(3), 605–623. https://doi.org/10.1175/2007jpo3791.1

Johns, W. E., Devana, M., Houk, A., & Zou, S. (2021). Moored Observations of the Iceland-Scotland Overflow Plume Along the Eastern Flank of the Reykjanes Ridge. *Journal of Geophysical Research: Oceans*, 126(8), 1–26. https://doi.org/10.1029/2021JC017524

Johns, W. E., Shay, T. J., Bane, J. M., & Watts, D. R. (1995). Gulf Stream structure, transport, and recirculation near 68°W. *Journal of Geophysical Research*, 100(C1), 817. https://doi.org/10.1029/94JC02497

Johnson, G. C., Cadot, C., Lyman, J. M., McTaggart, K. E., & Steffen, E. L. (2020). Antarctic Bottom Water warming in the Brazil Basin: 1990s through 2020, from WOCE to Deep Argo. *Geophysical Research Letters*, 47(18), e2020GL089191. https://doi.org/10.1029/2020GL089191

Johnson, G. C., Lyman, J. M., & Purkey, S. G. (2015). Informing Deep Argo Array Design Using Argo and Full-Depth Hydrographic Section Data. *Journal of Atmospheric and Oceanic Technology*, 32(11), 2187–2198. https://doi.org/10.1175/JTECH-D-15-0139.1

Johnson, G. C., Purkey, S. G., Zilberman, N. V., & Roemmich, D. (2019a). Deep Argo Quantifies Bottom Water Warming Rates in the Southwest Pacific Basin. *Geophysical Research Letters*, 46(5), 2662–2669. https://doi.org/10.1029/2018GL081685

Johnson, H. L., Cessi, P., Marshall, D. P., Schloesser, F., & Spall, M. A. (2019b). Recent contributions of theory to our understanding of the Atlantic Meridional Overturning Circulation. *Journal of Geophysical Research: Oceans*, 1–24. https://doi.org/10.1029/2019jc015330

Johnson, K. M., Schneider, B., Mintrop, L., Wallace, D. W. R., & Kozyr, A. (1998). Carbon Dioxide, Hydrographic, and Chemical Data Obtained During the R/V Meteor Cruise 22/5 in the South Atlantic Ocean (WOCE Section A10, December-1992 January 1993). ORNL/CDIAC-113, NDP-066. Technical report, Carbon Dioxide Information Analysis Center, Oak Ridge National Laboratory, U.S. Department of Energy, Oak Ridge, Tennessee.

Johnson, K. M., Wallace, D. W. R., Wilke, R. J., & Goyet., C. (1995). Carbon Dioxide, Hydrographic, and Chemical Data Obtained During the R/V Meteor Cruise 15/3 in the South Atlantic Ocean

(WOCE Section A9, February - March 1991). ORNL/CDIAC-82, NDP-051. Technical report, Carbon Dioxide Information Analysis Center, Oak Ridge National Laboratory, Oak Ridge, Tennessee. https://doi.org/10.3334/CDIAC/otg.ndp051

Johnson, K. M., Wills, K., Koertzinger, A., Neill, C., & Wallace, D. W. R. (2002). Carbon Dioxide, Hydrographic, and Chemical Data Obtained During the R/V Meteor Cruise 28/1 inthe South Atlantic Ocean (WOCE Section A8, March 29 - May 12, 1994).ORNL/CDIAC-135, NDP-079. Technical report, Carbon Dioxide Information Analysis Center, Oak Ridge National Laboratory, U.S. Department of Energy, Oak Ridge, Tennessee.

Joyce, T. M., Hernández-Guerra, A., & Smethie, W. M. (2001). Zonal circulation in the NW Atlantic and Caribbean from a meridional World Ocean Circulation Experiment hydrographic section at 66°W. *Journal of Geophysical Research: Oceans*, 106(C10), 22095–22113. https://doi.org/10.1029/2000jc000268

Kanzow, T., Send, U., Zenk, W., Chave, A. D., & Rhein, M. (2006). Monitoring the integrated deep meridional flow in the tropical North Atlantic: Long-term performance of a geostrophic array. *Deep-Sea Research Part I: Oceanographic Research Papers*, 53(3), 528–546. https://doi.org/10.1016/j.dsr.2005.12.007

Katsumata, K. & Fukasawa, M. (2011). Changes in meridional fluxes and water properties in the Southern Hemisphere subtropical oceans between 1992/1995 and 2003/2004. *Progress in Oceanography*, 89(1-4), 61–91. https://doi.org/10.1016/j.pocean.2010.12.008

Kersalé, M., Meinen, C. S., Perez, R. C., Le Hénaff, M., Valla, D., Lamont, T., Sato, O. T., Dong, S., Terre, T., van Caspel, M., Chidichimo, M. P., van den Berg, M., Speich, S., Piola, A. R., Campos, E. J. D., Ansorge, I., Volkov, D. L., Lumpkin, R., & Garzoli, S. L. (2020). Highly variable upper and abyssal overturning cells in the South Atlantic. *Science Advances*, 6(32), eaba7573. https://doi.org/10.1126/sciadv.aba7573

Kersalé, M., Perez, R. C., Speich, S., Meinen, C. S., Lamont, T., Le Hénaff, M., Berg, M. A., Majumder, S., Ansorge, I. J., Dong, S., Schmid, C., Terre, T., & Garzoli, S. L. (2019). Shallow and Deep Eastern Boundary Currents in the South Atlantic at 34.5°S: Mean Structure and Variability. *Journal of Geophysical Research: Oceans*, 124(3), 1634–1659. https://doi.org/10.1029/2018JC014554

Key, R. M., Olsen, A., Van Heuven, S., Lauvset, S. K., Velo, A., Lin, X., Schirnick, C., Kozyr, A., Tanhua, T., Hoppema, M., Jutterström, S., Steinfeldt, R., Jeansson, E., Ishii, M., Perez, F. F., & Suzuki, T. (2015). *Global Ocean Data Analysis Project, Version 2 (GLODAPv2)*, volume 8. Carbon Dioxide Information Analysis Center, Oak Ridge National Laboratory, US Department of Energy. https://doi.org/10.3334/CDIAC/OTG.NDP093_GLODAPv2

Khatiwala, S., Primeau, F., & Hall, T. (2009). Reconstruction of the history of anthropogenic CO2 concentrations in the ocean. *Nature*, 462(7271), 346–349. https://doi.org/10.1038/nature08526

Khatiwala, S., Tanhua, T., Mikaloff Fletcher, S. E., Gerber, M., Doney, S. C., Graven, H. D., Gruber, N., McKinley, G. A., Murata, A., Ríos, A. F., & Sabine, C. L. (2013). Global ocean storage of anthropogenic carbon. *Biogeosciences*, 10(4), 2169–2191. https://doi.org/10.5194/bg-10-2169-2013

King, B. A., Sanchez-Franks, A., & Firing, Y. L. (2019). RRS James Cook Cruise JC159 28 February - 11 April 2018. Hydrographic sections from the Brazil to the Benguela Current across 24S in the Atlantic. Technical Report 60, National Oceanography Centre, Southampton, UK.

Koltermann, K. P., Sokov, A. V., Tereschenkov, V. P., Dobroliubov, S. A., Lorbacher, K., & Sy, A. (1999). Decadal changes in the thermohaline circulation of the North Atlantic. *Deep-Sea Research Part II: Topical Studies in Oceanography*, 46(1-2), 109–138. https://doi.org/10.1016/S0967-0645(98)00115-5

Koszalka, I. M., Haine, T. W. N., & Magaldi, M. G. (2013). Fates and Travel Times of Denmark Strait Overflow Water in the Irminger Basin. *Journal of Physical Oceanography*, 43(12), 2611–2628. https://doi.org/10.1175/JPO-D-13-023.1

Lauvset, S. K., Lange, N., Tanhua, T., Bittig, H. C., Olsen, A., Kozyr, A., Álvarez, M., Becker, S., Brown, P. J., Carter, B. R., Cotrim da Cunha, L., Feely, R. A., van Heuven, S., Hoppema, M., Ishii, M., Jeansson, E., Jutterström, S., Jones, S. D., Karlsen, M. K., Lo Monaco, C., Michaelis, P., Murata, A., Pérez, F. F., Pfeil, B., Schirnick, C., Steinfeldt, R., Suzuki, T., Tilbrook, B., Velo, A., Wanninkhof, R., Woosley, R. J., & Key, R. M. (2021). An updated version of the global interior ocean biogeochemical data product, GLODAPv2.2021. *Earth System Science Data*, 13(12), 5565–5589. https://doi.org/10.5194/essd-13-5565-2021

Lazier, J., Hendry, R., Clarke, A., Yashayaev, I., & Rhines, P. (2002). Convection and restratification in the Labrador Sea, 1990–2000. *Deep Sea Research Part I: Oceanographic Research Papers*, 49(10), 1819–1835. https://doi.org/10.1016/S0967-0637(02)00064-X

Le Bras, I. A., Straneo, F., Holte, J., & Holliday, N. P. (2018). Seasonality of Freshwater in the East Greenland Current System From 2014 to 2016. *Journal of Geophysical Research: Oceans*, 123(12), 8828–8848. https://doi.org/10.1029/2018JC014511

Lee, T. N., Johns, W. E., Zantopp, R. J., & Fillenbaum, E. R. (1996). Moored Observations of Western Boundary Current Variability and Thermohaline Circulation at 26.5° in the Subtropical North Atlantic. *Journal of Physical Oceanography*, 26(6), 962–983. https://doi.org/10.1175/1520-0485(1996)026⟨0962:MOOWBC⟩2.0.CO;2

Legeais, J.-F., Ollitrault, M., & Arhan, M. (2013). Lagrangian observations in the Intermediate Western Boundary Current of the South Atlantic. *Deep Sea Research Part II: Topical Studies in Oceanography*, 85, 109–126. https://doi.org/10.1016/j.dsr2.2012.07.028

Legeckis, R. & Gordon, A. L. (1982). Satellite observations of the Brazil and Falkland currents—1975 1976 and 1978. *Deep Sea Research Part A. Oceanographic Research Papers*, 29(3), 375–401. https://doi.org/10.1016/0198-0149(82)90101-7

Lherminier, P., Mercier, H., Huck, T., Gourcuff, C., Pérez, F. F., Morin, P., Sarafanov, A., & Falina, A. (2010). The Atlantic Meridional Overturning Circulation and the subpolar gyre observed at the A25-OVIDE section in June 2002 and 2004. *Deep Sea Research Part I: Oceanographic Research Papers*, 57(11), 1374–1391. https://doi.org/10.1016/j.dsr.2010.07.009

Li, F. & Lozier, M. S. (2018). On the linkage between Labrador Sea Water volume and overturning circulation in the Labrador Sea: A case study on proxies. *Journal of Climate*, 31(13), 5225–5241. https://doi.org/10.1175/JCLI-D-17-0692.1

Liu, W., Xie, S.-P., Liu, Z., & Zhu, J. (2017). Overlooked possibility of a collapsed Atlantic Meridional Overturning Circulation in warming climate. *Science Advances*, 3(1), e1601666. https://doi.org/10.1126/sciadv.1601666

Lozier, M. S. (2012). Overturning in the North Atlantic. *Annual Review of Marine Science*, 4(1), 291–315. https://doi.org/10.1146/annurev-marine-120710-100740

Lozier, M. S., Bacon, S., Bower, A. S., Cunningham, S. A., de Jong, M. F., de Steur, L., DeYoung, B., Fischer, J., Gary, S. F., Greenan, B. J. W., Heimbach, P., Holliday, N. P., Houpert, L., Inall, M. E., Johns, W. E., Johnson, H. L., Karstensen, J., Li, F., Lin, X., Mackay, N., & Zika, J. D. (2017). Overturning in the Subpolar North Atlantic Program: A New International Ocean Observing System. *Bulletin of the American Meteorological Society*, 98(4), 737–752. https://doi.org/10.1175/bams-d-16-0057.1

Lozier, M. S., Li, F., Bacon, S., Bahr, F., Bower, A. S., Cunningham, S. A., d Jong, M. F., De Steur, L., DeYoung, B., Fischer, J., Gary, S. F., Greenan, B. J. W., Holliday, N. P., Houk, A., Houpert, L., Inall, M. E., Johns, W. E., Johnson, H. L., Johnson, C., Karstensen, J., Koman, G., Le Bras, I. A., Lin, X., Mackay, N., Marshall, D. P., Mercier, H., Oltmanns, M., Pickart, R. S., Ramsey, A. L., Rayner, D., Straneo, F., Thierry, V., Torres, D. J., Williams, R. G., Wilson, C., Yang, J., Yashayaev, I., & Zhao, J. (2019a). A sea change in our view of overturning in the subpolar North Atlantic. *Science*, 363(6426), 516–521. https://doi.org/10.1126/science.aau6592

Lozier, M. S., Li, F., Bacon, S., Bahr, F., Bower, A. S., Cunningham, S. A., de Jong, M. F., De Steur, L., DeYoung, B., Fischer, J., Gary, S. F., Greenan, B. J. W., Holliday, N. P., Houk, A., Houpert, L., Inall, M. E., Johns, W. E., Johnson, C., Karstensen, J., Koman, G., Le Bras, I. A., Lin, X., Mackay, N., Oltmanns, M., Pickart, R. S., Ramsey, A. L., Rayner, D., Straneo, F., Torres, D. J., Yashayaev, I., & Zhao, J. (2019b). Meridional overturning circulation and the associated heat and freshwater transports observed by the OSNAP (Overturning in the Subpolar North Atlantic Program) array from 2014 to 2016. *Duke Digital Repository*. https://doi.org/10.7924/r4z60gf0f

Lumpkin, R. & Pazos, M. (2007). Measuring surface currents with Surface Velocity Program drifters: the instrument, its data, and some recent results. *Lagrangian Analysis and Prediction of Coastal and Ocean Dynamics*, 39–67. Cambridge University Press.

Macdonald, A., Baringer, M., Wanninkhof, R., Lee, K., & Wallace, D. (2003). A 1998–1992 comparison of inorganic carbon and its transport across 24.5° N in the Atlantic. *Deep Sea Research Part II: Topical Studies in Oceanography*, 50(22-26), 3041–3064. https://doi.org/10.1016/j.dsr2.2003.07.009

Macdonald, A. M. (1995). *Ocean Fluxes of Mass, Heat and Freshwater: A Global Estimate and perspective*. Massachusetts Institute of Technology & Woods Hole Oceanographic Institution. https://doi.org/DOI:10.1575/1912/5620

Macdonald, A. M. & Wunsch, C. (1996). An estimate of global ocean circulation and heat fluxes. *Nature*, 382, 436–439.

Machín, F., Hernández-Guerra, A., & Pelegrí, J. L. (2006). Mass fluxes in the Canary Basin. *Progress in Oceanography*, 70(2-4), 416–447. https://doi.org/10.1016/j.pocean.2006.03.019

Majumder, S., Schmid, C., & Halliwell, G. (2016). An observations and model-based analysis of meridional transports in the South Atlantic. *Journal of Geophysical Research: Oceans*, 121. https://doi.org/10.1002/2015JC011486.Received

Manta, G., Speich, S., Karstensen, J., Hummels, R., Kersalé, M., Laxenaire, R., Piola, A., Chidichimo, M. P., Sato, O. T., Cotrim da Cunha, L., Ansorge, I., Lamont, T., van den Berg, M., Schuster, U., Tanhua, T., Kerr, R., Guerrero, R., Campos, E., & Meinen, C. S. (2021). The South Atlantic Meridional Overturning Circulation and Mesoscale Eddies in the First GO-SHIP Section at 34.5°S. *Journal of Geophysical Research: Oceans*, 126(2), 1–25. https://doi.org/10.1029/2020JC016962

Matear, R. J., Wong, C. S., & Xie, L. (2003). Can CFCs be used to determine anthropogenic CO2? *Global Biogeochemical Cycles*, 17(1). https://doi.org/10.1029/2001GB001415

Maul, G. A. & Vukovich, F. M. (1993). The Relationship between Variations in the Gulf of Mexico Loop Current and Straits of Florida Volume Transport. *Journal of Physical Oceanography*, 23(5), 785–796. https://doi.org/10.1175/1520-0485(1993)023⟨0785:TRBVIT⟩2.0.CO;2

Maze, G., Mercier, H., Thierry, V., Memery, L., Morin, P., & Perez, F. F. (2012). Mass, nutrient and oxygen budgets for the northeastern Atlantic Ocean. *Biogeosciences*, 9(10), 4099–4113. https://doi.org/10.5194/bg-9-4099-2012

McCarthy, G., Frajka-Williams, E., Johns, W. E., Baringer, M. O., Meinen, C. S., Bryden, H. L., Rayner, D., Duchez, A., Roberts, C., & Cunningham, S. A. (2012). Observed interannual variability of the Atlantic meridional overturning circulation at 26.5° N. *Geophysical Research Letters*, 39, L19609. https://doi.org/10.1029/2012GL052933

McCarthy, G. D., Brown, P. J., Flagg, C. N., Goni, G., Houpert, L., Hughes, C. W., Hummels, R., Inall, M., Jochumsen, K., Larsen, K. M. H., Lherminier, P., Meinen, C. S., Moat, B. I., Rayner, D., Rhein, M., Roessler, A., Schmid, C., & Smeed, D. A. (2020). Sustainable Observations of the AMOC: Methodology and Technology. *Reviews of Geophysics*, 58(1), 1–34. https://doi.org/10.1029/2019RG000654

McCarthy, G. D., Smeed, D. A., Johns, W. E., Frajka-Williams, E., Moat, B. I., Rayner, D., Baringer, M. O., Meinen, C. S., Collins, J., & Bryden, H. L. (2015). Measuring the Atlantic Meridional Overturning Circulation at 26° N. *Progress in Oceanography*, 130, 91–111. https://doi.org/10.1016/j.pocean.2014.10.006

McCartney, M. S. & Talley, L. D. (1984). Warm-to-cold water conversion in the Northern North Atlantic Ocean. *Journal of Physical Oceanography*, 14, 922–935.

McDonagh, E. (2007). RRS Charles Darwin Cruise CD171, 01 May - 15 Jun 2005. A trans-Atlantic hydrographic section at 36N. Technical Report National Oceanography Centre Southampton Cruise Report, No. 14.

McDonagh, E. L., Bryden, H. L., King, B. A., & Sanders, R. J. (2008). The circulation of the Indian Ocean at 32° S. *Progress in Oceanography*, 79(1), 20–36. https://doi.org/10.1016/j.pocean.2008.07.001

McDonagh, E. L. & King, B. A. (2005). Oceanic fluxes in the South Atlantic. *Journal of Physical Oceanography*, 35(1), 109–122. https://doi.org/10.1175/JPO-2666.1

McDonagh, E. L., King, B. A., Bryden, H. L., Courtois, P., Szuts, Z., Baringer, M. O., Cunningham, S. A., Atkinson, C., & McCarthy, G. (2015). Continuous estimate of Atlantic oceanic freshwater flux at 26.5° N. *Journal of Climate*, 28, 8888–8906.

McDonagh, E. L., McLeod, P., King, B. A., Bryden, H. L., & Valdés, S. T. (2010). Circulation, Heat, and Freshwater Transport at 36° N in the Atlantic. *Journal of Physical Oceanography*, 40(12), 2661–2678. https://doi.org/10.1175/2010JPO4176.1

Mecking, J. V., Drijfhout, S. S., Jackson, L. C., & Graham, T. (2016). Stable AMOC off state in an eddy-permitting coupled climate model. *Climate Dynamics*, 47(7-8), 2455–2470. https://doi.org/10.1007/s00382-016-2975-0

Meinen, C. S., Garzoli, S. L., Johns, W. E., & Baringer, M. O. (2004). Transport variability of the Deep Western Boundary Current and the Antilles Current off Abaco Island, Bahamas. *Deep Sea Research Part I: Oceanographic Research Papers*, 51(11), 1397–1415. https://doi.org/10.1016/j.dsr.2004.07.007

Meinen, C. S., Johns, W. E., Moat, B. I., Smith, R. H., Johns, E. M., Rayner, D., Frajka-Williams, E., Garcia, R. F., & Garzoli, S. L. (2019). Structure and Variability of the Antilles Current at 26.5° N. *Journal of Geophysical Research: Oceans*, 124(6), 3700–3723. https://doi.org/10.1029/2018JC014836

Meinen, C. S., Perez, R. C., Dong, S., Piola, A. R., & Campos, E. (2020). Observed Ocean Bottom Temperature Variability at Four Sites in the Northwestern Argentine Basin: Evidence of Decadal Deep/Abyssal Warming Amidst Hourly to Interannual Variability During 2009–2019. *Geophysical Research Letters*, 47(18). https://doi.org/10.1029/2020GL089093

Meinen, C. S., Speich, S., Perez, R. C., Dong, S., Piola, A. R., Garzoli, S. L., Baringer, M. O., Gladyshev, S., & Campos, E. J. D. (2013). Temporal variability of the meridional overturning circulation at 34.5° S: Results from two pilot boundary arrays in the South Atlantic. *Journal of Geophysical Research: Oceans*, 118(12), 6461–6478. https://doi.org/10.1002/2013JC009228

Meinen, C. S. & Watts, D. R. (2000). Vertical structure and transport on a transect across the North Atlantic Current near 42° N: Time series and mean. *Journal of Geophysical Research: Oceans*, 105(C9), 21869–21891. https://doi.org/10.1029/2000JC900097

Mercier, H., Lherminier, P., Sarafanov, A., Gaillard, F., Daniault, N., Desbruyères, D. G., Falina, A., Ferron, B., Gourcuff, C., Huck, T., & Thierry, V. (2015). Variability of the meridional overturning circulation at the Greenland–Portugal OVIDE section from 1993 to 2010. *Progress in Oceanography*, 132, 250–261. https://doi.org/10.1016/j.pocean.2013.11.001

Mikaloff Fletcher, S. E., Gruber, N., Jacobson, A. R., Doney, S. C., Dutkiewicz, S., Gerber, M., Follows, M., Joos, F., Lindsay, K., Menemenlis, D., Mouchet, A., Müller, S. A., & Sarmiento, J. L. (2006). Inverse estimates of anthropogenic CO2 uptake, transport, and storage by the ocean. *Global Biogeochemical Cycles*, 20(2), GB2002. https://doi.org/10.1029/2005GB002530

Millero, F. J., Fiol, S., Campbell, D. M., Parrilla, G., Allison, L. J., & Kozyr, A. (2000). Carbon Dioxide, Hydrographic, and Chemical Data Obtained During the R/V Hesperides Cruise in the Atlantic Ocean (WOCE Section A5, July 14 - August 15, 1992). ORNL/CDIAC-125, NDP-074. Technical report, Carbon Dioxide Information Analysis Center, Oak Ridge National Laboratory, U.S. Department of Energy, Oak Ridge, Tennessee.

Moat, B. I., Josey, S. A., Sinha, B., Blaker, A. T., Smeed, D. A., McCarthy, G. D., Johns, W. E., Hirschi, J. J., Frajka-Williams, E., Rayner, D., Duchez, A., & Coward, A. C. (2016). Major variations in subtropical North Atlantic heat transport at short (5 day) timescales and their causes. *Journal of Geophysical Research: Oceans*, 121(5), 3237–3249. https://doi.org/10.1002/2016JC011660

Moat, B. I., Smeed, D. A., Frajka-Williams, E., Desbruyères, D. G., Beaulieu, C., Johns, W. E., Rayner, D., Sanchez-Franks, A., Baringer, M. O., Volkov, D., Jackson, L. C., & Bryden, H. L. (2020). Pending recovery in the strength of the meridional overturning circulation at 26° N. *Ocean Science*, 16(4), 863–874. https://doi.org/10.5194/os-16-863-2020

Morgan, E. J. (2021). Monthly average air-sea luxes of O2 , CO2 , and N2 from Earth System Models [Dataset]. *Zenodo*. https://doi.org/10.5281/ZENODO.4716840

Morris, M., Hall, M. M., St. Laurent, L. C., & Hogg, N. G. (2001). Abyssal Mixing in the Brazil Basin. *Journal of Physical Oceanography*, 31(11), 3331–3348. https://doi.org/10.1175/1520-0485(2001)031⟨3331:AMITBB⟩2.0.CO;2

Muir, L. C. & Fedorov, A. V. (2015). How the AMOC affects ocean temperatures on decadal to centennial timescales: the North Atlantic versus an interhemispheric seesaw. *Climate Dynamics*, 45(1-2), 151–160. https://doi.org/10.1007/s00382-014-2443-7

Muir, L. C. & Fedorov, A. V. (2017). Evidence of the AMOC interdecadal mode related to westward propagation of temperature anomalies in CMIP5 models. *Climate Dynamics*, 48(5-6), 1517–1535. https://doi.org/10.1007/s00382-016-3157-9

Müller, J., Gruber, N., Zhu, D., Gregor, L., Carter, B., Pérez, F., Olsen, A., Tanhua, T., & Lauvset, S. (2022). Decadal evolution of the oceanic sink for anthropogenic carbon from 1994 to 2014. *Ocean Science Meeting 2022*.

Munk, W. H. (1966). Abyssal recipes. *Deep-Sea Research*, 13, 707–730. https://doi.org/10.1016/0011-7471(66)90602-4

Murata, A., Kumamoto, Y., Sasaki, K., Watanabe, S., & Fukasawa, M. (2008). Decadal increases of anthropogenic CO2 in the subtropical South Atlantic Ocean along 30°S. *Journal of Geophysical Research*, 113(C6), C06007. https://doi.org/10.1029/2007JC004424

Myers, P., Kulan, N., & Ribergaard, M. H. (2007). Irminger Water variability in the West Greenland Current. *Geophysical Research Letters*, 34(17), L17601. https://doi.org/10.1029/2007GL030419

Myers, P. G., Donnelly, C., & Ribergaard, M. H. (2009). Structure and variability of the West Greenland Current in Summer derived from 6 repeat standard sections. *Progress in Oceanography*, 80(1-2), 93–112. https://doi.org/10.1016/j.pocean.2008.12.003

Naveira Garabato, A. C., Williams, A. P., & Bacon, S. (2014). The three-dimensional overturning circulation of the Southern Ocean during the WOCE era. *Progress in Oceanography*, 120, 41–78. https://doi.org/10.1016/j.pocean.2013.07.018

Olsen, A., Key, R. M., van Heuven, S., Lauvset, S. K., Velo, A., Lin, X., Schirnick, C., Kozyr, A., Tanhua, T., Hoppema, M., Jutterström, S., Steinfeldt, R., Jeansson, E., Ishii, M., Pérez, F. F., & Suzuki, T. (2016). The Global Ocean Data Analysis Project version 2 (GLODAPv2) – an internally consistent data product for the world ocean. *Earth System Science Data*, 8(2), 297–323. https://doi.org/10.5194/essd-8-297-2016

Olson, D. B., Schott, F. A., Zantopp, R. J., & Leaman, K. D. (1984). The Mean Circulation East of the Bahamas as Determined from a Recent Measurement Program and Historical XBT Data. *Journal of Physical Oceanography*, 14(9), 1470–1487. https://doi.org/10.1175/1520-0485(1984)014⟨1470:TMCEOT⟩2.0.CO;2

Orsi, A. H., Smethie Jr., W. M., & Bullister, J. L. (2002). On the total input of Antarctic waters to the deep ocean: A preliminary estimate from chlorofluorocarbon measurements. *Journal of Geophysical Research*, 107(C8), 3122. https://doi.org/10.1029/2001JC000976

Orsi, A. H., Whitworth, T., & Nowlin, W. D. (1995). On the meridional extent and fronts of the Antarctic Circumpolar Current. *Deep Sea Research Part I: Oceanographic Research Papers*, 42(5), 641–673. https://doi.org/10.1016/0967-0637(95)00021-W

Pacini, A., Pickart, R. S., Bahr, F., Torres, D. J., Ramsey, A. L., Holte, J., Karstensen, J., Oltmanns, M., Straneo, F., Le Bras, I. A., Moore, G. W. K., & Femke de Jong, M. (2020). Mean Conditions and Seasonality of the West Greenland Boundary Current System near Cape Farewell. *Journal of Physical Oceanography*, 50(10), 2849–2871. https://doi.org/10.1175/JPO-D-20-0086.1

Palter, J. B. (2015). The Role of the Gulf Stream in European Climate. *Annual Review of Marine Science*, 7(1), 113–137. https://doi.org/10.1146/annurev-marine-010814-015656

Parrilla, G., Lavín, A., Bryden, H. L., García, M., & Millard, R. (1994). Rising temperatures in the subtropical North Atlantic Ocean over the past 35 years. *Nature*, 369(6475), 48–51. https://doi.org/10.1038/369048a0

Pérez, F. F., Fontela, M., García-Ibáñez, M. I., Mercier, H., Velo, A., Lherminier, P., Zunino, P., de la Paz, M., Alonso-Pérez, F., Guallart, E. F., & Padin, X. A. (2018). Meridional overturning circulation conveys fast acidification to the deep Atlantic Ocean. *Nature*, 554(7693), 515–518. https://doi.org/10.1038/nature25493

Pérez, F. F., Mercier, H., Vázquez-Rodríguez, M., Lherminier, P., Velo, A., Pardo, P. C., Rosón, G., & Ríos, A. F. (2013). Atlantic Ocean CO2 uptake reduced by weakening of the meridional overturning circulation. *Nature Geoscience*, 6(2), 146–152. https://doi.org/10.1038/ngeo1680

Pérez, F. F., Vázquez-Rodríguez, M., Louarn, E., Padín, X. A., Mercier, H., & Ríos, A. F. (2008). Temporal variability of the anthropogenic CO2 storage in the Irminger Sea. *Biogeosciences*, 5(6), 1669–1679. https://doi.org/10.5194/bg-5-1669-2008

Pérez-Hernández, M. D., Hernández-Guerra, A., Comas-Rodríguez, I., Benítez-Barrios, V. M., Fraile-Nuez, E., Pelegrí, J. L., & Naveira Garabato, A. C. (2017). Differences between 1999 and 2010 across the Falkland Plateau: Fronts and water masses. *Ocean Science*, 13, 577–587. https://doi.org/10.5194/os-13-577-2017

Pérez-Hernández, M. D., Hernández-Guerra, A., Fraile-Nuez, E., Comas-Rodríguez, I., Benítez-Barrios, V. M., Domínguez-Yanes, J. F., Vélez-Belchí, P., & De Armas, D. (2013). The source of the Canary current in fall 2009. *Journal of Geophysical Research: Oceans*, 118(6), 2874–2891. https://doi.org/10.1002/jgrc.20227

Pérez-Hernández, M. D., Hernández-Guerra, A., Cana-Cascallar, L., Arumí-Planas, C., Caínzos, V., González-Santana, A. J., Gutierrez-Guerra, M., Martínez-Marrero, A., Mosquera Giménez, Á., Presas Navarro, C., Santana-Toscano, D., & Vélez-Belchí, P. (2023). On the Seasonal variability eastern boundary of the North Atlantic Subtropical Gyre. *Journal of Geophysical Research: Oceans*, Submitted, 11693.

Pérez-Hernández, M. D., McCarthy, G. D., Vélez-Belchí, P., Smeed, D. A., Fraile-Nuez, E., & Hernández-Guerra, A. (2015). The Canary Basin contribution to the seasonal cycle of the Atlantic Meridional Overturning Circulation at 26ºN. *Journal of Geophysical Research: Oceans*, 120, 1–23. https://doi.org/10.1002/2015JC010826.Received

Peterson, R. G. & Stramma, L. (1991). Upper-level circulation in the South Atlantic Ocean. *Progress in Oceanography*, 26(1), 1–73. https://doi.org/10.1016/0079-6611(91)90006-8

Petit, T., Lozier, M. S., Josey, S. A., & Cunningham, S. A. (2020). Atlantic deep water formation occurs primarily in the Iceland Basin and Irminger Sea by local buoyancy forcing. *Geophysical Research Letters*, 47(22), 1–9. https://doi.org/10.1029/2020GL091028

Piecuch, C. G. (2020). Likely weakening of the Florida Current during the past century revealed by sea-level observations. *Nature Communications*, 11(1), 3973. https://doi.org/10.1038/s41467-020-17761-w

Pollard, R. T., Read, J., Holliday, N., & Leach, H. (2004). Water masses and circulation pathways through the Iceland Basin during Vivaldi 1996. *Journal of Geophysical Research*, 109(C4), C04004. https://doi.org/10.1029/2003JC002067

Polyakov, I. V., Pnyushkov, A. V., Alkire, M. B., Ashik, I. M., Baumann, T. M., Carmack, E. C., Goszczko, I., Guthrie, J., Ivanov, V. V., Kanzow, T., Krishfield, R., Kwok, R., Sundfjord, A., Morison, J., Rember, R., & Yulin, A. (2017). Greater role for Atlantic inflows on sea-ice loss in the Eurasian Basin of the Arctic Ocean. *Science*, 356(6335), 285–291. https://doi.org/10.1126/science.aai8204

Polyakov, I. V., Rippeth, T. P., Fer, I., Alkire, M. B., Baumann, T. M., Carmack, E. C., Ingvaldsen, R., Ivanov, V. V., Janout, M., Lind, S., Padman, L., Pnyushkov, A. V., & Rember, R. (2020). Weakening of Cold Halocline Layer Exposes Sea Ice to Oceanic Heat in the Eastern Arctic Ocean. *Journal of Climate*, 33(18), 8107–8123. https://doi.org/10.1175/JCLI-D-19-0976.1

Racapé, V., Zunino, P., Mercier, H., Lherminier, P., Bopp, L., Pérez, F. F., & Gehlen, M. (2018). Transport and storage of anthropogenic C in the North Atlantic Subpolar Ocean. *Biogeosciences*, 15(14), 4661–4682. https://doi.org/10.5194/bg-15-4661-2018

Rahmstorf, S. (1996). On the freshwater forcing and transport of the Atlantic thermohaline circulation. *Climate Dynamics*, 12, 799–811. https://doi.org/10.1007/s003820050144

Rahmstorf, S., Box, J. E., Feulner, G., Mann, M. E., Robinson, A., Rutherford, S., & Schaffernicht, E. J. (2015). Exceptional twentieth-century slowdown in Atlantic Ocean overturning circulation. *Nature Climate Change*, 5(5), 475–480. https://doi.org/10.1038/nclimate2554

Reid, J. L. (1989). On the total geostrophic circulation of the South Atlantic Ocean: Flow patterns, tracers and transports. *Progress in Oceanography*, 23, 149–244.

Reid, J. L. (1994). On the total geostrophic circulation of the North Atlantic Ocean: Flow patterns, tracers and transports. *Progress in Oceanography*, 33, 1–92.

Rhein, M., Mertens, C., & Roessler, A. (2019). Observed Transport Decline at 47° N, Western Atlantic. *Journal of Geophysical Research: Oceans*, 124, 4875–4890. https://doi.org/10.1029/2019jc014993

Rintoul, S. R. (1991). South Atlantic interbasin exchange. *Journal of Geophysical Research: Oceans*, 96(C2), 2675–2692. https://doi.org/10.1029/90jc02422

Ríos, A., Velo, A., Pardo, P., Hoppema, M., & Pérez, F. F. (2012). An update of anthropogenic CO2 storage rates in the western South Atlantic basin and the role of Antarctic Bottom Water. *Journal of Marine Systems*, 94, 197–203. https://doi.org/10.1016/j.jmarsys.2011.11.023

Ríos, A. F., Vázquez-Rodríguez, M., Padin, X., & Pérez, F. F. (2010). Anthropogenic carbon dioxide in the South Atlantic western basin. *Journal of Marine Systems*, 83(1-2), 38–44. https://doi.org/10.1016/j.jmarsys.2010.06.010

Robbins, P. E. & Toole, J. M. (1997). The dissolved silica budget as a constraint on the meridional overturning circulation of the Indian Ocean. *Deep Sea Research Part I: Oceanographic Research Papers*, 44(5), 879–906. https://doi.org/10.1016/S0967-0637(96)00126-4

Roberts, C. D., Jackson, L., & McNeall, D. (2014). Is the 2004-2012 reduction of the Atlantic meridional overturning circulation significant? *Geophysical Research Letters*, 41(9), 3204–3210. https://doi.org/10.1002/2014GL059473

Rosón, G. (2003). Carbon distribution, fluxes, and budgets in the subtropical North Atlantic Ocean (24.5° N). *Journal of Geophysical Research*, 108(C5), 3144. https://doi.org/10.1029/1999JC000047

Rossby, T., Flagg, C. N., Donohue, K., Sanchez-Franks, A., & Lillibridge, J. (2014). On the long-term stability of Gulf Stream transport based on 20 years of direct measurements. *Geophysical Research Letters*, 41(1), 114–120. https://doi.org/10.1002/2013GL058636

Rousselet, L., Cessi, P., & Forget, G. (2020). Routes of the upper branch of the Atlantic Meridional Overturning Circulation according to an ocean state estimate. *Geophysical Research Letters*, 47(18), e2020GL089137. https://doi.org/10.1029/2020GL089137

Rousselet, L., Cessi, P., & Mazloff, M. R. (2023). What Controls the Partition between the Cold and Warm Routes in the Meridional Overturning Circulation? *Journal of Physical Oceanography*, 53(1), 215–233. https://doi.org/10.1175/JPO-D-21-0308.1

Rühs, S., Schwarzkopf, F. U., Speich, S., & Biastoch, A. (2019). Cold vs. warm water route – sources for the upper limb of the Atlantic Meridional Overturning Circulation revisited in a high-resolution ocean model. *Ocean Science*, 15(3), 489–512. https://doi.org/10.5194/os-15-489-2019

Sabine, C. L., Feely, R. A., Gruber, N., Key, R. M., Lee, K., Bullister, J. L., Wanninkhof, R., Wong, C. S., Wallace, D. W. R., Tilbrook, B., Millero, F. J., Peng, T.-H., Kozyr, A., Ono, T., & Ríos, A. F. (2004). The Oceanic Sink for Anthropogenic CO2. *Science*, 305(5682), 367–371. https://doi.org/10.1126/science.1097403

Sarafanov, A., Falina, A., Mercier, H., Sokov, A., Lherminier, P., Gourcuff, C., Gladyshev, S., Gaillard, F., & Daniault, N. (2012). Mean full-depth summer circulation and transports at the northern periphery of the Atlantic Ocean in the 2000s. *Journal of Geophysical Research: Oceans*, 117(C1). https://doi.org/10.1029/2011JC007572

Saunders, P. M. & King, B. A. (1995). Oceanic fluxes on the WOCE A11 section. *Journal of Physical Oceanography*, 25, 1942–1958.

Schmid, C. & Majumder, S. (2018). Transport variability of the Brazil Current from observations and a data assimilation model. *Ocean Science*, 14(3), 417–436. https://doi.org/10.5194/os-14-417-2018

Schmitz, W. J. & McCartney, M. S. (1993). On the North Atlantic Circulation. *Reviews of Geophysics*, 31(1), 29–49. https://doi.org/10.1029/92RG02583

Schmitz, W. J., Thompson, J. D., & Luyten, J. R. (1992). The Sverdrup circulation for the Atlantic along 24° N. *Journal of Geophysical Research*, 97(C5), 7251. https://doi.org/10.1029/92JC00417

Schott, F. A., Dengler, M., Zantopp, R., Stramma, L., Fischer, J., & Brandt, P. (2005). The Shallow and Deep Western Boundary Circulation of the South Atlantic at 5°–11°S. *Journal of Physical Oceanography*, 35, 2031–2053. https://doi.org/10.1175/jpo2813.1

Schuster, U., Watson, A. J., Bakker, D. C. E., de Boer, A. M., Jones, E. M., Lee, G. A., Legge, O., Louwerse, A., Riley, J., & Scally, S. (2014). Measurements of total alkalinity and inorganic dissolved carbon in the Atlantic Ocean and adjacent Southern Ocean between 2008 and 2010. *Earth System Science Data*, 6(1), 175–183. https://doi.org/10.5194/essd-6-175-2014

Sévellec, F. & Sinha, B. (2018). *Predictability of Decadal Atlantic Meridional Overturning Circulation Variations*. https://doi.org/10.1093/acrefore/9780190228620.013.81.hal-02136510

Siedler, G., Müller, T. J., R.Onken, Arhan, M., Mercier, H., King, B. A., & Saunders, P. M. (1996). The Zonal WOCE Sections in the South Atlantic. *The South Atlantic: present and past circulation*, 83–104. Springer-Verlag. https://doi.org/10.1007/978-3-642-80353-6_5

Sloyan, B. M. & Schröter, J. (2001). Correlation of ocean mass and temperature fluxes among hydrographic sections in the southern oceans. *Geophysical Research Letters*, 28(10), 2049–2052. https://doi.org/10.1029/2000GL012459

Smeed, D. A., McCarthy, G. D., Cunningham, S. A., Frajka-Williams, E., Rayner, D., Johns, W. E., Meinen, C. S., Baringer, M. O., Moat, B. I., Duchez, A., & Bryden, H. L. (2014). Observed decline of the Atlantic meridional overturning circulation 2004–2012. *Ocean Science*, 10(1), 29–38. https://doi.org/10.5194/os-10-29-2014

Smythe-Wright, D., Chapman, P., Rae, C., Shannon, L., & Boswell, S. (1998). Characteristics of the South Atlantic subtropical frontal zone between 15°W and 5°E. *Deep Sea Research Part I: Oceanographic Research Papers*, 45(1), 167–192. https://doi.org/10.1016/S0967-0637(97)00068-X

Sokolov, S. & Rintoul, S. R. (2009). Circumpolar structure and distribution of the Antarctic Circumpolar Current fronts: 2. Variability and relationship to sea surface height. *Journal of Geophysical Research*, 114(C11), C11019. https://doi.org/10.1029/2008JC005248

Spadone, A. & Provost, C. (2009). Variations in the Malvinas Current volume transport since October 1992. *Journal of Geophysical Research*, 114(C2), C02002. https://doi.org/10.1029/2008JC004882

Speer, K. G., Holfort, J., Reynaud, T., & Siedler, G. (1996). South Atlantic Heat Transport at 11ºS. *The South Atlantic: present and past circulation*, 105–120.

Speich, S., Blanke, B., & Cai, W. (2007). Atlantic meridional overturning circulation and the Southern Hemisphere supergyre. *Geophysical Research Letters*, 34(23), L23614. https://doi.org/10.1029/2007GL031583

Speich, S., Blanke, B., & Madec, G. (2001). Warm and cold water routes of an O.G.C.M. thermohaline conveyor belt. *Geophysical Research Letters*, 28(2), 311–314. https://doi.org/10.1029/2000GL011748

Srokosz, M., Baringer, M., Bryden, H., Cunningham, S., Delworth, T., Lozier, S., Marotzke, J., & Sutton, R. (2012). Past, Present, and Future Changes in the Atlantic Meridional Overturning Circulation. *Bulletin of the American Meteorological Society*, 93(11), 1663–1676. https://doi.org/10.1175/BAMS-D-11-00151.1

Srokosz, M. A. & Bryden, H. L. (2015). Observing the Atlantic Meridional Overturning Circulation yields a decade of inevitable surprises. *Science*, 348(6241). https://doi.org/10.1126/science.1255575

Steinfeldt, R., Rhein, M., Bullister, J. L., & Tanhua, T. (2009). Inventory changes in anthropogenic carbon from 1997-2003 in the Atlantic Ocean between 20°S and 65°N. *Global Biogeochemical Cycles*, 23(3). https://doi.org/10.1029/2008GB003311

Stendardo, I. & Gruber, N. (2012). Oxygen trends over five decades in the North Atlantic. *Journal of Geophysical Research: Oceans*, 117(C11), C11004. https://doi.org/10.1029/2012JC007909

Stendardo, I., Rhein, M., & Steinfeldt, R. (2020). The North Atlantic Current and its Volume and Freshwater Transports in the Subpolar North Atlantic, Time Period 1993–2016. *Journal of Geophysical Research: Oceans*, 125(9). https://doi.org/10.1029/2020JC016065

Stramma, L. (1989). The Brazil current transport south of 23°S. *Deep Sea Research Part A. Oceanographic Research Papers*, 36(4), 639–646. https://doi.org/10.1016/0198-0149(89)90012-5

Stramma, L. & England, M. (1999). On the water masses and mean circulation of the South Atlantic Ocean. *Journal of Geophysical Research: Oceans*, 104(C9), 20863–20883. https://doi.org/10.1029/1999JC900139

Stramma, L., Ikeda, Y., & Peterson, R. G. (1990). Geostrophic transport in the Brazil current region north of 20°S. *Deep Sea Research Part A. Oceanographic Research Papers*, 37(12), 1875–1886. https://doi.org/10.1016/0198-0149(90)90083-8

Talley, L. (2013). Closure of the Global Overturning Circulation Through the Indian, Pacific, and Southern Oceans: Schematics and Transports. *Oceanography*, 26(1), 80–97. https://doi.org/10.5670/oceanog.2013.07

Talley, L. D. (2008). Freshwater transport estimates and the global overturning circulation: Shallow, deep and throughflow components. *Progress in Oceanography*, 78(4), 257–303. https://doi.org/10.1016/j.pocean.2008.05.001

Talley, L. D., Feely, R. A., Sloyan, B. M., Wanninkhof, R., Baringer, M. O., Bullister, J. L., Carlson, C. A., Doney, S. C., Fine, R. A., Firing, E., Gruber, N., Hansell, D. A., Ishii, M., Johnson, G. C., Katsumata, K., Key, R. M., Kramp, M., Langdon, C., Macdonald, A. M., Mathis, J. T., McDonagh, E. L., Mecking, S., Millero, F. J., Mordy, C. W., Nakano, T., Sabine, C. L., Smethie, W. M., Swift, J. H., Tanhua, T., Thurnherr, A. M., Warner, M. J., & Zhang, J.-Z. (2016). Changes in ocean heat, carbon content, and ventilation: A review of the first decade of GO-SHIP global repeat hydrography. *Annual Review of Marine Science*, 8(1), 185–215. https://doi.org/10.1146/annurev-marine-052915-100829

Tanhua, T., Biastoch, A., Körtzinger, A., Lüger, H., Böning, C., & Wallace, D. W. R. (2006). Changes of anthropogenic CO2 and CFCs in the North Atlantic between 1981 and 2004. *Global Biogeochemical Cycles*, 20(4). https://doi.org/10.1029/2006GB002695

Tanhua, T., Jones, E. P., Jeansson, E., Jutterström, S., Smethie, W. M., Wallace, D. W. R., & Anderson, L. G. (2009). Ventilation of the Arctic Ocean: Mean ages and inventories of anthropogenic CO2 and CFC-11. *Journal of Geophysical Research*, 114(C1), C01002. https://doi.org/10.1029/2008JC004868

Thomas, H. & Ittekkot, V. (2001). Determination of anthropogenic CO2 in the North Atlantic Ocean using water mass ages and CO2 equilibrium chemistry. *Journal of Marine Systems*, 27(4), 325–336. https://doi.org/10.1016/S0924-7963(00)00077-4

Thornalley, D. J. R., Oppo, D. W., Ortega, P., Robson, J. I., Brierley, C. M., Davis, R. E., Hall, I. R., Moffa-Sánchez, P., Rose, N. L., Spooner, P. T., Yashayaev, I., & Keigwin, L. D. (2018). Anomalously weak Labrador Sea convection and Atlantic overturning during the past 150 years. *Nature*, 556(7700), 227–230. https://doi.org/10.1038/s41586-018-0007-4

Toole, J. M., Curry, R., Joyce, T. M., McCartney, M., & Peña-Molino, B. (2011). Transport of the North Atlantic Deep Western Boundary Current about 39°N, 70°W: 2004-2008. *Deep-Sea Research Part II*, 58, 1768–1780.

Touratier, F., Azouzi, L., & Goyet, C. (2007). CFC-11, $\triangle$14C and 3H tracers as a means to assess anthropogenic CO2 concentrations in the ocean. *Tellus B*, 59(2), 318–325. https://doi.org/10.1111/j.1600-0889.2006.00247.x

Trenberth, K. E. & Caron, J. M. (2001). Estimates of Meridional Atmosphere and Ocean Heat Transports. *Journal of Climate*, 14(16), 3433–3443. https://doi.org/10.1175/1520-0442(2001)014⟨3433:EOMAAO⟩2.0.CO;2

Tuchen, F. P., Brandt, P., Lübbecke, J. F., & Hummels, R. (2022). Transports and Pathways of the Tropical AMOC Return Flow From Argo Data and Shipboard Velocity Measurements. *Journal of Geophysical Research: Oceans*, 127(2). https://doi.org/10.1029/2021JC018115

Tynan, E., Griffiths, A. M., Fry, C. H., Garley, R., Clarke, J. S., Humphreys, M. P., & Achterberg, E. P. (2016). Seawater dissolved inorganic carbon and total alkalinity for RAGNARoCC/OSNAP cruise JR302. Technical report. https://doi.org/10.5285/29ea7e19-d89c-3ab1-e053-6c86abc0284b

Uchida, H., Fukasawa, M., & Murata, A. (2005). *WHP P6, A10, I3/I4 REVISIT DATA BOOK Blue Earth Global Expedition 2003 (BEAGLE2003). Volume 1,2*. JAMSTEC Publication.

Våge, K., Pickart, R. S., Sarafanov, A., Knutsen, Ø., Mercier, H., Lherminier, P., van Aken, H. M., Meincke, J., Quadfasel, D., & Bacon, S. (2011). The Irminger Gyre: Circulation, convection, and interannual variability. *Deep Sea Research Part I: Oceanographic Research Papers*, 58(5), 590–614. https://doi.org/10.1016/j.dsr.2011.03.001

Valla, D., Piola, A. R., Meinen, C. S., & Campos, E. (2018). Strong Mixing and Recirculation in the Northwestern Argentine Basin. *Journal of Geophysical Research: Oceans*, 123(7), 4624–4648. https://doi.org/10.1029/2018JC013907

Vázquez-Rodríguez, M., Padin, X., Pardo, P., Ríos, A., & Pérez, F. (2012). The subsurface layer reference to calculate preformed alkalinity and air–sea CO2 disequilibrium in the Atlantic Ocean. *Journal of Marine Systems*, 94, 52–63. https://doi.org/10.1016/j.jmarsys.2011.10.008

Vázquez-Rodríguez, M., Padin, X. A., Ríos, A. F., Bellerby, R. G. J., & Pérez, F. F. (2009a). An upgraded carbon-based method to estimate the anthropogenic fraction of dissolved CO2 in the Atlantic Ocean. *Biogeosciences Discussions*, 6(2), 4527–4571. https://doi.org/https://doi.org/10.5194/bgd-6-4527-2009

Vázquez-Rodríguez, M., Touratier, F., Monaco, C. L., Waugh, D. W., Padin, X. A., Bellerby, R. G., Goyet, C., Metzl, N., Ríos, A. F., & Pérez, F. F. (2009b). Anthropogenic carbon distributions in the Atlantic Ocean: Data-based estimates from the Arctic to the Antarctic. *Biogeosciences*, 6(3), 439–451. https://doi.org/10.5194/bg-6-439-2009

Vélez-Belchí, P., Pérez-Hernández, M. D., Casanova-Masjoan, M., Cana, L., & Hernández-Guerra, A. (2017). On the seasonal variability of the Canary Current and the Atlantic Meridional Overturning Circulation. *Journal of Geophysical Research: Oceans*, 122(6), 4518–4538. https://doi.org/10.1002/2017JC012774

Vivier, F. & Provost, C. (1999a). Direct velocity measurements in the Malvinas Current. *Journal of Geophysical Research: Oceans*, 104(C9), 21083–21103. https://doi.org/10.1029/1999JC900163

Vivier, F. & Provost, C. (1999b). Volume transport of the Malvinas Current: Can the flow be monitored by TOPEX/POSEIDON? *Journal of Geophysical Research: Oceans*, 104(C9), 21105–21122. https://doi.org/10.1029/1999JC900056

Warren, B. A. & Speer, K. G. (1991). Deep circulation in the eastern South Atlantic Ocean. *Deep Sea Research Part A. Oceanographic Research Papers*, 38(Supplement I), S281–S322. https://doi.org/10.1016/s0198-0149(12)80014-8

Waugh, D. W., Hall, T. M., Mcneil, B. I., Key, R., & Matear, R. J. (2006). Anthropogenic CO2 in the oceans estimated using transit time distributions. *Tellus B: Chemical and Physical Meteorology*, 58(5), 376–389. https://doi.org/10.1111/j.1600-0889.2006.00222.x

Weaver, A. J., Sedláček, J., Eby, M., Alexander, K., Crespin, E., Fichefet, T., Philippon-Berthier, G., Joos, F., Kawamiya, M., Matsumoto, K., Steinacher, M., Tachiiri, K., Tokos, K., Yoshimori, M., & Zickfeld, K. (2012). Stability of the Atlantic meridional overturning circulation: A model intercomparison. *Geophysical Research Letters*, 39(20), 2012GL053763. https://doi.org/10.1029/2012GL053763

Weber, S. L. & Drijfhout, S. S. (2007). Stability of the Atlantic Meridional Overturning Circulation in the Last Glacial Maximum climate. *Geophysical Research Letters*, 34(22), L22706. https://doi.org/10.1029/2007GL031437

Wedepohl, P. M., Lutjeharms, J. R. E., & Meeuwis, M. (2000). Surface drift in the South-East Atlantic Ocean. *South African Journal of Marine Science*, 22(1), 71–79. https://doi.org/10.2989/025776100784125672

Wefer, G., Berger, W. H., Siedler, G., Webb, D. J., & Reid, J. R. (1996). On the Circulation of the South Atlantic Ocean. *The South Atlantic*, 13–44. https://doi.org/10.1007/978-3-642-80353-6_2

Weijer, W., Cheng, W., Drijfhout, S. S., Fedorov, A. V., Hu, A., Jackson, L. C., Liu, W., McDonagh, E. L., Mecking, J. V., & Zhang, J. (2019). Stability of the Atlantic Meridional Overturning Circulation: A Review and Synthesis. *Journal of Geophysical Research: Oceans*, 124(8), 5336–5375. https://doi.org/10.1029/2019JC015083

Weijer, W., Cheng, W., Garuba, O. A., Hu, A., & Nadiga, B. T. (2020). CMIP6 models predict significant 21st century decline of the Atlantic Meridional Overturning Circulation. *Geophysical Research Letters*, 47(12). https://doi.org/10.1029/2019GL086075

Weijer, W., de Ruijter, W. P. M., Dijkstra, H. A., & van Leeuwen, P. J. (1999). Impact of Interbasin Exchange on the Atlantic Overturning Circulation. *Journal of Physical Oceanography*, 29(9), 2266–2284. https://doi.org/10.1175/1520-0485(1999)029⟨2266:IOIEOT⟩2.0.CO;2

Weijer, W. & van Sebille, E. (2014). Impact of Agulhas Leakage on the Atlantic Overturning Circulation in the CCSM4. *Journal of Climate*, 27(1), 101–110. https://doi.org/10.1175/JCLI-D-12-00714.1

Wijffels, S. E. (2001). Chapter 6.2 Ocean transport of fresh water. *Ocean Circulation & Climate: Observing and Modelling the Global Ocean*, (Chapter 6.2, 475–488). Academic Press. https://doi.org/10.1016/S0074-6142(01)80135-2

Woodgate, R. A. (2018). Increases in the Pacific inflow to the Arctic from 1990 to 2015, and insights into seasonal trends and driving mechanisms from year-round Bering Strait mooring data. *Progress in Oceanography*, 160(June 2017), 124–154. https://doi.org/10.1016/j.pocean.2017.12.007

Woodgate, R. A. & Aagaard, K. (2005). Revising the Bering Strait freshwater flux into the Arctic Ocean. *Geophysical Research Letters*, 32. https://doi.org/10.1029/2004GL021747

Worthington, E. L., Moat, B. I., Smeed, D. A., Mecking, J. V., Marsh, R., & McCarthy, G. D. (2021). A 30-year reconstruction of the Atlantic meridional overturning circulation shows no decline. *Ocean Science*, 17(1), 285–299. https://doi.org/10.5194/os-17-285-2021

Wunsch, C. (1978). The North Atlantic General Circulation West of 50ºW Determined by Inverse Methods. *Reviews of Geophysics and Space Physics*, 16(4), 583–620.

Wunsch, C. (1996). *The Ocean Circulation Inverse Problem*. Cambridge University Press.

Xu, Y., Wanninkhof, R., Osborne, E., Baringer, M., Barbero, L., Cai, W., & Hooper, J. (2022). Inorganic Carbon Transport and Dynamics in the Florida Straits. *Journal of Geophysical Research: Oceans*, 127(10). https://doi.org/10.1029/2022JC018405

Yashayaev, I. & Loder, J. W. (2016). Recurrent replenishment of Labrador Sea Water and associated decadal-scale variability. *Journal of Geophysical Research: Oceans*, 121(11), 8095–8114. https://doi.org/10.1002/2016JC012046

Yashayaev, I. & Loder, J. W. (2017). Further intensification of deep convection in the Labrador Sea in 2016. *Geophysical Research Letters*, 44, 1429–1438. https://doi.org/10.1002/2016GL071668

Zantopp, R., Fischer, J., Visbeck, M., & Karstensen, J. (2017). From interannual to decadal: 17 years of boundary current transports at the exit of the Labrador Sea. *Journal of Geophysical Research: Oceans*, 122, 1724–1748. https://doi.org/10.1002/2016JC012271.Received

Zenk, W. & Morozov, E. (2007). Decadal warming of the coldest Antarctic Bottom Water flow through the Vema Channel. *Geophysical Research Letters*, 34(14), L14607. https://doi.org/10.1029/2007GL030340

Zhang, R., Sutton, R., Danabasoglu, G., Kwon, Y.-O., Marsh, R., Yeager, S. G., Amrhein, D. E., & Little, C. M. (2019). A review of the role of the Atlantic Meridional Overturning Circulation in Atlantic Multidecadal Variability and associated climate impact. *Reviews of Geophysics*, 57(2), 316–375. https://doi.org/10.1029/2019RG000644

Zunino, P., Lherminier, P., Mercier, H., Padín, X. A., Ríos, A. F., & Pérez, F. F. (2015a). Dissolved inorganic carbon budgets in the eastern subpolar North Atlantic in the 2000s from in situ data. *Geophysical Research Letters*, 42(22), 9853–9861. https://doi.org/10.1002/2015GL066243

Zunino, P., Pérez, F. F., Fajar, N. M., Guallart, E. F., Ríos, A. F., Pelegrí, J. L., & Hernández-Guerra, A. (2015b). Transports and budgets of anthropogenic CO2 in the tropical North Atlantic in 1992-1993 and 2010-2011. *Global Biogeochemical Cycles*, 29(7), 1075–1091. https://doi.org/10.1002/2014GB005075